- -

Atmospheric Studies of brown-Dwarfs and Exoplanets: Insights into Planet Formation and Evolution

- -

Lavie, Baptiste

UNIVERSITÉ DE GENÈVE   FACULTÉ DES SCIENCES

Département d'Astronomie   **Professeur David Ehrenreich**

UNIVERSITÉ DE BERNE   FACULTÉ DES SCIENCES

Center for Space and Habitability   **Professeur Kevin Heng**

Atmospheric Studies Of Brown-Dwarfs And Exoplanets: Insights Into Planet Formation And Evolution

THÈSE

présentée à la Facultè des sciences de l'Université de Genève

pour obtenir le grade de Docteur ès sciences,

mention Astronomie et Astrophysique

par

Baptiste LAVIE

de

Limoges (France)

Thèse N° 5286

GENÈVE

Observatoire Astronomique de l'Université de Genève

2018

DOCTORAT ÈS SCIENCES,
MENTION ASTRONOMIE ET ASTROPHYSIQUE

Thèse de Monsieur Baptiste LAVIE

intitulée :

«Atmospheric Studies of Brown-Dwarfs and Exoplanets: Insights into Planet Formation and Evolution»

La Faculté des sciences, sur le préavis de Monsieur D. EHRENREICH, professeur associé suppléant et directeur de thèse (Département d'astronomie), Monsieur K. HENG, professeur et codirecteur de thèse (Center for Space and Habitability, University of Bern, Switzerland), Monsieur G. MEYNET, professeur ordinaire (Département d'astronomie), Monsieur V. BOURRIER, docteur (Département d'astronomie), Monsieur A. LECAVELIER DES ETANGS, professeur (Institut d'astrophysique de Paris, France), Monsieur M. BONNEFOY, docteur (Institut de Planétologie et d'astrophysique de Grenoble, Saint Martin d'Hères, France), autorise l'impression de la présente thèse, sans exprimer d'opinion sur les propositions qui y sont énoncées.

Genève, le 26 novembre 2018

Thèse - 5286 -

Le Doyen

Summary

This manuscript presents the research that I have performed during the four years of my Ph.D. under the supervision of Kevin Heng (university of Bern) and David Ehrenreich (university of Geneva) within the NCCR PlanetS. I studied the atmospheric properties of exoplanets and brown-dwarfs. I used the carbon to oxygen ratio as a proxy to constrain their formation mechanisms and I studied their atmospheric escape, which is one of the mechanism that can affect their properties.

There are two major formation mechanisms for giant planets. The core accretion is a multi-steps scenario in which the composition of the companion's atmosphere depends on its position within the protoplanetary disk during those steps. The gravitational instability is a quick one step mechanism that form companions with a composition similar to the composition of the stellar nebula. Comparing the carbon to oxygen ratio of the companion to the one of its host star provides insight on how the companion has formed. I have developed an atmospheric retrieval code, named `HELIOS_R`, that combines an emission atmospheric model and a nested sampling algorithm. The code is able to retrieve the carbon and oxygen abundances of a companion's atmosphere. It was applied to giant planets. The C/O ratio of the massive brown-dwarf HD 4747 B is compatible with its host star value, which indicate a formation by gravitational instability. The planets of the HR 8799 system possess C/O values that are different from their host star indicating a formation by core accretion. No conclusion can be drawn for the direct imaged companions GJ 504 b and HD 206893 b as well as the hot Jupiter WASP-12 b. Atmospheric retrieval is a data-driven technique and it may not be possible to extract useful information from the data, the retrieval results are driven by the choice of the priors (our knowledge of the model parameters before observing the data). A sub-stellar object evolves during time and the composition of its atmosphere may change. To fully address the link between atmospheric properties and formation mechanism, it is necessary to understand the mechanisms that can affect the atmospheric properties of exoplanets and brown-dwarfs over time. Atmospheric escape is one of them. It is dimmed to be responsible of the dearth zones between the jovian planets and the super-Earths - the evaporation desert - and between the sub-Neptune and the super-Earth populations - the evaporation valley. I studied observations

done with the Hubble Space Telescope in the ultraviolet of two stars, GJ 436 and HD 219134 during the transit of their inner most planets. Spectroscopic data of the Lyα line of GJ 436 confirm the shape of the huge exospheric tail surrounding the warm Neptune GJ 436 b. I confirm that both mechanisms, radiative pressure and stellar wind interactions are needed to interpret the Lyα absorption signature observed during its transit. Detection of silicon in the escaping outflow corroborates that the state of the atmospheric escape is hydrodynamical. I obtained and analysed the first transit of a super-Earth in the far ultraviolet at a high resolution (~114'000). The star HD 219134 is the closest system known to have a close-in transiting super-Earth and is therefore very bright as seen from Earth. Variations of the flux correlated to the primary transit of the planet is observed in the Lyα line, which hints the presence of atmospheric escape mechanism. More observations is needed to fully understand the signals. This manuscript is structured as follow: chapter one gives the astrophysical context; chapter two provides the key concept of Bayesian inference, which has been an important tool for my studies; chapter three and four present the two aspects of my work, atmospheric retrieval and atmospheric escape.

RÉSUMÉ

Ce manuscrit présente la recherche que j'ai effectuée au cours de mes quatre années de doctorat sous la supervision de Kevin Heng (université de Berne) et David Ehrenreich (université de Genève) dans le cadre du PRN PlanetS. Celle-ci se focalise sur les propriétés atmosphériques des exoplanètes et des naines brunes. Plus particulièrement, j'ai utilisé le ratio des abondances en carbone et oxygène (C/O) en tant que proxy pour déterminer les mécanismes de formation de ces objets. J'ai aussi étudié l'échappement atmosphérique, qui est l'un des mécanismes pouvant affecter leurs propriétés atmosphériques.

Il existe deux principaux mécanismes de formation pour les planètes géantes. Le mécanisme d'accrétion de coeur est un scénario à plusieurs étapes dans lequel la composition de l'atmosphère du compagnon dépend de sa position dans le disque protoplanétaire au cours de ces étapes. L'instabilité gravitationnelle est un mécanisme rapide en une étape qui forme des compagnons avec une composition similaire à celle de la nébuleuse stellaire. La comparaison du C/O du compagnon avec celui de son étoile hôte permet d'estimer son mécanisme de formation. J'ai développé un code de "récupération atmosphérique" [atmospheric retrieval], nommé HELIOS_R, qui combine un modèle atmosphérique en émission et un algorithme d'échantillonnage imbriqué [nested sampling]. Le code est capable de récupérer les abondances de carbone et d'oxygène de l'atmosphère d'un compagnon. Il a été utilisé pour différentes planètes géantes. Le C/O de la naine brune massive HD 4747 B est compatible avec celui de son étoile hôte, ce qui indique que ce compagnon s'est formé par instabilité gravitationnelle. Les planètes du système HR 8799, en revanche, possèdent des valeurs de C/O différentes de leur étoile hôte indiquant une formation par accrétion. L'analyse des données des companions en imagerie directe GJ 504 b et HD 206893 b, ainsi que du Jupiter chaud WASP-12 b n'a pas permis de contraindre leurs C/O. La récupération atmosphérique [atmospheric retrieval] est une technique basée sur les données et il est possible que les données actuelles ne permettent pas d'extraire d'information utile. Les résultats de la récupération [retrieval] sont déterminés par le choix des probabilités à priori (notre connaissance des paramètres du modèle avant les données). Un objet sous-stellaire évolue dans le temps et la composition de son atmosphère peut changer. Pour comprendre le lien entre ses propriétés atmosphériques et

sa formation, il est nécessaire de comprendre les différents mécanismes qui peuvent affecter ses propriétés atmosphériques. L'échappement atmosphérique est l'un d'entre eux. Il est considéré en partie responsable des zones de carence entre les planètes joviennes et les super-Terre - le désert de l'évaporation - et entre les populations de sub-Neptune et de super-Terre - la vallée de l'évaporation. J'ai étudié des observations effectuées avec le télescope spatial Hubble dans l'ultraviolet de deux étoiles, GJ 436 et HD 219134 lors du transit de leurs planètes les plus internes. Les données spectroscopiques de la raie Lyα de GJ 436 confirment la forme de la vaste queue exosphérique entourant la Neptune chaude GJ 436 b. L'analyse confirme aussi que les deux mécanismes, la pression radiative et les interactions avec le vent stellaire sont nécessaires pour interpréter la signature d'absorption observée lors de son transit. La détection de silicium dans le flux de gas s'échappant confirme que l'échappement atmosphérique est de type hydrodynamique. J'ai obtenu et analysé le premier transit d'une super-Terre dans l'ultraviolet lointain à haute résolution (~114'000). L'étoile HD 219134 est le système le plus proche connu avec une super-Terre en transit et est donc très brillant vu de la Terre. Des variations du flux dans la raie Lyα, en corrélation avec le transit de la planète sont observées indiquant la présence d'un mécanisme d'échappement atmosphérique. Ce manuscrit est structuré comme suit: le premier chapitre donne le contexte astrophysique; le chapitre deux présente les concepts clés de l'inférence bayésienne, qui a été un outil important pour les différentes études qui sont présentées dans les chapitres trois et quatre - la récupération atmosphérique [atmospheric retrieval] et l'échappement atmosphérique respectivement.

AVANT PROPOS

Alors que je venais de poser ma voiture devant le parking de l'observatoire de Genève, une jeune fille d'une dizaine d'année m'interpelle - "Vous travaillez ici ?". L'enfant est montée sur un poney tenu par sa mère. Je réponds positivement avec une certaine fierté, ajoutant que j'étudie l'atmosphère des exoplanètes, planètes qui n'appartiennent pas à notre système solaire et qui tournent autour des étoiles que l'on voit dans le ciel. Bien loin d'être impressionnée, l'enfant me répond avec un certain aplomb : "A quoi ça sert ?". Je ne peux m'empêcher de lâcher un petit rire, nerveux. Je me lance avec enthousiasme dans les grandes phrases, les grands mots: "la quête du savoir", "l'avenir de l'humanité", "la recherche de la vie", "les retombées économiques, sociales, philosophiques et technologiques dans le futur", j'agrémente ce dernier point avec quelques exemples de recherches fondamentales qui ont débouchés sur des inventions concrètes ou qui ont motivés de nouvelles inventions pour l'humanité : le laser dont le principe est décrit en 1916, la théorie de la relativité dont l'une des applications les plus concrètes pour le grand public est le GPS, l'invention du web au CERN afin de faciliter le partage d'informations entre les différents scientifiques du consortium, la découverte de l'électron antérieur à l'industrie électronique, la découverte des ondes électromagnétiques par Hertz avec les considérations théoriques de Maxwell et leur application moderne en communications...bref, je lui dis que les applications directes issues de travaux en recherche fondamentale sont totalement imprévues au moment de leur publication. Elle me regarde avec des grands yeux. Je sors l'artillerie lourde et lui cite le russe Constantin Tsiolkovski, père de l'astronautique moderne : "La Terre est le berceau de l'humanité, mais qui a envie de rester toute sa vie dans un berceau ?". Sa bouche fait une petite moue de désapprobation. Elle ne me semble pas convaincue. Je lui lâche finalement que " j'éprouve du plaisir à réfléchir sur ces sujets et l'astronomie me fait rêver" et lui file un bonbon qui traîne dans ma poche. Elle me parait un peu plus convaincue. Je m'échappe vers mon bureau. Cette question reste dans ma tête. Elle est relativement récurrente. Je suppose que nombre de mes collègues doivent aussi y faire face. La recherche fondamentale est motivée par la curiosité, contrairement à la recherche appliquée qui vise à répondre à un problème particulier. Au vu des nombreux exemples qui existent, dont ceux donnés à cette petite fille, la recherche fondamentale me semble effectivement utile pour l'humanité. En revanche, il semble

évident que ces exemples souffrent du biais du "survivant". Pour chacun d'entre eux combien de travaux de recherche sans application ? La recherche en astrophysique est utile mais il me parait très difficile, voire impossible, de dire si une recherche précise sera utile pour l'humanité. La seule conclusion qui s'impose est donc celle-ci:

Cette thèse ne sert à rien.

Difficile d'écrire cela alors que nous vivons dans une société où tout doit être quantifiable, trié et classifié. Il faut être utile à la société à travers son travail. Performance. Compétition. La recherche mondiale n'y échappe pas. Il faut être le premier. Il faut être le meilleur. Publish or Perish. Seulement un doctorant sur dix restera dans l'académique. Dans cette course effrénée vers la réussite j'aimerais m'adonner ici à un petit peu de philosophie de comptoir. Rien n'est éternel. Nous mourrons tous. Les étoiles meurent. L'univers s'avance vers une mort lente par refroidissement. Le proton lui-même est condamné à se désintégrer. Tout à une fin. La vie se termine par la mort - nous avons la même destination. Seul le voyage est important. Profitons-en ! Let it go, même la reine des neiges le dit. La vie est un jeu, mieux vaut ne pas la prendre trop au sérieux.

Ainsi, cette thèse ne sert à rien mais j'ai apprécié le long voyage pour en arriver là et je souhaite donc remercier tous mes compagnons de voyage.

Aussi loin que je me souvienne, devenir astrophysicien était l'un de mes rêves. Au moment du lycée, les perspectives d'embauches n'étaient - déjà à l'époque - pas très optimistes. Partir pour huit années d'études sans être certain d'avoir un travail ne semblait pas être une bonne décision. Reniant en partie mes racines communistes, je me suis donc lancé vers le fer de lance du capitalisme mondial: les marchés financiers. J'ai intégré l'école de commerce de Toulouse avant de partir pour la "City" à Londres afin de travailler pour différentes banques d'investissement. Je n'y ai pas trouvé le challenge intellectuel que je recherchais. J'enchaînais les heures sans passion ni défi et m'enfonçais petit à petit dans un pseudo quotidien finalement peu gratifiant. C'est bien évidemment une femme qui va chambouler ce petit équilibre fragile - Chloé. Ma petite copine qui ne se satisfait pas non plus de son poste dans le département d'origination de la dette italienne décide, à l'inverse de moi, de faire quelque chose pour y remédier. Elle démissionne et prépare son départ pour Paris. Je décide de la suivre. She is the one. La décision de reprendre mes études s'installe solidement dans ma tête. Quelle inconscience ! Seule la présence de Chloé dans ma vie peut expliquer cette folie. Elle a su m'insuffler suffisamment de confiance en moi pour me lancer dans ce long projet. C'est donc elle, puis l'arrivée de nos enfants, Aliénor, à la fin de mon bachelor et Margaux, à la fin de mon master qui m'ont permis d'aller au bout de ces neuf années de reconversion. Elles sont toutes les trois ce qu'il y a de plus cher à mes yeux et ce long voyage n'a été possible que grâce à elles.

Je remercie bien évidemment mes parents, Nadine et Serge, même s'ils savent très bien que je me suis "fait tout seul". Ce long voyage vers la thèse c'est aussi le fruit de leur vie. Ils ont réussi à faire de moi un humain libre. Je ne les remercierai jamais assez. J'espère être capable de réussir avec mes enfants ce qu'ils ont réussi avec mon frère, Thomas et moi. Merci à toi aussi petit frère et à ta famille, Sabine, Noa et Zoé, même si nous sommes loin les uns des autres vous êtes toujours dans mon coeur. Merci Pascal d'avoir rejoint la famille et pour tout l'aide que tu as apporté tout au long de ce voyage. Je remercie toute ma belle famille, Sandrine, Cauris, Elodie, Pierre-Louis, Patricia et mes petits neveux Elia et Noam. Un merci particulier à Cauris pour m'avoir laissé remporter la totalité des championnats d'été, des coupes de printemps, d'hiver et autre Pessah cups pendant ces neufs années afin de regonfler mon ego pour tenir dans les moments douloureux de cette reconversion. Je n'oublie pas ceux et celles qui, pendant ce voyage, sont redevenus poussières d'étoiles. Je clôture ces remerciements familiaux avec un merci global à toute ma famille. Le monde est beau. Je suis pour la paix dans le monde.

Il me parait très difficile de faire une liste exhaustive de toutes les personnes qui ont traversé ma route pendant ces neufs années. Il y a celles qui sont encore présentes dans ma vie et celles que je ne vois plus mais chaque rencontre à su égayer mon voyage. J'aimerai faire un remerciement personnalisé à chacun d'entre vous mais soyons réaliste, ce manuscrit a déjà beaucoup trop de retard. Sans prise de risque et sans état d'âme, je me contente donc d'un GRAND MERCI :

Toi lecteur, si tu as croisé mon chemin entre 2009 et 2018 je te remercie pour ce voyage!

Afin de ne pas complètement mettre à mal le protocole je souhaite tout de même procéder aux remerciements académiques d'usage. Gardons à l'esprit que mes univers personnel et professionnel sont intimement liés et donc, bien que protocolaires, ces remerciements sont entachés de toute mon affection. Je remercie mes deux directeurs de thèse Kevin Heng et David Ehrenreich pour leur supervision tout au long de ces quatre années ainsi que Vincent Bourrier qui a pris à coeur son rôle de co-superviseur. Je remercie bien évidemment les membres de mon jury de thèse: Georges Meynet, Mickael Bonnefoy et Alain Lecavelier des Etangs.

CONTENTS

ATMOSPHERIC CHARACTERISATION OF STARS' COMPANIONS

- Vous dites ça en riant !

- Je le dis en riant parce que c'est

très sérieux.

Jules Renard

You Know Nothing, Jon Snow

Ygritte

1.1   Context : Atmospheric studies

How does knowledge pass from one generation to another ? Isaac Newton, in a letter to Robert Hooke, wrote in 1675 "if I have seen further, it is by standing on the shoulders of giant" (Newton 1675). The origin of this metaphor can be dated at least back to the twelfth century. It was attributed to Bernard of Chartres by John of Salisbury, in 1159: "Bernard of Chartres used to compare us to dwarfs perched on the shoulders of giant. He pointed out that we see more and farther than our predecessors, not because we have keener vision or greater height, but because we are lifted up and borne aloft on their gigantic stature." The real purpose of Newton to use this citation is questionable (Hawking 2004, see also the preface by Jean-Pierre Luminet of the

french version). But, after four years in academia, this citation definitely echoes to me. The increase of our global knowledge is done incrementally, small steps at a time. This is especially true for modern science.

In this chapter, I want to introduce some astrophysical context and set the proper background to assess and understand the scientific goals of my Ph.D. work. I do not intend to explain extensively the global context of the science of exoplanets and brown-dwarfs. I also will not be exhaustive on atmospheric studies as I would rather focus on the questions that have driven my research and my (small) contribution to science.

1.1.1   Purpose of this thesis

Astrophysics or astronomy is the science that studies the celestial objects ("in the sky"). A growing field in astronomy is the science of planets outside our solar system (a.k.a. exoplanets). From the first discovery in 1992 (Wolszczan & Frail 1992) and 1995 (Mayor & Queloz 1995), exoplanetology has moved from a detection era towards an age of characterisation of the many exoplanets discovered since then. In parallel to this prosperous field, the science of brown-dwarfs was also booming with an increasing number of detections. Those objects lie between the realm of stars, which sustain the burning of their hydrogen and the realm of planets, which do not burn their deuterium. Brown-dwarfs were theorised in the 1960s (Kumar 1963, 1964) but only discovered in the 1990s.

Brown-dwarfs and planets are substellar objects and share the common property of having an atmosphere. Their atmospheres are accessible to us with direct or indirect observations and the study of its properties is the subject of this thesis. I, especially, focused on objects in a hot regime in regards to typical solar-system objects temperature. The leading scientific questions that have driven my analysis of a couple of those objects are of two types :

- the link between their atmospheric properties and their formation mechanisms.
- their stellar environment and the escape of their atmosphere.

There is a huge diversity among brown-dwarfs and planets in terms of radius, masses, compositions, orbital parameters and host stars properties. The observational techniques are diverse as well : ground based or spatial, high or low spectral resolution, emission or transmission spectroscopy. Different parts of those objects are probed and at different stages of their evolution depending on the observational technique. Characterisation of brown-dwarfs atmosphere benefited from the work done by stellar astrophysicists. And similarly, the characterisation of exoplanets atmosphere benefited from the brown-dwarfs community. Nowadays, the studies of the atmosphere of brown-dwarfs and exoplanets is very partitioned with group of specialists focusing in their realm of expertise on specific objects depending on the observational technique.

Specialisation is a dominant process in every branch of science. However, mingling among specialists is important in order to diffuse ideas and trigger cross-enrichment development.

As a shared Ph.D. between a theoretical group at the university of Bern and an observational group at the university of Geneva I had the chance to evolve in a cross-field manner within atmospheric studies of substellar companions. The brown-dwarfs and exoplanets that I have studied span a diverse range of properties both in their physical conditions and the observational techniques used to study them. Those objects are plotted in a traditional mass to semi-major axis population figure, Fig. 1.1. The objects observed with the direct imaging technique, HR8799b,c,d,e, HD 4747 B, GJ 504 b and HD 206893 b are young and orbit quite far from their host stars. They are observed in the infrared and most of the energy they emit comes from their cooling. The close-in objects, WASP-12 b, GJ 436 b and HD 219134 b are older and most of the energy they radiate comes from their host stars. They are observed with the transit technique, which allows to obtain transmission spectroscopy (HD 219134 b,GJ 436 b) or emission spectroscopy (WASP-12 b). Secondary eclipse observations in the infrared allow to probe the emission day-side of the companion (WASP-12 b). Transmission spectroscopy in the far-ultraviolet of HD 219134 and GJ 436 is used to study the host star properties and observed atmospheric escape on their orbiting planets. The mass of those objects can be well constrained (HD 4747 B, HD 219134 b,GJ 436 b,WASP-12 b) with radial velocity observations or poorly constrained in the absence of velocimetry data (HR8799b,c,d,e, GJ 504 b and HD 206893 b). Radii of those objects stretch from a couple of Earth radius for the super-Earth HD 219134 b to almost two Jupiter radii for the very inflated hot Jupiter WASP-12 b. The different wavelength range at which the objects are observed allow to probe their deep atmosphere (infrared - WASP-12 b, HR8799b,c,d,e, HD 4747 B, GJ 504 b and HD 206893 b) up to their exosphere (FUV - HD 219134 b and GJ 504 b).

On one hand, analysis in the infrared allowed me to assess the atmospheric composition to evaluate the link with the formation mechanism - WASP-12 b, HR8799b,c,d,e, HD 4747 B, GJ 504 b and HD 206893 b. Those observations are in emission, the flux emitted by the objects is measured. On the other hand, analysis in the far-ultraviolet probed the stellar environment and allow the detection and characterisation of the atmospheric escape of the planets. Those observations are done in transmission, the light of the star is observed, eventually filtered by the object's atmosphere.

Those cross-field studies are represented on Figures 1.1 to 1.4, which show the diversity of those objects as well as their common properties.
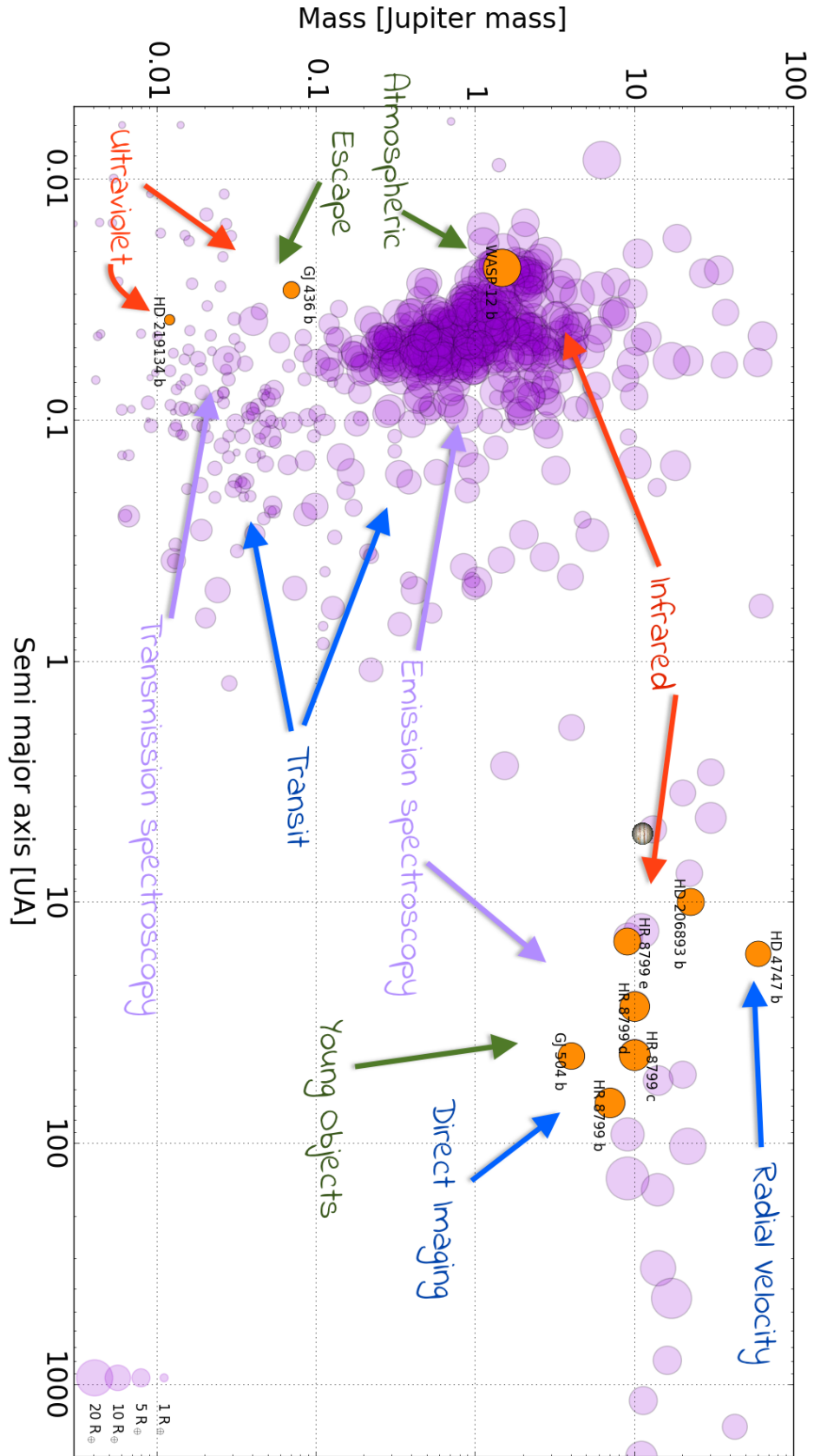
Figure 1.1: Road map of the thesis: Mass as a function of the semi-major axis. The objects in orange are the planets or brown-dwarfs analysed in this thesis. The size of the marker are proportional to Earth's radius.
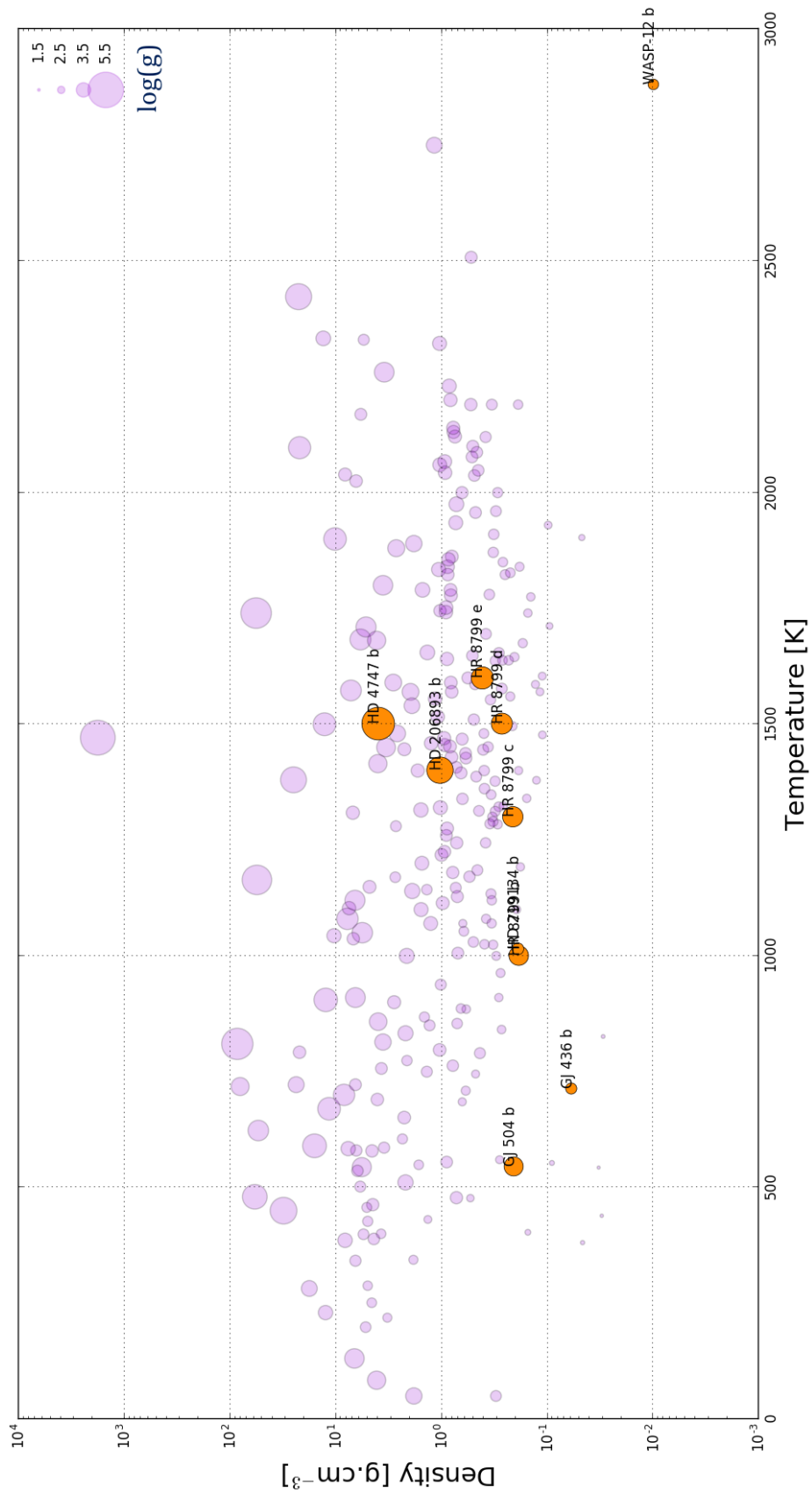
Figure 1.2: Road map of the thesis: Density versus effective temperature. The size of the circles are proportional to the surface gravity of the object.
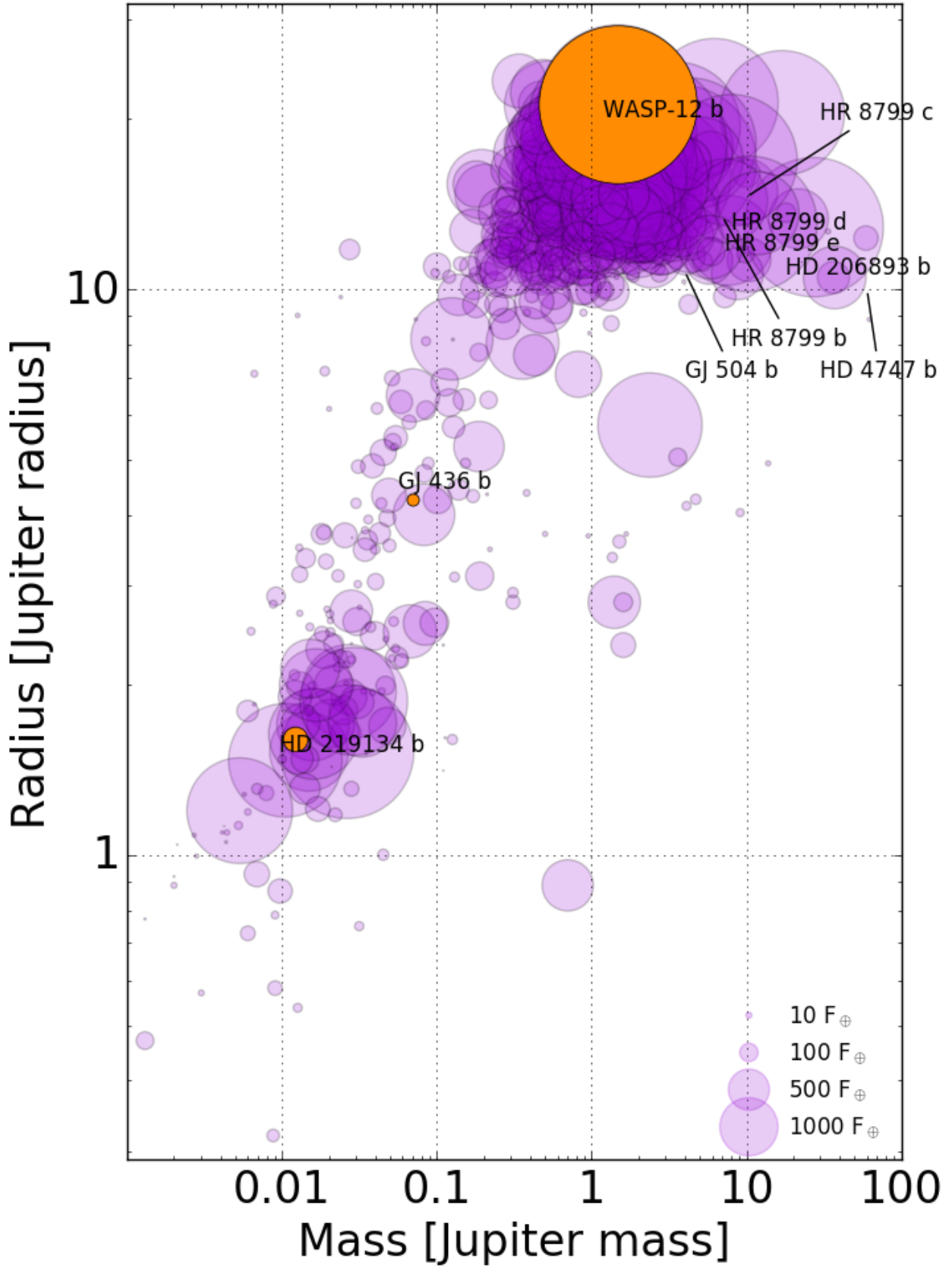
Figure 1.3: Road map of the thesis: mass-radius relationship. The circle are proportional to the incident flux.
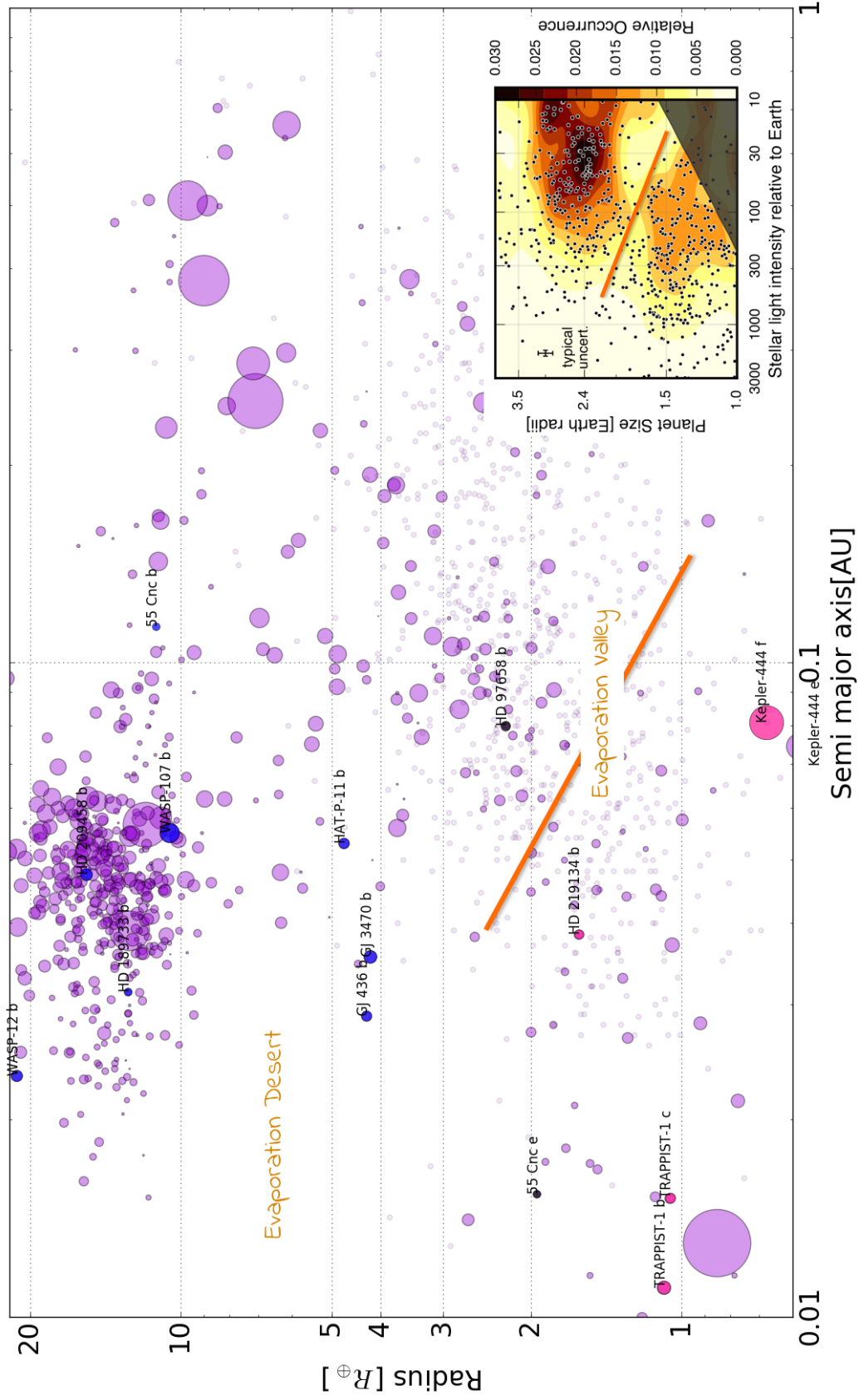
Figure 1.4: Road map of the thesis: the evaporation desert and the valley. Subplot: The evaporation valley from Fulton & Petigura (2018). Blue circles are planets that are know to endure atmospheric escape. Black points are planets observed that do not show endure atmospheric escape. Pink points are planets for which flux variation have been observed and need confirmation.

1.1.2   But, what objects did I really work on?

The first task in an astrophysics research manuscript is to define the physical objects that have been studied.

   The international astronomical union (IAU) has defined in 2006 that a planet in the solar system is "a celestial body that (a) is in orbit around the Sun, (b) has sufficient mass for its self-gravity to overcome rigid body forces so that it assumes a hydrostatic equilibrium (nearly round) shape, and (c) has cleared the neighbourhood around its orbit ". Applying this definition to exoplanets is not straight forward as changing point (a) to "is in orbit around a star" directly includes brown-dwarfs and exclude planetary-mass object around brown-dwarfs (i.e. 2M 1207-39 b, Chauvin et al. 2004) or free-floating planets (Lucas & Roche 2000; The Microlensing Observations in Astrophysics (MOA) Collaboration & The Optical Gravitational Lensing Experiment (OGLE) Collaboration 2011; Gaudi 2012). The question of distinguishing planets, brown-dwarfs and low-mass stars is still pending and no consensus has been reached yet (Boss et al. 2003; Bonnefoy & Chauvin 2013; Pinfield et al. 2013). It is known since the 1960s (Kumar 1963, 1964) that there is a lower edge to the stellar branch and a minimum mass for stable hydrogen burning ($\sim 75\ M_{jup}$), defining the upper limit of the brown-dwarf regime. Similar to this idea, the lower limit is defined by the deuterium-burning limit ($\sim 13\ M_{jup}$) (Shu et al. 1987; Bonnefoy & Chauvin 2013), which indicates the distinction between brown-dwarf and planets. As detailed modelling has allowed the estimation of the mass for both boundaries, the mass is often used as the natural discriminatory criterion to establish the classification of an object. The advantage of this definition is that it gives a well-defined boundaries : an exoplanet is below < 13 M_{Jup} and a star is > 75 M_{Jup}. In between lies the kingdom of brown-dwarfs. However, the masses derived for the deuterium and hydrogen burning limits depends on the assumptions of the model (see for example the metallicity dependancy of the hydrogen burning limit Chabrier & Baraffe 1997). Moreover, determining the mass of an object, especially direct-imaged objects remains challenging - the one sigma uncertainties on the mass of HR 8799 companions are of the order of 50%. Therefore, some studies suggest to use the formation mechanism as a tool to distinguish brown-dwarfs from planets (Burrows & Liebert 1993; Chabrier et al. 2007). For this criterion, a brown-dwarf form by gravitational instability in a disk or in a gas cloud and a planet form by core accretion. Although the distinction can be useful theoretically, it is very difficult nowadays to assess on the observational side and so the definition remained unusable in practice. New generation of instruments coupled with our increasing knowledge on those objects (retrieval of abundances, orbitals properties etc.) may help on this matter. Nevertheless, adopting this definition will invalidate the distinction based on deuterium-burning as formation by core accretion can produce massive objects above the

deuterium-burning mass. Others interesting criterions have been suggested such as the object equation of state (Boss et al. 2003) but yet have not close the debate.

I do not intent in this work to rule on the matter. For the purpose of this thesis, I will considered **substellar objects that are not fusing their hydrogen and that are bounded to a host star**. I use exoplanet and brown-dwarf when the identity of the object is not very controversial (for example a 4 Earth-mass object orbiting a star is -must be- a planet); I use companion or object to include both types and I use "a substellar object or companion" if doubts on the true nature of the object are legitimate.

The first exoplanets were discovered in 1992 around the pulsar around PSR B1257+12 (Wolszczan & Frail 1992) . In 1995, Michel Mayor and Didier Queloz discovered the first exoplanet around a sun-like star : 51 Pegasi b (Mayor & Queloz 1995). Incidentally, the first genuine brown-dwarfs were also discovered in 1995 (Rebolo et al. 1995; Nakajima et al. 1995). Despite their prediction in the 1960s (Kumar 1963, 1964), brown-dwarfs are very difficult to observe because most of the energy of gravitational contraction is radiated away very quickly (within 10^8 years, Nakajima et al. 1995). Finding and observing exoplanets and brown-dwarfs is a very challenging task because of the huge distance scales in the Milky Way and because they are very faint objects compared to stars. However, the accepted rule is that the majority of stars comes with a planetary system (Cassan et al. 2012; Mayor et al. 2011). When I started my Ph.D. in September 2014, there were around 1000 objects discovered. At the precise moment of submission of this manuscript on November the 1st, there are 3823 objects distributed in 2858 systems. With the systematic search by robotic telescope on the ground (i.e. NGTS) and with the launched of the next spatial missions (i.e. TESS, CHEOPS, PLATO) those numbers are probably going to continue rising.

1.1.3   What is an atmosphere?

The word 'atmosphere' is derived from the greek "atmos" and "sphaira", meaning vapour and sphere. In everyday life, we are all very familiar with what the atmosphere of Earth is. We are breathing it : 78% of nitrogen, 21% of oxygen and about 1% of trace gas such as carbon monoxide, methane, water vapour etc. For a terrestrial planet the atmosphere is the gas layer extending from the ground, the surface of the core, towards space. Giant companions, from brown-dwarfs to Neptune sizes planets, are composed mainly of gas and a solid core may not always exist (Guillot et al. 1997). Following the etymology of the word 'atmosphere', the entire companion can be considered as an atmosphere. More conservatively, like for stars, one can consider that the atmosphere of hydrogen-helium dominated objects starts at the layer where the gas becomes optically thin to visible light. That definition actually also suits well the definition of terrestrial planet's atmosphere.
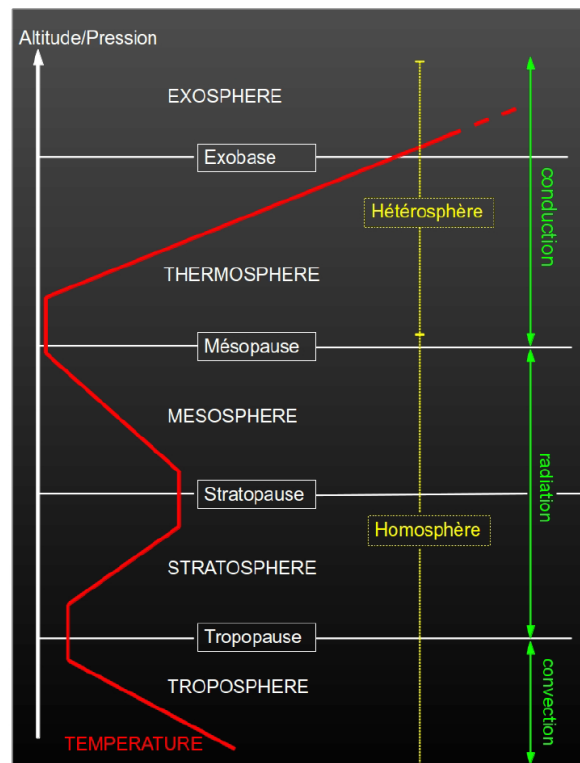
Figure 1.5: Vertical structure of the Earth' atmosphere.

The general vertical description of an atmosphere is mostly derived by the study of Earth's atmosphere. The different layers that compose it can be distinguished using different criterions:

- The temperature gradient, which defines the troposphere, stratosphere, mesosphere and thermosphere.
- The energy transport mechanism by convection, radiation or conduction.
- The theory used to describe the gas, either fluid mechanics or kinetic theory. It defines the barosphere, where the atmosphere can be described as a fluid and the exosphere, where modelling of the particles is necessary.
- the vertical change of composition : the homosphere, where the gases are well-mixed and the composition is relatively constant and the heterosphere, where the chemical composition is stratified according to the molecular weight.

Earth atmosphere is very well known compared to the atmosphere of objects outside our solar system. The view of Figure 1.5 is therefore probably very geo-centric. However, it gives an interesting view of the different regimes that could exist in an atmosphere. The distinction between the two leading scientific questions of my Ph.D. presented in the previous section also appears in terms of which part of the atmosphere is being studied. For the objects studied

by emission observations via direct imaging or secondary eclipses, the lower atmosphere is probed. In that region, the hydrostatic equilibrium $dP = -\rho g dz$ hypothesis is met, with P the pressure, ρ the density, g the surface gravity and z the altitude. Whereas, observations to study atmospheric escape probe the upper atmosphere (upper thermosphere and exosphere) where the gas cannot be considered as a fluid and a kinetic model of the gas particles is needed. This distinction also appears in terms of wavelength coverage of the observations (figures 1.1 and 1.2). The lower atmosphere is probed with the infrared (from 0.9 μm onwards) part of the spectrum and the upper atmosphere is mostly probed with the ultraviolet (from 0.4 μm inwards). The recent detection of helium with the Hubble Space telescope (*HST*) showed that the upper atmosphere can also be observed with near-infrared observations (Spake et al. 2018).

1.2 Observations in emission and transmission

Who was first, the observer or the theoretician? My conviction is that it was the observer. The solid ground of atmospheric studies presented in this work are observations. For the point of view of this thesis, spectroscopy and photometry observations hold the same type of information: some flux integrated over a certain wavelength band - broad for photometry, narrower for spectroscopy. Observations used in this work are of two types, the measurement of the emission spectrum of a light source (the companion or the star) or the transmission spectrum of the companion. Emission observations record the intensity of light emitted by the companion's atmosphere or by the star. Transmission observations record the light of the star filtered by the companion's atmosphere. A final possibility is to record the flux of the star reflected by the atmosphere of the companion but it has not been used in this thesis. In order to obtain those observations, the direct imaging and transit methods have been used. The direct imaging technique provides the emission spectrum of the companion and eventually the star (not relevant for this thesis). The transit technique provides the emission spectrum of the star, the transmission spectrum of the companion and eventually the emission spectrum of the companion if observed at the secondary eclipse point (Fig. 1.7).

1.2.1 Direct imaging

The direct imaging technique is the most natural method to detect star companions as it consists of taking a picture of those companions. However, planets or brown-dwarfs are very dim compared to the brightness of their host star. Therefore it is extremely difficult to image them and only a handful of planets and a couple of brown-dwarfs have been detected so far with this technique. The first object detected by Chauvin et al. (2004) via this technique was a planetary-mass orbiting a brown dwarf. The typical brightness contrast between the companion and its

host star ranges between 10^{-6} to 10^{-9}. The hotter the companion, the better the contrast is. The wider the separation, the easier the detection is. Therefore, the technique favours young objects at wide separation, which are hot because they did not have time to cool yet. The last generation of instruments such as the Spectro-Polarimetric High-contrast Exoplanet REsearch instrument (SPHERE) installed on the VLT at Paranal and the Gemini Planet Imager (GPI) installed on the Gemini South Telescope both in Chile allows to retrieve spectroscopic observations of direct imaged objects at low spectral resolution. If the object has been observed long enough, one can extract the mass of the companion using its motion around the central star. However, the direct imaging technique favours objects with long period. The field is still young enough that the uncertainties on the mass on all current detection remains too high to be useful for atmospheric studies. As part of my work on atmospheric retrieval (Chapter 3), I had the opportunity to work on several of those objects. The HR 8799 system is unique in a sense that it is the only direct imaged system with four planets orbiting the same star. It is therefore an extraordinary laboratory to do planets comparative studies. The massive brown-dwarf HD 4747B is detected by direct imaging but also in radial velocity with a long baseline, which allows a very good constraint on its mass. I have developed an atmospheric retrieval code named HELIOS R. Retrieval analysis on those systems led to two papers published in peer review journals:

- HELIOS-RETRIEVAL: An Open-source, Nested Sampling Atmospheric Retrieval Code; Application to the HR 8799 Exoplanets and Inferred Constraints for Planet Formation (Lavie et al. 2017b).

- Orbital and spectral analysis of the benchmark brown-dwarf HD 4747B (Peretti et al. 2018).

Retrieval analysis on two more direct imaged objects, HD 206893 b(Delorme et al. 2017) and GJ 504 b (Bonnefoy et al. 2018), were also done but did not procure significant contribution to the characterisation of the companion's atmosphere. The current wavelength coverage of the data on those two objects and the uncertainties attached to the observations do not allow for a robust extraction of information with a retrieval technique.

1.2.2 Transit

A transit occurs when the companion passes in front of its host star as seen from the observer view (see Fig. 1.7). The first exoplanet confirmed to transit its host star was the hot Jupiter HD 209458b (Mazeh et al. 2000; Charbonneau et al. 2000) although the first transiting detection may be β Pictoris b in 1981 (Lecavelier Des Etangs et al. 1994; Lecavelier des Etangs & Vidal-Madjar 2009). Knowing the radius of the host star (R_{star}), the radius of the companion (R_{comp}), the semimajor axis (a) and the orbital eccentricity of the planet (e), the transit probability

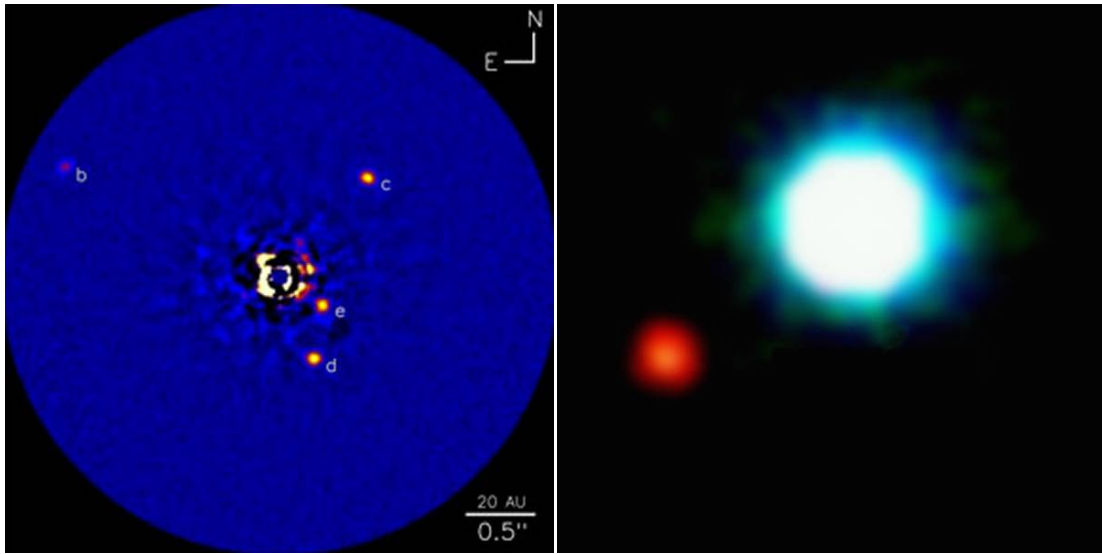**Figure 1.6:** Direct imaged of the first system obtained with this technique (2MASSWJ 1207334-393254, Chauvin et al. 2004) and of the HR 8799 system (left, Marois et al. 2010) . The HR 8799 is the only imaged system with four companions. It provides a unique opportunity to perform comparative studies.
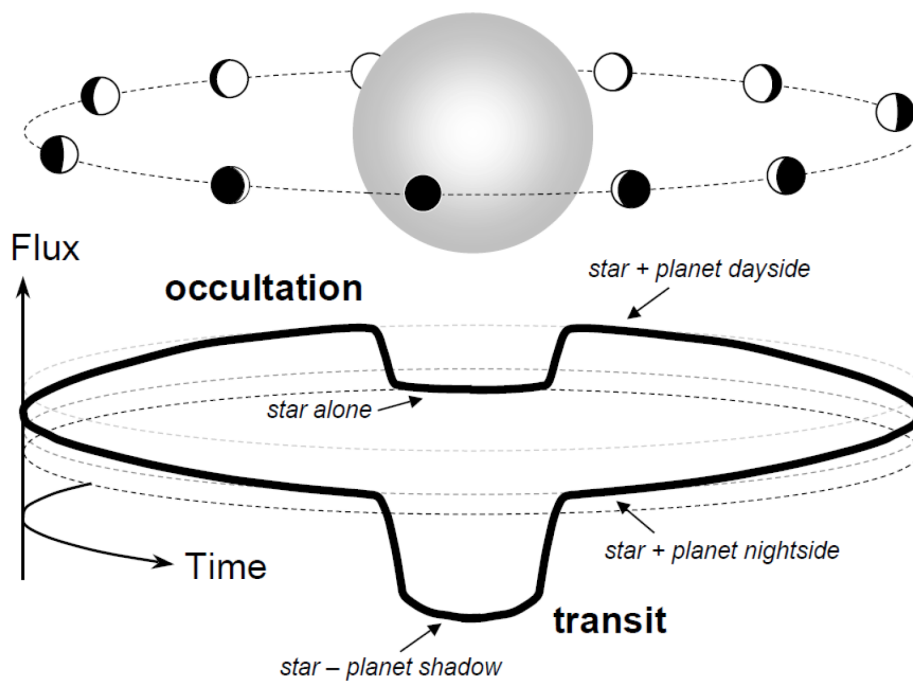
Figure 1.7: Flux variation as a function of time of a transiting planet. Source: Winn (2010)

(including grazing eclipses) is given by (Winn 2010) :

$$p_{transit} = \frac{R_{star} + R_{comp}}{a} \frac{1}{1 - e^2} \qquad (1.1)$$

For Earth and Jupiter around the sun the probability of transit is therefore less than 0.5% and 0.1%, respectively. For a Jupiter orbiting at short distance (0.1AU) of a sun like star, the probability increases to $\sim$ 5%. This technique thus favours large planets at short orbital distances from their host stars. A number of astrophysics events can mimic a companion transit (Santerne et al. 2013), which imposes the need of a confirmation using radial velocity. The radial velocity technique consists of using the Doppler effect of the light emitted by the star to measure its motion when orbited by a companion, see Lovis & Fischer (2010) for more insight on this technique.

The main output of the transit technique for the atmospheric studies is the transmission spectrum of the companion and the emission spectrum of the star. If the transmission spectrum is observed as a function of time then one can compute a light curve. It corresponds to the integrated flux of the star in a given wavelength range as a function of the orbital phase of the planet. In a wavelength band corresponding to a specific spectral feature of a chemical compound (i.e. the Lyα line of neutral hydrogen, D lines of neutral sodium etc.) one can observe an absorption during the transit of the companion indicating the presence of this species in the companion's atmosphere. If observed on a broad wavelength range, the transit technique can help to define the lower limit of the companion's atmosphere. Commonly when the broad wavelength range is in the visible the light curve is named "white" or "optical" light curve. It defines the optical radius of the companion, similar to the definition of Earth atmosphere. The absorption depth δ (i.e. the depth of the transit light curve) is proportional to the square ratio of the companion radius R_{comp} and host star radius R_{star} :

$$\delta \approx (\frac{R_{comp}}{R_{star}})^2 \qquad (1.2)$$

Combining the transit and the radial velocity techniques allow the determination of the mass and the radius of the companion. In atmospheric models (emission or transmission) of the lower atmosphere, those two quantities are used to compute the surface gravity, which play an important role in the shaping of the spectral features. The surface gravity parameter cannot be well constrained with sparse wavelength coverage and low resolution spectroscopy observations. Having an independent measurement of those two quantities helps to solve the degeneracy produced by the lack of knowledge on the surface gravity (see Section 3.3). For models of the exosphere the surface gravity is less important as the state of the atmosphere is not in the hydrodynamic regime.

The transit technique is a very powerful tool to extract information on a system (both the host star and the orbiting companions) with TTV, transmission spectroscopy, phases curves and the Rossiter-McLaughlin effect.

As part of my research, this method was used in the far ultraviolet (FUV) for GJ 436 and HD 219134 to study two planets orbiting those stars, a warm Neptune GJ 436 b and a super-Earth HD 219134 b. The retrieval code applied to the direct imaged objects was used with secondary eclipse observations (occultation in Fig. 1.7) in the near-infrared for WASP-12 b. It led to two two papers published to peer review journals:

- The long egress of GJ 436 b's giant exosphere (Lavie et al. 2017a).
- Retrieval analysis of the emission spectrum of WASP-12 b: sensitivity of outcomes to prior assumptions and implications for formation history Oreshenko et al. (2017).

and one paper in preparation (Lavie 2018).

1.3 Probing companions' atmosphere with emission observations

1.3.1 Formation and atmospheric properties

In this thesis, the scientific framework driven by the observations of emission spectrum is the link between the atmospheric properties of the companions and their formation mechanism. In this section I introduce the two schemes to form giant companions: the core accretion scenario and the gravitational instability. I then discuss how the carbon abundance, the oxygen abundance of the companion and their ratio (C/O) can be use to distinguish those different scenarios when compared to the abundances of their host star.

1.3.1.1 Core Accretion

The starting block of the core accretion scenario is a planetesimal of 1-100 km size. Although the processes to create those planetesimals from dust grains is not fully understood, the presence of those old objects in the solar system (in the asteroids belt for example) indicates their presence at an early stage of the planet formation mechanism.

In the classical form of this scenario (Pollack et al. 1996), this planetesimal goes through three phases :

- phase 1- accretion of solid materials
- phase 2- smooth accretion of a gas envelope
- phase 3- runaway accretion of gas

A critical core mass (M_{crit}) triggers a fast accretion of the surrounding gas, namely the runaway accretion phase. It depends on the protoplanetary disk parameters such as the opacity
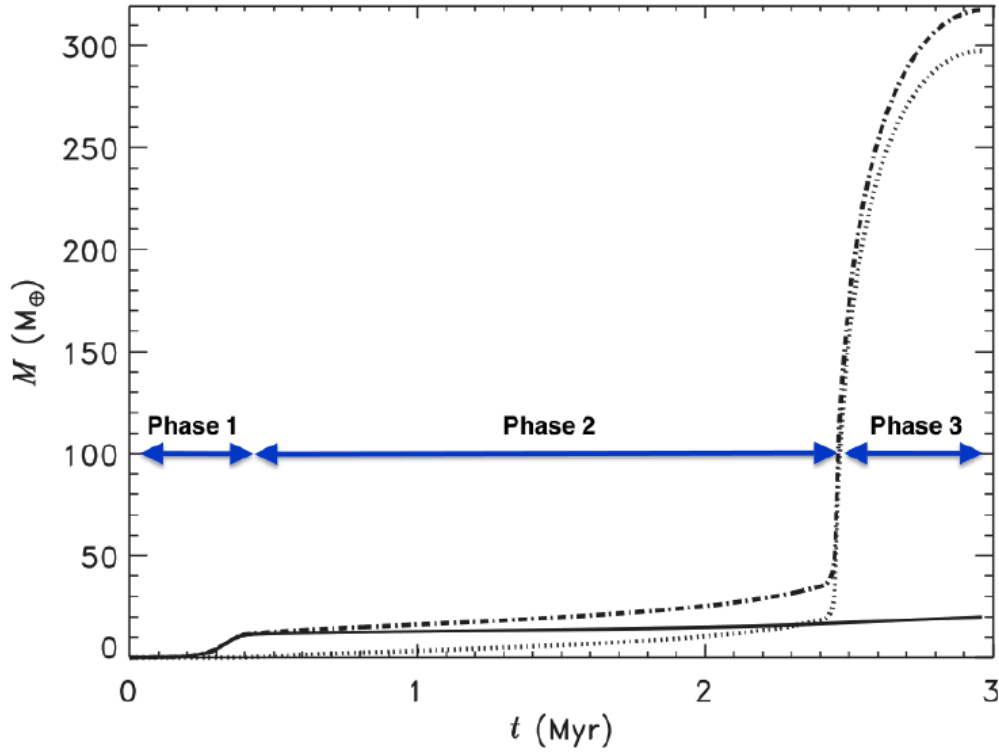
Figure 1.8:   A formation model of Jupiter from DAngelo & Lissauer (2018) (adapted from Lissauer et al. (2009). The solid line represents the mass of heavy elements in the condensed core. The dotted line represents the mass of hydrogenhelium in the envelope. The dash-dot line indicates the total mass of the planet.

and the core's accretion rate (Piso et al. 2015; Rafikov 2006). It is usually given as 10 Earth mass ($M_\oplus$). In order to form a gas giant, this critical mass needs to be reached within the lifetime of the gas disk. In the classical approach where the core grows through the accretion of planetesimals, this critical core mass can be reached for objects within a distance of less than 10 AU. However, growth timescales beyond this limit become longer than the disk dispersal timescale. The presence of giant objects past this distance (the HR 8799 system for example) has therefore triggered the emergence of a new growth mechanism taking into account the interaction between solid bodies and the gas disk : pebble accretion (Ida et al. 2016; Lambrechts & Johansen 2014, 2012; Levison et al. 2015; Morbidelli et al. 2015; Ormel & Klahr 2010; Ormel & Kobayashi 2012; Perets & Murray-Clay 2011; Rosenthal et al. 2018; Visser & Ormel 2016; Xu et al. 2017). However, pebble accretion may be too efficient and models need to be finely tuned to prevent any object to systematically reach the critical core mass and hence endure the runaway accretion phase. The core accretion scenario is not fully understood and investigation is still needed.

In any case, for the purpose of atmospheric characterisation of companions we will retain

that the core accretion scenario is a multiple steps process that can lead to a wide range of atmospheric compositions depending on where and when those different steps occurred in the disk.

1.3.1.2 Gravitational instability

The formation by disk instability of companions is similar to the formation of a star: a gravitational instability occurs in the gaseous medium that lead to fragmentation and to the formation of a self-gravitating clump. Historically, the giant planets of the solar system were thought to have formed by this process (Kuiper 1951). Departure from the classical Jeans instability, in rotating disks, arise from the differential rotation of the gas that prevents its collapse. Gravitational instabilities in a differentially rotating disk is governed by the Toomre stability parameter (Toomre 1964):

$$\mathcal{T} = \frac{c_s \Omega}{\pi G \Sigma} \tag{1.3}$$

where c_s is the speed of sound in the gas (which is proportional to the square root of the temperature), Ω is the epicyclic frequency (linked to the rotation frequency of the disk), G is the gravitational constant and Σ is the surface density of gas in the disk. A higher temperature (hence a higher c_s and a faster rotation (higher Ω) tends to prevent the gas to collapse, while a higher gas surface density Σ favours collapse. The higher the value of $\mathcal{T}$ is, the more stable that region of the disk is. The gravitational collapse is expected in the disk when the Toomre parameter is inferior to some critical value $\mathcal{T}_{crit}$, $\mathcal{T} < \mathcal{T}_{crit}$. This critical value depends on what is driving the instabilities, for axisymmetric perturbations $\mathcal{T}_{crit} = 1$ and for non-axisymmetric perturbations $1 < \mathcal{T}_{crit} < 2$. This condition is difficult to meet near the star as the temperature is too high and the rotation of the gas too fast. Simulations indicate that fragmenting the disk at several tens of AU is possible(Rafikov 2005; Rogers & Wadsley 2011; Durisen 2011) . The evolution of the instabilities in the gas is controlled by gas cooling. The entire process of cooling, contraction and finally collapse of the clumps of gas to a protoplanet happens very quickly, on a typical timescale of less than a million years.

For our purpose we will retain that formation by disk instabilities is a very quick one step process resulting in the composition of the planet to be similar to the composition of the gas.

1.3.2 Carbon to oxygen ratio : linking atmospheric properties to formation scenario

The idea of comparing a planet composition with that of its host star in order to appreciate its formation mechanism has been around for some times especially in the planetary science

community : "*The composition of the planets [...] differs appreciably from that of the sun...A comparison of the planetary composition with the [sun] composition will therefore [...gives] many clues to the condensation process itself.*" (Kuiper 1951). The oxygen and the carbon are respectively the third and fourth most abundant elements in the universe (Table 1.1) after hydrogen and helium. Those two elements are both produced by Type Ia and Type II supernovae. Their abundances in stars have been measured for decades by stellar astrophysicists, especially with regards to the iron abundance in order to probe the chemical enrichment past of the Galaxy (Clegg et al. 1981; Laird 1985; Tomkin et al. 1992; Wheeler & Sneden 1989; Takeda & Honda 2005). As stars are bright, it is relatively easy to obtain high resolution (> 50'000) spectrum that allow observers to resolve carbon and oxygen atomics lines individually (Schuler et al. 2011; Teske et al. 2013, 2014).

The importance of the C/O ratio on the composition of circumstellar grains and the atmospheric properties of star has been pointed out as early as in the 1960s (Suess 1962; Gilman 1969; Lambert 1968; Larimer 1975) . The discovery of the first circumstellar disk in 1980 by Smith & Terrile (1984) confirmed the existence of protoplanetary disk of dust and gas around stars inferred by theory.

Apart from very extreme object such as KELT-9b (Gaudi et al. 2017), most giant planets are colder than the coolest star. Carbon and oxygen are thus mostly trapped in molecules and do not exist in there atomic form. Moreover, it is highly difficult to obtain high quality, high resolution data for exoplanets with the current observing facilities and the methods developed to establish abundances in stars' atmosphere are not well suited. The carbon and oxygen abundances are therefore derived using proxies such as the abundances of molecules bearing those elements. In the case of hot objects such as hot Jupiters or young imaged companions the main absorbers in the infrared are the water (H_2O), the carbon monoxide (CO_2), the methane (CH_4) and the carbon dioxide (CO_2). They contribute the most to the emission or absorption features in the spectrum because they have high opacities and are expected from chemistry theory. The carbon and oxygen can be derived from the mixing ratios, i.e. the abundance of those molecules relative to the total abundance of hydrogen:

$$C/H = \frac{X_{CO} + X_{CO_2} + X_{CH_4}}{2X_{H_2} + 4X_{CH_4} + 2X_{H_2O}},$$
$$O/H = \frac{X_{CO} + 2X_{CO_2} + X_{H_2O}}{2X_{H_2} + 4X_{CH_4} + 2X_{H_2O}}. \tag{1.4}$$

With X_i the mixing ratio of molecule i. Once the abundances of carbon and oxygen of the host star and the companion have been determined, the C/H, the O/H and the C/O ratio ($C/O = (C/H)/(O/H)$) can be used as a proxies to determine where the object has formed and from which mechanism. As it is a quick on step process, we expect gravitational instability to

Table 1.1: From Asplund et al. (2009). Comparison of the proto-solar abundances from (^{a}) Grevesse & Sauval (1998) and (^{b}) Asplund et al. (2009) with the abundances from nearby B stars (^{c}) Lanz et al. (2008); Morel et al. (2006); Przybilla et al. (2008) and H II (^{d}) Chiappini et al. (2003); Esteban et al. (2005, 2004). The H II numbers include the estimated elemental fractions tied up in the dust; the dust corrections for Mg, Si and Fe are very large and thus too uncertain to provide meaningful values. Given in the last column is the relative abundance of the element from the first column. See Asplund et al. (2009) for more information.

Elem.	Sun^a	Sun^b	B stars^c	H II^d	Relative abundance
H			12		91.160 %
He	10.98±0.01	10.98±0.01	10.98±0.02	10.96±0.01	8.706 %
O	8.87±0.06	8.73±0.05	8.76±0.03	8.80±0.01	0.068 %
C	8.56±0.06	8.47±0.05	8.35±0.03	8.66±0.06	0.033 %
Ne	8.12±0.06	7.97±0.10	8.08±0.03	8.00±0.08	0.012 %
N	7.96±0.06	7.87±0.05	7.76±0.05	7.85±0.06	0.008 %
Mg	7.62±0.05	7.64±0.04	7.56±0.05		0.004 %
Si	7.59±0.05	7.55±0.04	7.50±0.02		0.004 %
Fe	7.55±0.05	7.54±0.04	7.44±0.04		0.003 %
S	7.37±0.11	7.16±0.03	7.21±0.13	7.30±0.04	0.002 %
Ar	6.44±0.06	6.44±0.13	6.66±0.06	6.62±0.06	

form companion with similar composition as the gaseous medium, hence similar to the host star composition. In case of formation by accretion, a multi-steps scenario, departure from the host star composition is expected depending on when and where those different steps occurred.

Öberg et al. (2011) proposed a simple framework, but very useful, to assess where the companion has formed in the protoplanetary disk. This framework is based on the condensation temperature of the main carbon and oxygen bearers in the disk : CO, CO_2 and H_2O. The zone in the disk where the temperature reaches the condensation temperature of an element is call the snow-line. As we cross this snow-line going outwards from the host star, the species bearing the oxygen and carbon elements condensate, depleting the carbon or oxygen in the gas and enhancing it in the grains. Figure 1.9 from Öberg et al. (2011) provides a visual on the effect of those snow-line on the C/O ratio in the grains and in the gas, assuming a typical protoplanetary disk around a solar-type star. Based on his model, Öberg et al. (2011) draws first order results providing useful insight on the link between observed atmospheric composition and formation mechanism :

- Stellar C/O: gravitational instabilities or core accretion inside the H2O snow line.
- Sub-stellar or stellar C/O with super-stellar C/H: core accretion or gravitational instability with contamination by icy bodies.
- Super-stellar C/O and super-stellar C/H: core accretion closed to the CO or CO2 snow lines or high pollution by carbon-grains.
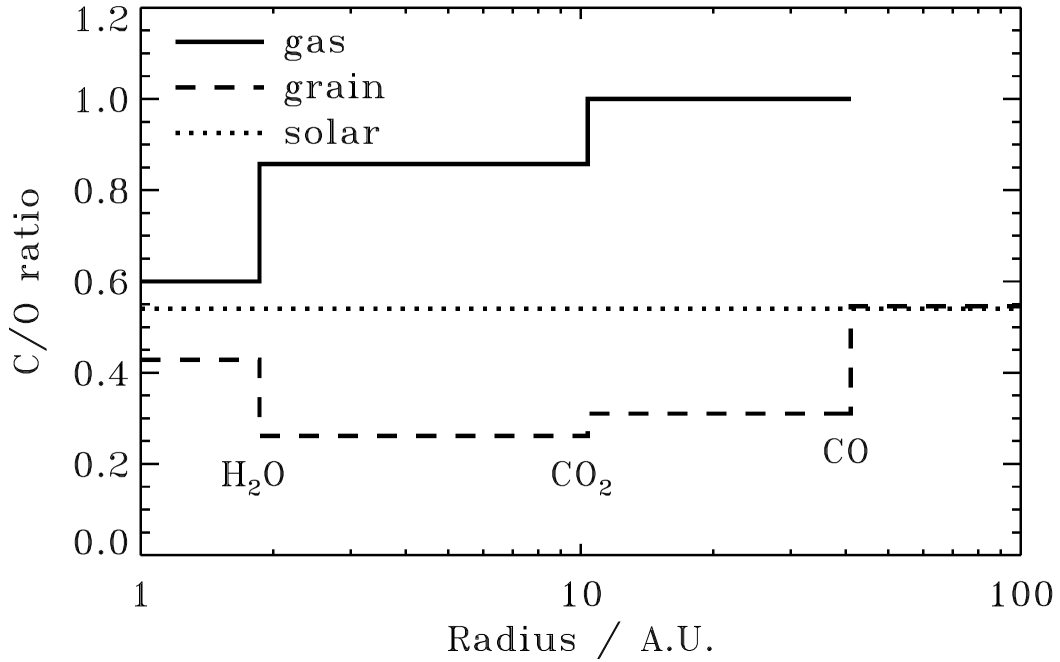
Figure 1.9: The C/O ratio in the gas and in the grains, assuming the temperature structure of a 'typical' protoplanetary disk around a solar-type star. The H_2O, CO_2 and CO snow-lines are marked for reference. Source : Öberg et al. (2011)

- Super-stellar C/O and sub-stellar C/H: Core accretion beyond the H2O snow line.

1.4   Planet formation and evolution

Constraining the carbon to oxygen ratio of the direct imaged objects HD 4747 B and the companions of the HR 8799 system (chapter 3) allowed me to draw first order scenario on their formation mechanism. Using the mechanism described in the previous section, HD 4747 B has a C/O ratio compatible with its host star and is therefore compatible with the gravitational instability scenario. Whereas, the HR 8799 companions span different carbon and oxygen compositions compared to their host star, which indicates formation by core accretion. Linking the formation mechanism to the actual composition of the companion atmosphere still endures a lot of caveats :

- (a) Which part of the atmosphere is probed and does it represent the bulk composition of the brown-dwarf or exoplanet?
- (b) Which fraction of the carbon and oxygen are trapped into condensates?
- (c) How the carbon and oxygen abundances are impacted by the evolution of the companion's atmosphere?

To address items (a) and (b) requires the assumption that any process affecting the carbon abundances will impact in a same order of magnitude the oxygen abundance. Hence, the carbon and oxygen ratio should indeed reflect the bulk composition of the companions even if the abundances do not. However, to validate such an assumption will require a significant increase in our current knowledge of atmospheric dynamics and chemistry. Item (c) can be addressed by scanning a statistical amount of objects at different time of their evolution to draw global results on the link between atmospheric composition and formation mechanism. The carbon and oxygen ratio is also an intense research field for the population of hot Jupiters (Madhusudhan et al. 2011; Teske et al. 2014; Line et al. 2014; Benneke 2015). Those giant planets orbits very close to their host star and are usually older than the direct imaged objects. There are some hints that some of them originate beyond the ice line following the core accretion mechanism (Brewer et al. 2017) and have migrated to their current position. But in situ formation scenario are possible (Batygin et al. 2016). Nevertheless, reported uncertainties for the carbon to oxygen ratios of those hot Jupiters are too high to distinguish unequivocally the formation mechanism. The study of the hot Jupiter WASP-12 b (section 3.4) with the retrieval code that I have developed highlight the difficulty of constraining hot Jupiters' C/O ratio. It shows that no information can be extracted from the current data and that retrieved abundances are prior-dominated (i.e. "you get what you put in"). It seems therefore difficult to analyse the impact of a companion's evolution over time on its atmospheric properties by scanning a broad range of substellar companions at different steps of their evolution.

Instead, it is necessary to study the mechanism that may drive significant changes to the atmosphere of a companion. Atmospheric escape is one of them. For close-in companions a significant amount of energy is deposited in their atmosphere by the UV light of the star, which has strong influence on the energy balance of the object and can eventually lead to the escape of its atmosphere. The processes at play to set off atmospheric escape depends mainly on the properties of the stellar environment, which leads us to the second part of my Ph.D. work on transiting close-in planets and far-ultraviolet observations.

1.5 Probing atmospheric escape

1.5.1 The evaporation desert and valley

There is a dearth of objects at small orbital distances with sizes in between super-Earth and hot Jupiters populations(Fig. 1.4). Theoretical studies suggest that atmospheric escape plays a major role in shaping this dearth (Lopez et al. 2012; Lopez & Fortney 2013; Jin et al. 2014; Kurokawa & Nakamoto 2014). The mass-loss computed for the giant planets (several tons per second) that have been observed to endure atmospheric escape is not sufficient to impact

their evolution (Vidal-Madjar et al. 2003; Lecavelier des Etangs et al. 2010; Vidal-Madjar et al. 2013). However, for a given mass, a planet can start to be affected by evaporation if it orbits to close to its star. Inversely, for a given incident flux, a planet can start to be affected by evaporation if its initial mass is small enough. This creates a gap in the radius (or mass) and semi-major axis (or incident flux) often referred to as the evaporation desert, Fig. 1.4. This evaporation desert extends towards a deficit zone between the rocky super-Earths and the gas-dominated sub-Neptunes, the so-called evaporation valley (Beaugé & Nesvorný 2013; Sanchis-Ojeda et al. 2014; Lundkvist et al. 2016; Fulton et al. 2017; Van Eylen et al. 2018; Fulton & Petigura 2018). Some of the rocky super-Earths could therefore be remnants of more massive planets that have lost their atmospheric envelope. Those planets have been nicknamed Chtonian planets (Hébrard et al. 2003; A. Lecavelier des Etangs et al. 2004). This desert could also be also a result of formation processes (e.g., rapid migration and in-situ formation; Hansen & Murray 2012), but the relative roles of both phenomena are unknown.

Close-in planets can not be imaged directly with today's observing facilities. To probe their atmosphere requires that they transit their host star. Understanding atmospheric escape is an important if we want to understand the link between atmospheric properties and formation mechanism for close-in objects. While the host star's optical and infrared radiation heats the exoplanet's lower atmosphere, ultraviolet and shorter wavelength are responsible for the photochemistry and mass loss from the exoplanet's upper atmosphere (Linsky 2014). The observation used in that part of this thesis are done in the far ultraviolet.

1.5.2   Atmospheric escape of giant planets

Observations in the UV of the hot Jupiter HD 209458b revealed the presence of neutral hydrogen atoms H I , ionised carbon C II, neutral oxygen O I and neutral magnesium Mg I in the planet's atmosphere (Vidal-Madjar et al. 2003, 2004; Ehrenreich et al. 2008; Linsky et al. 2010; Vidal-Madjar et al. 2013). The transit depth signals observed for those species are significantly deeper ($\sim$ 15% for H I) than the white transit depth of the planet ($\sim$ 1%). Using equation 1.2, the corresponding radius to those absorption indicates the presence of gas at several planetary radii, beyond the Roche lobe hence indicating that those planets endure atmospheric escape. The heavy elements carried away by the flow of hydrogen indicate the hydrodynamic state of the escape. Atmospheric escape of hydrogen with temporal variations was detected for the Hot Jupiter HD 189733b (Lecavelier des Etangs et al. 2010, 2012; Bourrier et al. 2013) and possibly neutral oxygen and ionized carbon (Ben-Jaffel & Ballester 2013). A huge cloud of hydrogen surrounding the warm Neptune GJ 436 has been detected and studied (Kulow et al. 2014; Ehrenreich et al. 2015; Bourrier et al. 2015, 2016b) . Its transit absorbed more than 50% of light from its host star and is to date the deepest transit depth observed for an

exoplanet. Finally, observations revealed escaping hydrogen atoms in the partially transiting upper atmosphere of the warm-Jupiter 55 Cnc b (Ehrenreich et al. 2012). Observation of hydrogen lines is challenging because of the Interstellar Medium (ISM) absorption, see section 4.5. The recent discovery of escaping Helium around the warm Neptune WASP 107b (Spake et al. 2018) provides a new window to probe atmospheric escape in the near future. With two Jupiter radii, WASP-12 b is very inflated and is enduring atmospheric escape (Manso Sainz & González 2012). However, no detection of helium has been observed for this planet (Kreidberg & Oklopčić 2018) and it is situated too far from us (432 parsecs) to probe hydrogen with UV Lyα observations.

In this scope, I have worked on the warm Neptune GJ 436 b to confirm the nature of the mechanism shaping the huge cometary tail. I also report a possible detection of ionised silicon Si III (Lavie et al. 2017a and section 4.4.2). The mass-loss endured by those giant planets through the escape of their atmosphere only weakly impacts their long-term evolution, despite escape rates of thousands of tons per second (Hubbard et al. 2007; Ehrenreich & Désert 2011; Bourrier & Lecavelier des Etangs 2018), but they are open laboratory to study the mechanism responsible for atmospheric escape.

1.5.3 Probing terrestrial planets with UV spectroscopy

The science of exoplanets is still at the premise of unveiling the atmospheric properties of small, telluric exoplanets. Rocky planets around other stars show a surprising diversity compared to samples from our Solar System: exoplanets with high bulk densities have been found with masses up to 10 Earth masses. Unfortunately, the atmospheres of these super-Earths, which could contain key answers about the evolution of such planets, are extremely challenging to probe at optical and near-infrared wavelengths, because the expected signatures of the lower atmospheric layers are of order ~ 10 ppm (Ehrenreich et al. 2006; Kaltenegger & Traub 2009). As can be seen for giant planets, observations in the UV of the upper atmosphere and the exosphere can provide stronger signal to noise, hence helping to overcome the low signature signal from longer wavelength observations. Attempts to detect exospheric hydrogen envelope around the Earth-like planets 55 Cnc e (Ehrenreich et al. 2012) and HD 97658 b (Bourrier et al. 2016a) have shown no presence of such extended atmosphere. Flux variations during the transits of TRAPPIST-1b and c, as well as Kepler-444 e and f could hint at the presence of an extended hydrogen atmosphere around those planets but stellar activity cannot be entirely ruled out (Bourrier et al. 2017a,c). Terrestrial planets formed beyond the snow-line are expected to be composed dominantly by water (Marboeuf et al. 2008). The photodissociation of water in the upper layers of the atmosphere can provide a source for escaping hydrogen (Wu & Chen 1993; Jura 2004; Léger et al. 2004). In our own solar system, Earth is surrounded by a hydrogen

envelope extending beyond ten planetary radii. However, the hydrogen escape is limited by a cold trap, preventing water to reach high altitudes (Vidal-Madjar et al. 1973; Vidal-Madjar & Thomas 1978). The early Venus is thought to have lost its water from atmospheric escape (Watson et al. 1981; Kasting & Pollack 1983)

In this framework, I have obtained Hubble Space Telescope (HST) data to observe the super-Earth HD 219134 b in the ultraviolet. A hint on the presence of hydrogen surrounding the planet is reported, see section 4.5.

1.5.4   Atmospheric escape

A particle of gas is said to have escaped its atmosphere when it is not bounded gravitationally to the planet or the brown-dwarf anymore.Initially, the exobase has been defined as the atmospheric level where the mean free path of a particle is similar to the atmospheric scale height (Hunten et al. 1989). A. Lecavelier des Etangs et al. (2004) defines it as the atmospheric level where the mean free path of a particle is longer than the distance to the Roche lobe. The mean free path of a particle is the average distance the particle travels between two collisions; the atmospheric scale height is the typical longer of an atmospheric layer where the pressure decreases by a factor e; and the Roche lobe is the gravitational potential limit around the companion beyond which a particle can freely escape into space or to the star. Below the exobase, in the thermosphere and below, the atmosphere is dense enough that a given particle will undergo several collisions within one atmospheric layer, preventing its escape. In the exosphere above the exobase, particles can move without collisions and can reach the Roche lobe of the planet and escape the gravitational force of the companion. A companion close to its host star has a Roche limit closer to its surface in the direction of the star, hence facilitating the escape of the atmosphere at this point. The escaping flow of particles is then shaped by the gravitational potential of the star and the planet, by the radiative pressure and other interactions from the star (stellar wind, magnetic interactions etc.)

1.5.4.1   Jeans escape

The Jeans (J.H. 1916) thermal escape is the consequence of the kinetic energy of the gas particles described by the Maxwell distribution. The process is controlled by the escape parameter, the ratio between the gravitational energy and the kinetic energy of the particles (Öpik & Singer 1961; Chamberlain 1963; Tian 2015). Particles in the high velocity tail of the distribution may reach the escape velocity of the planet and may escape the planet (Chamberlain & Hunten 1987). This mechanism has been long studied for the escaping mechanism of Earth's hydrogen (Liwshitz & Singer 1966; Liwshitz 1967) and for the other terrestrial planets of the solar

system (Hunten & Donahue 1976). The escape rate of particles under this regime depends on the temperature, the density and the mass of the gas particles and the escape velocity of the companion. For giant planets and brown-dwarfs the escape rate is too low to impact significantly the total mass of the object (Bourrier & Lecavelier des Etangs 2013).

1.5.4.2 hydrodynamic escape

Like Jeans' escape, hydrodynamic escape is a thermal process (Kasting & Pollack 1983; Tian 2015). If the collisions between gas particles in the upper layers of the atmosphere occur frequently, the kinetic description of the gas is not necessary and description using fluid dynamics can be use. The escape is said to be hydrodynamical. Particles do not escape one by one but rather as a group. The switch between Jeans and hydrodynamic escape happens when the escape parameter is of the order of unity (Yelle 2004; Volkov et al. 2011; Tian 2015). Part of the atmosphere can then massively escape the companions if the velocity of the bulk is high enough or if the thermosphere extend up to the Roche lobe. The extension of the exosphere tends to diminish with the increase of the temperature in the thermosphere until this latter reaches the Roche lobe triggering a geometrical blow-off of the hot companion, Figure 1.10 (A. Lecavelier des Etangs et al. 2004). Lammer et al. (2003) and Vidal-Madjar et al. (2003) showed that the energy deposited into the planet atmosphere by the optical light of the star is not enough to bring the temperature sufficiently high to produce the hydrodynamical expansion of the atmosphere and contribution from the X and UV (XUV) part of the spectrum is needed (A. Lecavelier des Etangs et al. 2004; Yelle 2004). This latter statement highly motivated the need for observations in the XUV and the need to characterise stellar flux at those wavelength. This hydrodynamical "blow-off" of the atmosphere was proposed as the mechanism leading to the escape of hydrogen from some of the terrestrial bodies (Earth, venus,mars, Titan) of the solar system (Hunten 1973; Kasting & Pollack 1983). For objects orbiting very closely to their host star (Hot Jupiters for example), tidal forces can modify significantly the density distribution in the upper atmosphere, hence favoring a hydrodynamic escape towards the star and in the opposite direction (Lecavelier des Etangs et al. 2004).

1.5.4.3 Stellar radiation pressure

The radiative pressure is the force exerted on the gas particles by the photons from the host star.

$$F \approx \sum_{i=0}^{n} f_{osc}^{i} F_{star} \tag{1.5}$$

where n is the number of transitions considered, F_{star} is the stellar flux and f_{osc}^{i} is the oscillator strength of transition i. Particles of gas in the upper atmosphere of the planet are receiving

impulse from the star's photons. Initial particles that did not have the proper velocity to escape the gravitational influence of the planet can reach the escape velocity. Moreover, if the stellar radiation pressure is high enough to compensate the gravitational effect of the star, the escaping flow of particles is pushed away radially (Etangs et al. 2008; Bourrier & Lecavelier des Etangs 2013).

1.5.4.4   Ionisation: XUV and stellar wind

Neutral atoms and molecules of the upper atmosphere of a planet may be ionised by photoionisation or charge exchange with the stellar wind ions. Once ionised those particles can be dragged away of the planet influence via magnetic interactions (Tian 2015). Furthermore, charge exchanges with the stellar wind change the velocity distribution of neutral gas observed around an evaporating planet. Energetic neutral atoms (ENAs) are produced by this phenomena and have been observed on the planet of the solar system (Collier et al. 2001; Futaana et al. 2006; Galli et al. 2008). The two protagonists atoms in this interaction keep their initial velocity (Holmström et al. 2008). Therefore, this mechanism doesn't provoke the escape of the planet atmosphere as, technically, only stolen electrons are actually escaping the planet atmosphere as newly neutral atom observed originate from the star.

1.5.4.5   others mechanisms

Others mechanism such as cosmic impacts or volcanism are possible but are not relevant for the work presented here.
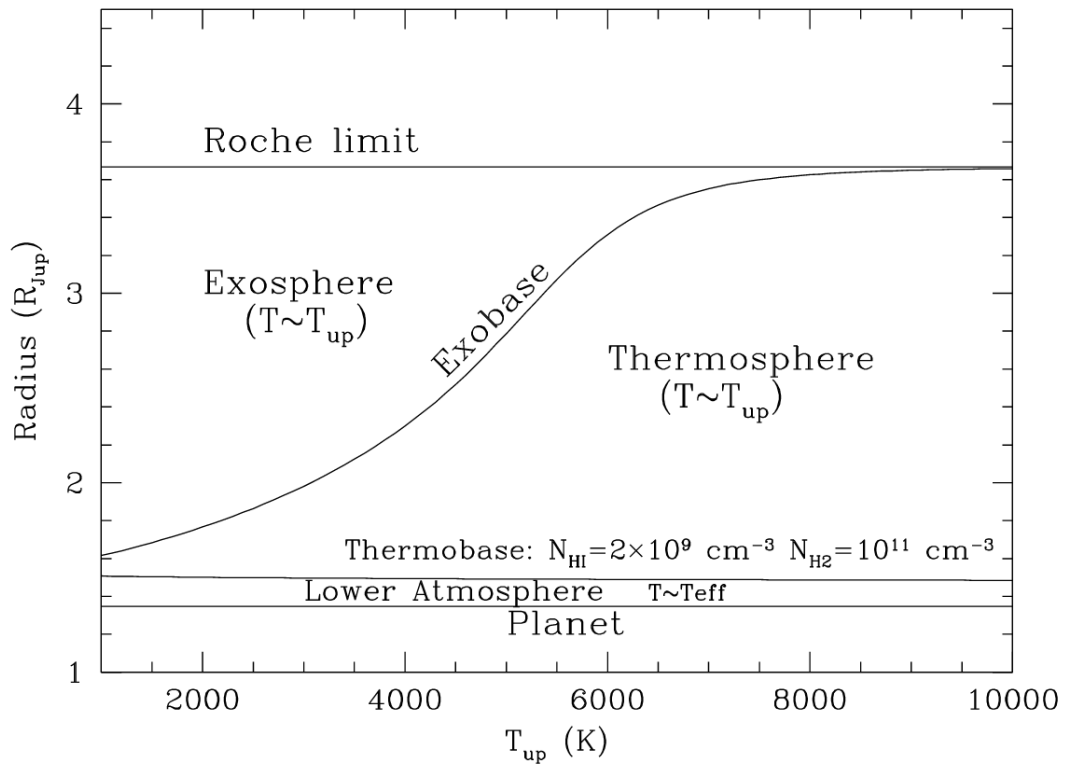
Figure 1.10: Vertical structure of the atmosphere of HD 209458b as a function of the temperature of the upper atmosphere. At the top of the thermosphere, the exobase is the critical level where the mean free path of a particle is equal to the distance to the Roche lobe. For high temperatures, the exobase reaches the Roche lobe; this leads to a geometrical blow-off Source: A. Lecavelier des Etangs et al. (2004)

INFERENCE FOR ATMOSPHERIC STUDIES

"With four parameters I can fit an elephant, and with five I can make him wiggle his trunk"

J.von Neumann(Dyson 2004)

Quand on veut être sûr de son coup, Seigneur Dagonet...on plante des navets. On ne pratique pas le putsch.

Loth d'Orcanie

2.1   Inference : a scientific method

2.1.1   What is a model?

Studying a physical system implies to gather some data, $\mathcal{D}$. In order to unlock Nature's secrets hidden in those data we need to develop a model, a mental construction to help us understand this physical system. It incorporates a set of assumptions represented by mathematical equations and parameters as well as our current knowledge on those parameters (hereafter our **prior**). Those equations and parameters are then translated (which may not be trivial) into a computer. Numerically, a model is defined by three types of parameters (see also section 2.3) :

- Physical parameters that are of interest for our study and that may or may not be directly observable.

- Some "muted" physical parameters that are needed but are not the subject of our study. Physical constants are part of those muted parameters.

- Numerical parameters that aim at ensuring that the purpose of the model is reached numerically. In practice, there are two types of numerical parameters. "Hidden" parameters that are set in routines written by someone else and that have already been tested. "Known" parameters which are numerical parameters link to a specific routine newly created for the study we are performing. Those numerical 'known' parameters need to be tested.

On a computer, a model is represented by the value of its n_{dim} parameters $\theta = \theta_1, \theta_2, ..., \theta_{n_{\text{dim}}}$; the value of its muted parameters and numerical parameters. Finally to complete our model, we need the value of the prior $\pi(\theta)$ on the parameters θ. The physical state of the system is represented by the n_{dim} parameters, which represent the parameter space of the model. Traditionally there are two ways of conceiving a model depending on what one tries to achieve : predicting an observation or analysing available observations :

- Forward modelling [forward problem] (Model parameters –> Data)
  Gathering our current knowledge about some physical system, one set up a numerical model that represents the current state of the system and uses it to predict a result, that can afterwards be observed. The model is often call "forward" model.

- Inverse modelling [inverse problem] (Data –> Model parameters)
  Given a set of data one tries to invert the forward model and calculates the best parameters that reproduce the observations. Inverting a forward model is not trivial and may not be possible. Moreover, two others phenomena forbid a unique solution in the inverse problem: the observations are always noisy and degeneracies within the model parameters can exist. However, the inverse problem can be solved with a Bayesian analysis.

In terms of probabilities calculations, those two ways of modelling can be expressed in terms of forward probability and inverse probability (MacKay 2003). Both problems involve a generative model that describes a process that is assumed to give rise to some data. In forward probabilities problems the task is to compute the probability distribution of some quantity (produced by the process) that depends on the data. For inverse problems the conditional probability of one or more of the unobserved variables in the process are computed given the observed variables.

In this work we are interested in the second problem, which is also called inference. This requires the use of Bayes' theorem. The goal of this section is to give insight on the way Bayesian inference has been used in my Ph.D. work. For a deep review of inference and

information theory, see for example Mackay (2003) or Gregory (2010). For an astrophysical view on Bayesian inference see Trotta (2008).

2.1.2 Bayes' rule

The root of any Bayesian analysis is Bayes'rule :

$$p(\theta|\mathcal{D}) = \frac{\mathcal{L}(\theta) \times \pi(\theta)}{Z} \tag{2.1}$$

The posterior distribution $p(\theta|\mathcal{D})$ is the probability distribution of the model parameters knowing the data. The likelihood function $\mathcal{L}(\theta)$ indicates the goodness of fit of the model to the data. The prior distribution $\pi(\theta)$ is the probability of the model's parameters before receiving the data. It expresses our knowledge of the system. Finally, Z is the Bayesian Evidence which is the normalising constant to ensure that $\int_\theta p(\theta|\mathcal{D}) \, d\theta = 1$.

It is worth noting that as θ is a multidimensional variable, all the probability distributions introduced here are also multidimensional. Until recently, it was difficult to evaluate such multidimensional integrals when no analytical solution existed. With the increase of computational power in the past two decades, a diverse range of old and new algorithms to compute those integrals became accessible to computers. It is then not surprising that Bayesian statistics is a rapidly increasing area in a lot of sciences including astrophysics.

Independently of the algorithm, we want a way to explore the n_{dim} parameter space under the constraints of our prior in order to localise areas of possible solutions to explain our data. If the data do not provide any information then the posterior distribution will reflect the prior. If the data strongly favour a certain region of the parameter space then the posterior distribution will be highly peaked towards this area. In practice, the bulk of the posterior is very small compared to the volume of the parameter space and therefore difficult to find. The problem of exploring the parameter space with some algorithm based on the Bayes' rule is different than an optimisation problem (minimisation or maximisation). In an optimisation problem the goal is to find some specific point in the parameter space. In Bayesian inference, the entire parameter space need to be somehow probed in order to provide the correct Bayesian evidence and posterior distributions.

2.1.3 Model selection

2.1.3.1 Bayes factor

In the case of atmospheric studies, different atmospheric states, processes and mechanisms can produce the spectrum observed. In science in general, multiple models coexist to explain observations and predict new ones. The first question that an analysis should answer is which

model is the most relevant for the question that is addressed. To answer this question one should balance between Occam's razor principle and goodness of fit. Adding extra parameters to a model will automatically increase the goodness of fit to the data but may not add any knowledge to our understanding of the mechanisms underlying the data. In Bayesian inference, the key variable to such an exercise is the Evidence Z (the Bayesian Evidence).

$$Z = \int_{\theta} \pi(\theta) \mathcal{L}(\theta) \, d\theta \tag{2.2}$$

It is the integral of the posterior distribution times the prior distribution on all the parameter space. Therefore it holds information on the volume occupied in the parameter space by the goodness of fit of our model to the data under constrain of our prior. To compare a certain model $\mathcal{M}_1$ to another model $\mathcal{M}_2$ we can use the Bayes factor :

$$B_f = \frac{Z_{\mathcal{M}_1}}{Z_{\mathcal{M}_2}} \frac{p(\mathcal{M}_1)}{p(\mathcal{M}_2)} \tag{2.3}$$

Where $Z_{\mathcal{M}_i}$ is the Evidence for model i. Our prior knowledge on models is embedded in $p(\mathcal{M}_i)$. Effectively, we can favour one model over the other because of our physical intuitions and our current knowledge. For example, (a) there are strong evidence that all brown-dwarfs and exoplanets spectra will be imprinted by some spectral features if the spectral resolution is sufficiently high to distinguish them. Therefore we may be inclined to set a stronger prior on an atmospheric model capable of reproducing spectral features than a simple blackbody model. (b) For hot objects, the chemistry timescale becomes very short and it is more difficult to depart from chemical equilibrium. So, models enforcing chemical equilibrium should be favoured in regards to our physical intuition. In practice, it is difficult to choose the correct prior scale between two models. So, we consider that each model is equiprobable and $\frac{p(\mathcal{M}_1)}{p(\mathcal{M}_2)} = 1$. The Bayes factor is then only the ratio of the models evidence and the value can be compared to some reference scale, Tab. 2.1.

2.1.3.2   On the importance of model selection

The interest of the exoplanets community on the C/O ratio was picked by the first tentative estimation of a high C/O ratio in the very hot exoplanet WASP-12 b by Madhusudhan et al. (2011). The authors of the study based their analysis on seven "multi-wavelength photometry" datapoints (Fig. 2.1). Indeed, in section 1.3.2, we reviewed the importance of the carbon to oxygen ratio in the perspective to constrain the formation mechanism of a companion. But, the C/O ratio also provides important constraints on chemical and dynamical processes in the atmospheres, mainly because the main carbon and oxygen bearers in the atmosphere of a stellar

Table 2.1: Empirical scale for evaluating the strength of evidence when comparing two models. Threshold values are empirically set, and they occur for values of the logarithm of the Bayes factor of 1.0, 2.5 and 5.0. The right-most column gives a convention for noting different levels of evidence above these threshold. The probability column refers to the posterior distribution probability of the favoured model, assuming non-committal priors on the two competing models, i.e. $p(\mathcal{M}_1) = p(\mathcal{M}_2) = 1/2$ and that the two models exhaust the model space, $p(\mathcal{M}_1|\mathcal{D}) + p(\mathcal{M}_2|\mathcal{D}) = 1$. Source : Trotta (2008)

Bayes factor	Odds	Probability	"sigma"	Strength of evidence
< 1.0	< 3 :1	< 0.750	< 2.1σ	Inconclusive
1.0	≈ 3 :1	0.750	2.1σ	Weak evidence
2.5	≈ 12:1	0.923	$2.7\,\sigma$	Moderate evidence
5.0	≈ 150:1	0.993	3.6σ	Strong evidence

companion are also among the main absorbers in the infrared (Madhusudhan 2012; Mollière et al. 2015; Heng et al. 2016). Other strong results have also been claimed based on few photometric points like thermal inversion (Knutson et al. 2008) or disequilibrium chemistry (Stevenson et al. 2010). Not so long after those claims, Hansen et al. (2014) compared the fitting significance of models with spectral features and a simple blackbody model (i.e. with no features) using the same photometric dataset for 44 planets. The conclusion of their analysis was that all of the claims were premature and that observations were better fit (in a Bayesian sense) by a blackbody rather than by a more complex model, apart maybe for HD 189733 b.

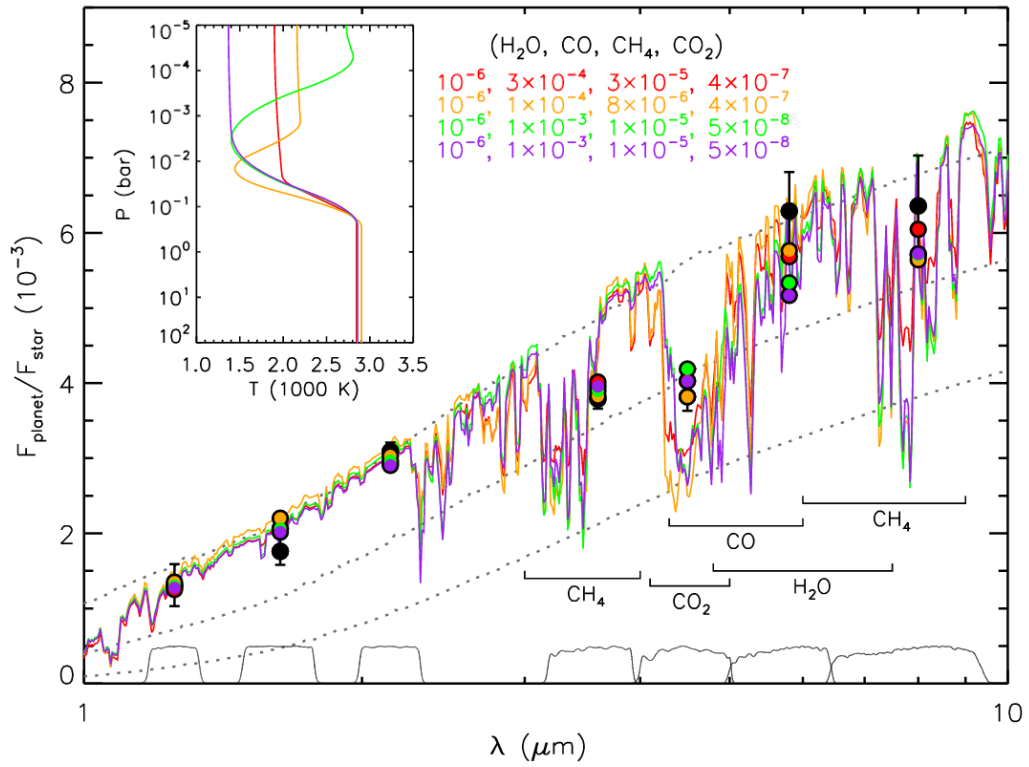**Figure 2.1:** An example to model selection. Observations and model spectra for dayside thermal emission of WASP-12 b. The seven data point used in the analysis are the black dots with error bars. A high carbon to oxygen ratio has been derived for this planet based on those observations. Using Bayesian model selection Hansen et al. (2014) showed that such claims were premature. Source: Madhusudhan et al. (2011)

2.1.4 Prior and likelihood

In a Bayesian analysis there are often difficulties to set priors on the parameters of the model. If we have information from another source of data, then we can enforce directly this knowledge in our priors. For example, if the distance of a system have been measured by GAIA we can directly set a gaussian prior centred on the GAIA's distance with the published uncertainty. If the stellar host has been followed by velocimetry, then constraint on the mass is available and can be enforced in our prior similarly. The difficulty arises when there is none or partial knowledge on the parameter's value. In that case, we are left with no choice but to assume broad priors. In the context of my Ph.D. I have only considered uniform priors and gaussian priors. Uniform priors in physics have most of the time finite boundaries (the temperature is superior to zero Kelvin, the radius of a companions is positive etc.). If the noise is assumed to be Gaussian, the likelihood function takes the following form:

$$\mathcal{L}(\mathcal{D}|\mathcal{M}_i, \theta) = \prod_{k=1}^{N} \frac{1}{\sigma_k \sqrt{2\pi}} exp\left\{ -\frac{[\mathcal{D}_{k,obs} - \mathcal{D}_{k,model}(\theta)]^2}{2\sigma_k^2} \right\} \tag{2.4}$$

with N the total number of data $\mathcal{D}_{obs}$ and σ_k the uncertainty on the k observation. $\mathcal{D}_{model}$ is the output of our model for parameters θ.

2.1.5 Nested Sampling

2.1.5.1 Transforming Z into a 1d integral

The key concept of Nested Sampling algorithm is to transform the multi-integral Z into a one dimensional integral. Let's X be the prior mass which represent the volume of the parameter space where the likelihood is higher than a defined likelihood L^* :

$$X(\mathcal{L}^*) = \int_{\mathcal{L}(\theta) > \mathcal{L}^*} \pi(\theta)\, d\theta \tag{2.5}$$

By construction it is a smooth decreasing function. When $\mathcal{L}^* = \mathcal{L}_{min}$ we incorporate all the prior space, and the prior mass is 1. When $L^* = \mathcal{L}_{max}$ no points in the prior space has a higher value and the prior mass is 0. With L_{max} and L_{min} being the highest and the smallest likelihood value respectively. We can introduce the inverse function of $X(L)$, $L(X)$ which is a decreasing function bounded by $\mathcal{L}(0) = \mathcal{L}_{max}$ and $\mathcal{L}(1) = 0$. The evidence becomes

$$Z = \int_0^1 \mathcal{L}(X)\, dX \tag{2.6}$$

Figure 2.2 bottom plot shows a generic view of the form of the likelihood as a function of the prior mass. Computing the integral of such a function can be done with a simple integrator such as a rectangle or trapezoidal sum.
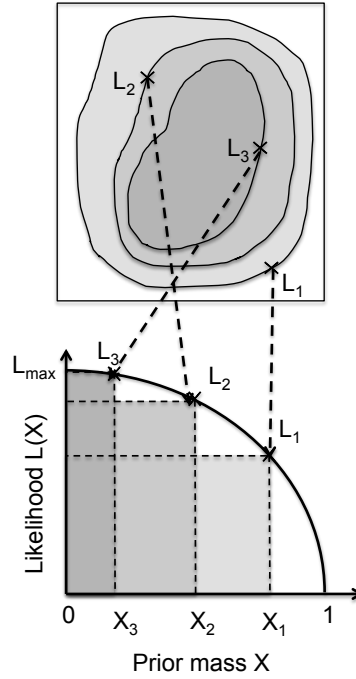
Figure 2.2: Schematic view of how the likelihood has a function of the prior mass is constructed. The purpose of the nested sampling algorithm is to evaluate the Bayesian evidence, which is the integral of the curve (bottom figure). The posterior distribution is obtained as a by-product of the algorithm (top figure). The algorithm progresses in "nested" sequence of $\mathcal{L}_3 > \mathcal{L}_2 > \mathcal{L}_3$.

2.1.5.2   Computing Z

The nested sampling algorithm gives a way to generate the sequence of M points $[X_m, L(X_m)]$ on the likelihood as a function of prior mass curve . To initialise the algorithm, N_{points} "living" points are randomly picked from the prior probability distribution $\pi(\theta)$. This sample is uniformly distributed in the prior space and the prior mass is set to $X_0 = 1$. On the first iteration, the point with the worst likelihood $L_{worst,1}$ value is removed and replaced by a new point with a higher likelihood value. The new set of "living" point is now uniformly distributed in the restricted prior space contained within an iso-likelihood contour $L_{worst,1}$. The new prior mass can be written as $X_1 = t_1 X_0$, where t_1 is a positive number smaller than 1 called the shrinkage ratio. On each step i of the algorithm the point with the lowest likelihood $L_{worst,i}$ is recorded and replaced by a new point with a higher likelihood. The prior mass is shrunk by t_i. The algorithms progresses through nested shell (in θ coordinate) of iso-likelihood contours until it reaches the region of the highest likelihood (posterior bulk). By monitoring the contribution of each step to the total integral one can decide when to stop the algorithm - ie when the contribution becomes negligible.

Evaluating the values of the likelihood L_i for the N_{points} or the new point at each step of the

algorithm is feasible as the likelihood function is known. However evaluating the shrinkage ratio is usually not possible. Instead, we consider the probability distribution $p(t_i)$ to describe the shrinkage of the prior mass between two step of the algorithm. One point worth noticing is that the likelihood as a function of the prior mass is a very skewed function. The posterior bulk is expected to represent a very small volume in the parameter space. Therefore, sampling ought to be linear in $\log X$ rather than in X. Hence, our exploration is geometrical and the shrinkage ratio is $\log(t_i) = \log(X_i/X_{i-1})$. Choosing the lowest likelihood point at each step is equivalent to choosing the largest of N_{points} uniformly distributed points from the interval [0,1]. So, t_i follows a Beta-distribution Beta(N,1), which has the density :

$$p(t) = N_{\text{points}} t^{N_{\text{points}}-1} \tag{2.7}$$

The sucessive $\log(t)$ are independent and identically distributed random variables so their distribution can be fully characterised by its mean $E(\log(t)) = 1/N_{\text{points}}$ and its standard deviation $\sigma(\log(t)) = 1/N_{\text{points}}$. After i steps of the algorithm the prior mass is expected to shrink to $\log(X_i) = -i/N_{\text{points}}$. The uncertainties of such an approximation can then be taken into account using the standard deviation of the distribution.

2.1.5.3 Drawing new points

In the previous paragraph we have described the algorithm considering that a new point can be drawn from the restricted prior space. However, finding such a point is the main challenge in the implementation of the Nested Sampling algorithm. The Multinest package (Feroz & Hobson 2008; Feroz et al. 2009, 2013), used in my work, uses the ellipsoid clustering (see Fig. 2.3). In the ellipsoid clustering algorithm, the "living" points are enclosed into a variable number of ellipsoids. One ellipsoid is randomly picked and a rejection algorithm is performed within this ellipsoid until a new point is found. Other methods of parameter space exploration can be used such as Galilean Monte Carlo or other MCMC-like algorithm. All the codes developed during my thesis are using python as the main skeleton. The Multinest algorithm is used through the python wrapper Pymultinest (Buchner et al. 2014). which was created to study X-ray spectral modelling of AGN.

2.1.5.4 Nested Sampling versus other Bayesian algorithms

Choosing the nested sampling algorithm for this work was logical in order to answer our needs about model selection and posterior distribution calculation. The algorithm has now been used in a lot of different domain including exoplanetary atmosphere characterisation (Benneke & Seager 2013; Waldmann et al. 2015a,b). Waldmann et al. (2015a) also plugged an adaptive MCMC routine to cross-check the results with the nested sampling algorithm. Allison &
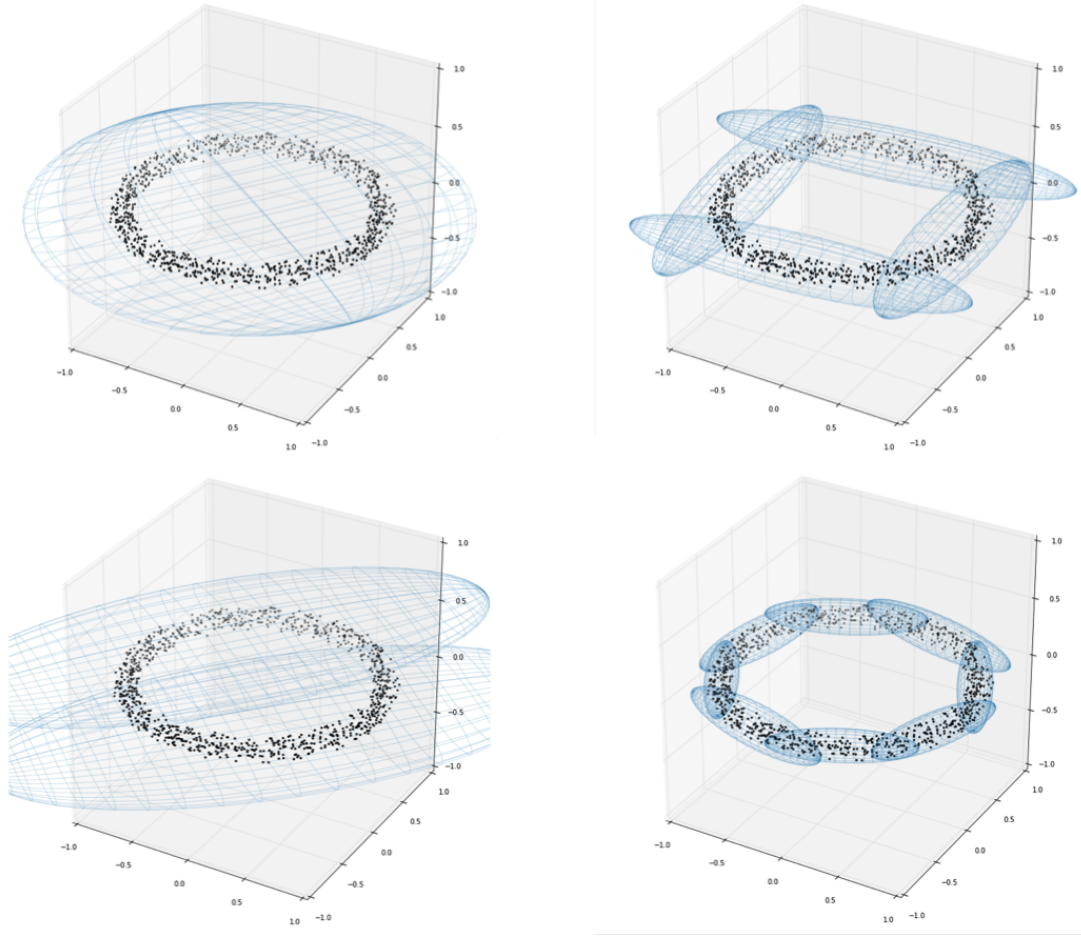
Figure 2.3: Ellipsoidal clustering of a toroid. On the first iteration (top left panel), the entire parameter space is encompassed in one ellipsoid. Step after step the algorithm increases the number of ellipsoid until the toroid is fully sampled. The multinest algorithm uses the ellipsoidal clustering to find high posterior bulks in the parameter space of the model.

Dunkley (2014) compared different sampling techniques for Bayesian estimation including the nested sampling algorithm. The Nested Sampling algorithm has proven to provide similar results to other techniques. If the parameter space is too vast (i.e. superior to 20 parameters), the ellipsoidal clustering start to be inefficient and the multinest package have difficulties to draw new points in the parameters space with increasing likelihood values.

2.2   Computation with GPU

In order to perform statistical inference we need to be able to compute our forward model from thousands to millions of time. If the forward model is too slow to compute then the Bayesian algorithm, for example the nested sampling algorithm, is unable to converge in a decent amount

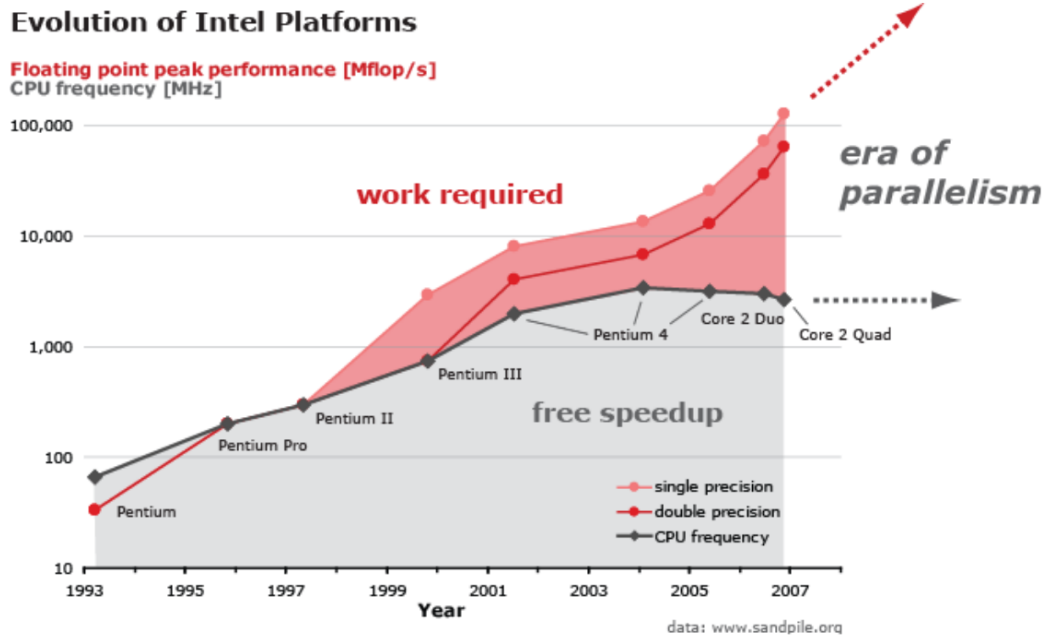**Figure 2.4:** The evolution of computing platform's performance versus CPU frequency. It becomes harder to increase the CPU frequency, hence other options are needed such as parallelism.

of time. In order to remedy to this, there is three ways:

- better computing facilities.
- better algorithms to explore the parameter space (i.e. to spot the posterior bulk efficiently).
- make the forward model faster either by sacrificing physical insight (parameterisation or simplification) or by improving the code.

For the first point, I had access to a cluster of 12 graphics processing unit (GPU) NVIDIA K20. The nested sampling is already a fine tuned algorithm to explore the parameter space of a model in an efficient way. Finally, I learned how to code with GPU in order to provide significant speed-up in forward models computation.

2.2.1 Why using GPUs?

For 30 years, microprocessor performance were correlated with the increase in the number of transistors, which follows Moore's law. This law states that the number of transistors in a dense integrated circuit doubles about every two years. But it seems that semiconductor physics limits have been reached as CPU clock speed performance now only grows by 10% per year. To sustain the increase in performance new code must employ some sort of parallelism, see Fig. 2.4. Parallel computing is a type of computation in which many calculations or the execution of processes are carried out simultaneously (Almasi & Gottlieb 1989). This can be carried away

either using normal CPU or by using GPU. The company NVIDIA, which manufactures graphic cards has created a parallel computing platform named CUDA. The company also projects to provide a 1000 times speed-up by 2025 compared to single threaded performance[a].

2.2.2   GPU architecture

GPU architectures are different from normal multithreads CPUs. In order to take the best of GPU programming it is important to understand how GPU are designed. A GPU chip is partitioned into Streaming Multiprocessors (SMs) that act independently of each other. Each SM has multiple cores. A group of cores that perform the same instruction (but on different data elements) is called a warp. The number of SMs and cores per SM depends on the GPU type. High-end GPUs have thousand of cores.

2.2.3   GPU programming

The physical architecture of the GPU is translated to the software as follow:

- Thread: the single computing element
- Warp: a set of threads (32 commonly but depends on the GPU type) that all work in a lockstep fashion, which mean they run the same set of operations at the same time in parallel.
- Block: a set of warps. Threads within a block can synchronise and cooperate via shared memory. Threads in different blocks cannot cooperate.
- Grid: a set of blocks launched in one kernel
- Kernel: a parallel portion of an application that is executed on the GPU.

In GPU's programming the CPU is named the host and the GPU the device. The host is in charge of executing the main program and dispatched some slow pieces of the code to the GPU for a speed-up. The GPU possesses its own memory and transfer from the host to the device is necessary. The memory on the GPU is limited as compared to the memory available on the host. To be efficient, the gain in computation time using GPU needs to be higher than the time needed to transfer memory from the host to the device. Finally, the hardware is free to schedule thread blocks on any processor and in any order. The CUDA language is derived from the C++ language and can be access in python via the wrapper PyCUDA.

The NVIDIA website swarms with useful information and the book Sanders & Kandrot (2011) can be a good place to start for interested readers.
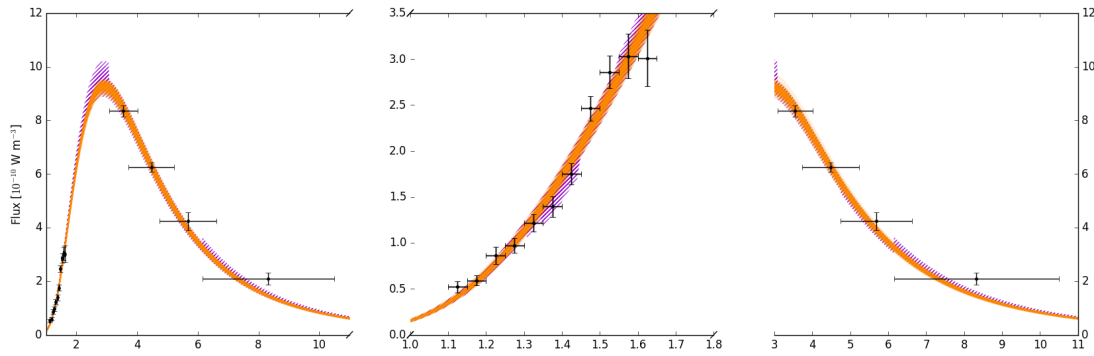
Figure 2.5: Mock data set (black dots with error bars) and one sigma best fit models for a simple blackbody ($\mathcal{M}_2$ - orange) and the model with water features ($\mathcal{M}_3$ - violet).

2.3 A pedagogical example for atmospheric studies

The idea of this section is to study a simple case of inference in order to understand the different steps of the Bayesian inference. This simple "toy" inference studies has helped me to apprehend inference and build intuition on atmospheric retrieval for exoplanets. Those studies also stress the points below:

- The better the data, the more information you can extract.
- Ill-posed problems can not be solved even with the best data imaginable.
- One can not do inference without making assumptions

As exoplanets are very far away from us we cannot send probes to gather data on their atmospheres. The only information we receive is either the light of the star filtered by the atmosphere of the planet (transmission spectroscopy/photometry - transit), the light emitted by the planet itself (emission spectroscopy/photometry - direct imaging) or the stellar light reflected by the planet. Therefore, the data available to us are spectroscopic and/or photometric observations. Even if the observational techniques to obtain photometric data and spectroscopic data are different, the information we obtain for both method is the integrated flux over a certain bin of wavelength. For photometry, this bin will be large while for spectroscopy this bin will be smaller.

Let's consider some mock emission observation of a giant companion, presented in fig. 2.5 and three models $\mathcal{M}_{1,2,3}$, that are described below in parallel to the inference process. The mock data set is created using the model $\mathcal{M}_3$ with some gaussian noise. But for the sack of the example, the following subsections describe the inference as if we don't have this information. The wavelength coverage is similar to the WFC3 onboard HST and the Spitzer bands. We neglect any instrumental effect or physical systematic effects (such as stellar activities). The

---

[a]https://www.nvidia.com/en-us/about-nvidia/ai-computing/

noise only comes from the photons noise (Poisson noise), which in our case converges to a gaussian distribution because we will assume that our observations are "photon-rich" (this is the case for infrared observations - chapter 3 and less so for FUV observations - chapter 4).

2.3.1 $\mathcal{M}_1$ - Blackbody

Facing those data we consider atmospheric models to unveil some properties on the object. One of the simplest physical model is the blackbody function. Our assumption is that the stellar companion is in thermal equilibrium and emits light as a blackbody. This assumption is described by the planck function :

$$F_{\text{TOA}}(\lambda, T) = \pi \frac{2hc}{\lambda^5} \frac{1}{e^{hc/\lambda k_B T} - 1} \tag{2.8}$$

Where the flux at the top of the atmosphere (TOA) has already been integrated on the disk. It is evaluated at a certain wavelength λ with h the Planck constant, c the celerity of light in vacuum, k_B the Boltzmann constant and T the temperature of the companion. The companion is at a certain distance and we therefore need to propagate the flux to the observer :

$$F_{\text{obs}} = \left(\frac{R_{\text{comp}}}{d} \right)^2 F_{\text{TOA}}, \tag{2.9}$$

where d is the distance between the observer and the companion and R_{comp} is its radius.

2.3.1.1   Numerical implementation

The physical parameters are any combinations of three parameters: the temperature T, the radius of the companion R_{comp} and the distance of the system. Effectively, those parameters are of interest in our model and may be constrained with the data we have. However, we can choose to focus only on the temperature if for example other observations have constrained the radius (if the object transit in front of its host star) or the distance between us and the star (astrometry measurement). The "muted" physical parameters are the physical constants : the Boltzmann and the planck constant and eventually the radius and the distance depending on our choices above. The speed of light is not a parameter since the meter have been defined from it.

For one data point, the flux is integrated within a certain wavelength bin. Therefore the model needs to be computed at a higher resolution. The number of points chosen inside one wavelength bin is a numerical parameter of the model. As the blackbody function is relatively smooth a sampling of 100 points per bins is sufficient. I am also using two routines from the python package numpy (Oliphant 2015), the power and the exponential functions, which have numerical parameters (hidden) already tested and validated.

2.3.1.2 Inverse problem

Inverting our simple forward model is possible because the equation of the Planck function is simple. However, the problem is ill-posed as there are three unknowns for only two equations, Eq. 2.8 and 2.9. The radius of the companion and the distance are clearly degenerate, there is an infinite number of combination of those two parameters to generate the data we observe. On top of this, our data have noise.

To do the inference, we are going to use the nested sampling algorithm. As our noise is assumed to be gaussian we set up a gaussian likelihood function as in equation 2.4.

2.3.1.3 Priors

First, we need prior functions for our physical parameters. There are some arguments, both theoretical and observational to believe that the radius of a stellar companion is between 0.8 and 3.0 Jupiter radius. This is a very conservative prior and also includes inflated Hot Jupiters. Let's therefore choose a uniform prior within these domain. The companion is in our galaxy, the milky way and probably not too far because we were able to observe it. Nonetheless, as we have no information on the distance let's choose a broad uniform prior from 1 to 8000 parsecs.

A sanity check that I always perform, is to compute the likelihood of a model that will reproduce exactly the dataset. For this dataset and our likelihood function this "perfect" likelihood is $\log \mathcal{L}_{best} = 361$, which provide some order of magnitude level for the Bayesian evidence. I chose to run a dozen of different nested sampling, which should be enough to fully explore our parameter space. The concatenation of all the runs provides a bayesian evidence for this model of $\log Z_1 = 335$. The posterior distribution, which is given as a by-product of the nested sampling is shown on Fig. 2.7. The temperature of the companion is well constrained around 1000K. As expected the radius and the distance are degenerate. The posterior distribution of the radius is the same as the prior distribution. The distance posterior have shrunk to a uniform distribution between ~ 8 and ~ 16 parsecs, which basically is the translation of our prior on the radius through equation 2.9. With no extra information, it is not possible to gain anything else from the data with this model.

2.3.2 $\mathcal{M}_2$: New information on the distance

Let's assume now, that we receive some information on the host star. The distance of the system has been measured with GAIA (Gaia Collaboration et al. 2016b,a) and is 10 ± 0.01 parsecs. We enforce this new information in our model by setting a gaussian prior on the distance parameter. We rerun a dozen of nested sampling algorithm and the new Bayesian
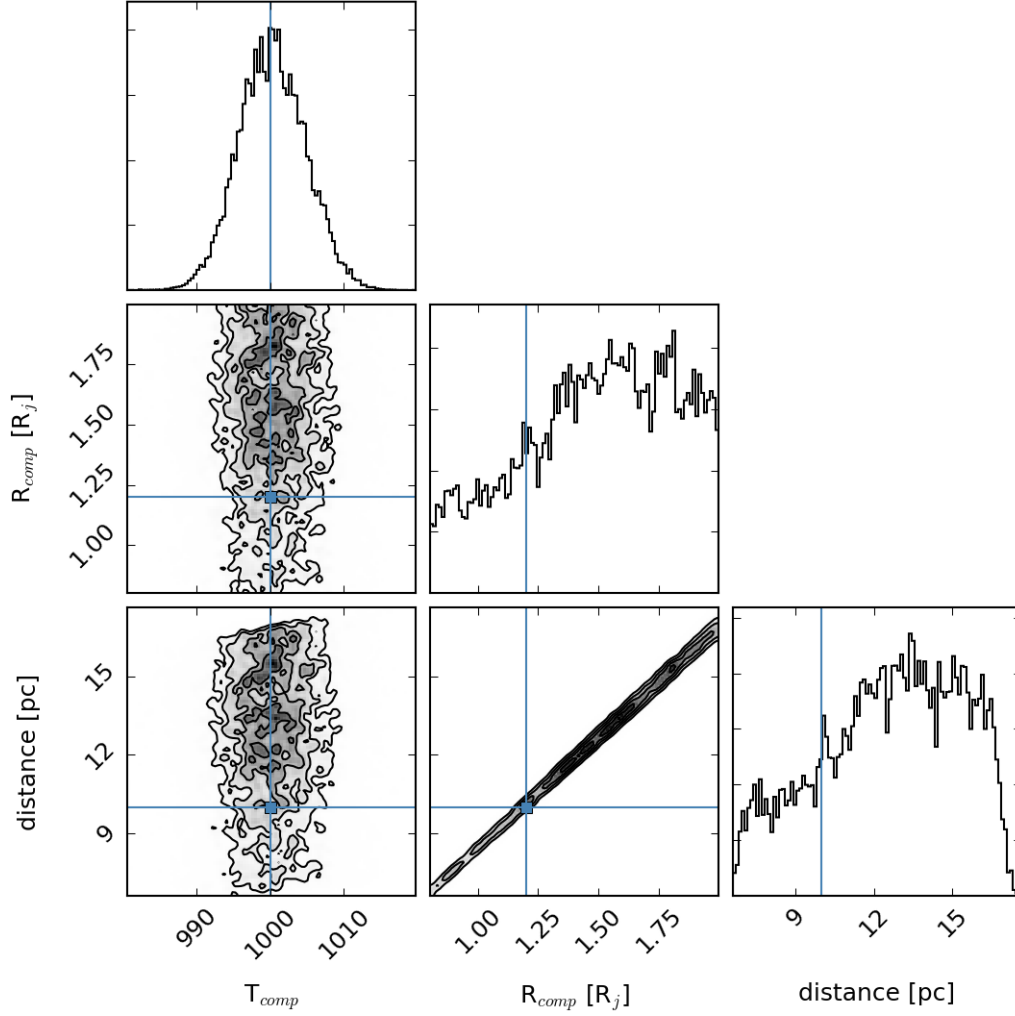
Figure 2.6:   Posterior distribution of the parameters for blackbody model $\mathcal{M}_1$ with no information on the radius of the companion or the distance of the system. Those two parameters are degenerate and only the product of those are actually constrained.

evidence is $\log Z_2 = 342.1$. The Bayes factor between the previous model and this new model is $B_f = \log Z_2 - \log Z_1 = 7$, which indicate that model $\mathcal{M}_2$ is strongly preferred over $\mathcal{M}_1$.

The posterior distribution is given in Fig. 2.7. Compared to model $\mathcal{M}_1$, the radius of the companion is now constrained. However, it is clear that this newly constrained parameters is not the fruit of our inference with the emission observations. The information on the radius is a consequence of the GAIA observations of the distance. Our model can not constrain the radius and the distance because they are degenerate. However, the product of those two parameters can be constrain. The constraint on the temperature has not be changed by this new information.
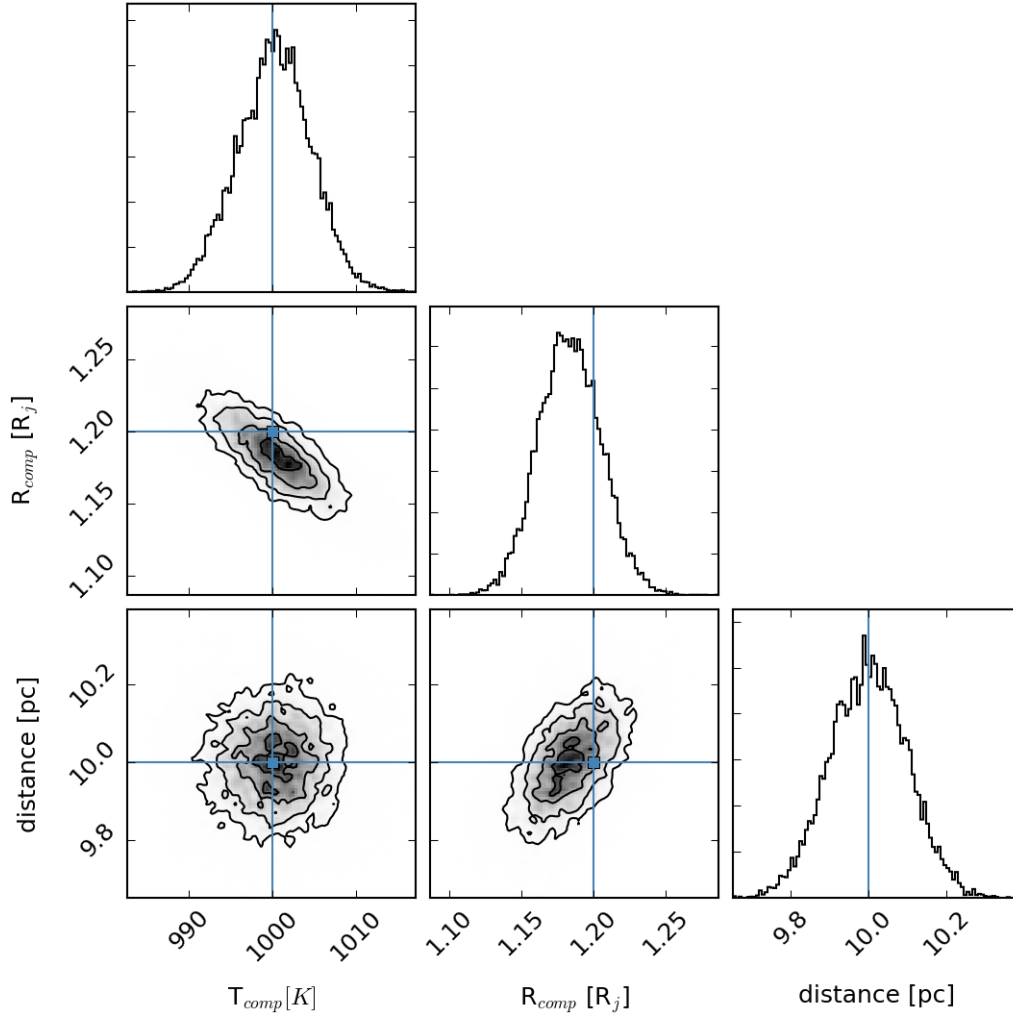
Figure 2.7: Posterior distribution of the parameters for blackbody model $\mathcal{M}_2$ with GAIA information on the distance of the system. The distance and the radius in the model are degenerate. The posterior distribution of the distance only reflect our prior, i.e. the GAIA distance.

2.3.3 $\mathcal{M}_3$: A spectral feature

Spectral lines form when a molecule is present in a layer of the atmosphere with a different temperature than the continuum emission. Fig. 2.8 is a cartoon showing the process of formation of spectral lines. This process occurs for all the molecules and in the many layers of the atmosphere and can be described with the two stream approximation (Heng et al. 2014; Lavie et al. 2017b):

$$F_{\uparrow_{j+1}} = F_{\uparrow_j} \mathcal{T} + \pi B \left(1 - \mathcal{T}\right), \tag{2.10}$$

where the fluxes are computed at the j- and $(j + 1)$-th layer interfaces. The Planck function (B) is evaluated within each layer. The transmission function is given by :

$$\mathcal{T} = (1 - \Delta\tau)\exp(-\Delta\tau) + (\Delta\tau)^2 \,\mathcal{E}_1, \qquad (2.11)$$

with $\mathcal{E}_1(\Delta\tau)$ being the exponential integral of the first order. The optical thickness of each layer is given by $\Delta\tau$, which assuming hydrostatic equilibrium, isothermal layers and that the surface gravity is constant throughout our model atmosphere is :

$$\Delta\tau = \sum_i \frac{X_i \sigma_i}{\bar{m}g}\,\Delta P, \qquad (2.12)$$

where X_i and σ_i are the mixing ratio and cross section of the i-th molecule, respectively. ΔP is the thickness of the layer in terms of the difference in pressure. The mean molecular mass is given by $\bar{m} = \mu m_{\mathrm{u}}$, where μ is the mean molecular weight and m_{u} is the atomic mass unit.

When a molecule has a lot of lines very close within a short wavelength range, the absorption or emission can be seen as a band, especially at low resolution. The molecule of water for example has a strong band feature around 1.4 μm, which is probed by our mock dataset. And indeed, it seems some absorption can be seen around 1.4 μm (Fig. 2.5). Building a full emission atmospheric model to catch any feature of water (and/or other molecules) using the above equations is out of the scope of this section and will be described in chapter 3 and in Lavie et al. (2017b). Instead, let's assume that the absorption is the consequence of the presence of water in one layer of the atmosphere and that the optical depth can be approximated by $\Delta\tau = 5.10^{27}X_{H_2O} * \sigma_{H_2O}$ (this is correct for a single layer with a thickness of 0.005 bars, a surface gravity of 30 m s^{-1} and mean molecular weight of 2). We determine the cross section for each wavelength bin as the average cross section of all the lines within this wavelength bin. Our new model now has one extra parameter X_{H_2O} and one new equation $F_{\mathrm{obs}} = F_{\mathrm{TOA}}\mathcal{T}(\Delta\tau)$. Our prior on the new parameter is uniform between 10^{-15} and 10^{-1}. The nested sampling algorithm provides a Bayesian evidence for this new model of 342.5, which compared to the model $\mathcal{M}_2$ is slightly higher but not significant. We know that $\mathcal{M}_3$ is actually the "right" one because we have created our mock data set with it. However, our inference on those mock data tells us that we can explain them with only a blackbody function. The constraint we obtain on our water abundance proxy is actually not bad as the posterior distribution picked at the correct value. So we may be willing to trust this information. If instead of using the cross-section of water (i.e. $\mathcal{M}_3$), we now assume the same model but with another molecule (CO for instance - $\mathcal{M}_4$). The Bayesian evidence for this model is 342.3 and the CO abundance proxy presents the same posterior shape as for the water (Fig. 2.10). This is happening because CO and H_2O have some close wavelength values for their spectral lines in certain band. However, we know that no CO was present in the original mock dataset. In a real case we won't be able to distinguish
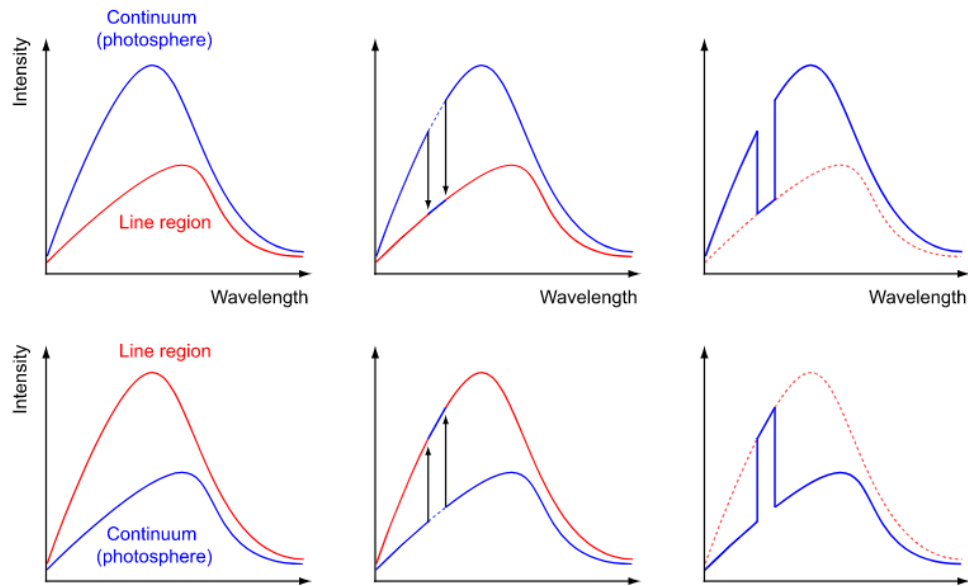
Figure 2.8: Schematic view of line formation process in an atmosphere of a star or a planet. The deep atmosphere emits as a blackbody function, the continuum emission. Molecules or atoms in higher layers absorb photons at specific wavelengths and remit photons at a different intensity depending on their temperatures. If a layer has a higher temperature than the deep atmosphere, an emission line is observed. If the layer has a smaller temperature then an absorption line is observed. Source: M. Galfalk - Stockolm Observatory.

the reality from the degeneracies of our model. Self-consistent modelling is a way to address this problem by enforcing our knowledge of chemistry in the interpretation of the data.

Figure 2.9:   Posterior distribution of the parameters for the model $\mathcal{M}_3$ with water spectral features and GAIA information on the distance of the system. The blackbody temperature, the radius of the companion and the distance of the system are constrained to the "correct value". The water abundance is peaked towards the input value but the distribution spreads to lower values.
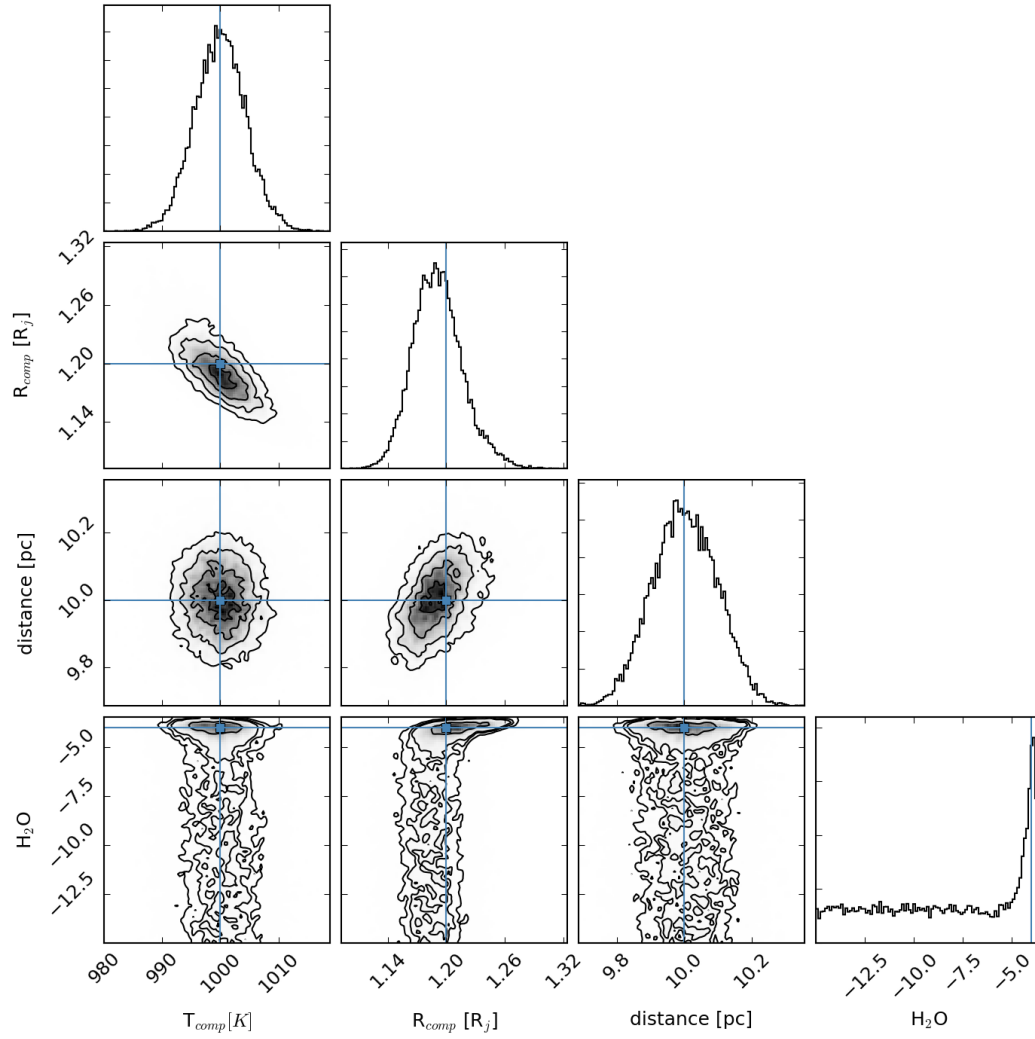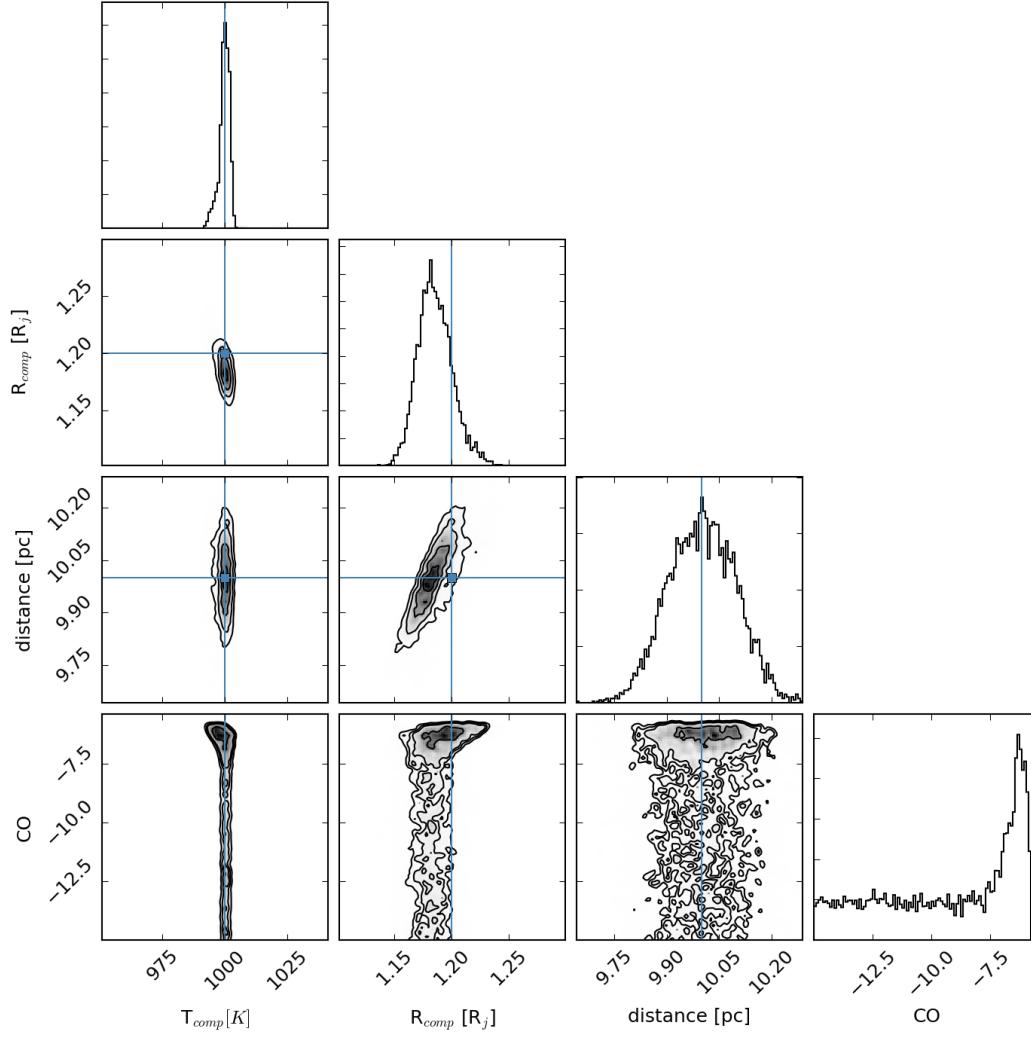
Figure 2.10: Posterior distribution of the parameters for the model $\mathcal{M}_3$ with CO spectral features and GAIA information on the distance of the system. The blackbody temperature is centred to the correct value but has a broader distribution than the retrieval from the "correct" model. The radius of the companion and the distance of the system are constrained to the "correct value". The CO abundance as a similar profile to the abundance of water retrieved with the "correct" model. In this toy inference, the solution is known. There were no CO in the initial data. The degeneracies between molecules abundances is inputed by their opacities, figure 3.2.

Probing the Lower Atmosphere - Atmospheric Retrieval

Just because it's what's done doesn't mean it's what should be done.

Cinderella

If you wish to make an apple pie from scratch, you must first invent the universe.

Carl Sagan

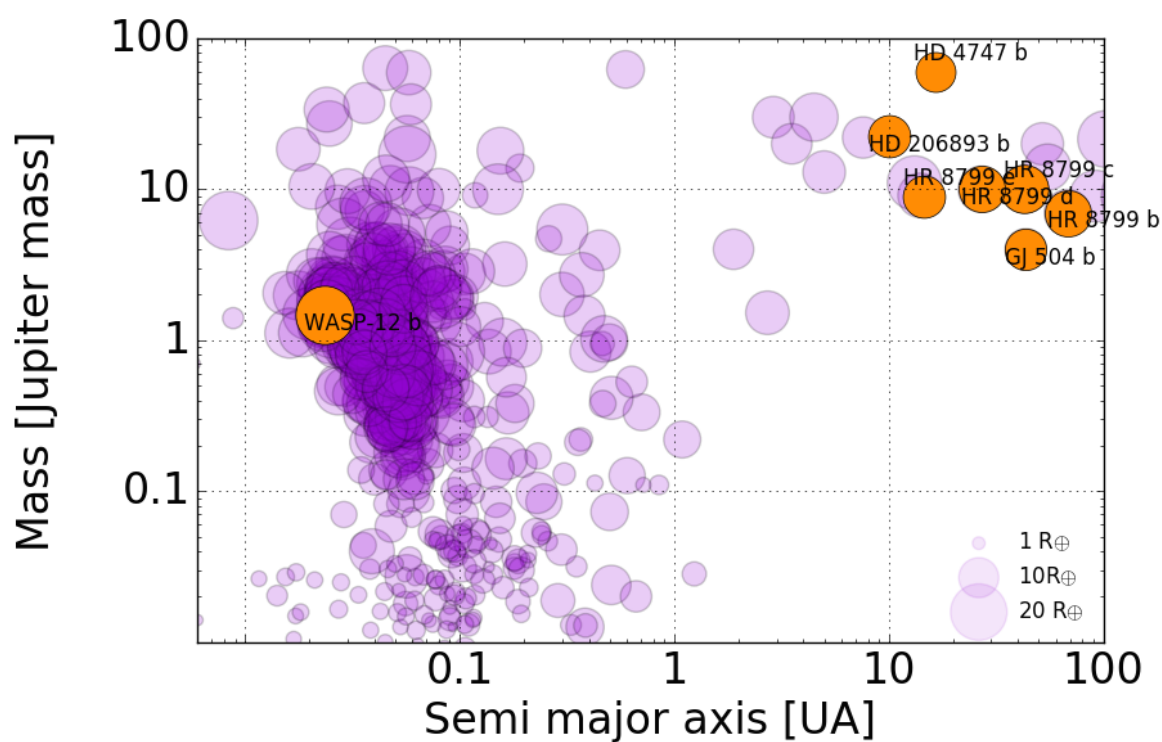In this chapter, the work carried out on emission observations in the infrared is presented. I built an emission atmospheric model coupled with a nested sampling algorithm in order to perform atmospheric retrieval. The code is named HELIOS_R. Using this framework, I constrained the carbon and oxygen abundances of several direct imaged objects (HR 8799 b,c,d,e, HD 4747 B, GJ 504 b and HD 206893 b) for the purpose of identifying their formation mechanism. The code was also used to analyse the hot Jupiter WASP-12b.

3.1   Atmospheric retrieval

3.1.1   Forward or Inverse problems / Self-consistent or parametric models

The common objective of atmospheric studies is to provide insight on the physical characteristics of the atmosphere of the exoplanet or brown-dwarf (every physical quantities that have an impact on the atmosphere properties). As we have seen in section 2.1 we can either use forward modelling or an inverse modelling to do this. Let's consider the atmosphere of a planet (i.e. the physical system). The state of the atmosphere can be described by some parameters θ (physical variables, i.e. the temperature, the abundances of the molecules present in the atmosphere of the planet). In the forward modelling, the parameters θ are known or guess and a model is used to produce the value of some quantity that is measurable, for example the spectrum of the planet. The model is often call a forward model because it provides a mapping from the parameter to the data : $\mathcal{M}_{\text{fwd}}(\theta) = \text{data}$. In the inverse problem, the data are used to constrain the parameters θ that are not directly observable. The inverse model is the inverse of the forward model and provides a mapping from the data to the model parameters : $\mathcal{M}_{\text{fwd}}^{-1}(\text{data}) = \theta$. Inverting the model $\mathcal{M}_{\text{fwd}}$ is not possible (see section 2.1.1). However, if we can solve the forward problem, we can use Bayesian methods to solve the inverse problem as shown in our pedagogical example.

The forward approach is predictive. I know some characteristic of the atmosphere and I use the model $\mathcal{M}_{\text{fwd}}$ to predict an observable. The inverse approach is the other way, given the data I constrain the parameters of model $\mathcal{M}_{\text{fwd}}$. Obviously, there is a recursive cycle between forward and inverse approaches. Let's consider a model of earth's atmosphere. I use this model to predict the weather of tomorrow, which is a forward problem. Tomorrow comes and the data that I gather about the weather (temperature, humidty etc.) do not exactly match my prediction. I now use inverse methods to better constrain the parameters of the model. And I predict the weather for the next day with those updated parameters values and so on and so forth. As we gather more and more data the model may not be able to reproduce them all. A better model is therefore needed. To quantify how a model is better than another requires the Bayesian evidence or one of its proxy (BIC, AIC...), see section 2.1.3.

For exoplanet and brown-dwarf atmospheres, in situ measurements are not possible, the only physical quantity we actually observe is either the flux emitted by the planet or the flux of the star extinguished by the planet atmosphere. The data is therefore a spectrum (spectroscopy and/or photometry) or one of its derivatives (lightcurve, phase curve etc.). The natural output of an atmospheric forward model studying exoplanets or brown-dwarfs must be a spectrum or a derivative of it. Common parameters for atmospheric studies of emission observations include the chemical composition, the temperature-pressure profile, the clouds, the gravity, the radius etc., see next section.

Two types of model have emerged in the community to characterise exoplanets or brown-dwarfs atmosphere: self-consistent models and parameterised models. In the case of the self-consistent model, the physic is solved in a self-consistent way within our assumptions. For the parameterised model, some of this physic is parameterised. The parameterisation aims at reducing drastically the computation time of the model in order to perform a thorough exploration of the parameter space, to do a Bayesian analysis. Parameterisation of some part of a physical model is common across all science domain. For example, engineering uses parametrised models call surrogate, metamodels or emulators (Lavie et al. 2015). The self-consistent and the parameterised models can both be used for inverse or forward problems. In practice, self-consistent models are slow to compute and are used in forward problem. Parameterised models are faster and hence well-suited for inverse problems. The degree of parameterisation is driven by what physics one is ready to sacrifice and what computation time one need to gain in order to be able to perform the inference.

Atmospheric retrieval aims at solving the inverse problem and has been a growing method in exoplanetary and brown dwarf science (Madhusudhan & Seager 2009; Barstow et al. 2013; Benneke & Seager 2012; Line et al. 2012; Benneke & Seager 2013; Waldmann et al. 2015b; Line et al. 2016; Lavie et al. 2017b). It implies exploring the parameter space of a model $\mathcal{M}_{\mathrm{fwd}}$ in a statistical way in order to extract useful information from the data. At the moment all published work on atmospheric retrieval use some forms of parameterised models. On top of the gain in speed, parameterised models allow us to catch some unknown physics hidden in the data. Nature may surprise us.

3.1.2 Building an atmospheric model for emission observations

A blackbody model such as the one presented in 2.3 is helpful. It provides the temperature of the photosphere probe by our spectral observations of the object. However, it is too simple when spectroscopic observations are available with spectral features clearly visible as it is the case for direct imaged objects.

The first commonly employed assumption in atmospheric models for stellar companions is to consider a 1-dimensional atmosphere (plan-parallel atmosphere). By nature, atmospheres are three dimensional. This approximation is therefore questionable (Feng et al. 2016; Line 2016). However, a 3-dimensional radiative transfer model is computationally challenging, especially for atmospheric retrieval. Efforts are being made in Global Circulation Models (Mendonça et al. 2016, 2018) but performing retrieval is out of the question as those models take days, weeks or even months to compute. Hence, all models used in atmospheric retrievals study for exoplanets and brown-dwarfs are 1-dimensional (Madhusudhan & Seager 2009; Barstow et al. 2013; Benneke & Seager 2012; Line et al. 2012; Benneke & Seager 2013; Waldmann et al. 2015b; Line et al. 2016; Gandhi & Madhusudhan 2018)

The one dimensional atmosphere is divided into a certain number of layers, usually in pressure space assuming hydrostatic equilibrium. Radiative transfer is performed throughout those layers from the bottom of the atmosphere (BOA) to the top of the atmosphere (TOA) to produce the synthetic spectrum. `HELIOS_R` uses the two-stream approximation with the formalism developed in Heng et al. (2014). For each layer the two-stream approximation considers a pair of outgoing and incoming fluxes. To perform this radiative scheme we need the temperature, the pressure and the optical depth. The optical depth depends on the chemistry, what molecules are present and how do they interact with radiation. The opacity tables (opacities of each molecules as a function of wavelength, temperature and pressure) that describe those interactions are produced from lines lists database (such as HITRAN, EXOMOL etc.) with the opacity calculator $HELIOS\_K$ (Grimm & Heng 2015).

Within this assumption, a self-consistent model such as $HELIOS$ (Malik et al. 2017) is solving the radiative transfer equations until radiative equilibrium is reached. The output of this process is the temperature profile of the atmosphere. As Malik et al. (2017) describe it, this process is iterative : "within each model layer of the atmosphere, its temperature and pressure determine its absorption and scattering properties, given by molecular abundances and opacities, which in turn determine the transmission function and fluxes. However, as flux enters and exits the layer, the temperature changes, which in turn changes the opacity. [Clearly, this is an iterative process]". It is therefore time consuming and not well suited to perform atmospheric retrieval. A parameterised model such as `HELIOS_R` (see section 3.2.1) is not performing this iterative process and only propagates the flux upwards to the top of the atmosphere. The temperature profile as a function of pressure is computed using an analytical function. `HELIOS_R` can use different types of a physical functions such as derived in Guillot (2010) or Heng et al. (2014). Others parametrisation of the temperature profile have been proposed. Irwin et al. (2008) use a free parameter for each layer temperature, Madhusudhan & Seager (2009) use analytical function not bounded to any physical properties or Waldmann et al.

(2015a) use a combination of both free parameters and analytical function. The parameterisation forces the loss of consistency between the temperature-pressure profile and the chemistry in each of the atmospheric layers. One is loosing some physical insight but is gaining a significant amount of time. On one hand, the danger is to obtain chemical abundances far from what we may expect in the atmosphere based on our current understanding of chemistry (Heng & Tsai 2016). On the other hand, it may help us to catch some non predictable behaviour, for example a strong departure from chemistry equilibrium.

3.2 Presentation of the code

3.2.1 `HELIOS_R`: a retrieval code

The retrieval code that I have developed and the analysis of the HR 8799 planetary system is presented in the following paper, which is published in the astronomical journal.

`HELIOS−RETRIEVAL`: An Open-source, Nested Sampling Atmospheric Retrieval Code; Application to the HR 8799 Exoplanets and Inferred Constraints for Planet Formation

Baptiste Lavie[1,2,3] , João M. Mendonça[1] , Christoph Mordasini[2] , Matej Malik[1] , Mickaël Bonnefoy[4,5],
Brice-Olivier Demory[1] , Maria Oreshenko[2], Simon L. Grimm[1] , David Ehrenreich[3] , and Kevin Heng[2]

[1] University of Bern, Space Research and Planetary Sciences, Sidlerstrasse 5, CH-3012, Bern, Switzerland; baptiste.lavie@space.unibe.ch
[2] University of Bern, Center for Space and Habitability, Sidlerstrasse 5, CH-3012, Bern, Switzerland; kevin.heng@csh.unibe.ch
[3] Observatoire de l'Université de Genève, 51 chemin des Maillettes, 1290, Sauverny, Switzerland
[4] Université Grenoble Alpes, IPAG, F-38000, Grenoble, France
[5] CNRS, IPAG, F-38000, Grenoble, France
Received 2016 October 9; revised 2017 June 26; accepted 2017 July 4; published 2017 August 11

Abstract

We present an open-source retrieval code named `HELIOS−RETRIEVAL`, designed to obtain chemical abundances and temperature–pressure profiles by inverting the measured spectra of exoplanetary atmospheres. In our forward model, we use an exact solution of the radiative transfer equation, in the pure absorption limit, which allows us to analytically integrate over all of the outgoing rays. Two chemistry models are considered: unconstrained chemistry and equilibrium chemistry (enforced via analytical formulae). The nested sampling algorithm allows us to formally implement Occam's Razor based on a comparison of the Bayesian evidence between models. We perform a retrieval analysis on the measured spectra of the four HR 8799 directly imaged exoplanets. Chemical equilibrium is disfavored for HR 8799b and c. We find supersolar C/H and O/H values for the outer HR 8799b and c exoplanets, while the inner HR 8799d and e exoplanets have a range of C/H and O/H values. The C/O values range from being superstellar for HR 8799b to being consistent with stellar for HR 8799c and being substellar for HR 8799d and e. If these retrieved properties are representative of the bulk compositions of the exoplanets, then they are inconsistent with formation via gravitational instability (without late-time accretion) and consistent with a core accretion scenario in which late-time accretion of ices occurred differently for the inner and outer exoplanets. For HR 8799e, we find that spectroscopy in the *K* band is crucial for constraining C/O and C/H. `HELIOS−RETRIEVAL` is publicly available as part of the Exoclimes Simulation Platform (http://www.exoclime.org).

Key words: methods: statistical – planets and satellites: atmospheres – planets and satellites: composition –
planets and satellites: formation – planets and satellites: gaseous planets – planets and satellites: individual (HR 8799)

1. Introduction

1.1. Motivation

Traditionally, the masses and radii of brown dwarfs and substellar objects have been inferred by applying evolutionary tracks to measurements of their luminosities and ages (e.g., Burrows et al. 1997; Chabrier et al. 2000; Baraffe et al. 2002). On rare occasions, brown dwarfs and low-mass stars may transit their binary companions and allow for their other properties to be studied (see Burrows et al. 2011 and references therein). A particularly important study was conducted by Konopacky et al. (2010), who were able to obtain dynamical masses for 15 brown dwarfs residing in binaries. By comparing the dynamical and photometric masses, Konopacky et al. (2010) showed that both the Burrows et al. (1997) and Chabrier et al. (2000) models underpredicted the masses of M and L dwarfs and overpredicted the mass of the lone T dwarf in their sample by ∼10% (tens of percent). By studying a sample of 46 L dwarfs, Hiranaka et al. (2016) suggested that a dust haze of sub-micron-sized particles exist in their upper atmospheres, which are neglected by the standard evolutionary tracks.

Taken together, these results suggest that the traditional approach of using self-consistent evolutionary tracks may be incomplete and motivates alternative and complementary ways of interpreting the spectra of brown dwarfs and substellar objects. We expect this train of thought to apply to the recently discovered directly imaged exoplanets as well, since the interpretation of their photometry and spectroscopy is typically performed using the evolutionary tracks computed for brown dwarfs (e.g., Bonnefoy et al. 2016).

1.2. Theoretical Improvements

Self-consistent forward modeling starts with a set of assumptions and computes forward to predict the temperature–pressure profile and synthetic spectrum of an object. Atmospheric retrieval is a complementary approach borrowed from the Earth's remote sensing community, where one applies an inversion method to obtain the temperature–pressure profile and chemical abundances from finding the best-fit solution to the measured spectrum (e.g., Madhusudhan & Seager 2009; Benneke & Seager 2013; Lee et al. 2013; Line et al. 2013, 2016; Barstow et al. 2015; Waldmann et al. 2015). It sacrifices self-consistency and sophistication for simplicity, which allows for a more thorough exploration of parameter space. Atmospheric retrieval is particularly well-suited for addressing questions regarding planet formation, since it allows for the posterior distributions of the carbon-to-oxygen ratio (C/O) and the elemental abundances of carbon (C/H) and oxygen (O/H) to be computed.

The HR 8799 system hosts four exoplanets (Marois et al. 2008, 2010), whose formation mechanisms remain an enigma (Kratter et al. 2010). Spectra with resolutions of about 30 to 4000 have been obtained by, e.g., Barman et al. (2011, 2015), Konopacky et al. (2013), Oppenheimer et al. (2013), Ingraham et al. (2014), and Zurlo et al. (2016). Since these spectra have resolutions that are considerably higher than those obtained for hot Jupiters using WFC3 on the *Hubble Space Telescope* (e.g.,
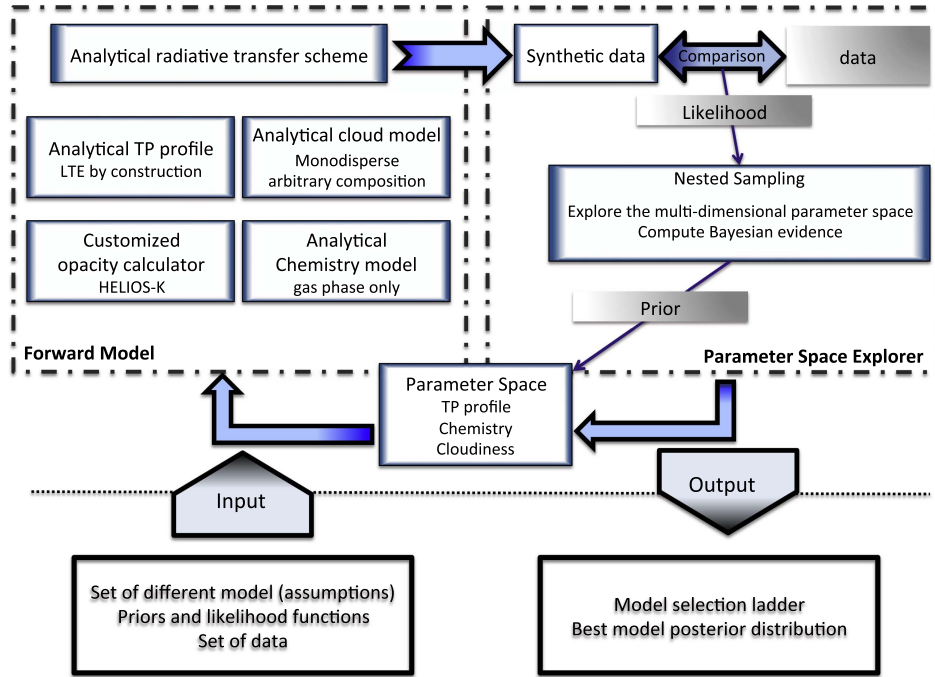
Figure 1. Flow chart for `HELIOS-R` and a description of its main components. Note that enforcing equilibrium chemistry is optional and our approach for distinguishing between equilibrium and non-equilibrium chemistry is completely data-driven.

Deming et al. 2013; Mandell et al. 2013; Kreidberg et al. 2014; Stevenson et al. 2014), they present an opportunity for performing remote sensing of exoplanetary atmospheres that is similar to what planetary scientists had to work with a few decades ago, before the advent of probes. A key difference is that the radii and masses of these directly imaged exoplanets are unknown,[6] unlike for transiting exoplanets. A recent review of directly imaged exoplanets, which includes the HR 8799 system, may be found in Bowler (2016).

The first atmospheric retrieval analysis of directly imaged exoplanets was performed by Lee et al. (2013), who studied only the HR 8799b exoplanet. In the current study, we collect all of the published spectra of the HR 8799b, c, d, and e exoplanets and subject them to the same retrieval method with the intention of using the retrieved chemistry to constrain planet formation scenarios.

Besides the novelty of our analysis, the current study is also a method paper for our new atmospheric retrieval code named `HELIOS-R`, which we constructed from scratch to study exoplanetary atmospheres. `HELIOS-R` is part of the `HELIOS` radiation package of the Exoclimes Simulation Platform[7] and has the following features (Figure 1).

1. We have implemented a nested sampling algorithm to explore the multi-dimensional parameter space (Skilling 2006; Feroz et al. 2009; Benneke & Seager 2013; Waldmann et al. 2015; Line et al. 2016). Unlike other approaches (e.g., Markov Chain Monte Carlo, nonlinear optimal estimation), nested sampling allows for the Bayesian evidence to be directly calculated, which in turn allows for models with different parametrizations

(and number of parameters) to be compared on an equal footing. Models with extra complexity are penalized, which allows for Occam's Razor[8] to be formally enforced. For example, our retrieval analysis allows us to formally determine if chemical equilibrium is favored or disfavored in an atmosphere in a completely data-driven manner. As another example, it allows us to determine the number and types of molecules to be included in the retrieval.

2. Our temperature–pressure profile is taken from Heng et al. (2014), who generalized the work of Guillot (2010) and Heng et al. (2012) to include non-isotropic scattering and non-constant opacities. When stellar irradiation and scattering are omitted, the temperature–pressure profile reduces to the classical solution of Milne for self-luminous objects (Mihalas 1970). By construction, it conserves energy in an analytical and exact sense.

3. Our atmospheric cross-sections are computed using our customized opacity calculator named `HELIOS-K`, which was previously published by Grimm & Heng (2015).

4. To combine the cross-sections of different molecules, one needs to have a chemistry model that calculates their relative abundances. We use the analytical solutions of Heng et al. (2016), Heng & Lyons (2016), and Heng & Tsai (2016), which have been shown to be accurate at the ∼1% level (or better) when benchmarked against numerical solutions using Gibbs free energy minimization. These analytical solutions allow for fast computation if one wishes to enforce chemical equilibrium.

5. Our radiative transfer scheme, which translates cross-sections and temperatures into fluxes (and hence allows us to compute the synthetic spectrum), uses the exact

---

[6] Meaning that they are typically not directly measured, but rather inferred using evolutionary models, which means the radii and masses are model-dependent.
[7] http://www.exoclime.org

[8] Whether Occam's Razor always yields the correct answer is another matter. In the current study, we are guided by Occam's Razor in the limit of sparse data.

Table 1
Shorthand Notation for the Suite of Models Tested in This Study

Notation	Meaning
U	Unconstrained chemistry
E	Equilibrium chemistry
B	Cloud-free ("blue sky")
C	Cloudy
1	H_2O is included in retrieval
2	CO_2 is included in retrieval
5	CO is included in retrieval
6	CH_4 is included in retrieval
r	Planet radius R is included in retrieval
g	Planet surface gravity g is included in retrieval
d	Distance of the system d is included in retrieval

Note. "1," "2," "5," and "6" refer to the HITRAN/HITEMP labels for these molecules. When no number is specified, it means that all four molecules are included in the retrieval. For example, UBrg16 is a cloud-free model with unconstrained chemistry, where the mixing ratios of water and methane, as well as the planetary radius and surface gravity, are included as fitting parameters. By contrast, the UB model includes all four molecules in the retrieval, but fixes the planetary radius and surface gravity to user-specified values.

analytical solution in the limit of isothermal model layers and pure absorption (Heng et al. 2014). It allows us to analytically integrate over all of the incoming and outgoing angles associated with every ray.

6. Our cloud model is based on the basic principles of Mie theory (e.g., Pierrehumbert 2010). It assumes a mono-disperse set of particles, which may be interpreted as the dominant size in a size distribution of particles (e.g., Burrows et al. 2011). It includes a dimensionless parameter that is a proxy for the cloud composition. When the particles are small compared to the wavelength, it reproduces Rayleigh scattering. By contrast, models that implement a constant cloud-top pressure implicitly assume the cloud particles to be large (compared to the wavelength observed) and preclude Rayleigh scattering by construction.

While each component of HELIOS-R may not be novel by itself, the assembly of all of these components into a single code and retrieval tool is a novel endeavor. Furthermore, we have designed HELIOS-R to run on Graphics Processing Units (GPUs), which affords speed-ups of at least a factor of several compared to the CPU version. With a UCrg model (see Table 1) retrieval performed on the HR 8799b data set, the GPU version is five times faster than the CPU version on a macbook Pro laptop equipped with an NVIDIA GeForce GT 750M GPU card and an Intel Core i7 2.5 GHz CPU. For this analysis, we used our GPU cluster of NVIDIA K20 cards; it takes 10^{-2} s to evaluate one likelihood of this UCrg model.

In Section 2, we provide a detailed description of each component or ingredient of HELIOS-R. In Section 3, we subject HELIOS-R to several tests before applying it to the measured spectra of the HR 8799b, c, d, and e directly imaged exoplanets. In Section 4, we present our retrieval results of the HR 8799 system. In Section 5, we compare our study to previous work and describe opportunities for future work. Table 1 shows the suite of models tested in the current study. Table 2 states the priors used for our fitting parameters. Table 3 summarizes our retrieval results. Appendix A states our fast analytical formulae for evaluating the exponential integral of

Table 2
Priors Used in This Study

Symbol	Prior Used	Value
R	Gaussian	$R = 1.2 \pm 0.1\, R_J$
g	Gaussian	$\log g = 4.1 \pm 0.3$ (cgs)
X_i	Log-uniform	10^{-20} to 10^{-1}
κ_0	Log-uniform	$\log \kappa_0 = 10^{-15}$–10 (mks)
T_{int}	Uniform	10–1500 K
Q_0	Uniform	1–100
r_c	Log-uniform	10^{-7}–10^{-3} m
f_{cloud}	Log-uniform	10^{-30}–10^{-4}
d	Gaussian	39.4 ± 1.0 pc

Note. cgs: centimeters, grams, and seconds. mks: meters, kilograms, and seconds.

the first order. Appendix B includes, for completeness, the full posterior distributions of the best models for the atmospheres of HR 8799b, c, d, and e.

2. Methodology

The executive summary is that each model of the retrieval contains up to 11 parameters: the radius, the surface gravity, 2 for the temperature–pressure profile, 2 or 4 for the chemistry (depending on whether one adopts equilibrium or uncon-strained chemistry), and 3 for the cloud model. The mean molecular weight is not a parameter and is constructed from the mixing ratios. Each HR 8799 exoplanet typically has between 40 and 120 data points for its measured spectrum: 68 for b, 105 for c, 115 for d, and 48 for e.

To construct an atmospheric retrieval model, we need a forward model. By "forward model," we refer to the temperature–pressure profile, atmospheric opacities, chemistry model, radiative transfer scheme, and cloud model. We also need a method to scan the vast multi-dimensional parameter space of our forward model to locate the highest likelihood region, i.e., the best solution that fits the data (e.g., for a review, see Press et al. 2007).

2.1. Nested Sampling

We use a nested sampling algorithm (Skilling 2006) to scan the diverse, multi-dimensional parameter space describing our one-dimensional model atmospheres. Benneke & Seager (2013) previously gave a detailed overview of the nested sampling method. Waldmann et al. (2015) and Line et al. (2016) also used nested sampling. Here, we provide a concise description of our implementation.

Consider a model with a set of parameters $\theta = \{\theta_1, \theta_2, ..., \theta_{N_\theta}\}$, where N_θ is the number of parameters. Consider a set of models labeled by the index i: $\mathcal{M}_i$. The probability density function (PDF) on the parameters for a given model is $\mathcal{P}(\theta|\mathcal{M}_i)$, which is also known as the "prior."

Discussions of any Bayesian method necessarily start with Bayes's rule, which states that the PDF of a model given the data (denoted by D) is (e.g., Skilling 2006)

$$\mathcal{P}(\theta|D, \mathcal{M}_i) = \frac{\mathcal{P}(\theta|\mathcal{M}_i)\, \mathcal{L}(D|\theta, \mathcal{M}_i)}{\mathcal{Z}(D|\mathcal{M}_i)}. \qquad (1)$$

Table 3
Summary of Retrieved Results

Property	Exoplanet	Value
X_{H_2O}	HR 8799b	$-2.89^{+0.09}_{-0.09}$
X_{H_2O}	HR 8799c	$-2.60^{+0.12}_{-0.05}$
X_{H_2O}	HR 8799d	$[-2.29]$
X_{H_2O}	HR 8799e	$[-1.84]$
X_{CO_2}	HR 8799b	$-6.70^{+1.52}_{-6.33}$
X_{CO_2}	HR 8799c	$-4.63^{+0.13}_{-0.11}$
X_{CO_2}	HR 8799d	$[-18.84]$
X_{CO_2}	HR 8799e	$[-19.13]$
X_{CO}	HR 8799b	$-1.86^{+0.10}_{-0.09}$
X_{CO}	HR 8799c	$-2.48^{+0.14}_{-0.20}$
X_{CO}	HR 8799d	$[-16.32]$
X_{CO}	HR 8799e	$[-17.36]$
X_{CH_4}	HR 8799b	$-5.03^{+0.14}_{-0.16}$
X_{CH_4}	HR 8799c	$-5.03^{+0.17}_{-0.18}$
X_{CH_4}	HR 8799d	$[-28.11]$
X_{CH_4}	HR 8799e	$[-27.59]$
μ	HR 8799b	$2.18^{+0.00}_{-0.00}$
μ	HR 8799c	$2.19^{+0.00}_{-0.00}$
μ	HR 8799d	$[2.28]$
μ	HR 8799e	$[2.42]$
C/O	HR 8799b	$0.92^{+0.01}_{-0.01}$
C/O	HR 8799c	$0.55^{+0.10}_{-0.12}$
C/O	HR 8799d	$0.00^{+0.00}_{-0.00}$
C/O	HR 8799e	$0.00^{+0.00}_{-0.00}$
C/H	HR 8799b	$-2.11^{+0.10}_{-0.09}$
C/H	HR 8799c	$-2.73^{+0.14}_{-0.20}$
C/H	HR 8799d	$-16.62^{+4.08}_{-2.04}$
C/H	HR 8799e	$-11.93^{+4.62}_{-4.64}$
O/H	HR 8799b	$-2.07^{+0.09}_{-0.09}$
O/H	HR 8799c	$-2.47^{+0.09}_{-0.11}$
O/H	HR 8799d	$-3.20^{+0.19}_{-0.15}$
O/H	HR 8799e	$-2.75^{+0.57}_{-0.57}$
Q_0	HR 8799b	$1.21^{+0.49}_{-0.73}$
Q_0	HR 8799c	$0.79^{+0.25}_{-0.26}$
Q_0	HR 8799d	$1.39^{+0.27}_{-0.34}$
Q_0	HR 8799e	$0.95^{+0.53}_{-0.52}$
r_c	HR 8799b	$-4.37^{+0.49}_{-0.46}$
r_c	HR 8799c	$-4.44^{+0.25}_{-0.20}$
r_c	HR 8799d	$-6.68^{+0.18}_{-0.18}$
r_c	HR 8799e	$-4.69^{+0.79}_{-0.76}$
X_c	HR 8799b	$-21.22^{+0.80}_{-0.85}$
X_c	HR 8799c	$-20.55^{+0.41}_{-0.49}$
X_c	HR 8799d	$-15.96^{+1.20}_{-0.95}$
X_c	HR 8799e	$-20.56^{+1.55}_{-1.37}$
d	HR 8799b	$40.30^{+0.66}_{-0.79}$
d	HR 8799c	$39.73^{+0.22}_{-0.20}$
d	HR 8799d	$40.81^{+0.42}_{-0.50}$
d	HR 8799e	$39.40^{+0.70}_{-0.78}$

Note. We have listed the 1σ uncertainties, which were computed by locating the 15.87th and 84.13th percentile points on the horizontal axis. In the limit of a symmetric Gaussian function, these would yield the full-width at half-maximum of the Gaussian. For planets d and e, the molecule abundances and the mean molecular weight are given at 1 bar. Values are in $\log_{10}$ (except for C/O) and dimensionless (except for r_c, which is in meters).

The quantity $\mathcal{L}(\boldsymbol{D}|\boldsymbol{\theta}, \mathcal{M}_i)$ is the "likelihood." We assume $\mathcal{L}(\boldsymbol{D}|\boldsymbol{\theta}, \mathcal{M}_i)$ to be the same Gaussian function as Equation (5) of Benneke & Seager (2013).

We will term $\mathcal{P}(\boldsymbol{\theta}|\boldsymbol{D}, \mathcal{M}_i)$ the "posterior." Since it normalizes to unity, the Bayesian evidence is given by the multi-dimensional integral,

$$\mathcal{Z}(\boldsymbol{D}|\mathcal{M}_i) = \int \mathcal{P}(\boldsymbol{\theta}|\mathcal{M}_i) \mathcal{L}(\boldsymbol{D}|\boldsymbol{\theta}, \mathcal{M}_i) \, d\boldsymbol{\theta}. \qquad (2)$$

Fitting a model to a measured spectrum is an exercise in which a better fit is obtained when more free parameters (e.g., more molecules) are introduced. Model selection is essentially the enforcement of Occam's Razor, meaning that we select the model that has a level of sophistication or complexity that is commensurate with the quality of data available. It prevents the over-fitting of data by a model that is too complex. For example, Hansen et al. (2014) find that, for some of the exoplanets, the photometric data of *Spitzer* alone may be fitted with a Planck function and a more complex model is unnecessary. As the data quality improves, so does the complexity of the best model.

The essence of the nested sampling is to reduce the computation of the Bayesian evidence to a one-dimensional integral (Skilling 2006),

$$\mathcal{Z}(\boldsymbol{D}|\mathcal{M}_i) = \int_0^1 \mathcal{L}'(\mathcal{X}) \, d\mathcal{X}, \qquad (3)$$

where the likelihood now only depends on a single variable and is denoted by $\mathcal{L}'$. This variable $\mathcal{X}$ is termed the "prior mass" and is bounded between 0 and 1. A visualization of the prior mass and its relationship to the Bayesian evidence is given in Figure 3 of Skilling (2006) and Figure 1 of Benneke & Seager (2013). Numerically, we use the trapezoid rule to compute the Bayesian evidence as a finite sum,

$$\mathcal{Z}(\boldsymbol{D}|\mathcal{M}_i) = \sum_j \frac{\mathcal{X}_{j+1} - \mathcal{X}_j}{2} (\mathcal{L}'_{j+1} + \mathcal{L}'_j). \qquad (4)$$

We begin by randomly drawing N_{live} points from the parameter space(θ) subjected to the constraint of the chosen prior. We use either Gaussian (radius, logarithm of gravity, distance), log-uniform (mixing ratios, mean opacity, cloud particle radius, cloud mixing ratio), or uniform (temperature, cloud composition parameter) priors. For a set of points drawn, we compute their likelihood values. At each step of the algorithm, we discard the worst point and replace it with a newly drawn point until the convergence criteria is met (see Skilling 2006). This newly drawn point needs to have a higher likelihood than the worst point that was just discarded. Specifically, we use the open-source software named PyMultiNest[9] (Buchner et al. 2014), which is a Python wrapper for the open-source MultiNest[10] program written in Fortran 90 (Feroz & Hobson 2008; Feroz et al. 2009, 2013). For each model, we run the nested sampling algorithm using 40,000 living points parallelized into 20 runs of 2000 "living points" each. For comparison, Waldmann et al. (2015) uses $N_{live} = 4000$ living points. Benneke & Seager (2013) use between $N_{live} = 50$ and 10,000 living points. Line et al. (2016) do not specify the number of living points used. Equation (4) is used to compute the Bayesian evidence. As a byproduct of this

---

[9] https://github.com/JohannesBuchner/PyMultiNest/
[10] https://ccpforge.cse.rl.ac.uk/gf/project/multinest/

procedure, one also obtains posterior-distribution samples of the model parameters.

For the purpose of comparing two models, which we denote by $\mathcal{M}_i$ and $\mathcal{M}_{i+1}$, it is useful to define a quantity known as the Bayes factor, which is the ratio of the Bayesian evidences (Trotta 2008),

$$\mathcal{B} = \frac{\mathcal{Z}(\boldsymbol{D}|\mathcal{M}_i)}{\mathcal{Z}(\boldsymbol{D}|\mathcal{M}_{i+1})}. \qquad (5)$$

The Bayes factor is equal to the posterior odds when both models are considered equally likely. As shown in Table 2 of Trotta (2008), which is reproduced in Table 2 of Benneke & Seager (2013), there is a relationship between the Bayes factor, the p-value of the frequentists and the significance in terms of the number of standard deviations. We use the Jeffreys scale (Kass & Raftery 1995) to evaluate model significances. Weak, moderate, and strong evidence for favoring the ith model over the $(i + 1)$th model correspond to $\ln \mathcal{B} = 1$, 2.5, and 5, respectively.

2.2. Temperature–Pressure Profile

For the temperature–pressure profile, we assume a one-dimensional, plane–parallel model atmosphere. Its layers are evenly spaced in the logarithm of pressure between 1 μbar and 1 kbar. We implement equation (126) of Heng et al. (2014), who previously generalized the work of Guillot (2010; pure absorption limit and constant opacities) and Heng et al. (2012; isotropic scattering, constant shortwave/optical opacity) to include non-isotropic scattering and a non-constant shortwave/ optical opacity. Since the HR 8799 exoplanets are non-irradiated, we essentially use a reduced version of Equation (126) of Heng et al. (2014),

$$T^4 = \frac{T_{int}^4}{4}\left[\frac{8}{3} + \frac{3\tilde{m}}{\beta_L^2}\left(\kappa_0 + \frac{\kappa_{CIA}\tilde{m}}{2\tilde{m}_0}\right)\right], \qquad (6)$$

where T_{int} is the internal/interior temperature, β_L is the longwave/infrared scattering parameter, κ_0 is the constant component of the longwave/infrared opacity, and κ_{CIA} is the opacity associated with collision-induced absorption (CIA). The column mass is denoted by $\tilde{m}$, while $\tilde{m}_0$ is the column mass referenced to the bottom of the model atmosphere. We set $P_0 = \tilde{m}_0 g = 1$ kbar, where g is the surface gravity.

Equation (6) is essentially a generalization of the classical Milne's solution (Mihalas 1970) to include scattering and CIA. In the limit of pure absorption ($\beta_L = 1$) and in the absence of CIA, we obtain $T = T_{int}$ when $\kappa_0\tilde{m} = 4/9$, which is somewhat different from the classical Milne value of $2/3$. It is worth emphasizing that Equation (6) is, by construction, a temperature–pressure profile in radiative equilibrium, which implies that both local and global energy conservation are guaranteed in an exact, analytical sense (Heng et al. 2014; Heng & Lyons 2016). By contrast, the versatile fitting function used by Madhusudhan & Seager (2009) does not, by construction, obey energy conservation and this has to be enforced as a separate numerical condition. However, by using a mean opacity, Equation (6) sacrifices accuracy for simplicity, which makes the temperature–pressure profile more isothermal at high altitudes than if a more realistic radiative transfer calculation was performed.

In principle, κ_0 and κ_{CIA} are mean opacities that may be calculated directly from the spectroscopic line lists. However,

while deriving these analytical temperature–pressure profiles Guillot (2010) and Heng et al. (2012, 2014) have assumed that the absorption, flux, Planck, and Rosseland mean opacities are equal, which makes it unclear how to exactly compute κ_0 and κ_{CIA}. Therefore, we opt to use κ_0 and κ_{CIA} as fitting parameters instead. In other words, our temperature–pressure profile is not self-consistent with the atmospheric opacities used.

We find that using κ_{CIA} and β_L as fitting parameters has a negligible effect on our results (not shown). In practice, the use of Equation (6) with only T_{int} and κ_0 as fitting parameters (i.e., setting $\beta_L = 1$ and $\kappa_{CIA} = 0$) is sufficient for our retrieval calculations.

We use a constant value of the surface gravity, as we are sensing 6 orders of magnitude in pressure at most, which corresponds to 13.8 scale heights. This means that the region of the atmosphere being sensed is only several percent of the radius of the exoplanet. A constant surface gravity is thus not unreasonable.

2.3. Atmospheric Cross-sections

We first distinguish between our use of the terms "cross-section" and "opacity." The former has units of area. The latter is the cross-section per unit mass. We previously designed and wrote an open-source opacity calculator (Grimm & Heng 2015), based on implementing Algorithm 916 (Zaghloul & Ali 2012) to perform fast computations of the Voigt profile by recasting it as a Faddeeva function. Typically, HELIOS-K is able to compute an opacity or cross-section function with $\sim 10^5$ spectral lines in ~ 1 s on an NVIDIA K20 GPU. In principle, it is agnostic about the spectroscopic line list being used and is able to take any line list as an input. The details of how to take the inputs of a line list and use them to compute the integrated line strengths and line shapes have previously been summarized in Grimm & Heng (2015), and we will not repeat them here.

We restrict ourselves to only four molecules: carbon monoxide (CO), carbon dioxide (CO_2), water (H_2O), and methane (CH_4). For CO and CO_2, we use the HITEMP database (Rothman et al. 1996, 2010, 2013). For H_2O and CH_4, we use the ExoMol line list (Barber et al. 2006; Yurchenko & Tennyson 2014). Acetylene, ammonia, ethylene, and hydrogen cyanide have been omitted because they are subdominant at the photospheric temperatures of the HR 8799 exoplanets (Madhusudhan 2012; Heng & Tsai 2016; Moses et al. 2016). In particular, see Figure 10 of Moses et al. (2016).

In the current study, we choose to deal with cross-sections instead of opacities. For our HELIOS self-consistent radiative transfer code, we chose to use opacities instead (Malik et al. 2017). There are various strategies to construct the cross-section function of the atmosphere. By "cross-section function," we refer to the function that depends on temperature, pressure, wavenumber, and type of molecule. The cross-section function is a theoretical construction: it may be defined continuously or be sampled at an arbitrary number of discrete points. We consider the way in which the cross-section function is sampled as an issue of implementation, which we will now discuss. Regardless of the approach used to construct and sample the cross-section function, the end goal is the same: to use them to construct transmission functions and ultimately integrate fluxes over a waveband.

The first approach is to use the "k-distribution method," which resamples the highly erratic cross-section function into a

monotonically increasing cumulative distribution function (Lacis & Oinas 1991; Fu & Liou 1992; Grimm & Heng 2015). Since the k-distribution method is only exact for a homogeneous atmosphere with one molecule (Grimm & Heng 2015), one has to apply the "correlated-k approximation" as well, which assumes that the spectral lines are perfectly correlated (see Chapter 4.4.5 of Pierrehumbert 2010).

The second approach is to use "opacity sampling," which is to discretely sample the opacity function, typically at a smaller number of points than there are lines. In our context, it is perhaps more accurate to use the term "cross-section sampling."

The "line-by-line" limit occurs when the integrated fluxes over a waveband is exact (to machine precision). It is essentially the second approach, but where the cross-section function is sampled at more wavenumber points than there are lines. Since there are $\sim 10^9$ (or more) lines for the water molecule alone, this is a formidable computational challenge and is currently infeasible for any retrieval code dealing with hot exoplanetary atmospheres. We note that a cross-section function that includes all of the lines of a given line list does not qualify it as being "line-by-line," if the sampling is not fine enough to resolve each line profile.

In the current study, we adopt the second approach, which is also used by Madhusudhan & Seager (2009), Benneke & Seager (2013), Line et al. (2013), and Waldmann et al. (2015). Our spectral resolution used is $1 \, \text{cm}^{-1}$, evenly sampled across the wavenumber. We note that Line et al. (2013, 2015) and Waldmann et al. (2015) also used a spectral resolution of $1 \, \text{cm}^{-1}$. Some authors do not specify the spectral resolution of their atmospheric cross-section function (e.g., Madhusudhan & Seager 2009; Benneke & Seager 2013; Barstow et al. 2015; Line et al. 2016). We precompute our cross-sections on a grid across wavenumber, pressure, and temperature: 100–2900 K (in increments of 200 K) and 1 μbar to 1 kbar (with two points per dex in pressure) for CO, CO_2, CH_4, and H_2O. The grid is then interpolated to obtain values of the cross-sections for any temperature and pressure within the stated ranges.

A lingering issue, which stems from an unsolved physics problem, is that the far line wings of Voigt profiles do not accurately represent the wings of real lines. Various groups have adopted different ad hoc approaches to truncating the Voigt profiles (see Grimm & Heng 2015 and references therein). Hedges & Madhusudhan (2016) discuss this issue, but do not provide any solution for it. In the current study, we adopt a $100 \, \text{cm}^{-1}$ cutoff.

2.4. Chemistry

Once the cross-sections have been computed, they may be used to compute the optical depth of each model layer for all of the molecules,

$$\Delta\tau = \sum_i \frac{X_i \sigma_i}{\bar{m} g} \, \Delta P, \qquad (7)$$

where X_i and σ_i are the mixing ratio and cross-section of the ith molecule, respectively. ΔP is the thickness of the layer in terms of the difference in pressure. The mean molecular mass is given by $\bar{m} = \mu m_u$, where μ is the mean molecular weight and m_u is the atomic mass unit. The preceding expression assumes hydrostatic equilibrium, isothermal layers, and that the surface gravity is constant throughout our model atmosphere.

Generally, the mixing ratios of molecular hydrogen and helium only show up via CIA as a contribution to the continuum of a spectrum, which implies that they cannot be as definitively determined as that of the molecules. Our CIA opacities are obtained from Richard et al. (2012). In the range of $X_{H_2} \approx 0.8$–0.9, the effect on the continuum of the synthetic spectrum is very similar (not shown). The effects of H_2-He CIA are even more subtle. As such, we adjust X_{H_2} to render the sum of the mixing ratio's unity,

$$1.1 X_{H_2} + \sum_i X_i = 1, \qquad (8)$$

where we have assumed that $X_{He} = 0.1 X_{H_2}$ to reflect cosmic abundance. By denoting the mass of the ith molecule by m_i, the corresponding mean molecular weight is calculated using

$$\mu = 2 X_{H_2} + 4 X_{He} + \sum_i \frac{m_i X_i}{m_u}. \qquad (9)$$

For example, if we have $X_{H_2} = 0.85$, $X_{He} = 0.085$, and $X_{CO} = 0.065$, then we have $\mu = 3.86$. In models with equilibrium chemistry, the mean molecular weight changes slightly for each layer, because the molecular abundances vary from layer to layer even for the same metallicity.

In the current study, we consider two chemistry models. "Unconstrained chemistry" refers to using each X_i as a fitting parameter in the retrieval. "Equilibrium chemistry" means that the X_i may be determined using only the elemental abundances of carbon (f_C) and oxygen (f_O), if C–H–O gaseous chemistry is considered. In this case, the four-parameter system of unconstrained chemistry reduces to two parameters. To compute the four X_i values given f_C and f_O, we use the validated analytical formulae of Heng et al. (2016), Heng & Lyons (2016), and Heng & Tsai (2016). Specifically, we implement Equations (12), (20), and (21) of Heng & Lyons (2016) for gaseous C–H–O chemistry. The benchmarking of these formulae against calculations of Gibbs free energy minimization was previously performed by Heng & Tsai (2016), who showed that they are accurate at the $\sim 1\%$ level or better. Further validation of these formulae comes from matching the trends found by Madhusudhan (2012) and Moses et al. (2013).

For unconstrained chemistry, the carbon-to-oxygen ratio is computed using

$$C/O = \frac{X_{CO} + X_{CO_2} + X_{CH_4}}{X_{CO} + 2 X_{CO_2} + X_{H_2O}}. \qquad (10)$$

The elemental abundances are inferred using

$$C/H = \frac{X_{CO} + X_{CO_2} + X_{CH_4}}{2 X_{H_2} + 4 X_{CH_4} + 2 X_{H_2O}},$$
$$O/H = \frac{X_{CO} + 2 X_{CO_2} + X_{H_2O}}{2 X_{H_2} + 4 X_{CH_4} + 2 X_{H_2O}}. \qquad (11)$$

Each mixing ratio is assumed to be constant over the entire model atmosphere. The alternative, which is to have a different value of the mixing ratio for each of the 100 model layers we assume, would result in 400 free parameters. This is unwarranted given the sparseness of the data, i.e., we have less than 400 data points.

For equilibrium chemistry, the carbon-to-oxygen ratio is simply

$$C/O = \frac{f_C}{f_O},\qquad(12)$$

and $f_C \equiv C/H$ and $f_O \equiv O/H$ are directly the fitting parameters of the retrieval. Since the mixing ratios of all of the molecules can be exactly specified for each layer, which has its own temperature and pressure, the assumption of constant mixing ratios across height/pressure is unnecessary for the models with equilibrium chemistry. The 400 values of the mixing ratios are specified by just two free parameters: f_C and f_O.

Unlike in previous studies, we do not manually decide whether to pick unconstrained or equilibrium chemistry. Rather, we compute both of these models and select between them based on the Bayesian evidence computed.

We note that, as part of the ESP, we have previously developed a chemical kinetics solver named VULCAN (Tsai et al. 2017).

2.5. Radiative Transfer Scheme

With the cross-sections and temperature–pressure profiles in hand, one may compute the optical depth and hence the transmission function for each layer of the model atmosphere. To propagate fluxes through the atmosphere and thus obtain the synthetic spectrum, we need a radiative transfer scheme. Beer's law[11] is the simplest example of such a scheme, where incident radiation through a passive medium is exponentially attenuated. A more sophisticated radiative transfer scheme needs to account for both the fluxes incident upon a layer and the thermal emission associated with the layer itself, since each layer has a finite temperature. To this end, we use Equation (B4) of Heng et al. (2014),

$$F_{\uparrow_{j+1}} = F_{\uparrow_j}\mathcal{T} + \pi B(1 - \mathcal{T}),\qquad(13)$$

where the fluxes are computed at the j and $(j + 1)$th interfaces. The Planck function (B) is evaluated within each layer. The transmission function is given by Equation (B5) of Heng et al. (2014)

$$\mathcal{T} = (1 - \Delta\tau)\exp(-\Delta\tau) + (\Delta\tau)^2 \mathcal{E}_1,\qquad(14)$$

with $\mathcal{E}_1(\Delta\tau)$ being the exponential integral of the first order. The optical thickness of each layer is given by $\Delta\tau$. Appendix A describes an analytical fitting formula for $\mathcal{E}_1$ that is highly accurate and allows for the computation to be significantly sped up.

We use Equation (13) to propagate the boundary condition at the bottom of the atmosphere (i.e., the internal/interior heat flux), which is the Planck function with a temperature given by the temperature–pressure profile at the bottom boundary. The outgoing flux at the top of the atmosphere is then the synthetic spectrum.

We emphasize that Equation (13) is an exact solution of the radiative transfer solution in the limit of isothermal layers and pure absorption. It is an improvement over using approximate solutions (e.g., two-stream solutions) and allows us to implement a radiative transfer scheme without taking any approximations

---

[11] Also known as the Beer–Lambert–Bouguer law.

besides assuming pure absorption. Equation (13) is equivalent to the approach of Line et al. (2016), who used four-point Gaussian quadrature to account for angle-dependent flux propagation. In our exact solution, the integration over angle has been performed analytically and is encapsulated in the exponential integral of the first order. We gain computational efficiency both by bypassing the need for performing Gaussian quadrature and also by evaluating $\mathcal{E}_1$ using an analytical approach (Appendix A). The overall accuracy is relegated to the number of discrete layers used.

The radius of the exoplanet (R) only appears as a scaling factor between the observed flux (F_{obs}) and the flux escaping from the top of the atmosphere (F_{TOA}),

$$F_{obs} = \left(\frac{R}{d}\right)^2 F_{TOA},\qquad(15)$$

where d is the distance between the observer and the object. The HR 8799 system is located at 39.4 ± 1.0 pc (van Leeuwen 2007), but the measured fluxes are usually reported as if it were located at $d = 10$ pc (i.e., absolute fluxes).

2.6. Cloud Model

The need for a cloud model is motivated by previous suggestions that the atmospheres of the HR 8799 exoplanets are cloudy (Barman et al. 2011; Madhusudhan et al. 2011; Marley et al. 2012), and also by the finding that each cloud configuration essentially corresponds to a different mass–radius relationship (Burrows et al. 2011; Lee et al. 2013). Our cloud model is based on the notion that, while cloud formation is challenging to model from first principles (e.g., Helling & Woitke 2006), once clouds do form it is somewhat easier to describe their effects on the synthetic spectrum, since this is derived from our knowledge of classical optics and Mie theory (Pierrehumbert 2010).

Following Lee et al. (2013), we consider the presence of clouds to add an extra contribution to the optical depth,

$$\Delta\tau_c = Q_{ext}\pi r_c^2 n_{cloud}\,\Delta z = Q_{ext}\pi r_c^2 f_{cloud}\frac{\Delta P}{\bar{m}g},\qquad(16)$$

where Q_{ext} is the extinction efficiency, r_c is the radius of the (spherical) particles, n_{cloud} is the number density of clouds, and $\Delta z = \Delta P/n\bar{m}g$ is the spatial thickness of the layer. The cloud mixing ratio is $f_{cloud} = n_{cloud}/n$ and it is this quantity that we set a prior on (see Table 2 for its range of values). We assume the cloud to be uniformly distributed throughout the atmosphere.

In a departure from the approach of Lee et al. (2013), we do not use a specific composition of the cloud (e.g., enstatite). Specifically, we adopt their approximate fitting formula (listed in the appendix of Lee et al. 2013 but not used in their analysis),

$$Q_{ext} = \frac{5}{Q_0 x^{-4} + x^{0.2}},\qquad(17)$$

where $x \equiv 2\pi r_c/\lambda$ and λ is the wavelength. When the particles are small ($x \ll 1$), we recover Rayleigh scattering: $Q_{ext} \propto \lambda^{-4}$. Large particles ($x \gg 1$) produce a roughly constant Q_{ext}. By contrast, Benneke & Seager (2013) assume their clouds to be described by only one number, which is the cloud-top pressure. Their model carries the implicit assumption that the cloud
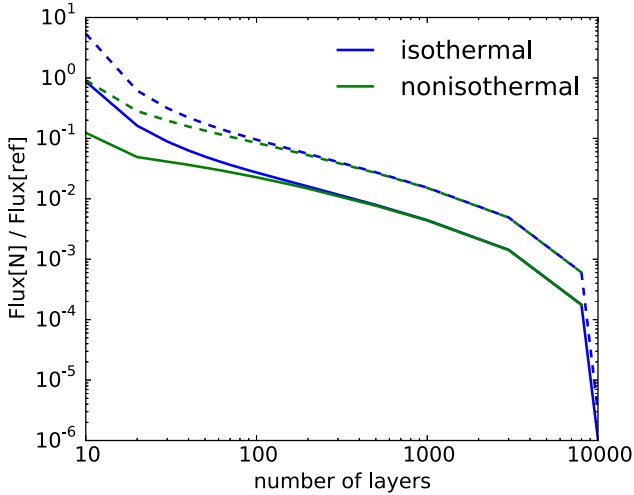
Figure 2. Mean (solid curves) and maximum (dashed curves) errors in the synthetic spectrum as a function of the number of model layers used, computed by performing retrievals on the measured spectrum of HR 8799b. The reference used is the retrieval with 10,000 model layers (see the text). When about 100 layers are used, the models with isothermal and non-isothermal layers yield the same answers.

Figure 3. Validation of our `HELIOS-R` forward model (green dashed curve and upward-facing triangles) against that used in the `HELIOS` self-consistent radiative transfer code (blue solid curve and downward-facing triangles). The insert shows the temperature–pressure profile used as an input.

particles are large compared to the range of wavelengths examined.

The dimensionless quantity Q_0 serves as a proxy for the cloud composition. Refractory species (e.g., silicates) have $Q_0 \approx 10$, while volatile species (e.g., ammonia, methane, and water) have $Q_0 \approx 40$–80. By using Q_0 as a fitting parameter in the retrieval, we can constrain the composition of the clouds. The other fitting parameters in our cloud model are r_c and f_{cloud}.

Since we do not self-consistently treat the cloud physics and gaseous chemistry, the caveat is that our retrieved C/O values are representative of only the gaseous component of the atmosphere. It is conceivable that the true C/O values, which must account for the material sequestered in the cloud particles, are different.

2.7. Data Selection: Spectra of HR 8799b, c, d, and e

The spectra and photometric data points of the HR 8799b, c, d, and e exoplanets have been taken from Bonnefoy et al. (2016) and Zurlo et al. (2016). The new SPHERE data were presented in Zurlo et al. (2016), while Bonnefoy et al. (2016) unified all of the previous data of the four exoplanets. Specifically, we use the data from Figure 4 of Bonnefoy et al. (2016).

To compute the flux in a photometric waveband, we simply integrate the synthetic spectrum over the range of wavelengths of the filter and assume a Heaviside function with a value of unity throughout. Unlike Lee et al. (2013), we do not apply filter functions with non-unity values to our synthetic spectrum, because this correction has already been done en route to reporting the observed fluxes in Bonnefoy et al. (2016) and Zurlo et al. (2016). It is unclear what has been done in previous studies. Madhusudhan et al. (2011) display filter functions in their Figure 1, but do not describe whether these filter functions were applied to their synthetic spectra. Line et al. (2013) state that, "For the broadband points we simply integrate the flux from the high-resolution model spectrum with the appropriate filter function for that point," but do not provide quantitative descriptions of their filter functions. It cannot be ruled out that
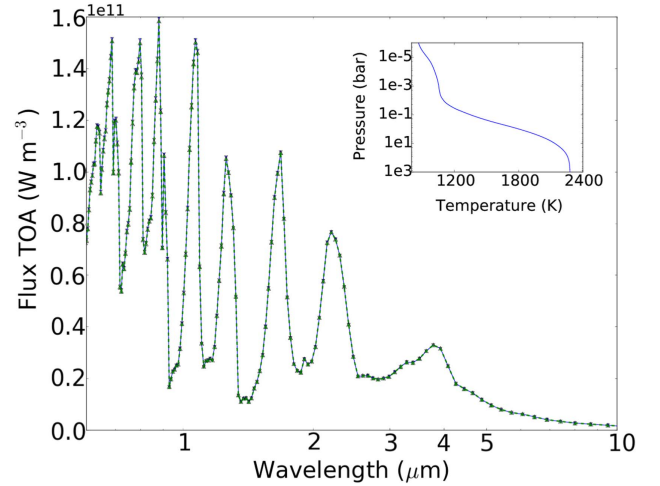
these filter functions have values of unity throughout. For the spectroscopic data points, we do not convolve the synthetic spectrum with the instrument's response function, because the impact is minor for low-resolution spectra.

3. Tests

Before analyzing the measured spectra of the HR 8799b, c, d, and e directly imaged exoplanets, we subject `HELIOS-R` to a battery of tests.

3.1. Number of Atmospheric Layers

The number of layers used in a one-dimensional model atmosphere is a critical but often overlooked or unexplored detail. We wish to quantify the mean and maximum errors associated with assuming a specific number of model layers. We use the measured spectrum of HR 8799b as an illustration. We consider an ensemble of 10^3 cloud-free models with unconstrained chemistry. For each model, we randomly select our parameter values: two parameters for the temperature–pressure profile, four parameters for the mixing ratios, and one for the surface gravity. The range of parameter values used is listed in Table 2. No model selection is performed for this test. We consider forward models with both isothermal and non-isothermal layers. For the latter, we use Equation (B6) of Heng et al. (2014).

For each of the 10^3 models, the spectrum computed with 10,000 non-isothermal layers is used as a reference. We then compute coarser models with between 10 and 8000 isothermal or non-isothermal layers and calculate the fractional error on the synthetic spectrum compared to the reference model. In Figure 2, we show both the mean and maximum errors associated with the synthetic spectrum. With 100 layers, we see that models with isothermal and non-isothermal layers have the same mean and maximum errors of about 2.5% and 8%, respectively. For the rest of the paper, we will use 100 isothermal layers. For comparison, Madhusudhan & Seager (2009), Lee et al. (2013), and Line et al. (2013) used 100, 43, and 90 layers, respectively.
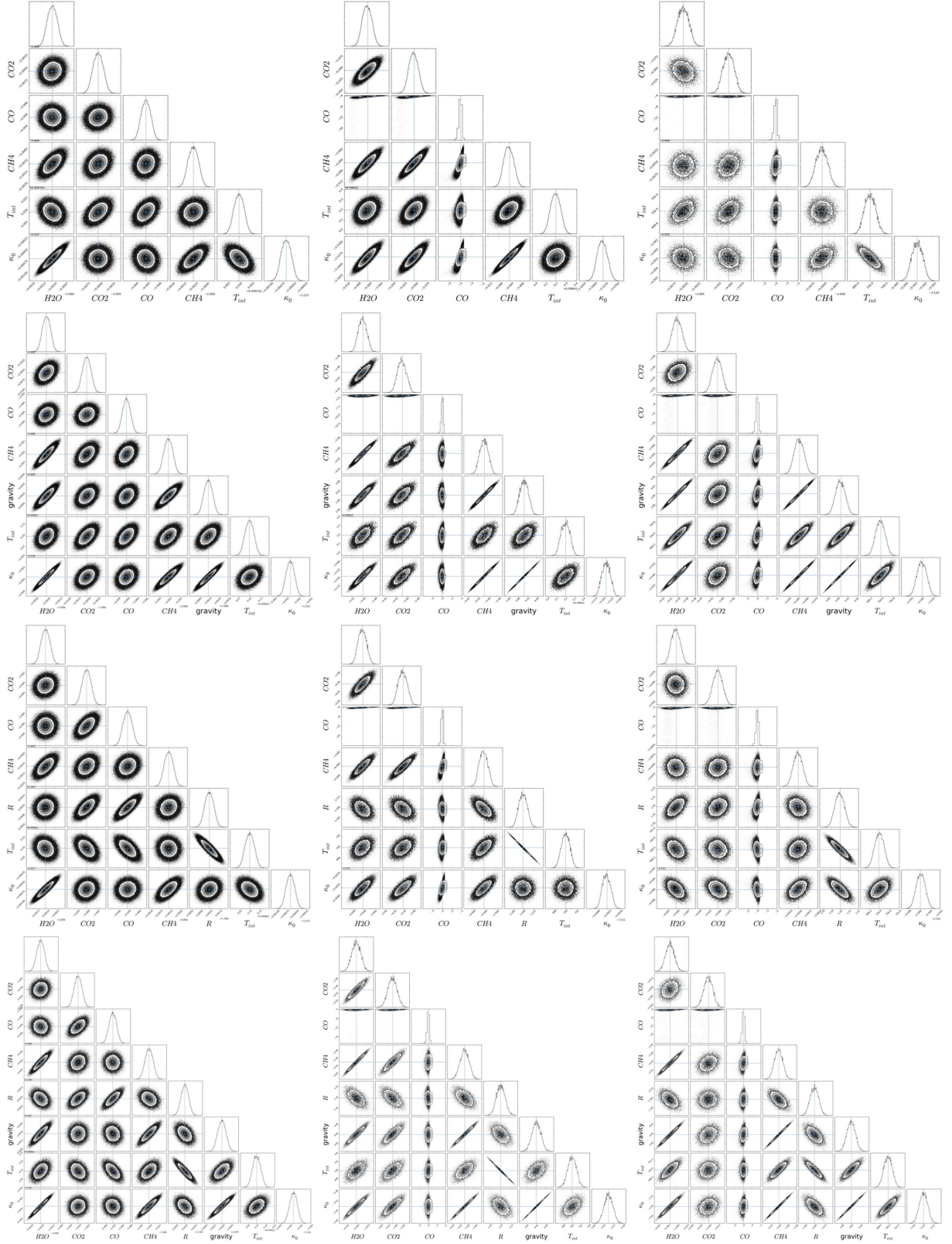
Figure 4. Performing retrieval on a mock data set, where the "ground truth" is known (see the text for input parameters). We focus on performing retrieval with the UB model (see Table 1). The columns represent the different wavelength coverages: 0.7–5 μm with 0.01 μm resolution (first column), HR 8799b-like data (second column) and HR 8799e-like data (third column). The rows represent different assumptions for R and g: fixed R and g (first row), fixed R but g is a fitting parameter (second row), fixed g but R is a fitting parameter (third row), both R and g are fitting parameters (fourth row). The labels "CO," "CO2," "CH4," and "H2O" refer to the mixing ratios of carbon monoxide, carbon dioxide, methane, and water, respectively. $T_{\rm int}$ is in units of K. The labels "κ_0" and "gravity" are for log κ_0 and log g in mks and cgs units, respectively.

3.2. Validating the Forward Model

We previously developed a self-consistent radiative transfer code named HELIOS, which solves the radiative transfer equation in tandem with the first law of thermodynamics to obtain one-dimensional model atmospheres in radiative equilibrium (Malik et al. 2017). HELIOS was validated against the radiative transfer model of Miller-Ricci & Fortney (2010). In the limit of pure absorption, we also demonstrated that the two-stream and exact solutions produce excellent agreement if the diffusivity factor is set to two (Heng et al. 2014; Malik et al. 2017).

The forward model of HELIOS uses the same equation as HELIOS-R, but was implemented independently by the first author of each study. Here, we compare the forward models of HELIOS-R and HELIOS to verify that our implementation is bug-free. In Figure 3, we constructed a cross-section function consisting purely of water and used the k-distribution method to compute the fluxes. Malik et al. (2017) used an opacity function instead, but theirs also consisted purely of water, and they used the k-distribution method as well. The k-distribution tables were constructed using a resolution of $10^{-5}\,\mathrm{cm}^{-1}$ evenly distributed across the wavenumber (not shown). Other assumptions include a hydrogen-dominated atmosphere ($\mu = 2$), a water mixing ratio of 10^{-3}, and a surface gravity of $\log g = 3.3$ in cgs units ($\approx 19.5\,\mathrm{m\,s^{-2}}$). We then assumed an input temperature–pressure profile, as shown in the insert of Figure 3, in tandem with the k-distribution tables to compute the synthetic spectrum using both HELIOS-R and HELIOS. The excellent agreement validates our implementation of the forward model.

3.3. Retrieval on a Mock Data Set

A useful test is to create a mock data set in which we know what the "ground truth" is concerning the synthetic spectrum, temperature–pressure profile, molecular abundances, surface gravity, etc. We assume a cloud-free model with unconstrained chemistry, which has the following input parameters.

$$X_{CO} = X_{CO_2} = X_{CH_4} = X_{H_2O} = 10^{-4},$$
$$R = 1.2\,R_J, \; \log g = 4.0(\mathrm{cgs}),$$
$$T_{int} = 700\,\mathrm{K}, \; \kappa_0 = 2.9 \times 10^{-4}\,\mathrm{m^2\,kg^{-1}}, \tag{18}$$

where R_J is the radius of Jupiter. Using this setup, we create three mock data sets: a full mock spectrum from 0.7 to 5 μm with 0.01 μm resolution, HR 8799b-like and HR 8799e-like data coverage. We assume this mock object to be located $d = 10$ pc away.

Such a test serves three purposes. First, if R and g are fixed to their input values (and excluded from being fitting parameters in the retrieval), then it is a test of the ability of our nested sampling algorithm to correctly recover the molecular abundances and temperature–pressure profile. Second, if we now include g and R as fitting parameters, it allows us to study the degeneracies associated with our ignorance of the surface gravity and/or radius. Third, by adapting and degrading the mock spectrum to the data resolution and spectral coverage of HR 8799b and HR 8799e, we may study the effects of incomplete or sparse data on the retrieved molecular abundances. The key difference between the currently available data for HR 8799b and HR 8799e is that the latter does not have K-band spectroscopy.
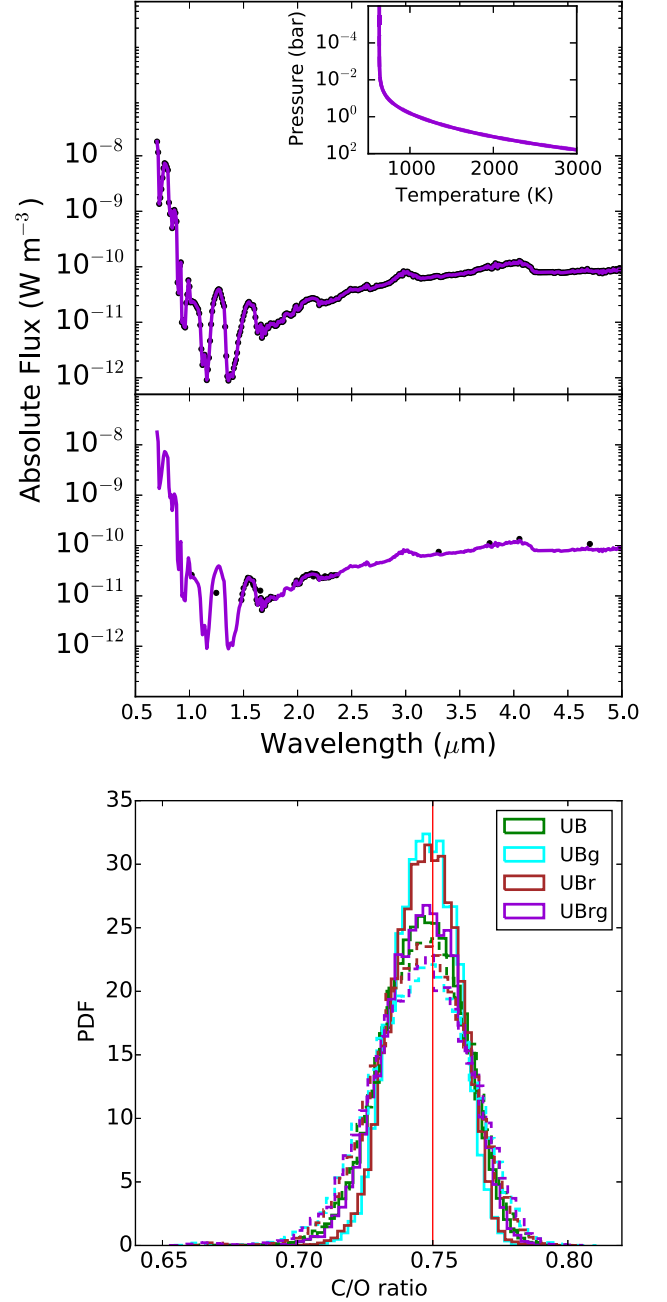

Figure 5. Further results from the retrievals on the mock data set. The top panel shows the mock data set at full resolution (0.01 μm), and also with HR 8799b-like data coverage (circles). The mock data set and best-fit spectrum overlap exactly (to within the resolution of the plot). The insert shows the retrieved temperature–pressure profile. The bottom panel shows the retrieved posterior distributions of C/O, assuming different models (see Table 1). The solid and dotted curves are for HR 8799b-like and HR 8799e-like data coverage. The broader posterior distributions of C/O associated with HR 8799e-like data coverage are primarily due to the lack of K-band data.

Figure 4 shows the outcomes of these tests. When R and g are fixed to their input values, HELIOS-R correctly recovers the input values of the mixing ratios and T–P profile parameters from the full mock spectrum (first row, first column). Surprisingly, our ability to recover these input values appears to be insensitive to whether the mock spectrum is degraded or not (first row, second and third columns), if R and g are known.
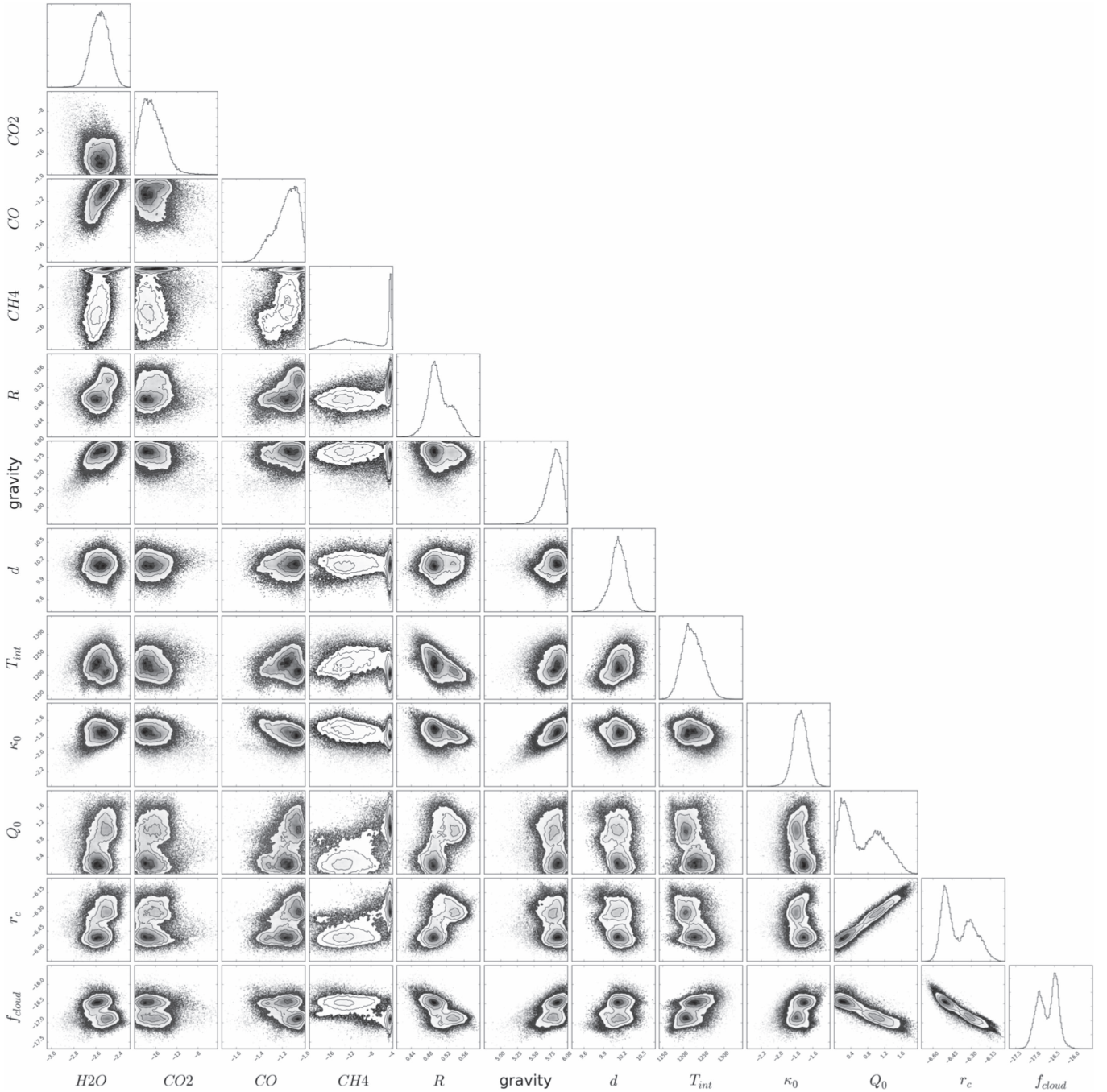
Figure 6. Montage of posterior distributions from performing retrieval on the measured spectrum of HR 8799b and allowing the radius, surface gravity, and mean molecular weights to be uniform or log-uniform priors. The retrieved value of the radius ($R \approx 0.5\ R_J$) is unphysical (see the text for a discussion). The labels "CO," "CO2," "CH4," and "H2O" refer to the mixing ratios of carbon monoxide, carbon dioxide, methane, and water, respectively. R and T_{int} are in units of R_J and K, respectively. The labels "κ_0" and "gravity" are for $\log \kappa_0$ and $\log g$ in mks and cgs units, respectively.

When the radius is implemented as a uniform prior, its value is correctly recovered, though the posterior distributions of the other fitting parameters become a little broader (third row of Figure 4). With HR 8799e-like data coverage, we see clear signs of degeneracies being introduced into the posterior distributions. It suggests that the K-band spectrum contains important information on the molecular abundances, an issue we will explore further in Section 4.4.

Allowing the surface gravity to be a fitting parameter has more serious consequences, as it introduces degeneracies into

all of the other fitting parameters (second row of Figure 4). Even full data coverage does not lift these degeneracies (second row, first column). It suggests that an informative prior needs to be set on the surface gravity.

Surprisingly, the retrieved posterior distribution of C/O appears to be robust to the different model assumptions (Figure 5). It suggests that the C/O is a robust outcome of the retrieval.

Overall, these exercises teach us that wavelength coverage and spectral resolution are generally not as important as

knowledge of the surface gravity, though the *K*-band spectrum appears to encode crucial information on the molecular abundances. In Section 4.1, we will argue for setting Gaussian priors on log *g* as well as *R* when analyzing real data from the HR 8799 exoplanets.

4. Results

4.1. Setting Priors on Radius and Surface Gravity

The strongest demonstration of why our assumptions for the prior distributions of input parameters are important comes from examining a model where the radius and surface gravity are implemented as uniform priors in the retrieval. Specifically, we perform a retrieval on the measured spectrum of HR 8799b using model UBrg in Figure 6, where *R* and *g* are specified as uniform priors. We see that the retrieved solution is $R \approx 0.5\,R_J$, which is physically unreasonable. The surface gravity takes on unphysical values of $\log g \approx 5.5$–6. As we have learned from the mock-retrieval exercises in Section 3.3, these difficulties stem from specifying the radius and surface gravity as unconstrained fitting parameters.

We now discuss why the values for *R* are physically unreasonable. There are indirect arguments for why retrieved solutions with radii well below a Jupiter radius should be rejected. First, brown dwarfs and low-mass stars with masses between 20 and 100 Jupiter masses have transit radii that are at least $0.8\,R_J$ (see Burrows et al. 2011 and references therein), including CoRoT-3b, which is a low-mass brown dwarf with a dynamical mass of $M = 21.66 \pm 1.0\,M_J$ and a transit radius of $R = 1.01 \pm 0.07\,R_J$ (Deleuil et al. 2008). Second, a review of the data for all of the transiting Jupiter-like exoplanets also reveals that objects with radii below $0.8\,R_J$ do not exist (Figure 7). When a cut is made to only include objects with zero-albedo equilibrium temperatures below 1000 K (to exclude objects that are "inflated" by some unknown mechanism related to stellar heating, e.g., Demory & Seager 2011), we find that the radii are bound between 0.8 and $1.2\,R_J$. The single outlier with $R = 1.65^{+0.59}_{-0.56}\,R_J$ is Kep-447b, which has an extremely grazing transit (Lillo-Box et al. 2015) that may render its radius measurement unreliable. Third, objects with a mass of Jupiter (or higher) are partially degenerate and it is theoretically challenging to get their radius to be less than that of Jupiter's (Burrows & Liebert 1993).

While it may be tempting to fix our model radius at between 0.8 and $1.2\,R_J$, we should be reminded of the fact that these radii are measured for >1 Gyr old objects, whereas the HR 8799 exoplanets are estimated to be ~10–100 Myr old. Guided by evolutionary models (Mordasini et al. 2012; Spiegel & Burrows 2012), we set $R = 1.2 \pm 0.1\,R_J$ as a Gaussian prior of our retrievals. The uncertainty of $0.1\,R_J$ is the full-width at half-maximum of the Gaussian. We note that Moses et al. (2016) assume a fixed value of $R = 1.2\,R_J$ for their self-consistent model of HR 8799b.

The bottom panel of Figure 7 is also revealing, as it shows the measured surface gravities of transiting Jupiter-sized exoplanets to be hovering around $\log g \approx 4$ for objects with masses of $M > 2\,M_J$, where M_J is the mass of Jupiter. Since we expect the HR 8799 exoplanets to have radii that are slightly larger than Jupiter's, we expect their surface gravities to also be $\log g \approx 4$. Surface gravities of $\log g \approx 4.5$–5.0 are only appropriate when one crosses over into the brown dwarf
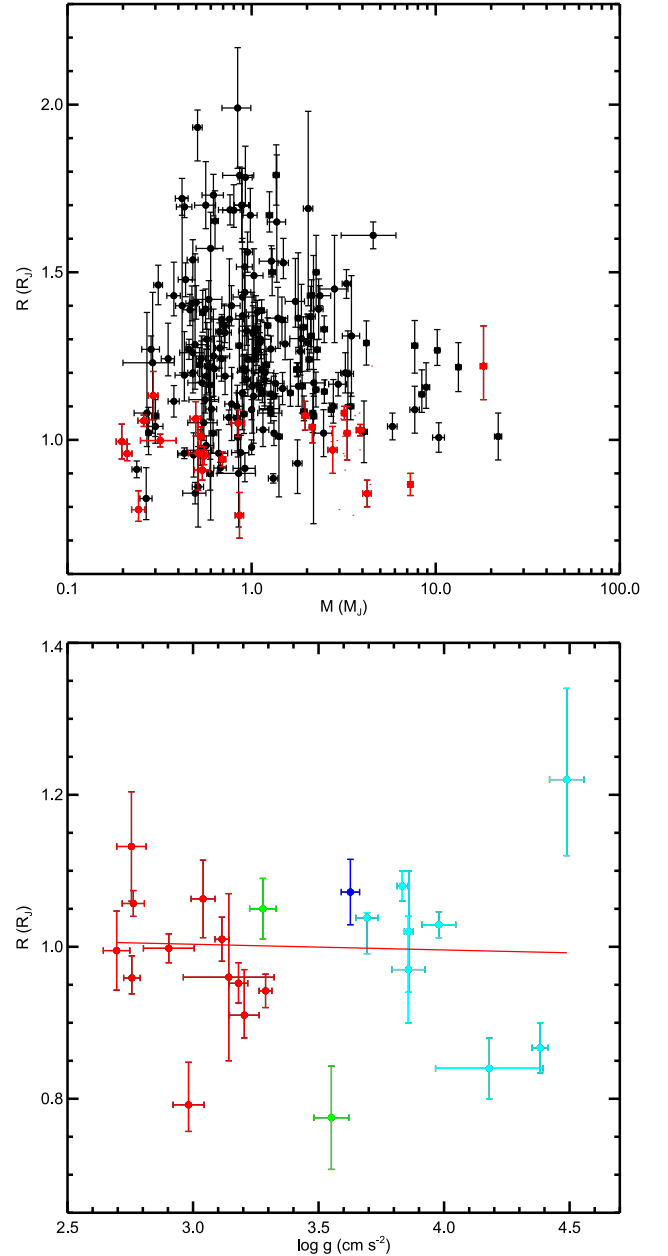

Figure 7. Top panel: transit radius vs. surface gravity of a sample of transiting Jupiter-sized exoplanets around main-sequence stars (black data points). The red data points are the sub-sample of transiting exoplanets with zero-albedo equilibrium temperatures below 1000 K. The single outlier is Kep-447b (see the text). Bottom panel: the same sub-sample, but color-coded by mass. The red, green, blue, and cyan points are for $<0.8\,M_J$, $0.8 < M < 1.2\,M_J$, $1.2 < M < 2\,M_J$, and $>2\,M_J$, respectively. Data taken from http://www.exoplanets.org (Han et al. 2014).

regime ($\gtrsim 13\,M_J$), e.g., CoRoT-3b has $\log g = 4.72 \pm 0.07$. The photometric masses of HR 8799b, c, d, and e are less than half that of CoRoT-3b (Marois et al. 2008, 2010). Based on the evolutionary calculations of Marleau & Cumming (2014), who estimated $M \approx 4$–$13\,M_J$ for the HR 8799 exoplanets, we set a Gaussian prior of $\log g = 4.1 \pm 0.3$ on the surface gravity (taking into account $R = 1.2 \pm 0.01\,R_J$). This range of surface gravities is somewhat higher than the $\log g = 3.5 \pm 0.5$ values considered by Barman et al. (2015).
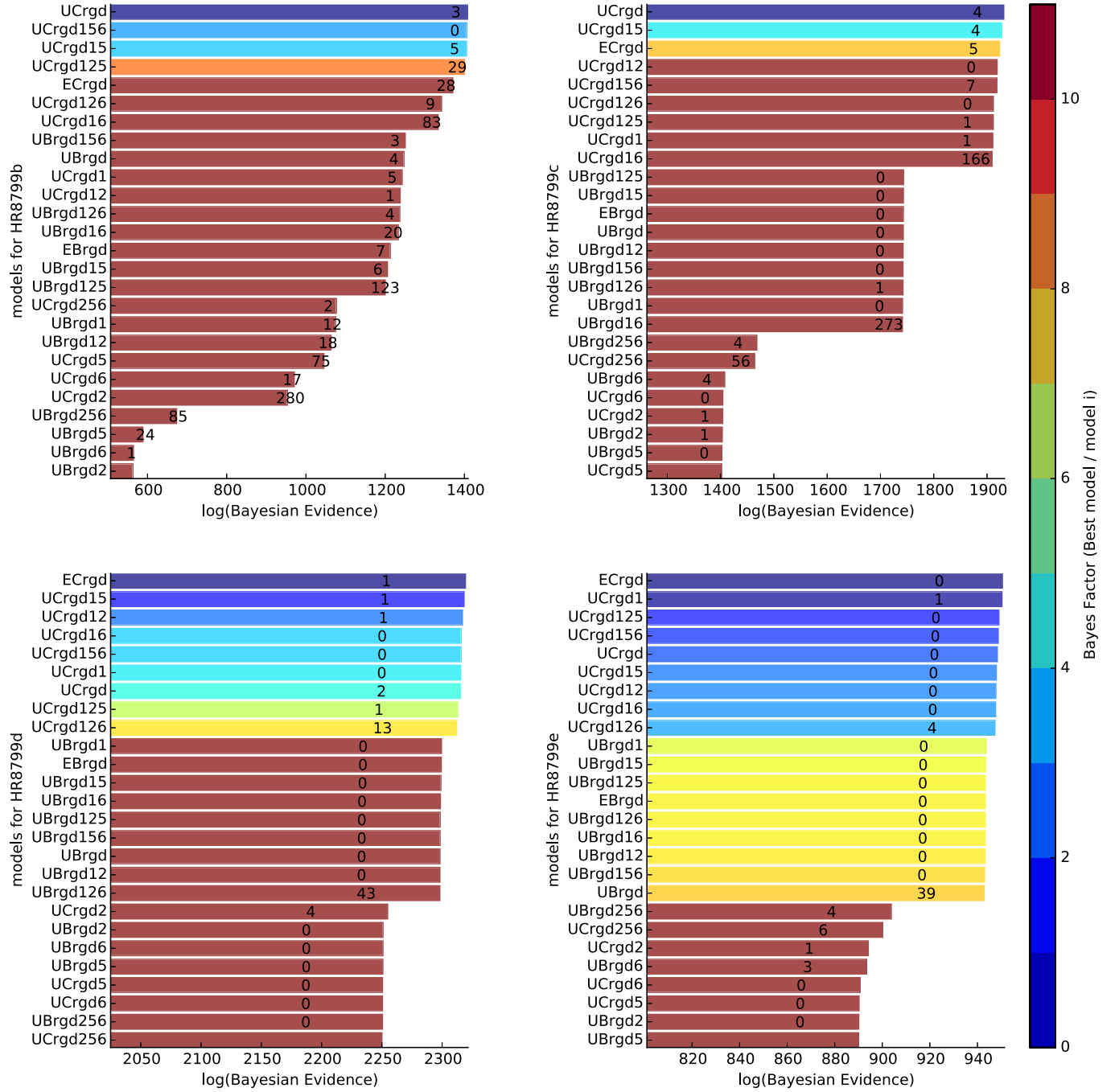
Figure 8. Bayes factors from a suite of models for each HR 8799 exoplanet. See Table 1 for an explanation of the shorthand notation used to mark each model. All of the models assume Gaussian priors on R and $\log g$ (see Table 2). For HR 8799b and c, the Bayesian evidence clearly favors cloudy models with non-equilibrium (unconstrained) chemistry. For HR 8799e, the lack of K-band spectroscopy implies that none of the models are strongly favored. The number associated with each histogram is the logarithm of the Bayes factor between the model in question and its neighbor below. The color bar shows the logarithm of the Bayes factor between the model in question and the best model, which is the model placed at the top of each panel.

In summary, we find that what we assume for the prior distributions of the input quantities is critical to the outcome of the retrieval. Uniform or log-uniform priors may not always be the best choice because they may lead to unphysical or even nonsensical outcomes. Gaussian priors are better choices in these instances, but only when they are guided by physics. We find our retrievals to be physically meaningful only when Gaussian priors are set on the radius and surface gravity, which is a departure from the HR 8799b analysis of, e.g., Lee et al. (2013).

4.2. Model Selection Using Bayesian Evidence

Traditionally, model selection is performed manually by the modeler or theorist. One starts with a set of assumptions, computes forward and arrives at a prediction for the thermal structure and synthetic spectrum. These assumptions include chemical equilibrium or disequilibrium, a value for the strength of atmospheric mixing, the number of atoms and molecules included in the model, the metallicity, and C/O, etc. Other assumptions are more closely related to technique, e.g., the

13
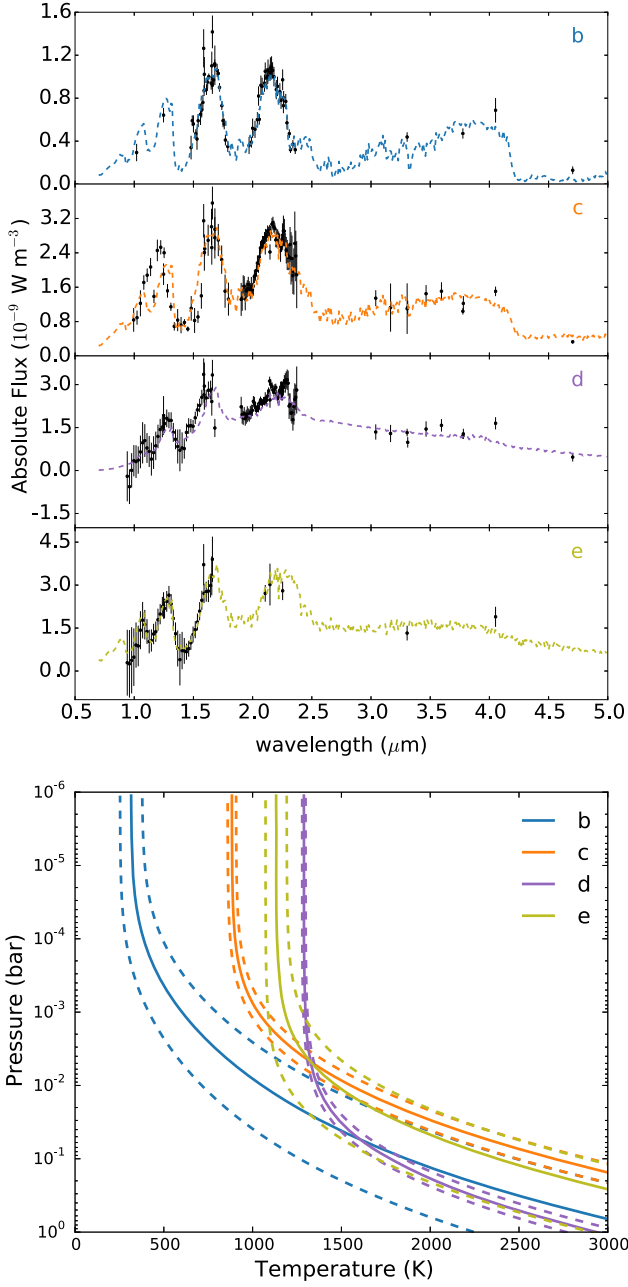
Figure 9. Best-fit spectra and temperature–pressure profiles for HR 8799b, c, d, and e.

approximate or limiting form of the radiative transfer equation being solved.

Like all of the other previous studies involving both forward modeling and retrieval, we inevitably make a set of both physical and technical assumptions. However, we use our nested sampling approach to go a step further: we compute the Bayesian evidence for models with and without equilibrium chemistry. We then compare them in order to formally quantify whether equilibrium chemistry is a warranted assumption. Instead of assuming a fixed set of cloud parameters for each retrieval, as was done by Lee et al. (2013), we allow our cloud model to be part of the retrieval and also compare its Bayesian evidence to a retrieval that assumes a cloud-free atmosphere. In
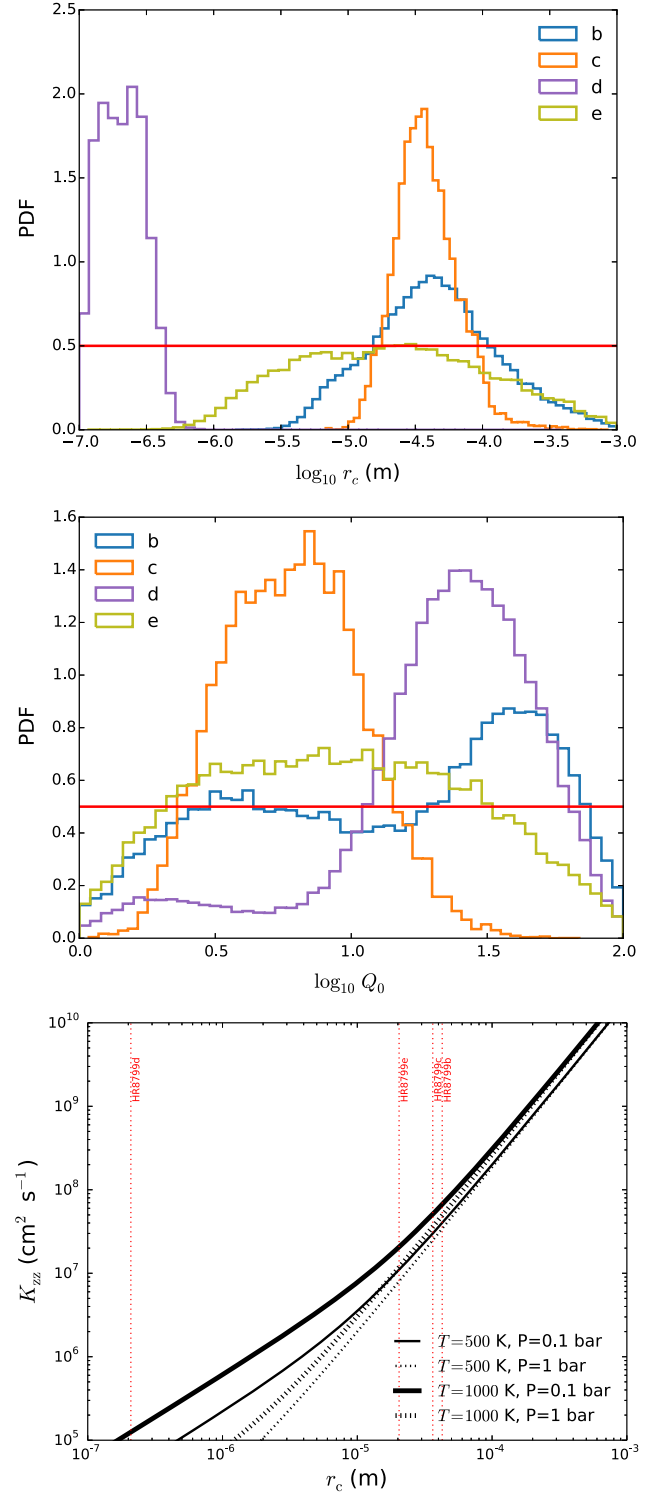
Figure 10. Top and middle panels show the retrieved cloud particle radius and composition parameter for the HR 8799b, c, d, and e directly imaged exoplanets, where the flat line is the prior. The bottom panel shows the eddy diffusion coefficient and demonstrates that its inferred value corresponding to the peak value of the posterior distribution for r_c are not unreasonable and broadly consistent with the assumed K_{zz} values in previous studies. PDF stands for "probability density function."

these ways, we allow model selection based on the Bayesian evidence to inform us of whether the atmosphere is cloudy or cloud-free and in chemical equilibrium or disequilibrium.
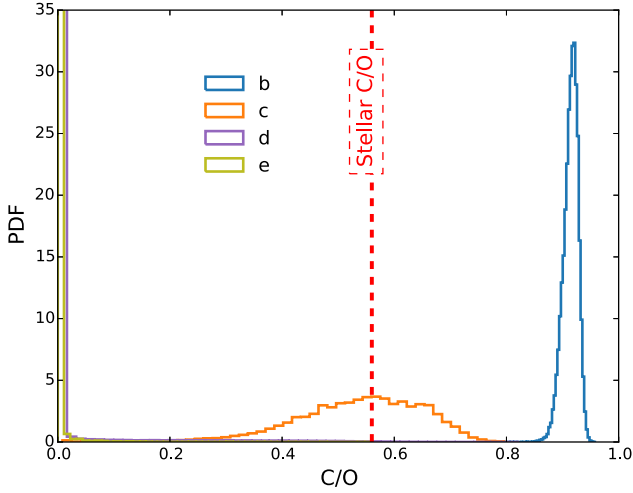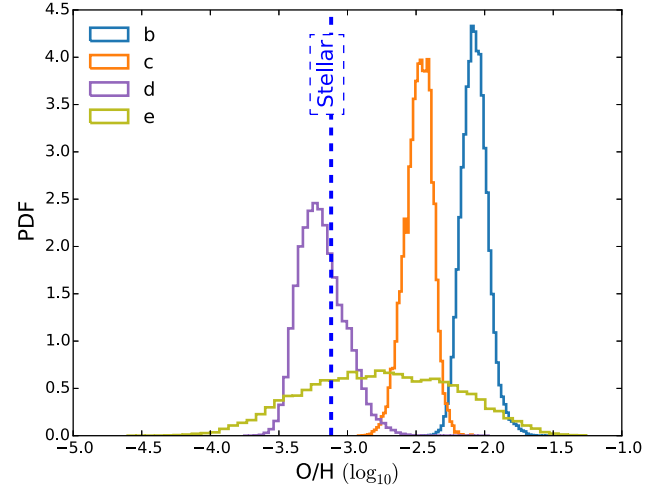
Figure 11. Retrieved C/O values for the HR 8799b, c, d, and e directly imaged exoplanets. The stellar C/O value is about 0.56. PDF stands for "probability density function."
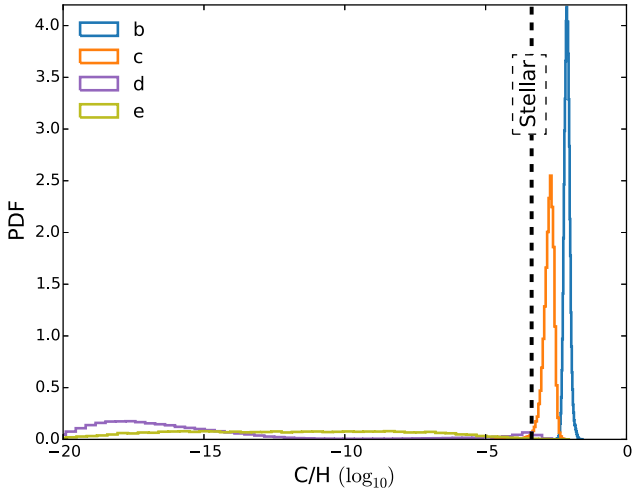
Figure 12. Retrieved C/H values for the HR 8799b, c, d, and e directly imaged exoplanets. The stellar C/H value is about 4.3×10^{-4}. PDF stands for "probability density function."

Figure 13. Retrieved O/H values for the HR 8799b, c, d, and e directly imaged exoplanets. The stellar O/H value is about 7.6×10^{-4}. PDF stands for "probability density function."
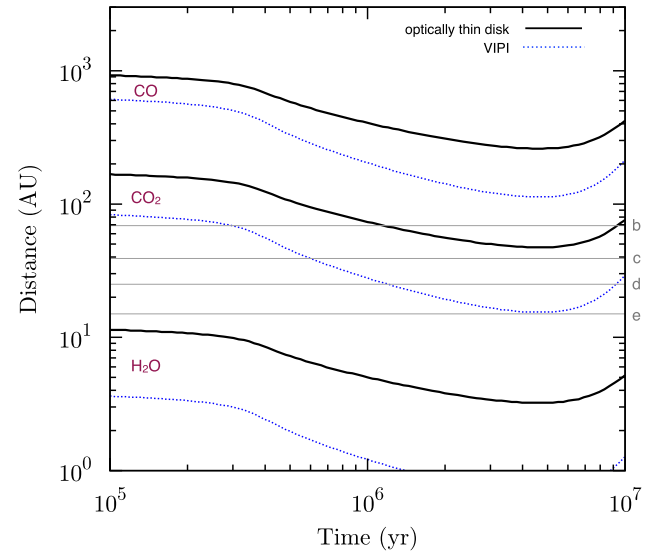

Figure 14. Positions of the CO, CO_2, and H_2O snowlines or icelines as functions of the stellar age of the HR 8799 system. The solid curves are calculated assuming an optically thin disk. The dotted curves are calculations from a vertically isothermal, passively irradiated (VIPI) disk.

Figure 8 shows a montage of all of the models tested for all four HR 8799 exoplanets. Table 1 explains what the labels of the models correspond to. For HR 8799b, c, and d, we see that the Bayesian evidence favors model atmospheres that are not in chemical equilibrium and are cloudy. For HR 8799e, the relative lack of data, compared to the other HR 8799 exoplanets, means that we are unable to strongly select between the different models.

Figure 9 shows the best-fit spectra. Our retrieval procedure generally manages to find good fits to the data, except for the band-head near $1\,\mu m$ for HR 8799c. We speculate that this mismatch could be due to the influence of an additional molecule we have not included in our analysis, but we deem it beyond the scope of the present paper to identify it. In the Appendix, Figure 16 elucidates the effects of using ExoMol methane and water versus HITRAN methane and HITEMP water.

For the rest of this paper, we will discuss the retrieved properties of the HR 8799b, c, and d exoplanets based on the best-fit models only. For HR 8799e, we will discuss results from the model with equilibrium chemistry and that includes all four molecules in the retrieval. In Figures 18–21 of

Appendix B, we provide the full posterior distributions of the best models for all exoplanets for completeness.

4.3. Retrieving the Cloud Properties and Inferring K_{zz}

Figure 10 shows the retrieved posterior distributions of the cloud particle radius (r_c) and composition parameter (Q_0). Unsurprisingly, the retrieved values of Q_0 span a broad enough range (three to four orders of magnitude) that they are uninformative with regards to distinguishing between different compositions, consistent with the expectation that the absorption and scattering properties of the cloud are mainly determined by the particle size and less by the composition (Heng & Demory 2013).

The inferred values of r_c span a broad range and lie between about 1 and $100\,\mu m$. The presence of these cloud particles implies that they are being held aloft by atmospheric motion. Since these exoplanets are not being heavily irradiated (unlike

for hot Jupiters), we can safely assume that the underlying mechanism driving this motion is convection (Burrows et al. 1997; Chabrier et al. 2000; Baraffe et al. 2002) and estimate approximate values for the associated "eddy diffusion coefficient," which we denote with K_{zz}. We use Equations (15) and (17) of Spiegel et al. (2009), as well as Equations (6) and (8) of Heng & Demory (2013), to calculate the terminal speed associated with a particle of radius r_c, which we denote by $v_{terminal}$. The eddy diffusion coefficient is roughly

$$K_{zz} \sim 0.1 v_{terminal} H, \qquad (19)$$

where the pressure scale height is $H = k_B T / \tilde{m} g$ and k_B is the Boltzmann constant. We follow the prescription of Smith (1998) and use $0.1H$ as the characteristic length scale, which is more conservative than what was assumed in Lee et al. (2013). We note that the preceding expression for K_{zz} has no dependence on g, as it appears in the numerator of $v_{terminal}$ and the denominator of H. We assume the intrinsic density of the particles to be $3\,\mathrm{g\,cm^{-3}}$.

In Figure 10, we see that K_{zz} spans a broad range of values from $\sim 10^5\,\mathrm{cm^2\,s^{-1}}$ to $\sim 10^{10}\,\mathrm{cm^2\,s^{-1}}$ as r_c increases from 1 μm to 1 mm. The deviation in the curves between $P = 0.1$ and 1 bar arises from the Cunningham–Millikan–Davies "slip factor correction" kicking in when the mean-free path for collisions between the hydrogen molecules becomes comparable to the cloud particle radius. If we place the retrieved values of r_c corresponding to the peak of each posterior distribution on the plot, we infer $K_{zz} \sim 10^5$–$10^8\,\mathrm{cm^2\,s^{-1}}$, in agreement with Barman et al. (2015). Madhusudhan et al. (2011) assume $K_{zz} = 10^2$–$10^6\,\mathrm{cm^2\,s^{-1}}$, while Barman et al. (2011) and Marley et al. (2012) assume $K_{zz} = 10^4\,\mathrm{cm^2\,s^{-1}}$.

4.4. Retrieving C/O, C/H, and O/H for the HR 8799b, c, d, and e Exoplanets and Implications for Planet Formation

4.4.1. The Star of HR 8799

We refer to the "metallicity" as the set of elemental abundances with atomic mass numbers that are larger than that of hydrogen and helium. In our current study, these would be $f_C \equiv$ C/H and $f_O \equiv$ O/H. For comparison, their values in the solar photosphere are $f_C \approx 3 \times 10^{-4}$ and $f_O \approx 6 \times 10^{-4}$, such that C/O ≈ 0.5 (Lodders 2003). For the star of the HR 8799 system, Sadakane (2006) has found that

$$\mathrm{C/H_\star} \approx 4.3 \times 10^{-4}, \ \mathrm{O/H_\star} \approx 7.6 \times 10^{-4}, \ \mathrm{C/O_\star} \approx 0.56.$$
$$(20)$$

4.4.2. Retrieved C/O, C/H, and O/H Values

Given the interest in the possibility of carbon-rich exoplanets (Gaidos 2000; Kuchner & Seager 2005), our retrieval analysis yields the posterior distributions of C/O, C/H, and O/H for the atmospheres of HR 8799b, c, d, and e in Figures 11–13, respectively, which we then compare to the values for the star listed in Equation (20). A caveat is that the retrieved values are only for the gaseous phase and the true C/O ratio may be hidden in a condensed phase such as graphite (Moses et al. 2013). The retrieved posterior distributions of C/O and C/H for HR 8799e are not as definitive as for the other three exoplanets, because its K-band spectrum has not been measured.

4.4.3. Locations of Snowlines/Icelines

Konopacky et al. (2013) have previously estimated that the H_2O, CO_2, and CO snowlines or icelines are located at about 10, 90, and 600 au, respectively. We wish to point out that the iceline locations depend on the formation history of the HR 8799 exoplanets.

In Figure 14, we show calculations of the locations of the CO, CO_2, and H_2O icelines as functions of the age of the HR 8799 system. We consider two scenarios: an optically thin disk and a vertically isothermal, passively irradiated disk. For the optically thin disk, the temperatures are simply the zero-albedo equilibrium temperatures at a given distance from the star informed by the Pisa stellar evolution models (Tognelli et al. 2007). By "passively irradiated," we mean that viscous heating associated with turbulence is neglected (Chiang & Goldreich 1997). Both models consider the evolution of stellar heating as the star ages. We expect more sophisticated calculations that involve temperature gradients, photoevaporation, and viscous heating to produce iceline curves that are intermediate between these two scenarios. The calculations are shown for $t = 10^5$–10^7 years because this encompasses the gas-clearing phase of the protoplanetary disk. Curiously, the CO_2 iceline sits between different pairs of HR 8799 exoplanets as its location evolves during the gas-clearing phase ($t \sim 10^6$ years), implying that a variation in the C/O, C/H, and O/H values of these exoplanets may be a natural outcome of the planet formation process.

4.4.4. Implications for Planet Formation

Our findings have implications for planet formation, if we assume the retrieved C/O, C/H, and O/H values to be representative of the bulk composition of each exoplanet. Öberg et al. (2011) previously elucidated the chemical signatures associated with the planet formation mechanism and history of an exoplanet. If an exoplanet forms by gravitational instability, the zeroth-order expectation is that its C/O, C/H, and O/H values mirror that of the star, unless late-time accretion occurred. This is clearly at odds with our inferred values of C/O, C/H, and O/H for the HR 8799b, c, d, and e exoplanets.

In the context of the core accretion formation mechanism, all four exoplanets should have C/O values that are enhanced above stellar, but below unity, if they formed in situ and in between the water and carbon dioxide snowlines/icelines (Öberg et al. 2011). Our retrieved values of C/O for HR 8799b and c are consistent with this scenario, whereas HR 8799d and e have sub-solar C/O values. Öberg et al. (2011) have suggested that substellar C/O values are still consistent with core accretion if the late-time accretion of planetesimals has occurred to pollute the atmospheres. The link between late-time planetesimal accretion and atmospheric composition has been emphasized by Mordasini et al. (2016). The HR 8799b and c exoplanets have superstellar C/H and O/H values, which suggests that they accreted both carbon- and oxygen-rich ices. The HR 8799d and e exoplanets, which reside closer to the star, have substellar C/H values but stellar to superstellar O/H values, which suggests the accretion of only oxygen-rich ices.

Overall, our retrieved values of C/O, C/H, and O/H appear to be consistent with the core accretion formation mechanism and inconsistent with gravitational instability without late-time accretion, as has been suggested by, e.g., Kratter et al. (2010).
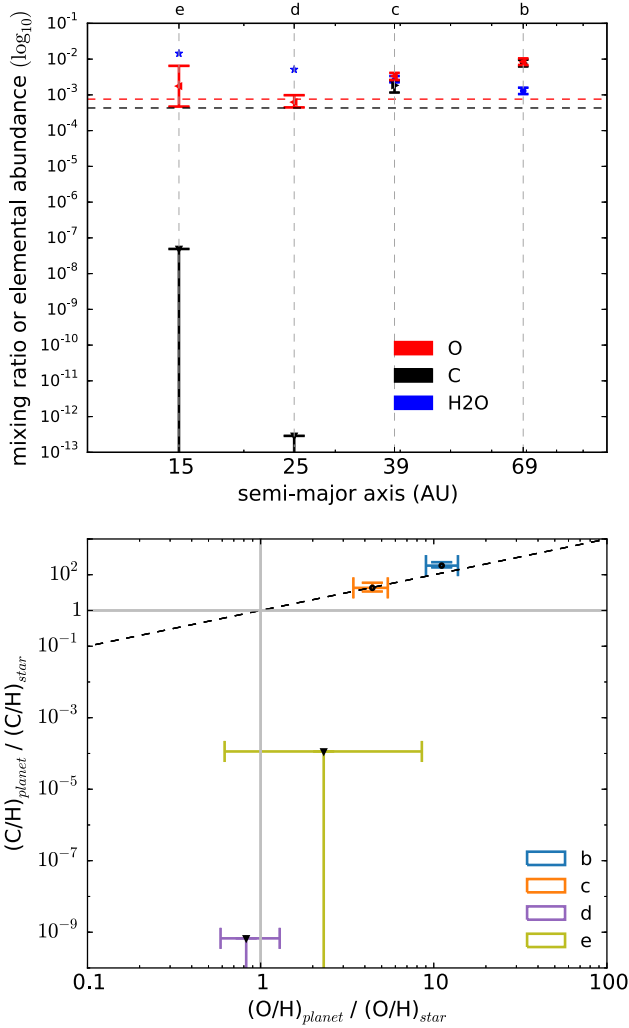
Figure 15. Summary of our main results. The top panel shows the retrieved water mixing ratios and elemental abundances of carbon and oxygen for all four HR 8799 exoplanets. For HR 8799d and e, we show the water abundance in chemical equilibrium at 1 bar (represented by the blue stars). For C/H and O/H, we also show the corresponding values of the HR 8799 star (horizontal dashed lines). The bottom panel shows the exoplanetary elemental abundances normalized to their stellar values with the dashed line denoting parity.

4.4.5. Why Spectroscopy in the K Band is Crucial

A lesson we have learned from our analysis is that spectroscopy in the K band is crucial for obtaining meaningful constraints on C/H and C/O, as it affects the ability of the retrieval approach to constrain the abundances of CO and/or CH_4. The lack of K-band spectroscopy for HR 8799e hampers our ability to make stronger statements on its C/H and C/O values. These findings have implications for the design of future instruments on the European Extremely Large Telescope (ELT). Furthermore, multiple wavebands should be monitored simultaneously in order to detect variability (Apai et al. 2016).

5. Discussion

5.1. Summary and Comparison to Previous Work

We have presented the complete methodology for a nested sampling atmospheric retrieval code named HELIOS-R, which allows us to insert arbitrary prior distributions of parameters and also compute the full posterior distributions of the retrieved quantities. In its current implementation, we used analytical formulae for the forward model, temperature–pressure profile, and equilibrium chemistry, as well as a customized opacity calculator (HELIOS-K). By computing the Bayesian evidence, we can compare models that assume equilibrium versus unconstrained chemistry and determine which scenario is favored by the data.

We apply HELIOS-R to the measured spectra of the HR 8799b, c, d, and e directly imaged exoplanets. We find that the outer HR 8799b and c exoplanets are enriched in carbon and have superstellar and stellar C/O values, respectively. The inner HR 8799d and e exoplanets are diminished in carbon and C/O. All four exoplanets are possibly enriched in oxygen relative to the star, which is a clear signature of late-time accretion of water-rich planetesimals. Figure 15 provides a summary of our findings. We note that our retrieved water abundances are about two to three orders of magnitude higher than what was found by Madhusudhan et al. (2014) for three hot Jupiters, though it should be noted that these authors do not include a cloud model in their retrievals. The inclusion of a cloud model should worsen the discrepancy between these outcomes. Our retrieved molecular abundances and C/O for HR 8799b are in broad agreement with Lee et al. (2013), despite differences in our retrieval techniques. Table 3 summarizes the properties of the four exoplanets inferred from the retrieval.

Our conclusions differ somewhat from previous studies, which reach a diversity of conclusions. Barman et al. (2011) used self-consistent models to interpret the H- and K-band spectra of HR 8799b. They infer $R = 0.75^{+0.17}_{-0.12} R_J$ and $M = 0.72^{+2.6}_{-0.6} M_J$. We deem this radius value to be unphysical for the reasons described in Section 4.1. Marley et al. (2012) also used self-consistent models and found that if the theoretical interpretation is made of the photometry alone, then the inferred radius for the HR 8799b exoplanet is 1.11 R_J but with a surface gravity of $\log g = 4.75$, considerably higher than the $\log g = 3.5 \pm 0.5$ value of Barman et al. (2011). Madhusudhan et al. (2011) used self-consistent models[12] with various cloud configurations to conclude that the HR 8799b, c, and d exoplanets have masses of 2–12, 6–13, and 3–11 M_J, respectively, and surface gravities $\log g \approx 4$. In these studies, solar abundance is assumed. The diversity of reported results from these studies already hint at the difficulty of using photometry and spectroscopy to infer the radius and mass of a directly imaged exoplanet from the traditional use of forward modeling.

Barman et al. (2015) performed a manual fitting of the *H*- and *K*-band spectra of HR 8799b and HR 8799c. They first held the CO and CH_4 abundances fixed to their solar values, then fitted for the abundance of H_2O. The bandheads involving CO and CH_4 are masked or excluded from the fit. Next, the H_2O abundance is held at its best-fit value (and CH_4 is again held fixed at its solar value) and the abundance of CO is inferred. The final step involves fitting for CH_4. Such an approach is plausible as a first step, but does not explore the model degeneracies. It is likely that the reported value of C/O = 0.61 ± 0.05 for HR 8799b has uncertainties that are underestimated. Barman et al. (2015) themselves remark that, "The various sources of uncertainty in the models (are) not accounted for in the formal mole fraction error-bars." Building on the work of Barman et al. (2015), Moses et al. (2016) assumed fixed values for the equilibrium temperature, surface gravity, radius, C/O, metallicity, and K_{zz}, as well as a fixed temperature–pressure profile. They explored thermo- and photochemical models of HR

---

[12] Strictly speaking, these are parametric models because the cloud physics is not treated self-consistently with the gaseous chemistry and is instead parametrized.
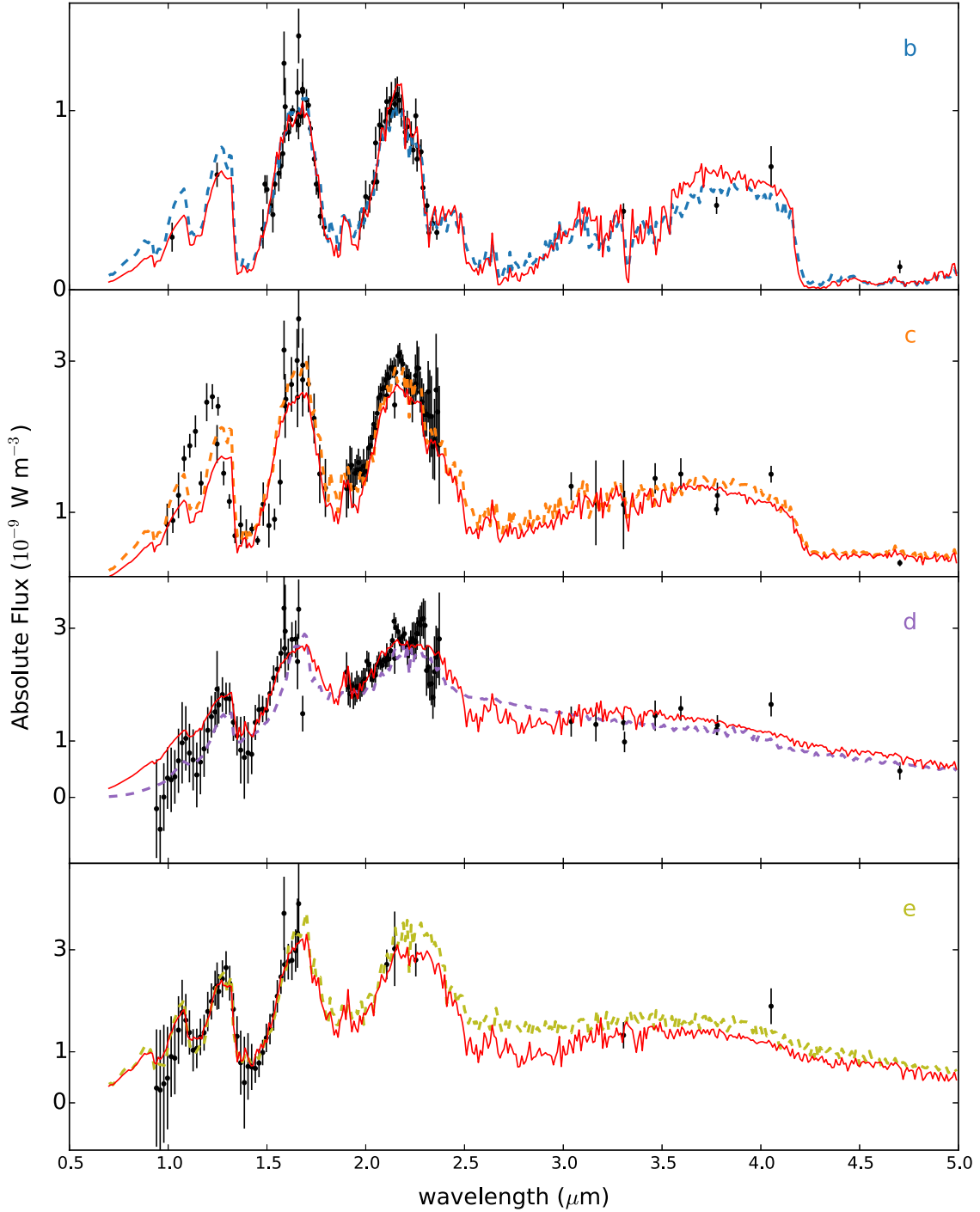
Figure 16. Elucidating the effects of using different spectroscopic line lists. The dashed curves in each panel show the retrievals using ExoMol data for water and methane. The red, continuous curves use the retrieved parameters to produce model spectra but using HITEMP water and HITRAN methane (post-processing).

8799b and produced synthetic spectra that somewhat match the measured spectrum (see their Figure 14).

Lee et al. (2013) analyzed the HR 8799b exoplanet and reported supersolar metallicities for their best fits, consistent with the present study. They considered two cloud models, where the monodisperse cloud particle radius is fixed manually and not formally included as part of the retrieval. The cloud composition is also assumed to be enstatite, whereas we have allowed the cloud composition to be part of the retrieval. The models of Lee et al. (2013) allowed for R

and g to be uniform or log-uniform priors, whereas in the current study we have chosen R and log g to be Gaussian priors. Somewhat surprisingly, despite these differences, they retrieve a C/O value that is similar to what we find (see Figure 11). On the technical side, Lee et al. (2013) used the NEMESIS code, which implements a nonlinear optimal estimation (versus the nested sampling algorithm we implemented). This technique, which is also used by Barstow et al. (2015), assumes that the priors and posteriors are Gaussian and is unable to formally perform model
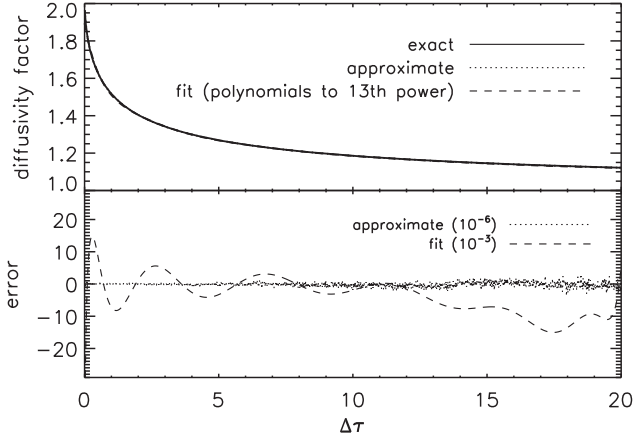
Figure 17. Calculations of the diffusivity factor using a canned routine ("exact") vs. those performed using our fitting formulae for $\mathcal{E}_1$ in Equation (21) ("approximate"). The calculation labeled "fit" is a 13th order polynomial fit to the exact solution, which performs poorly even at the $\sim 10^{-3}$ level.

selection via Bayesian evidence comparison. Lee et al. (2013) also do not consider equilibrium chemistry in their comparison of models. (See Line et al. 2013 for a comparison of these optimization methods.) Overall, HELIOS-R implements a number of improvements over NEMESIS that are more appropriate for the sparse data regime of exoplanetary atmospheres (compared to the remote sensing data of solar system objects) and is able to more rigorously explore a broader range of parameter space.

5.2. Opportunities for Future Work

There are ample opportunities for future work. Instead of unconstrained chemistry, disequilibrium chemistry may be described by some form of atmospheric mixing (e.g., eddy diffusion). More molecules may be added to the analysis, including acetylene, ethylene, and hydrogen cyanide, which are known to be spectroscopically active in the infrared at temperatures higher than for the photospheres of the HR 8799 exoplanets. Ultimately, it is our hope that the collective body of work on atmospheric retrieval will stimulate and connect to work on disk chemistry (e.g., Cridland et al. 2016). It will also be insightful to train HELIOS-R on a large sample of brown dwarf photometry and spectra, as Line et al. (2015) have done for two T dwarfs.

Software: Corner (Foreman-Mackey et al. 2016), HELIOS-K (Grimm & Heng 2015), MultiNest (Feroz & Hobson 2008; Feroz et al. 2009, 2013), PyMultiNest (Buchner et al. 2014), VULCAN (Tsai et al. 2017).

Appendix A
Analytical Formula for the Exponential Integral of the First Order

We may avoid the numerical integration of the exponential integral of the first order by using the approximate, but highly accurate, analytical formulae presented in Abramowitz & Stegun (1970),

$$\mathcal{E}_1 = \begin{cases} -\ln \Delta\tau + \sum_{j=0}^{5} \mathcal{A}_j (\Delta\tau)^j, & \Delta\tau \leqslant 1, \\ (\Delta\tau)^{-1} \exp(-\Delta\tau) \dfrac{\sum_{j=0}^{4} \mathcal{B}_j (\Delta\tau)^{4-j}}{\sum_{j=0}^{4} \mathcal{C}_j (\Delta\tau)^{4-j}}, & \text{otherwise.} \end{cases} \quad (21)$$

The fitting coefficients $\mathcal{A}_j$, $\mathcal{B}_j$, and $\mathcal{C}_j$ are given in equations (5.1.53) and (5.1.56) of Abramowitz & Stegun (1970), but we reproduce them here for convenience: $\mathcal{A}_0 = -0.57721566$, $\mathcal{A}_1 = 0.99999193$, $\mathcal{A}_2 = -0.24991055$, $\mathcal{A}_3 = 0.05519968$, $\mathcal{A}_4 = -0.00976004$, and $\mathcal{A}_5 = 0.00107857$; $\mathcal{B}_0 = \mathcal{C}_0 = 1$, $\mathcal{B}_1 = 8.5733287401$, $\mathcal{B}_2 = 18.059016973$, $\mathcal{B}_3 = 8.6347608925$, $\mathcal{B}_4 = 0.2677737343$, $\mathcal{C}_1 = 9.5733223454$, $\mathcal{C}_2 = 25.6329561486$, $\mathcal{C}_3 = 21.0996530827$, and $\mathcal{C}_4 = 3.9584969228$. As originally stated by Abramowitz & Stegun (1970), the formula involving $\mathcal{A}_j$ has a precision better than 2×10^{-7}, while that involving $\mathcal{B}_j$ and $\mathcal{C}_j$ is precise to better than 2×10^{-8}. In Figure 17, we check these claims by evaluating $\mathcal{E}_1$ using a canned routine (expint in IDL) and computing the diffusivity factor using

$$\mathcal{D} = -\frac{1}{\Delta\tau} \ln \left[(1 - \Delta\tau) \exp(-\Delta\tau) + (\Delta\tau)^2 \mathcal{E}_1 \right]. \quad (22)$$

We label these calculations as "exact." The calculations labeled "approximate" were performed using the fitting formulae in Equation (21). We see that the error is better than 10^{-6}. By contrast, a 13th order polynomial fit to the exact solution incurs large errors ($\gtrsim 10^{-3}$).

Appendix B
Full Posterior Distributions for Best Models of HR 8799b, c, d, and e

For completeness, in Figures 18–21, we show the full posterior distributions for our best models of HR 8799b, c, d, and e, which elucidate the model degeneracies between each pair of parameters.
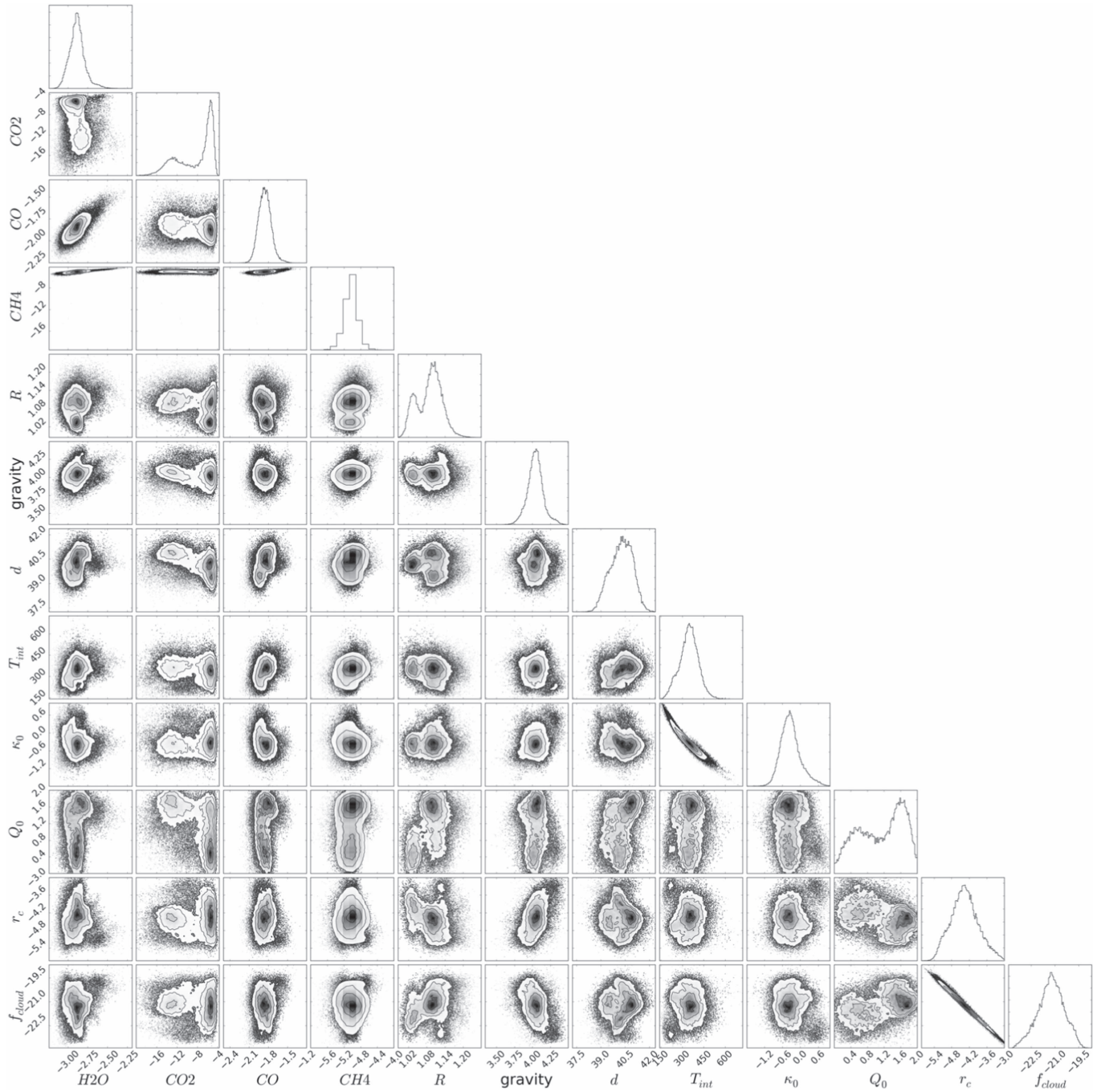
Figure 18. Montage of posterior distributions from the best-fit retrieval model of HR 8799b.
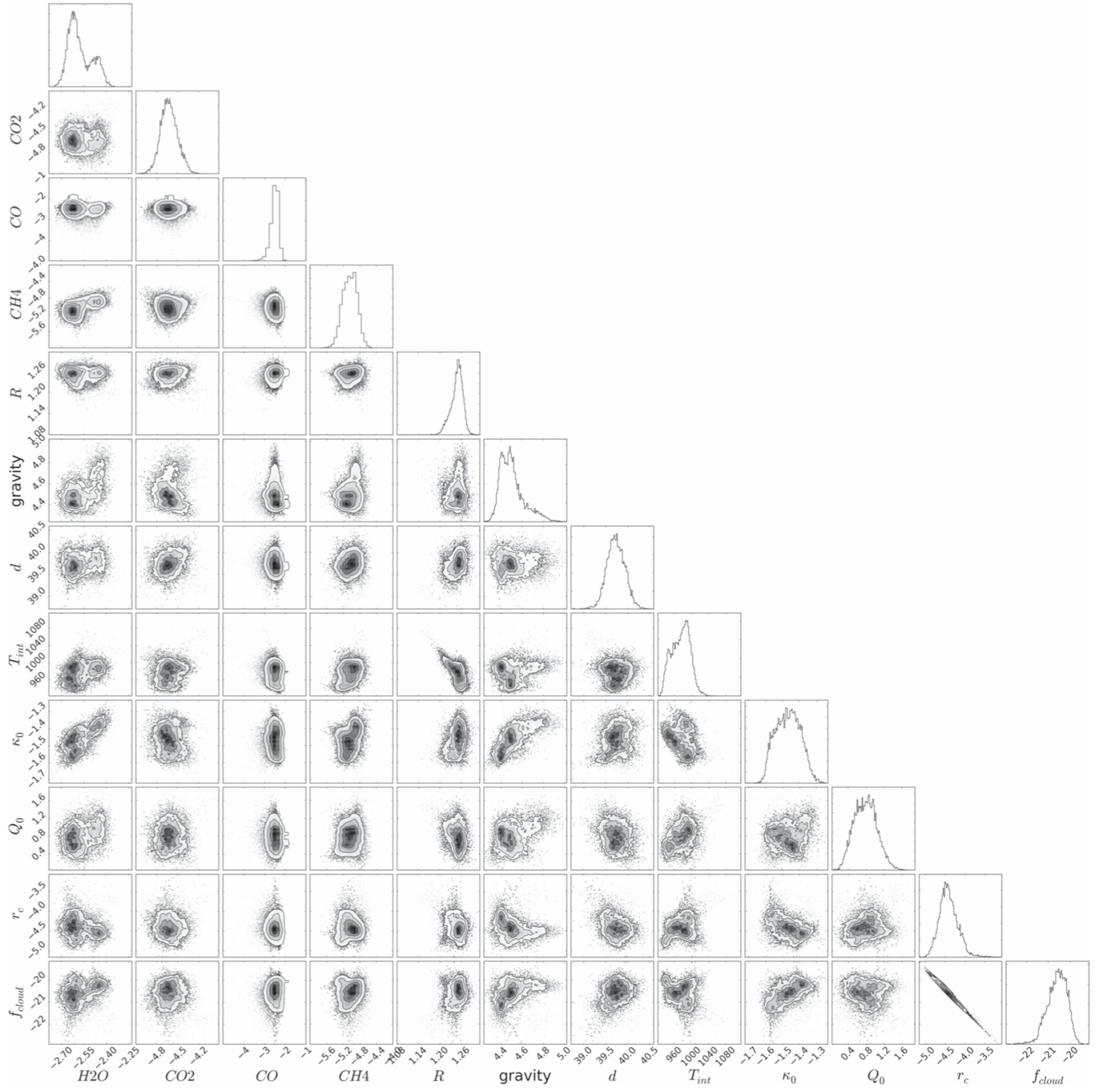
Figure 19. Same as Figure 18, but for HR 8799c.

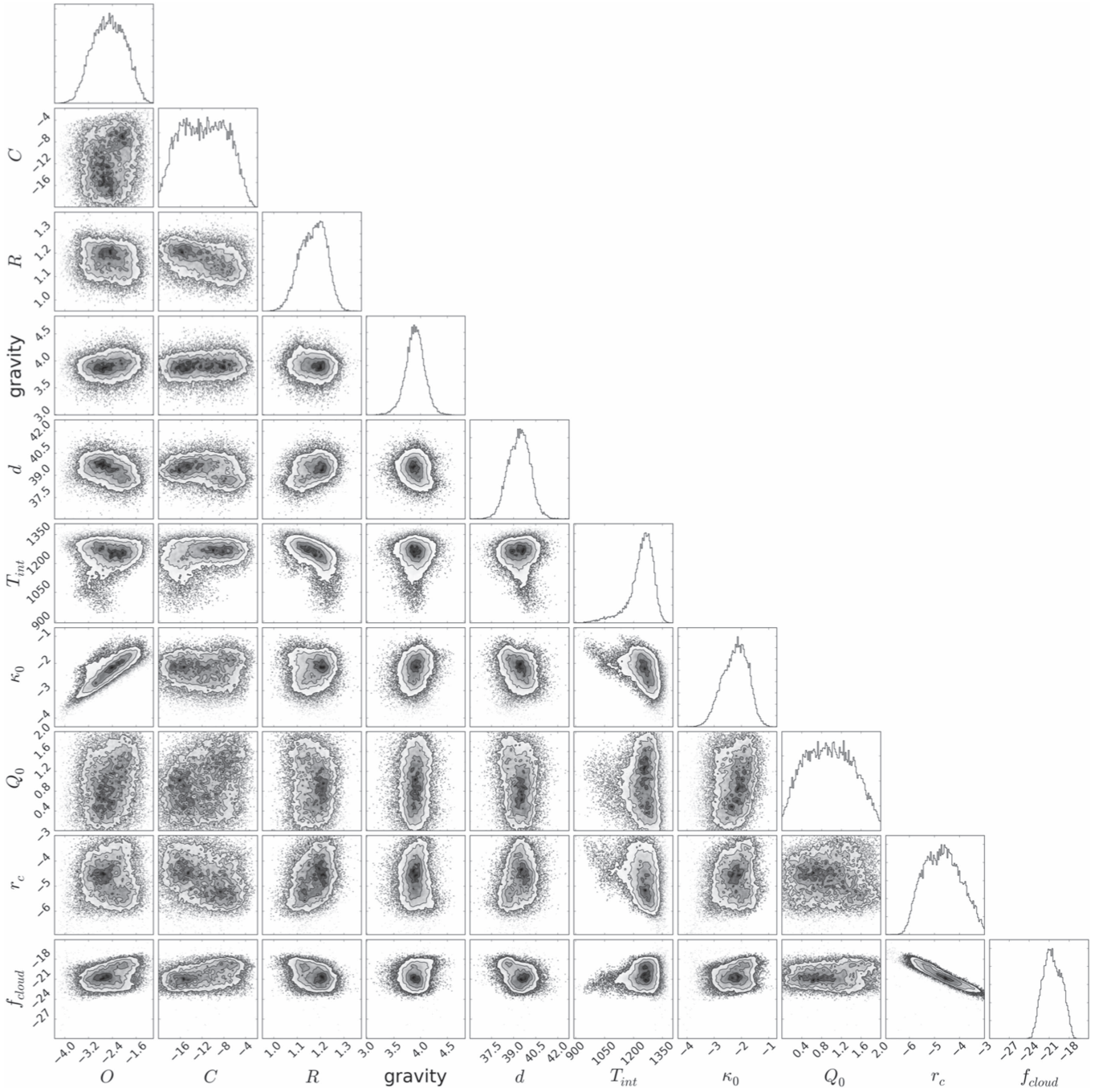**Figure 20.** Same as Figure 18, but for HR 8799d.

Figure 21. Same as Figure 18, but for HR 8799e.

ORCID iDs

Baptiste Lavie https://orcid.org/0000-0001-8884-9276
João M. Mendonça https://orcid.org/0000-0002-6907-4476
Christoph Mordasini https://orcid.org/0000-0002-1013-2811
Matej Malik https://orcid.org/0000-0002-2110-6694
Brice-Olivier Demory https://orcid.org/0000-0002-9355-5165
Simon L. Grimm https://orcid.org/0000-0002-0632-4407
David Ehrenreich https://orcid.org/0000-0001-9704-5405

Kevin Heng https://orcid.org/0000-0003-1907-5910

References

Abramowitz, M., & Stegun, I. A. 1970, Handbook of Mathematical Functions, 9th Printing (New York: Dover)
Apai, D., Kasper, M., Skemer, A., et al. 2016, ApJ, 820, 40
Baraffe, I., Chabrier, G., Allard, F., & Hauschildt, P. H. 2002, A&A, 382, 563
Barber, R. J., Tennyson, J., Harris, G. J., & Tolchenov, R. N. 2006, MNRAS, 368, 1087
Barman, T. S., Konopacky, Q. M., Macintosh, B., & Marois, C. 2015, ApJ, 804, 61

Barman, T. S., Macintosh, B., Konopacky, Q. M., & Marois, C. 2011, ApJ, 733, 65

Barstow, J. K., Aigrain, S., Irwin, P. G. J., Kendrew, S., & Fletcher, L. N. 2015, MNRAS, 448, 2546

Benneke, B., & Seager, S. 2013, ApJ, 778, 153

Bonnefoy, M., Zurlo, A., Baudino, J. L., et al. 2016, A&A, 587, A58

Bowler, B. P. 2016, PASP, 128, 102001

Buchner, J., Georgakakis, A., Nandra, K., et al. 2014, A&A, 564, A125

Burrows, A., Heng, K., & Nampaisarn, T. 2011, ApJ, 736, 47

Burrows, A., & Liebert, J. 1993, RvMP, 65, 301

Burrows, A., Marley, M., Hubbard, W. B., et al. 1997, ApJ, 491, 856

Chabrier, G., Baraffe, I., Allard, F., & Hauschildt, P. 2000, ApJ, 542, 464

Chiang, E. I., & Goldreich, P. 1997, ApJ, 490, 368

Cridland, A. J., Pudritz, R. E., & Alessi, M. 2016, MNRAS, 461, 3274

Deleuil, M., Deeg, H. J., Alonso, R., et al. 2008, A&A, 491, 889

Deming, D., Wilkins, A., McCullough, P., et al. 2013, ApJ, 774, 95

Demory, B.-O., & Seager, S. 2011, ApJS, 197, 12

Feroz, F., & Hobson, M. P. 2008, MNRAS, 384, 449

Feroz, F., Hobson, M. P., & Bridges, M. 2009, MNRAS, 398, 1601

Feroz, F., Hobson, M. P., Cameron, E., & Pettitt, A. N. 2013, arXiv:1306.2144

Foreman-Mackey, D., Vousden, W., Price-Whelan, A., et al. 2016, doi:10.5281/zenodo.53155

Fu, Q., & Liou, K. N. 1992, JAtS, 49, 2139

Gaidos, E. J. 2000, Icar, 145, 637

Grimm, S. L., & Heng, K. 2015, ApJ, 808, 182

Guillot, T. 2010, A&A, 520, A27

Han, E., Wang, S. X., Wright, J. T., et al. 2014, PASP, 943, 827

Hansen, C. J., Schwartz, J. C., & Cowan, N. B. 2014, MNRAS, 444, 3632

Hedges, C., & Madhusudhan, N. 2016, MNRAS, 458, 1427

Helling, Ch., & Woitke, P. 2006, A&A, 455, 325

Heng, K., & Demory, B.-O. 2013, ApJ, 777, 100

Heng, K., Hayek, W., Pont, F., & Sing, D. K. 2012, MNRAS, 420, 20

Heng, K., & Lyons, J. R. 2016, ApJ, 817, 149

Heng, K., Lyons, J. R., & Tsai, S.-M. 2016, ApJ, 816, 96

Heng, K., Mendonça, J. M., & Lee, J.-M. 2014, ApJS, 215, 4

Heng, K., & Tsai, S.-M. 2016, ApJ, 829, 104

Hiranaka, K., Cruz, K. L., Douglas, S. T., Marley, M. S., & Baldassare, V. F. 2016, arXiv:1606.09485

Ingraham, P., Marley, M. S., Saumon, D., et al. 2014, ApJL, 794, L15

Kass, R. E., & Raftery, A. E. 1995, JASA, 90, 773

Konopacky, Q. M., Barman, T. S., Macintosh, B. A., & Marois, C. 2013, Sci, 339, 1398

Konopacky, Q. M., Ghez, A. M., Barman, T. S., et al. 2010, ApJ, 711, 1087

Kratter, K. M., Murray-Clay, R. A., & Youdin, A. N. 2010, ApJ, 710, 1375

Kreidberg, L., Bean, J. L., Désert, J.-M., et al. 2014, ApJL, 793, L27

Kuchner, M. J., & Seager, S. 2005, arXiv:astro-ph/0504214

Lacis, A. A., & Oinas, V. 1991, JGR, 96, 9027

Lee, J.-M., Heng, K., & Irwin, P. G. J. 2013, ApJ, 778, 97

Lillo-Box, J., Barrado, D., Santos, N. C., et al. 2015, A&A, 577, A105

Line, M. R., Stevenson, K. B., Bean, J., et al. 2016, arXiv:1605.08810

Line, M. R., Teske, J., Burningham, B., Fortney, J. J., & Marley, M. S. 2015, ApJ, 807, 183

Line, M. R., Wolf, A. S., Zhang, X., et al. 2013, ApJ, 775, 137

Lodders, K. 2003, ApJ, 591, 1220

Madhusudhan, N. 2012, ApJ, 758, 36

Madhusudhan, N., Burrows, A., & Currie, T. 2011, ApJ, 737, 34

Madhusudhan, N., Crouzet, N., McCullough, P. R., Deming, D., & Hedges, C. 2014, ApJL, 791, L9

Madhusudhan, N., & Seager, S. 2009, ApJ, 707, 24

Malik, M., Grosheintz, L., Mendonça, J. M., et al. 2017, AJ, 153, 56

Mandell, A. M., Haynes, K., Sinukoff, E., et al. 2013, ApJ, 779, 128

Marleau, G.-D., & Cumming, A. 2014, MNRAS, 437, 1378

Marley, M. S., Saumon, D., Cushing, M., et al. 2012, ApJ, 754, 135

Marois, C., Macintosh, B., Barman, T., et al. 2008, Sci, 322, 1348

Marois, C., Zuckerman, B., Konopacky, Q. M., et al. 2010, Natur, 468, 1080

Mihalas, D. 1970, Stellar Atmospheres (San Francisco: Freeman)

Miller-Ricci, E., & Fortney, J. J. 2010, ApJL, 716, L74

Mordasini, C., Alibert, Y., Georgy, C., et al. 2012, A&A, 547, A112

Mordasini, C., van Boekel, R., Mollière, P., Henning, T., & Benneke, B. 2016, ApJ, 832, 41

Moses, J. I., Line, M. R., Visscher, C., et al. 2013, ApJ, 777, 34

Moses, J. I., Marley, M. S., Zahnle, K., et al. 2016, ApJ, 829, 66

Öberg, K. I., Murray-Clay, R., & Bergin, E. A. 2011, ApJL, 743, L16

Oppenheimer, B. R., Baranec, C., Beichman, C., et al. 2013, ApJ, 768, 24

Pierrehumbert, R. T. 2010, Principles of Planetary Climate (New York: Cambridge Univ. Press)

Press, W. H., Teukolsky, S. A., Vetterling, W. T., & Flannery, B. P. 2007, Numerical Recipes: The Art of Scientific Computing (3rd ed.; New York: Cambridge Univ. Press)

Richard, C., Gordon, I. E., Rothman, L. S., et al. 2012, JQSRT, 113, 1276

Rothman, L. S., Gordon, I. E., Babikov, Y., et al. 2013, JQSRT, 130, 4

Rothman, L. S., Gordon, I. E., Barber, R. J., et al. 2010, JQSRT, 111, 2139

Rothman, L. S., Rinsland, C. P., Goldman, A., et al. 1996, JQSRT, 60, 665

Sadakane, K. 2006, PASJ, 58, 1023

Skilling, J. 2006, BayAn, 1, 833

Smith, M. D. 1998, Icar, 132, 176

Spiegel, D. S., & Burrows, A. 2012, ApJ, 745, 174

Spiegel, D. S., Silverio, K., & Burrows, A. 2009, ApJ, 699, 1487

Stevenson, K. B., Désert, J.-M., Line, M. R., et al. 2014, Sci, 346, 838

Tognelli, E., Prada Moroni, P. G., & Degl'Innocenti, S. 2007, A&A, 533, A109

Trotta, R. 2008, ConPh, 49, 71

Tsai, S.-M., Lyons, J. R., Grosheintz, L., et al. 2017, ApJS, 228, 20

van Leeuwen, F. 2007, A&A, 474, 653

Waldmann, I. P., Tinetti, G., Rocchetto, M., et al. 2015, ApJ, 802, 107

Yurchenko, S. N., & Tennyson, J. 2014, MNRAS, 440, 1649

Zaghloul, M. R., & Ali, A. N. 2012, ACM Transactions on Mathematical Software, 38, 15

Zurlo, A., Vigan, A., Galicher, R., et al. 2016, A&A, 587, A57

3.2.2   Numerical parameters

The state of the atmosphere is represented by the n_{dim} physical parameters in `HELIOS_R`. The model contains up to eleven parameters : the distance, two between the radius of the object, its surface gravity or its mass [a]; two or four parameters for the abundances depending on the chemistry chosen, two parameters for the temperature-profile and three parameters for the clouds. Other models can have different setting and/or assumptions and the state of the atmosphere can be represented by slightly different parameters.

Those n_{dim} physical parameters are relevant for the study of the atmosphere of stellar companions and are likely to be constrained by the data we possess. On top of those parameters, every model contain other physical parameters that are fixed and numerical parameters (hidden and known, see section 2.1.1) that need to be set correctly so that the numerical implementation of the model is correct.

- The fixed physical parameters are constrained by others experiments or by other theoretical models and cannot (or very poorly) be constrained with a typical emission spectrum. This is the case of all the physical constants (gravitational constant, Boltzmann constant etc.); parameters used to produce the opacity tables (wavelength position, intensity of spectral lines etc.) and instrument response parameters (photometric filter response, point spread function for spectroscopy etc.).
- The known numerical parameters are the number of layers, the pressure boundaries and the sampling resolution, i.e. the resolution at which the radiative calculations are done. This resolution is higher than the spectral resolution of the data.

3.2.2.1   Number of layers and pressure boundaries

The test to determine the number of layers is presented in the paper.
The pressure boundaries come from the self-consistent model $HELIOS$ (Malik et al. 2017), which insures the convergence of the radiative transfer scheme. `HELIOS_R` is iterating for radiative equilibrium and only propagates the flux upward, as a result opting for a lower boundary of 10^3 bars is probably not necessary. However, the raw opacity tables for both papers (Malik et al. 2017; Lavie et al. 2017b) have the same source : $HELIOS\_K$ and are stored on a server in Bern. So, the choice was made because information at this pressure were available and to remain consistent between the two codes. A lower limit in the atmosphere at 10^3 bars is conservative, Benneke & Seager (2012) use 100 bars, Lee et al. (2013) and Waldmann et al. (2015a) use 10 bars for example. A proper test of the impact of those boundaries was not

---

[a]the mass was added in an updated version presented in the next section 3.3
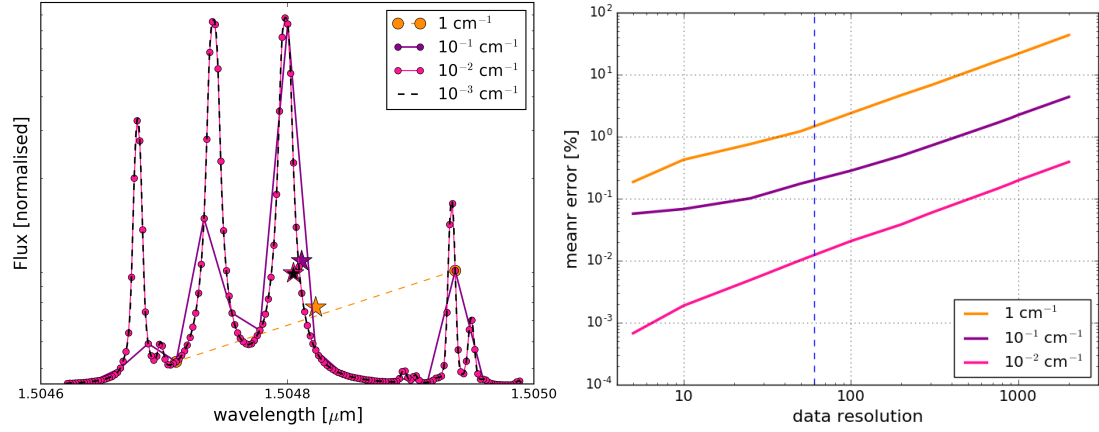
Figure 3.1: Sampling resolution test. Left panel : Spectrum example for one data point. The lines colour coded represent the high resolution spectrum of the model. The colour coded stars represent the spectrum at the resolution of the data, which is just one data point (integration of the the high resolution spectrum over some wavelength range. In this example between 1.5046 and 1.5050 Å). Right panel : the mean error between the calculations done at a certain resolution and the correct value assumed to be achieved with a resolution of 10^{-3} cm^{-1} as a function of the spectral resolution.

done in the scope of this thesis and, to my knowledge, has not be done in the literature. It is worth considering doing a test to assess the impact of our choices on the retrieval results.

3.2.2.2 Sampling resolution

As explained in section 2.3, a datapoint is the total flux received from the source in a given wavelength band. The wavelength bin is broad for a photometric datapoint and will depend on the resolution for a spectroscopic datapoint. The higher the resolution, the smallest the wavelength bin is. In the theoretical case of a perfect instrument, the datapoint is the integration of the flux received. Therefore, an atmospheric model producing a synthetic spectrum that can be compared directly to the data, needs somehow to perform an integral calculation of a higher resolution spectrum. Traditionally two approaches are used in atmospheric retrieval of exoplanets or brown-dwarfs, the opacity sampling and the k-distribution methods, see section 2.3 Lavie et al. (2017b). By default, `HELIOS_R` (and most of the retrieval codes using opacity sampling) performs the radiative transfer calculation using opacity sampling, but the k-distribution can also be use. However, it turns out that building the k-distribution tables take more time than to build the opacity sampling tables for a negligible gain in the computation time. By contrast, the k-distribution method is useful for self-consistent models because those models are interested in the energy deposited in a certain wavelength bin. So, the k-distribution is faster to reach radiative equilibrium and with a minimum number of wavelength bins (Malik et al. 2017). However, to produce a spectrum comparable to the data the number of bins needs to be increased and the gain with the opacity sampling method is not evident. `HELIOS_R` uses
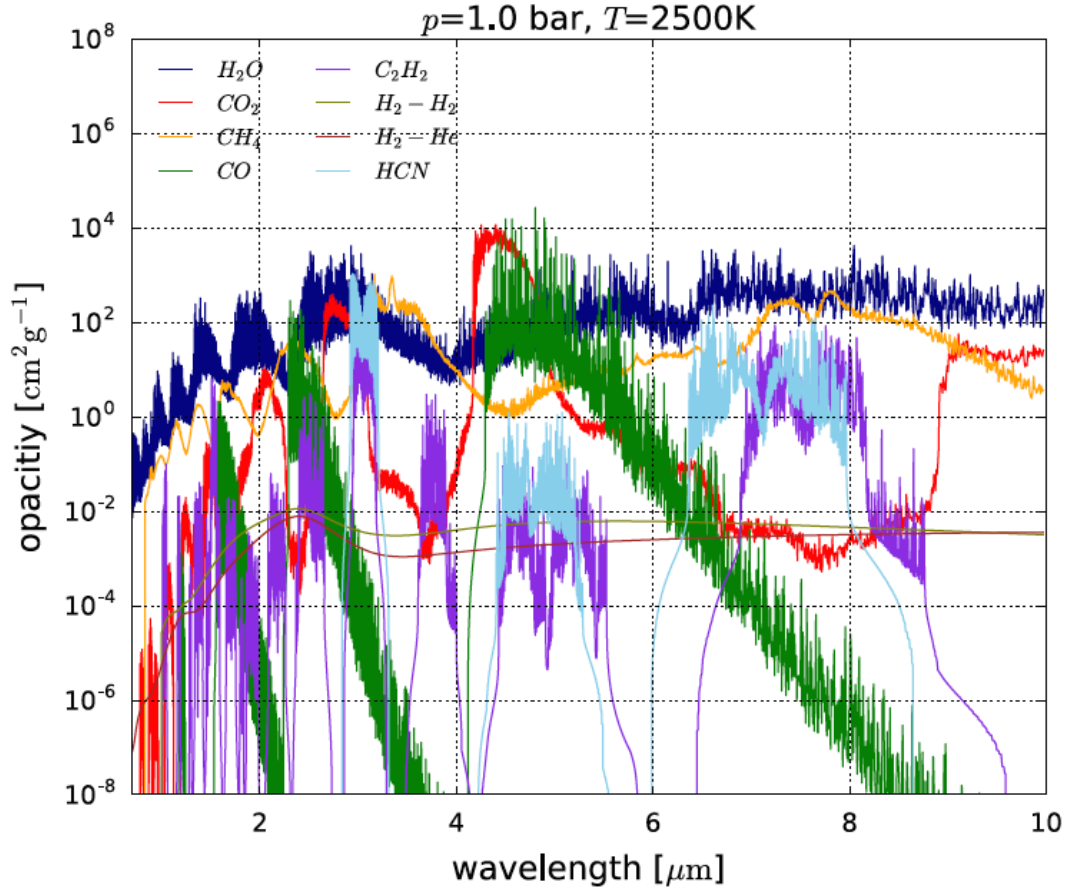
Figure 3.2: Examples of opacities computed using our *HELIOS_K* opacity calculator for a temperature of 2500 K and a pressure of 1 bar. The ExoMol database is the source of our H_2O and CH_4 opacities. The CO and CO_2 opacities are from HITEMP, while the C_2H_2 and HCN opacties are from HITRAN. Source : Oreshenko et al. (2017)

a sampling resolution of 1 cm^{-1}, linelist databases naturally provide information in terms of wavenumber. This corresponds to a spectral resolution in wavelength of 10000 and 400 at 1 and 5 μm respectively. The default integrator used in HELIOS_R is a trapezoidal algorithm but can be switched to use Simpson's rule (Press 2007). The choice of the integrator is a balance between the error of the integral computation and the computing time.

To check for the robustness of the sampling resolution choice I perform the following test:

- We consider several synthetic data (spectrum) with different spectral resolution ($\lambda/\varDelta\lambda$ from 5 to 2500) between 1 and 2.5 μm for a water dominated companion. The water molecule possesses a rich number of spectral lines all over the infrared (see Fig. 3.2 from Oreshenko et al. 2017).

- Given a set of parameters for the atmospheric model, we perform radiative calculation at different sampling resolution : 1, 10^{-1}, 10^{-2}, 10^{-3} cm^{-1} for all the wavelength bins

between 1 and 2.5 μm. For example, when the synthetic data has a spectral resolution of 100, there is 115 wavelength bins, Fig. 3.1.

- The higher resolution 10^{-3} cm^{-1} is considered to provide the "correct" value. This may be debatable. However, the difference between 10^{-2} cm^{-1} resolution and 10^{-3} cm^{-1} is very small, about 100 ppm and the lines are clearly resolved, Fig. 3.1. Therefore the gain by going to an even higher resolution will not be very important. Also, the typical size of an opacity table of one molecule at a resolution of 10^{-4} cm^{-1} is about 130 Go with the pressure and temperature setting of `HELIOS_R` which makes the computation difficult and slow.

- Comparison of the radiative calculations at different sampling resolution with the "correct" value is performed. We compute the mean error of all the bins for all the spectral resolution.

- I iterate the previous step for a dozen of parameter values and I average the mean error.

The result of this test is presented in Fig. 3.1. The dash line represent the typical resolution of the data for direct imaged objects used during my thesis. The mean error at a sampling resolution of 1 cm^{-1} and a spectral resolution of 60 is of the order of a percent. Typical uncertainties on the observation of direct imaged objects is of the order of 20% or more. The error due to the sampling resolution depends on the parameter of the model. A spectrum with a lot of deep features (mainly influenced by the TP profile) has a larger error. Although a stronger test to assess the correlations between the mean error and the model parameters is needed. As we reach the 10^{-2} cm^{-1} sampling resolution, all the lines are resolved, which is highlighted by a significant drop in the mean error as compared to the drop between 1 and 10^{-1} cm^{-1}. A conservative solution would be to perform the radiative calculation at a resolution of 10^{-2} cm^{-1}. However, it implies a significant increase in the computing time of the model, which prevents the Bayesian framework from converging in a decent amount of time. Solutions may exist to speed up the model computation but request a significant investment, especially to handle the memory hassles for the GPU. For the next generation of instruments with better uncertainties and/or higher spectral resolution, the sampling resolution for the radiative calculation will need to be increased. For example, at a spectral resolution of 1000 the mean error at a sampling resolution is at the level of today's observations uncertainties $\approx 20\%$.

Finally, I want to emphasise the point made in our paper on the distinction between the number of lines used to build the cross-section tables and the sampling resolution at which the radiative calculation is done. A model using a sampling resolution of 1cm^{-1} cannot be defined as a "line-by-line" code because the uncertainties are bigger (a lot) than the machine precision, few % compared to an expected 10^{-16} for double precision calculations. All the "line-by-line" codes that I have come across are not real "line-by-line" codes. Most of the time, the argument

used by authors to knighted their "line-by-line" codes is the comparison between the spectral resolution and the sampling resolution, i.e. if the sampling resolution is much higher than the spectral resolution then those authors considered the code to be line-by-line. I consider this argument false until proven otherwise by a similar test than the one done in this section.

3.3   Radial Velocity and direct Imaging

3.3.1   The impact of gravity on the emission spectrum

As discussed in our paper Lavie et al. (2017b), constraining simultaneously the radius and the gravity (or the mass as those three quantities are linked - by equation 3 in Peretti et al. (2018)) with only emission observations of the object is challenging. The lack of knowledge on those quantities leads to huge degeneracies between the model parameters. Especially when the data are not numerous and have big uncertainties. In the initial paper, the radius only appear in the equation 15 of the physical model of `HELIOS_R` and is merely a scaling factor for the entire flux. It is degenerate with the distance of the system and affects the entire wavelength range in a similar way. The gravity appears in two equations : Eq. 6 of the temperature-pressure profile via the column mass and Eq. 7 of the optical depth. In case of the assumption of clouds the gravity also appears in the optical depth add-on (Eq. 16). On a first order basis, the surface gravity impacts the spectral features. The higher the surface gravity is the smaller the features are. Figure 3.3 shows the result of a test on the influence of the gravity on `HELIOS_R` spectrum output. All parameters are fixed to some mock values (HR 8799 b with no clouds) and we only study the Top Of the Atmosphere (TOA) flux, so that the radius value does not impact us. First we change the gravity from 1 to 1000 ms^{-1} and plot the spectrum (top panel). In a second test, we do the same but with fixing the gravity value to 10 ms^{-2} in Eq. 7 (middle panel) to study the impact of the gravity due to its change in the Temperature-Pressure profile computation. Finally, we do the same but with Eq. 6 in order to study the impact due to the change of gravity in optical depth computation (bottom panel).

When doing a retrieval, those changes in the flux will compete with the changes produced by the other parameters hence creating degeneracies. I have applied `HELIOS_R` to HD 206893 b (Delorme et al. 2017), HD 4747B (Peretti et al. 2018 reproduced in 3.3.2) and GJ 504 b (Bonnefoy et al. 2018). For the first two objects the data coverage is similar, while GJ 504 b dataset is constituted of photometric observations (see Fig. 3.4).

As the wavelength coverage is small and the uncertainties too high, it is not possible to use `HELIOS_R` to retrieve useful information if no strong prior is given on the surface gravity. There is too much degeneracies. For GJ 504 b and HD 206893 B, self-consistent models were used in order to give some insight on the properties of those objects. However strong assumptions
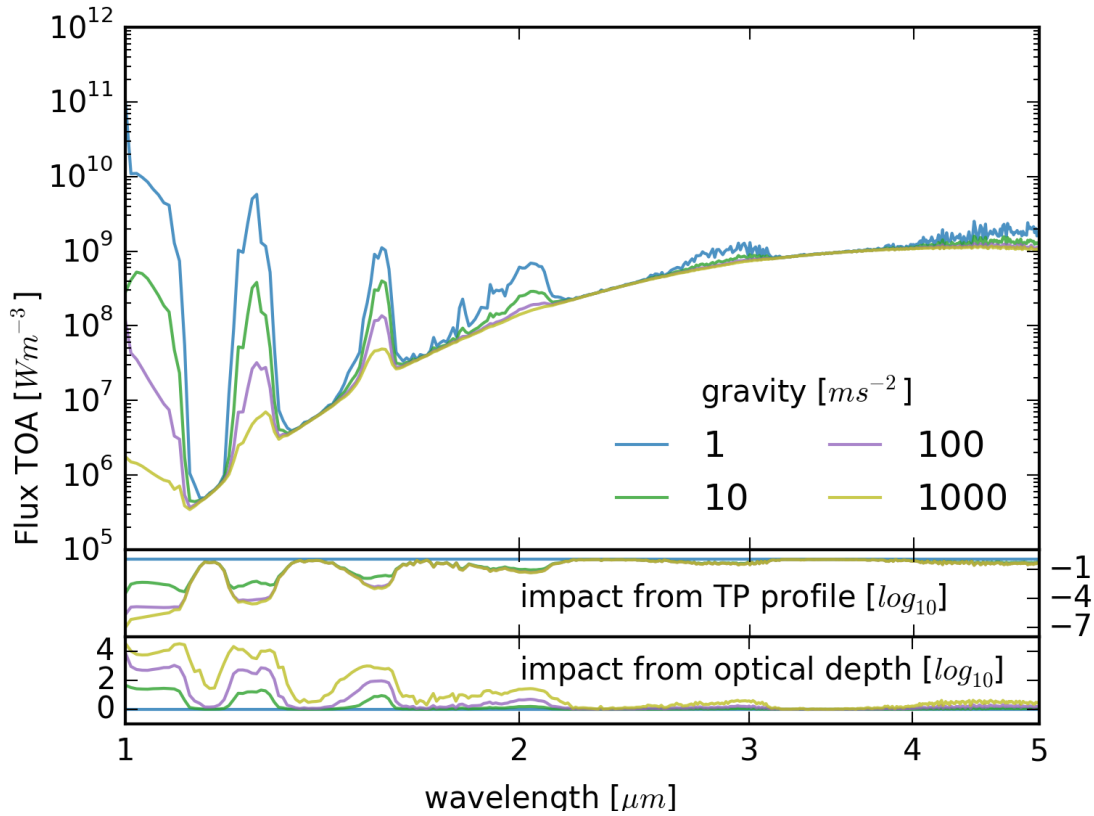
Figure 3.3: Impact of the surface gravity on the spectrum. The top panel shows spectra of a companion similar to HR 8799 b planets with different surface gravity. The two bottom panels show the relative difference of each spectrum with the spectrum produced with a $1\mathrm{ms}^{-2}$ surface gravity.

are needed. In a sense it is equivalent of running a retrieval with `HELIOS_R` but with choosing strong (maybe false ?) priors on the parameters.

The case of HD 4747 B is unique in this framework as on top of the spectroscopic observations radial-velocity data were obtained. This extra-information provides a very good constrain on the mass of the object. Adapting the code to be able to take as an input the mass (equation 3 in Peretti et al. (2018)) allowed us to extract useful information on the molecules abundances of the object by breaking some of the degeneracies. HD 4747 B is a very massive companion, which gives evidence of a formation mechanism by gravitational instability. Indeed, it seems very difficult with the current scenario of core accretion to form such a massive object. Using `HELIOS_R` we were able to constrain the carbon and oxygen ratios and find that they are compatible with the abundances of the host star. Uncertainties retrieved are still too high to disentangle unambiguously the formation mechanism but follow-up observations at higher resolution may solve this. The paper is reproduced in the next section.
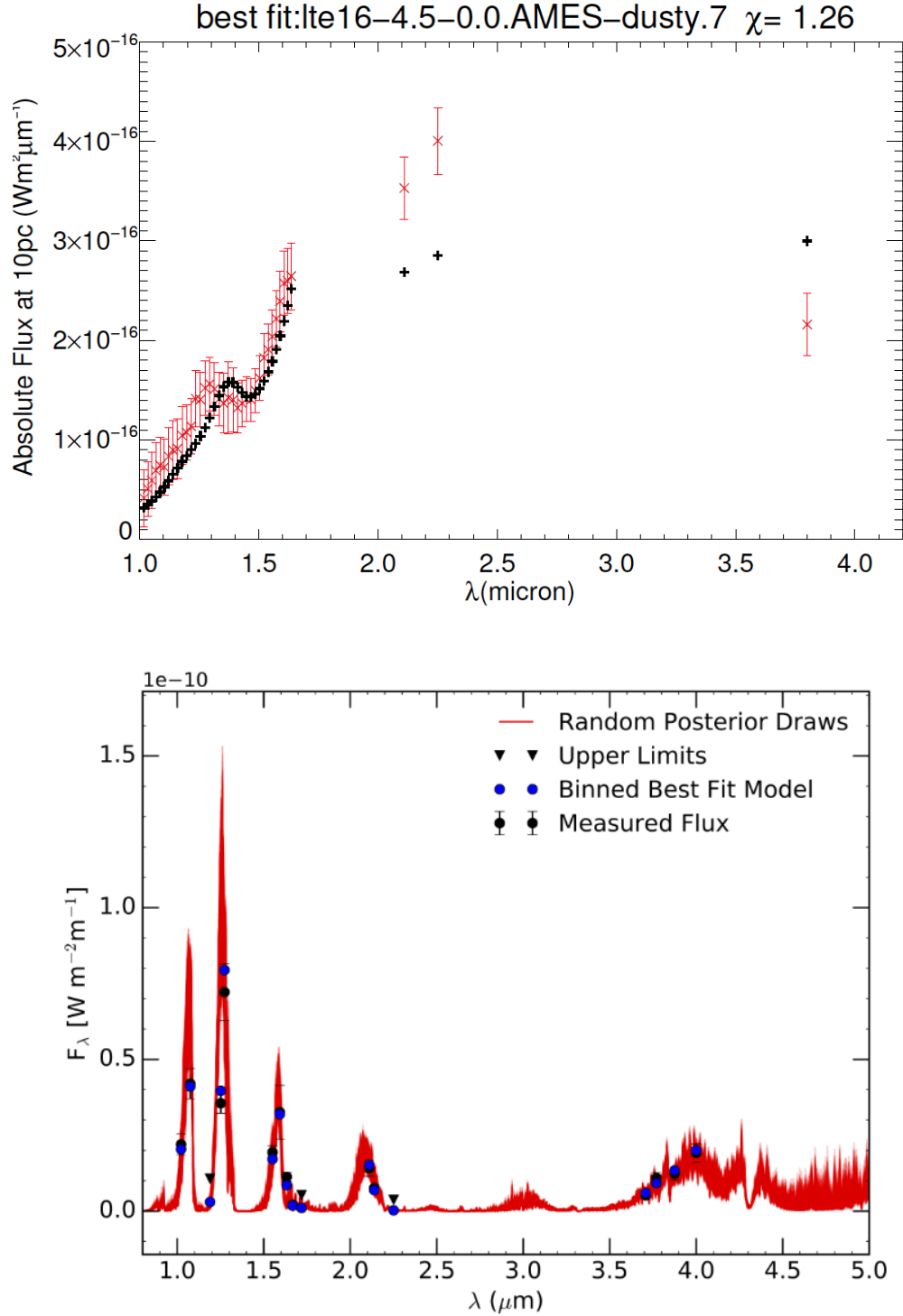
Figure 3.4: Data coverage. Top panel: HD 206893 b, Delorme et al. 2017. Bottom panel: GJ 504 b, Bonnefoy et al. 2018. Uncertainties on the data and wavelength coverage do not allow to unambiguously choose between different models used in `HELIOS_R`.

3.3.2 HD 4747

This section reproduced the paper on the massive brown dwarf HD 4747 B.

Orbital and spectral analysis of the benchmark brown dwarf HD 4747B[⋆]

S. Peretti[1], D. Ségransan[1], B. Lavie[1], S. Desidera[2], A.-L. Maire[3], V. D'Orazi[2], A. Vigan[4], J.-L. Baudino[5, 6], A. Cheetham[1], M. Janson[3, 7], G. Chauvin[8], J. Hagelberg[8], F. Menard[8], K. Heng[9], S. Udry[1], A. Boccaletti[5], S. Daemgen[11], H. Le Coroller[4], D. Mesa[2], D. Rouan[5], M. Samland[3], T. Schmidt[5], A. Zurlo[4, 17, 18], M. Bonnefoy[8], M. Feldt[3], R. Gratton[2], A-M. Lagrange[8], M. Langlois[4, 13], M. Meyer[11, 14], M. Carbillet[10], M. Carle[4], V. De Caprio[12], L. Gluck[8], E. Hugot[4], Y. Magnard[8], T. Moulin[8], A. Pavlov[3], J. Pragt[15], P. Rabou[8], J. Ramos[3], G. Rousset[5], A. Sevin[5], C. Soenke[16], E. Stadler[8], L. Weber[1], and F. Wildi[1]

1. Observatoire astronomique de l'Université de Genève, 51 Ch des Maillettes, 1290 Sauverny, Switzerland
   e-mail: sebastien.peretti@unige.ch
2. INAF - Osservatorio Astronomico di Padova, Vicolo dell'Osservatorio 5, 35122, Padova, Italy
3. Max Planck Institute for Astronomy, Koenigstuhl 17 69117 Heidelberg Germany
4. Laboratoire d'Astrophysique de Marseille, 38, rue Frédéric Joliot-Curie 13388 Marseille cedex 13 FRANCE
5. LESIA, Observatoire de Paris, PSL Research University, CNRS, Sorbonne Universités, UPMC Univ. Paris 06, Univ. Paris Diderot, Sorbonne Paris Cité, 5 place Jules Janssen, 92195 Meudon, France
6. Department of Physics, University of Oxford, Oxford, UK
7. Department of Astronomy, Stockholm University, AlbaNova University Center, 106 91 Stockholm, Sweden
8. Univ. Grenoble Alpes, CNRS, IPAG, 38000 Grenoble, France
9. University of Bern, Center for Space and Habitability, Sidlerstrasse 5, CH-3012, Bern, Switzerland
10. Université Cote d'Azur, OCA, CNRS, Lagrange, France
11. Institute for Astronomy, ETH Zurich, Wolfgang-Pauli-Strasse 27, 8093 Zurich, Switzerland
12. INAF - Osservatorio Astronomico di Capodimonte, Salita Moiariello 16, 80131 Napoli, Italy
13. Centre de Recherche Astrophysique de Lyon, CNRS, Université Lyon 1, 9 avenue Charles André, F-69561 Saint Genis-Laval-Cedex, France
14. The University of Michigan, Ann Arbor, MI 48109, USA
15. NOVA Optical Infrared Instrumentation Group, Oude Hoogeveensedijk 4, 7991 PD Dwingeloo, The Netherlands
16. European Southern Observatory (ESO), Karl-Schwarzschild-Str. 2, 85748 Garching, Germany
17. Núcleo de Astonomía, Facultad de Ingeniería, Universidad Diego Portales, A. Ejercito 441, Santiago, Chile
18. Escuela de Ingeniería Industrial, Facultad de Ingeniería y Ciencias, Universidad Diego Portales, Av. Ejercito 441, Santiago, Chile

ABSTRACT

Context. The study of high contrast imaged brown dwarfs and exoplanets depends strongly on evolutionary models. To estimate the mass of a directly imaged substellar object, its extracted photometry or spectrum is used and adjusted with model spectra together with the estimated age of the system. These models still need to be properly tested and constrained. HD 4747B is a brown dwarf close to the H burning mass limit, orbiting a nearby ($d = 19.25 \pm 0.58 pc$), solar-type star (G9V) and has been observed with the radial velocity method over almost two decades now. Its companion was also recently detected by direct imaging, allowing a complete study of this particular object.

Aims. We aim to fully characterize HD 4747B by combining a well constrained dynamical mass and a study of its observed spectral features in order to test evolutionary models for substellar objects and characterize its atmosphere.

Methods. We combine the radial velocity measurements of HIRES and CORALIE taken over two decades and high contrast imaging of several epochs from NACO, NIRC2 and SPHERE to obtain a dynamical mass. From the SPHERE data we obtain a low resolution spectrum of the companion from Y to H band, as well as two narrow band-width photometric measurements in the K band. A study of the primary star allows in addition to constrain the age of the system as well as its distance.

Results. Thanks to the new SPHERE epoch and NACO archival data combined with previous imaging data and high precision radial velocity measurements, we have been able to derive a well constrained orbit. The high eccentricity ($e = 0.7362 \pm 0.0025$) of HD 4747B is confirmed, and the inclination as well as the semi-major axis are derived ($i = 47.3 \pm 1.6°$, $a = 10.01 \pm 0.21$ au). We derive a dynamical mass of $m_B = 70.0 \pm 1.6$ M_{Jup} which is higher than a previous study, but in better agreement with the models. By comparing the object with known brown dwarfs spectra, we derive a spectral type of L9 and an effective temperature of 1350 ± 50 K. With a retrieval analysis we constrain the oxygen and carbon abundances and compare them with the ones from the HR 8799 planets.

Key words. stars: binaries: general – stars: binaries: spectroscopic – stars: binaries: visual – stars: low-mass, brown dwarfs – techniques: radial velocities – techniques: adaptive optics

1. Introduction

Brown dwarfs (BD) are substellar objects, not massive enough to sustain hydrogen burning, with masses below ~75 Jupiter masses (e.g. Burrows et al. 1997). Since the first brown dwarfs were discovered in 1995 (Nakajima et al. 1995; Oppenheimer et al. 1995; Rebolo et al. 1995) by imaging, only few of these objects were detected around sun-like stars with respect to the number of planetary mass objects, and binaries (e.g. Anderson et al. 2011; Sahlmann et al. 2011a; Siverd et al. 2012; Bayliss et al. 2017). Numerous studies based on transiting, radial velocity and astrometry methods have indeed demonstrated that the "brown dwarf desert" is observed at separations below 10 au and that brown dwarfs have a frequency around sun like stars of less than 1% (Halbwachs et al. 2000; Marcy & Butler 2000; Grether & Lineweaver 2006; Sahlmann et al. 2011b; Wilson et al. 2016). However, a recent study showed that this "desert" might exists only for separations smaller than ~ 0.1 - ~ 0.2 au (e.g. Troup et al. 2016). At larger separation, BD are found as abundantly as very low mass stars. However the much wider range in spectral types in comparison with RV's surveys probed by Troup et al. (2016) might explain the high number of BD found.

Due to observing biases, direct imaging is much better suited to exploring the outer reaches of stellar systems to search for such brown dwarf companions. A few brown dwarfs have been detected by direct imaging (e.g. Thalmann et al. 2009; Biller et al. 2010; Chauvin et al. 2010), allowing to constrain their effective temperature and atmospheric properties thanks to spectrophotometry analysis (e.g. Maire et al. 2016a; Vigan et al. 2016) and the age of the system through the host stars. To determine the mass of an imaged BD companion, the key parameter for the evolution of substellar objects, we usually rely on evolutionary models (e.g. Baraffe et al. 2003). These models still need to be tested and properly calibrated through observations. To achieve this, observations of objects for which we can constrain independently the age, the effective temperature and the mass are needed.

Free floating BD have been detected and provided high resolution spectra, allowing to better understand these objects (see e.g. Kirkpatrick 2005; Helling & Casewell 2014, and ref. therein), but independent mass and age estimations cannot be derived in most cases. BD companions to solar type stars have been discovered at wide orbits (e.g. Burgasser 2007b; Pinfield et al. 2012; Burningham et al. 2013, and ref. therein), allowing an age determination from their host stars and effective temperature from their spectra. However their wide orbits prevent from a dynamical mass measurement. Dynamical masses of BD have been determined for BD pairs (e.g. Dupuy & Liu 2017), but no independent age estimation could be extracted for these sub-stellar systems. For some objects we have high resolution spectra and dynamical masses, but these often also lack independent age measurements (e.g. King et al. 2010; Line et al. 2015). The majority of directly imaged brown dwarf companions from high contrast imaging surveys have been detected around young and massive stars, as they are brighter at young ages (Chabrier & Baraffe 2000). These detections can provide age estimations of the system from the stellar host, as well as astrometric orbits, but model-independent dynamical masses cannot be easily obtained due to the difficulties in achieving precise radial velocities of young, massive stars (e.g. Galland et al. 2005). In addition the

orbital period of these directly imaged brown dwarfs are usually of decades if not centuries, and therefore obtaining a complete orbit will need long term monitoring.

HD 4747B is a perfect candidate to test the evolutionary models. It is orbiting a late G type star (HD 4747), which was observed through two decades by the HIRES instrument at the Keck (Vogt et al. 1994), as well as with the CORALIE spectrograph (Queloz et al. 2000) to obtain radial velocities. Two thirds of the orbit has been already completed, and the important periastron passage was covered. This allowed a minimum mass determination of the companion that pointed towards a brown dwarf at large separation (Nidever et al. 2002; Sahlmann et al. 2011b). Thanks to the high precision of the RV data and the number of points, the minimum mass is well constrained and only a few astrometric points can provide a high precision orbit and dynamical mass. HD 4747B was directly imaged for the first time by Crepp et al. (2016) who confirmed its substellar nature and gave a dynamical mass estimation of $m_B = 60.2 \pm 3.3$ M_{Jup}[1]. However the isochronal mass estimate of $m_B = 72^{+3}_{-13}$ M_{Jup} was in marginal agreement with its dynamical mass. A color-magnitude diagram led to a late L spectral type.

To improve the orbital parameters and characterize the atmosphere of HD 4747B, we have observed HD 4747 with the SPHERE instrument installed on the VLT (Spectro-Polarimetric High-contrast Exoplanet REsearch; Beuzit et al. 2008) in December 2016. In Sect. 2 we detail our analysis of the host star, which gives the age and distance of the system. We describe in Sect. 3 the observations we used in this paper. In Sect. 4 we report on the extraction of spectrophotometry and astrometry from the SPHERE images and we describe also the analysis of an archival NACO dataset in which we could detect the companion. Sect. 5 presents our orbital analysis combining radial velocity and imaging data. Sect. 6 describes the spectrophotometric analysis, by comparing our extracted spectra with real objects, models and a retrieval analysis, and we conclude in Sect. 7.

2. Host star properties

As a close (d = 19.3±0.6 pc, this paper) solar type star, HD 4747 was extensively studied in the literature. Several spectroscopic analyzes were performed by different groups (Table 1), indicating an effective temperature around 5300-5400 K, a gravity log$g$=4.5-4.65 and a mildly subsolar metallicity ([Fe/H] about -0.2). Similar values were also derived from Strömgren photometry.

We used an archival spectrum of HD 4747 taken with the visible high resolution spectrograph FEROS[2] (Kaufer et al. 1997), to re-derive its stellar parameters. The effective temperature (T_{eff}), the gravity (log$g$), the microturbulence (ξ) and the metallicity ([Fe/H]) were retrieved using the standard approach described in D'Orazi et al. (2017). We obtain T_{eff}=5400±60 K, log$g$=4.60±0.15 dex, ξ=0.75±0.2 km s^{-1} and [Fe/H]=−0.23±0.05 dex. Our results, also reported in Table 1, are fully consistent with those from the literature. Moreover, we have derived abundances for elements produced in the slow (s) neutron-capture process, namely yttrium, barium and lanthanum. As done in all our previous investigations, we have carried out spectral synthesis calculations, including isotopic splitting and hyperfine structure as needed

---

[1] During the referee process of this paper, additional results from observations taken with GPI were published by Crepp et al. (2018). The dynamical mass has been updated at $m_B = 65.3^{+4.4}_{-3.3}$ M_{Jup}.
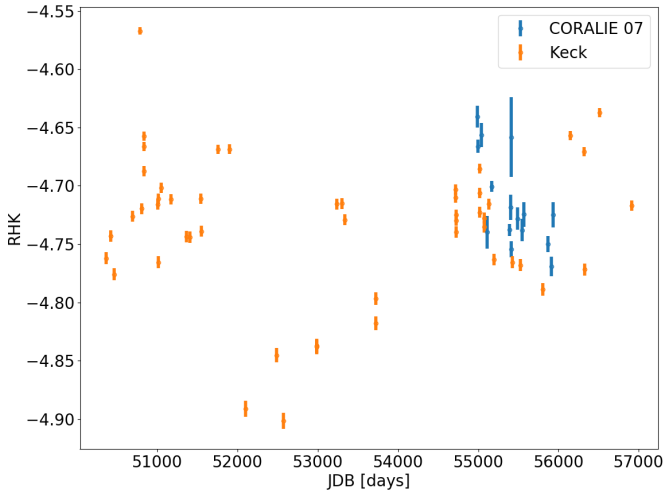[2] PI: Rolf Chini, Prog. ID 095.A-9029

Table 1: Spectroscopic parameters of HD 4747

T_{eff} [K]	log g [dex]	ξ [km s^{-1}]	[Fe/H] [dex]	v sin i [km s^{-1}]	Reference
5337±80	4.58±0.10	0.85±0.20	−0.25±0.07	2.3±1.0	Fuhrmann et al. (2017)
5347			−0.21		Mortier et al. (2013)
5422±75	4.61		−0.15		Casagrande et al. (2011)
5305	4.56		−0.24	2.1	Brewer et al. (2016)
5335	4.65		−0.22	1.1	Valenti & Fischer (2005)
5316±38	4.48±0.10	0.79±0.06	−0.21±0.05	0.79	Santos et al. (2005)
5340±40	4.65±0.06		−0.22±0.04	1.1±0.5	Crepp et al. (2016)
5400±60	4.60±0.15	0.75±0.20	−0.23±0.05	2.0±1.0	this paper

(see e.g., D'Orazi et al. 2012; D'Orazi et al. 2017). We have detected a modest enhancement in *s*-process element abundances, finding [Y/Fe]=+0.30±0.15, [Ba/Fe]=+0.35±0.20 dex and [La/Fe]=+0.20±0.12 dex. This might be in principle the signature of a weak contamination from a companion during the asymptotic giant branch (AGB) phase but no indication of the presence of a white dwarf companion at any separation was detected and the HD 4747B spectrum is not compatible with a white dwarf spectrum. Most importantly, we have also derived carbon abundance (pollution from low mass AGB stars results in enhanced C abundances), by synthesizing the CH band at 4300 Å: we have obtained a solar scaled abundance of [C/Fe]=0±0.13 dex, which points against the AGB pollution scenario. Moreover, when observation uncertainties are taken into account, the *s* process element abundances for HD 4747 are consistent with the scattered distribution as revealed from field stars (see e.g., Bensby et al. 2014).

A crucial information for the characterization of the low-mass companion HD 4747B is the stellar age. Literature shows quite discrepant values, due to different dating techniques employed. Indeed, as expected for a late G/early K dwarf close to main sequence, isochrone fitting allows only a poor constraint on stellar age (basically upper limits of about 7-9 Gyr). The spectrum shows no lithium, putting a lower limit to stellar age at about 700 Myr.

the CORALIE dataset described in Sect. 3.1, $\log R_{\text{HK}} = −4.718$ is obtained, with r.m.s. of 0.007 dex (see Fig. 1).

These values are intermediate between the activity levels of the Hyades and M67 open clusters and clearly above that of the Sun. The extension of the Keck dataset (50 epochs over almost 18 yr) ensures that intrinsic variability is averaged out. Using the age-$\log R_{\text{HK}}$ calibration by Mamajek & Hillenbrand (2008) an age of 2.3 Gyr is obtained. A very similar age, 2.1 Gyr, is obtained from X-ray emission (Katsova & Livshits 2011), when applying Mamajek & Hillenbrand (2008) calibration. On the basis of these results we favour an age of 2.3 Gyr with upper and lower limits of 0.9-3.7 Gyr as the activity level of HD 4747 is clearly distinct from the Hyades members one at the young side and from the Sun's one even at its maximum of the activity cycle at the old side. We also used the Mamajek & Hillenbrand (2008) calibration in order to compute the expected rotational period of HD 4747 and found $P_{\text{rot}} = 25.8 \pm 4.1$ days.

By looking at the periodograms of the $\log R_{\text{HK}}$ (Fig. 2a) we find a clear signal at 27.7 days. A signal is observed at the same period in the periodogram of the residual of the radial velocity data (Fig. 2b). We favor then a rotational period of $P_{\text{rot}} = 27.7 \pm 0.5$ days.

Fig. 1: log(R_{HK}) from the Keck and CORALIE data

(a) Periodogram of $\log R_{\text{HK}}$.

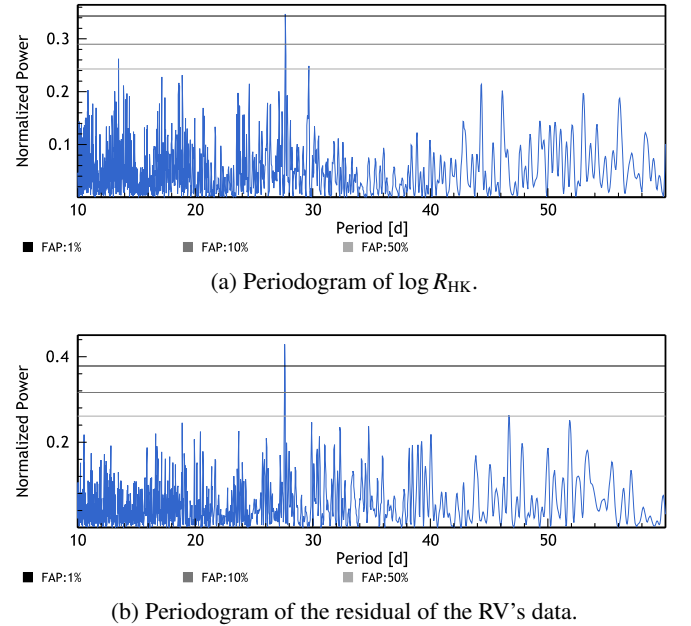(b) Periodogram of the residual of the RV's data.

Fig. 2: GLS periodogram (Zechmeister & Kürster 2009) of the $\log R_{\text{HK}}$ and the residu of the radial velocity data from the HIRES and CORALIE spectrographs (see Sect. 5 for the orbital parameters)[3].

The best constraints are derived from coronal and chromospheric emission. Using the Keck S index values as reported in Butler et al. (2017) and B-V from Hipparcos, we derived a median values of $\log R_{\text{HK}} = −4.725$ with a r.m.s of 0.023 dex. From

Table 2: Stellar parameters of HD 4747

Parameter	Value	Ref
V (mag)	7.15	Hipparcos
B−V (mag)	0.769±0.009	Hipparcos
V−I (mag)	0.82±0.02	Hipparcos
J (mag)	5.813±0.021	2MASS
H (mag)	5.433±0.049	2MASS
K (mag)	5.305±0.029	2MASS
Parallax (mas)	53.51±0.53	van Leeuwen (2007)
Parallax (mas)	50.37±0.55	Gaia Collaboration et al. (2016)
Parallax (mas)	51.94±1.57	Adopted for this paper
μ_α (mas yr^{-1})	516.92±0.55	van Leeuwen (2007)
μ_δ (mas yr^{-1})	120.05±0.45	van Leeuwen (2007)
μ_α (mas yr^{-1})	515.509±0.032	Gaia Collaboration et al. (2016)
μ_δ (mas yr^{-1})	125.472±0.031	Gaia Collaboration et al. (2016)
$T_{\rm eff}$ (K)	5400±60	this paper
log g	4.60±0.15	this paper
[Fe/H]	−0.23±0.05	this paper
$v \sin i$ (km s^{-1})	2±1	this paper
log $R_{\rm HK}$	-4.725	Keck
log $R_{\rm HK}$	-4.718	CORALIE
$P_{\rm rot}$ (days)	27.7±0.5	this paper
log $L_{\rm X}/L_{\rm bol}$	-5.52	Katsova & Livshits (2011)
EW Li (mÅ)	0	this paper
Age (Gyr)	2.3±1.4	this paper
$M_{\rm star}$ (M$_\odot$)	0.856±0.014	this paper
$R_{\rm star}$ (R$_\odot$)	0.769±0.016	this paper

Fuhrmann et al. (2017) noted that the kinematic parameters support membership in the Hyades stream but also the much lower metallicity of HD 4747 with respect to the Hyades. They also mention a possible inconsistency between the low metallicity and the activity level (moderately young age) and speculated about the possibility of accretion of angular momentum to make the star appearing younger (see D'Orazi et al. 2017, for a description of this mechanism in the case of GJ504). Conclusive proof that this mechanism is really at work in the case of HD 4747 is much challenging to obtain with respect to GJ504, because of the different main sequence lifetimes. However, to further shed light on this possibility, we investigated whether the age/metallicity obtained for HD 4747 is really peculiar using the extensive database of the Geneva-Copenhagen survey (Nordström et al. 2004). Exploiting the latest age and metallicity determination by Casagrande et al. (2011), we searched for stars with ages within our adopted upper limit for HD 4747 and metallicity within ±0.05 dex. Hundreds of objects were returned, typically F type stars, indicating that the age/metallicity combination of HD 4747 is not particularly unusual. Extended moving groups like the Hyades stream were also shown to host a mixture of stellar populations (Famaey et al. 2005), then HD 4747 is not particularly anomalous also from this point of view. We then conclude that, while accretion events altering the angular momentum evolution and then the age from activity cannot be firmly ruled out, there are no specific indications supporting that this kind of evolution affected our target. Therefore, we dismiss such an hypothesis and we adopt in the following the age from coronal and chromospheric activity.

The stellar mass was derived from isochrones using the PARAM web interface[4] (da Silva et al. 2006) isolating the age

---

range allowed by indirect methods (see Desidera et al. 2015). Our spectroscopic $T_{\rm eff}$ and [Fe/H] were adopted. The outcome is slightly dependent on the adopted distance. Hipparcos and Gaia DR1 distance are formally discrepant at more than 4 σ level, possibly due to the unaccounted orbital motion due to the brown dwarf companion[5]. Adopting the average of the two measurements, the stellar mass results in 0.856±0.014 M$_\odot$.

Finally, the star was observed with Spitzer and Herschel, resulting in no detectable IR excess (Gáspár et al. 2013). The stellar parameters are summarized in Table 2.
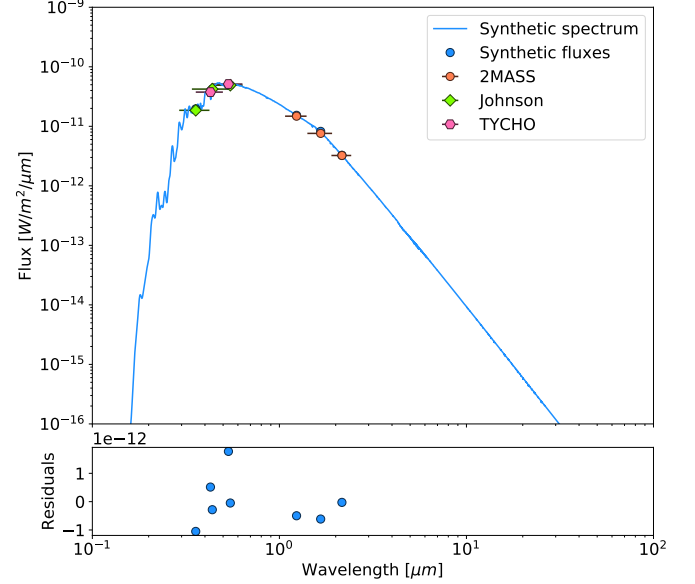

Fig. 3: BT-NextGen synthetic spectrum of HD 4747, scaled to match SED of optical and mid-infrared photometry

3. Observations

Radial velocity and direct imaging observations were combined to constrain the orbit of HD 4747B. The good orbital coverage of the radial velocity time series allows to constrain HD 4747B's period, minimum mass, eccentricity, argument of periastron ω and time of periastron passage T_0. Combined to the few direct imaging observations spread over ∼ 27% of the period we are able to retrieve both longitude of ascending node Ω and the orbit inclination i. In addition, the SPHERE direct imaging observations allow us to obtain a spectrum of the brown dwarf companion.

3.1. Radial velocity

HD 4747 has been observed since 1999 with the CORALIE spectrograph (Queloz et al. 2000) installed on the 1.2 m EULER Swiss telescope at La Silla observatory (Chile). Since its installation in 1998, CORALIE has undergone two upgrades (in 2007 and 2014) that introduced small RV offsets that vary from star to star. In the RV modeling procedure, we adjust the RV offsets corresponding to C98 for the data prior to 2007, to C07 for the period between 2007-2014, and C14 for the data acquired since 2014.
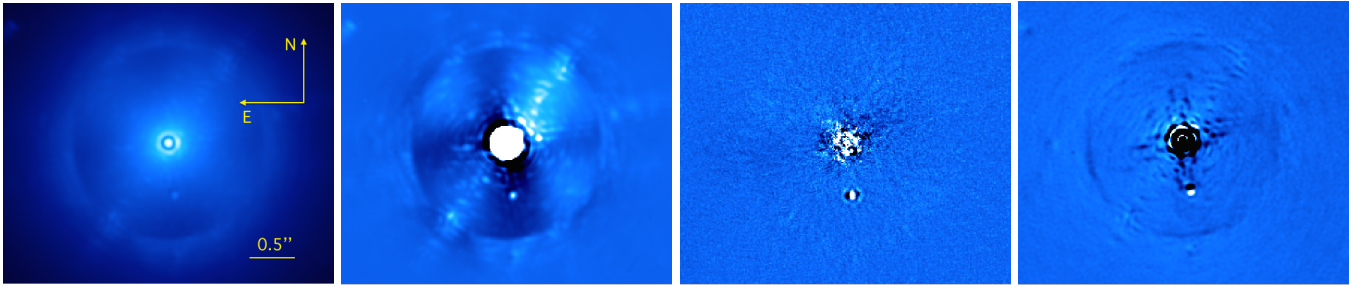
(a) IRDIS reduction using median combine only (b) IRDIS reduction using radial-profile subtraction (c) IRDIS reduction using ADI (TLOCI) (d) IRDIS reduction using SDI and simple derotation

Fig. 4: IRDIS different reductions of HD 4747. The companion is observed in each reduction. The north and east directions and the scale are indicated on the image (a).

We combined these data with observations conducted between 1996 and 2014 (Butler et al. 2017), with the High Resolution Echelle Spectrometer (HIRES) at Keck (Vogt et al. 1994). All of the observations have been taken with high signal to noise ratios, thanks to the relative brightness of the primary star (V=7.155). The high eccentricity ($e = 0.736 \pm 0.002$) of the companion and the fact that we have the periastron passage with the HIRES observations, together with the very long time spanned (20 years) and the high precision of the data allow us to constrain very well the orbital elements, even if the orbit is not complete (57% of the complete orbit is covered).

3.2. Direct imaging

HD 4747 was observed on the 12th of December 2016 and the 28th of September 2017 as part of SHINE (SpHere INfrared survey for Exoplanets). SPHERE (Spectro-Polarimetric High-contrast Exoplanet REsearch; Beuzit et al. 2008), is an extreme adaptive optics system (Fusco et al. 2014) installed on the VLT in Paranal (Chile). We used SPHERE in its IRDIFS-EXT mode which consists in two instruments working simultaneously, a dual-band imager and spectrograph (IRDIS; Dohlen et al. 2008), and an integral field spectrograph (IFS; Claudi et al. 2008). We used IRDIS in the dual band imaging mode (DBI; Vigan et al. 2010) in K12 ($\lambda^c_{K1} = 2.103$ μm, $FWHM_{K1} = 0.102$ μm; $\lambda^c_{K2} = 2.255$ μm, $FWHM_{K2} = 0.109$ μm), and IFS in YH band ($0.95 - 1.65$ μm, average spectral resolution per FWHM, R=29). As HD 4747 has a declination very close to the Paranal's latitude, the star passes almost at the zenith. This results in a small field rotation in our observation ($7.3°$), but thanks to the moderate contrast of the companion in the infrared ($\Delta K_1 = 9.11 \pm 0.15$), we managed to extract the spectrophotometry and astrometry from our data with a very high accuracy (see Sect. 6).

The observations were done using the standard SHINE strategy. The data sequences consist then of the science coronagraphic observations in IRDIFS-EXT mode with DIT=32s, followed by a star centering dataset with same DITs and with the satellite spots, induced by the deformable mirror, activated in order to recover the position of the star behind the coronagraph (Langlois et al. 2013). Then a flux calibration dataset was produced with DIT=2 s, with the star offset from the coronagraph, and a neutral density filter (ND_2.0) in order to prevent saturation. A set of sky frames have also been taken just after the sequence. The rest of the calibrations (flats, darks and spectral calibrations) were done after the end of the night with the instrument internal calibration hardware. The astrometric calibration (True North and pixel scale) was done on sky with the SPHERE GTO standard procedure (Maire et al. 2016b). The 2017 epoch was done in the same way as the 2016 but with a shorter coronagraphic sequence as it was mainly aiming to better constrain the orbit.

3.3. Archival NACO observation

An archival NACO dataset from the 7th of september 2008 was also reprocessed to search for and possibly retrieve the separation and position angle of the companion. It was taken in the SDI+4 mode (Maire et al. 2014) which combines the SDI mode of NACO with a four quadrant phase mask coronagraph (Boccaletti et al. 2004). The data was taken in the "double roll subtraction" procedure[6] with 5° of rotation offsets every 5 images, in order to subtract the speckles linked to pupil aberrations. We obtained a field rotation of 95°, using a single frame DIT of 30 s for a total observing time of 3 hours and 20 minutes.

4. Direct imaging data reduction, astrometry and spectrophotometric extraction

The data reductions were performed with three different pipelines, namely, the GRAPHIC pipeline (Hagelberg et al. 2016), the LAM-ADI pipeline (Vigan et al. 2015, 2016) and a reduction from the SPHERE Data Center (DC) using the SPHERE Data Reduction and Handling (DRH) automated pipeline (Pavlov et al. 2008) for the standard cosmetic and the SpeCal pipeline for the post-processing (Galicher et al., in prep). Different types of analysis were also conducted with these pipelines, to compare and take the full advantages of each of them and extract the astrometry and spectra of HD 4747B with the best accuracy. We built the SED of the host star (Fig. 3) based on a BT-NextGen model (Allard et al. 2012), and using VOSA (Bayo et al. 2008) to extract the photometry of the primary in the different band filters and find the best fit. All three pipelines gave similar results with astrometric and photometric standard deviations respectively 66% and 50% smaller than the error bars given hereafter.

---

[6] See NACO manual for Period 81 and 82:
https://www.eso.org/sci/facilities/paranal/
instruments/naco/doc/VLT-MAN-ESO-14200-2761_v81-2.pdf

(a) 25° double roll subtraction angle model

(b) 10° double roll subtraction angle

(c) 25° double roll subtraction angle

(d) Median χ^2 map over double roll subtraction angles. The cross shows the minimum χ^2 and so the position of the companion.
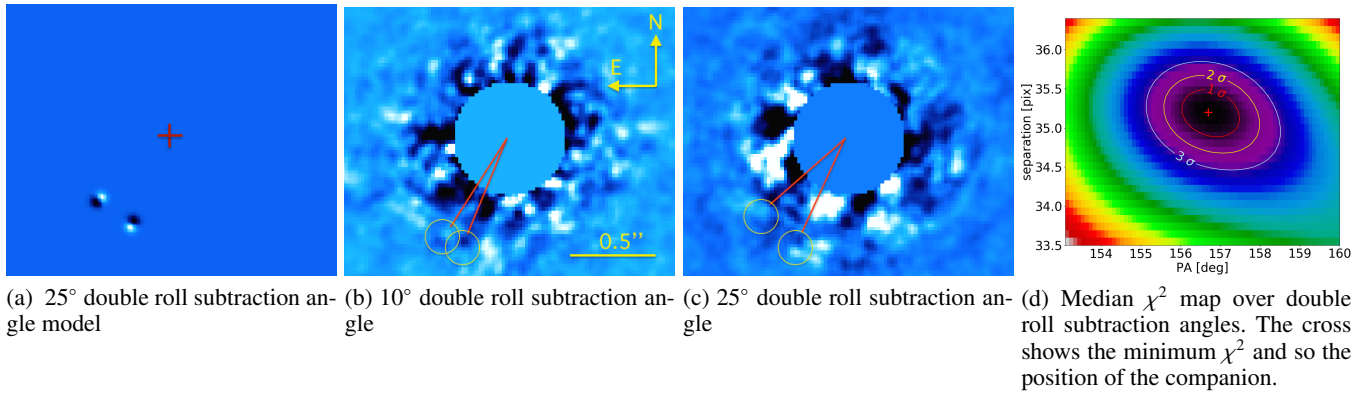
Fig. 5: NACO final images after SDI and double roll subtraction applied for different angles (5°, 10°, and 25°), and final χ^2 map of separation versus position angle.

4.1. IRDIS data reduction

We processed the IRDIS data with several algorithms, angular differential imaging (ADI), spectral differential imaging (SDI) and radial-profile subtraction (Fig. 4). With the small separation ($\rho \simeq 600$ mas) and field rotation (Sect. 3.2), the ADI and SDI self-subtraction are substantial. However the companion has a small contrast with respect to its host star in K12 (~9 mag) and is visible in the raw frames. We therefore decided to use a simple median combination of the frames with a background fit (Fig. 4a) for the photometry extraction in K_1 and K_2 and obtained magnitude contrasts of $\Delta K_1 = 9.11 \pm 0.15$ and $\Delta K_2 = 9.24 \pm 0.15$. The error bars take into account the error on the PSF fit as well as the variations of the PSF and speckle noise through the observational sequence. We derived then from the SED of the primary its flux in each filter, and finally extracted the flux of HD 4747B (Fig. 6).
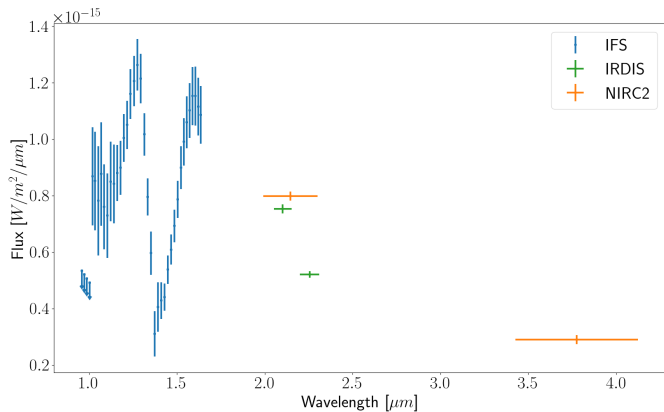
Fig. 6: Extracted spectrophotometry of HD 4747B. The blue points are SPHERE IFS data, the green and yellow ones are respectively IRDIS SPHERE and NIRC2 photometry. The NIRC2 data are taken from Crepp et al. (2016). The horizontal errorbars represent the width of the IRDIS and NIRC2 filters.

The astrometric extraction was done using a simple radial-profile subtraction (Fig. 4b), as it allows to increase the signal to noise ratio and it does not strongly affect the shape of the companion point spread function (PSF). The derived separations and position angles are listed in Table 3. The error bars given in the table include astrometric calibration errors that were quadratically added to the results of the adjustment.

4.2. IFS data reduction and spectral extraction

We used a TLOCI-ADI reduction to extract the IFS photometry (Marois et al. 2014, Specal implementation used), which was optimized for getting the best contrast in each wavelength with the least possible impact on the spectrum of the companion. The contrast in each wavelength channel is computed by injecting fake companions before the ADI processing. This allows to account for the self-subtraction effect from the ADI reduction. The apparent spectrum of the companion is then extracted with the same procedure as for the IRDIS data, by computing the primary flux in each channel given its SED. The extracted spectrum is shown in Fig. 6.

4.3. NACO data reduction and astrometric extraction

We reduced the NACO data following the standard data processing, bad-pixel cleaning, subtraction of sky and division by flats. The SDI sub-images were extracted and re-centered by adjusting a simple Gaussian profile to the wings of the primary star. We performed a frame selection based on the integrated flux of each image. Images with a flux higher than the median value are rejected, which allows to remove frame taken with lower seeing conditions and/or AO performances. The shorter wavelength images are resized by a factor $\lambda1/\lambda2$ and centered by the cross-correlation to the longer wavelength images. For each time step, the images taken at different wavelengths are subtracted. Images with the same derotator angle are co-added using their median value.

Finally, different sets of double roll subtractions are performed to remove residual pupils aberrations and to amplify the companion signature. For instance, we subtracted every image pair that have a pupil rotation offset of 10°, *ie.* Im(10°) − Im(0°), Im(15°) − Im(5°), ... , Im(95°) − Im(85°) and median combined them. We did the same on image pairs with 5°, 15°, 20°, and 25° pupil rotation offsets. This data analysis technique affects the companion signature in the final image, which is composed of 4 duplicated PSF as shown on Fig. 5a. The SDI part of the algorithm results in the radial positive/negative part of the companion signature, while the double roll subtraction duplicates the SDI pattern with the chosen rotation offset. We found that the 10° pupil rotation offset performs the best in term of noise reduction and signal amplification (see Fig. 5b) which allow us to detect HD 4747B in the archived NACO data. We retrieved the companion astrometry and corresponding confidence intervals
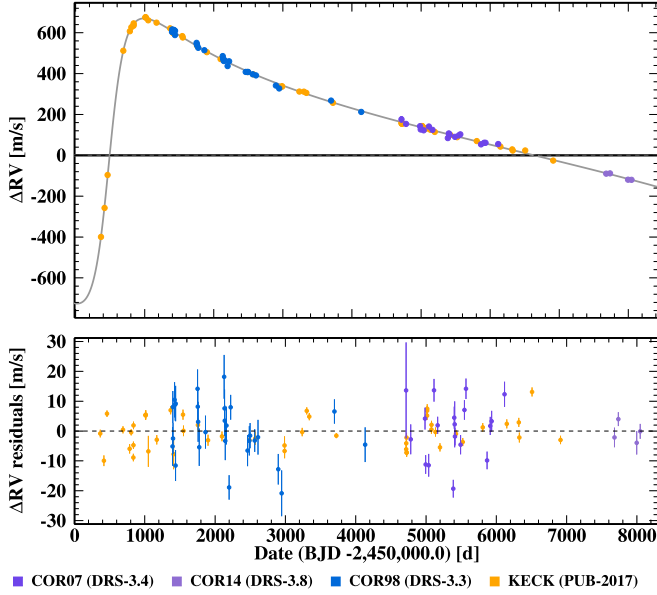
Fig. 7: Radial Velocity measurements for HD 4747 taken with the Keck-HIRES and CORALIE spectrographs. The different versions of CORALIE are indicated with different colors. The best fit model from the combined MCMC analysis with direct imaging is marked with the grey line.

by modelling the expected companion pattern and computing a χ^2 map for different companion's separations, position angles and flux ratio. A clear minimum in the χ^2 map is seen at the expected position of the companion as illustrated on Fig. 5d. Each individual full χ^2 maps for the different double roll subtraction angles are shown in Fig. A.1, while Fig. A.1f and Fig. 5d show the median (See Appendix A for more details about this analysis).

Deriving reliable confidence intervals for these archived data is also a challenging task. We computed the noise of the image for each separation using the standard deviation in annulus of 1 pixel width. This noise map was used to compute the χ^2 map and the 1,2 and 3 σ confidence intervals (see Fig. 5d). As the center of the star is difficult to determine behind the coronagraph, we decided to add quadratically a systematic error of 4 mas on the separation measurement, which corresponds to a quarter of a pixel. As no astrometric field was observed during this run with NACO, and no calibration could be found for the SDI+4 mode's pixel scale, we took the NACO manual value of 17.32 mas/px. We quadratically added an error of 0.05 mas/pixel to the budget value, which corresponds to an error of 1.8 mas at the separation of the companion. For the True North, we used the calibration from Ehrenreich et al. (2010) that was taken on the 20th of august 2008, 18 days before our dataset. The true north of NACO was at a $0° \pm 0.2°$ angle. We quadratically added an uncertainty of $0.5°$ as the detector could have moved slightly between the runs.

At the end, an angular separation of $\rho = 608 \pm 11$ mas and a position angle of $PA = 156.4° \pm 1.3°$ are retrieved.

We decided to not use the photometry of this data set. The detection is indeed at the noise limit, and the flux strongly polluted by the self-subtraction of both SDI and the double roll subtraction. Moreover, the filters are redundant with the SPHERE IFS channels and no PSF calibration flux were correctly done.
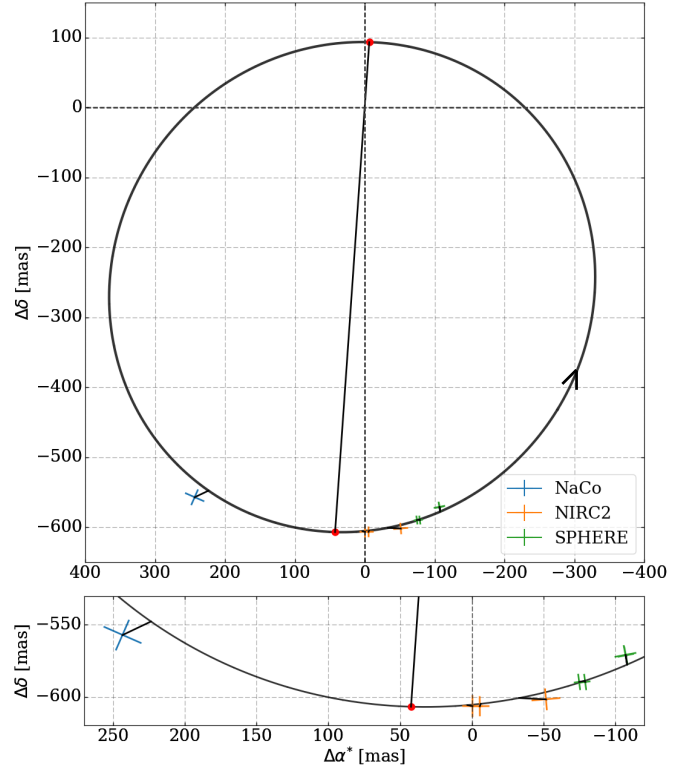
Fig. 8: Relative orbit of the HD 4747AB system. The black curve corresponds to the maximum likelihood of the combined RV and direct imaging MCMC analysis. The NaCo data point is shown in blue, the NIRC2 K_s and L' observations from Crepp et al. (2016) in yellow, and the SPHERE ones in green. The arrow shows the orbit rotational direction and the red dots show the apastron and periastron.

Table 3: Measured astrometry and contrast of HD 4747B from SPHERE (K_1 and K_2) and NACO (H, SDI mode) data.

Filter	Date (UT)	ρ (mas)	PA (deg)	Contr. (mag)
K_1	12.12.2016	594.4 ± 5.1	187.2 ± 0.3	9.11 ± 0.15
K_2	12.12.2016	595.0 ± 5.1	187.6 ± 0.3	9.24 ± 0.15
K_1	28.09.2017	581.2 ± 5.8	190.6 ± 0.5	-
K_2	28.09.2017	580.8 ± 6.3	190.6 ± 0.7	-
H	07.09.2008	608 ± 11	156.4 ± 1.3	-

5. Orbital analysis and dynamical mass estimation

We performed an MCMC analysis combining all radial velocity data available (see Sect. 3.1 and Fig. 7) with our direct imaging SPHERE epochs (see Sect. 4 and Fig. 8), the epochs from Crepp et al. (2016) and the NACO SDI+4 archival data point (See Sect. 4.3). This epoch allows us to constrain strongly the orbital parameters thanks to the much longer time baseline. The MCMC simulation was performed by using *emcee* (Foreman-Mackey et al. 2013), a python implementation of the affine-invariant ensemble sampler for MCMC proposed by Goodman & Weare (2010). The data are modeled with a Keplerian and 4 RV offsets (one for HIRES, and 3 for the different versions of CORALIE: C98, C07, C14). The noise in the radial velocity data is modeled with a nuisance parameter for each instrument. As we have direct imaging and radial velocity measurements, the parallax and mass of the primary are parameters that can be constrained with the fitting. We introduce these two parameters

with Gaussian priors taken from Table 2. More details about the MCMC orbital analysis are presented in Appendix B. The results of the orbital fit are presented in Table 4, Fig. B.1 and B.2.

Table 4: Orbital parameters from the maximum likelihood

Parameters	Values (1σ)
P [yr]	33.08 ± 0.70
K [m/s]	698.0 ± 10.4
ecc	0.7320 ± 0.0023
ω [deg]	-93.10 ± 0.47
T_0 [bjd]	50473.9 ± 5.2
Ω [deg]	89.9 ± 1.4
i [deg]	46.3 ± 1.1
$m\sin(i)$ [M_{Jup}]	50.7 ± 1.8
$m_1 + m_2$ [$M_\odot$]	0.918 ± 0.037
m_2 [M_{Jup}]	70.2 ± 1.6
a [au]	10.01 ± 0.21

Compared to the orbital solutions found by Crepp et al. (2016), we find significant differences in the results of our MCMC analysis. The period $P = 33.08 \pm 0.70$ yr is in good agreement with Sahlmann et al. (2011b), but disagrees with the Crepp et al. (2016) value at 6σ. The high eccentricity predicted in Sahlmann et al. (2011b) and confirmed by Crepp et al. (2016) is verified, $e = 0.7320 \pm 0.0023$, even if our value is slightly smaller. The inclination of $46.3° \pm 1.1°$ derived leads to a semi-major axis of $a = 10.01 \pm 0.21$ au and a mass estimation for HD 4747B of $m_B = 70.2 \pm 1.6 M_\odot$. This inclination is smaller by 3σ than the value from Crepp et al. (2016). This explains the difference in the mass measurement. The discrepancy between our orbital parameters and those of Crepp et al. (2016) likely arises from the Keck 2015 L' band measurement. This datapoint is off by more than 1σ and with more epochs, our fit is less sensitive to individual outliers.

6. Spectrophotometric analysis

6.1. Color-magnitude diagram

From the IRDIS K1 and K2 observations the color-magnitude diagram of HD 4747B shows a late L spectral type (Fig. 9). This is in good agreement with the prediction of Crepp et al. (2016), which used the broad bands Ks and L' filters from the NIRC2 camera at the Keck Telescope. HD 4747B falls close to the HR8799 c,d and e planets on the diagram and at the L-T transition.

6.2. Known standards comparison

To further constrain the spectral type of HD 4747B, a comparison of standard near-IR spectra of L1 to T8 known objects from the SpeX Prism Library (Burgasser 2014) was done. To do so we made use of the *splat* python package (Burgasser et al. 2016). Each standard spectrum is first normalized in flux and then calibrated to match the extracted data of HD 4747B. The fitting of each standard spectrum (F_k) on the one of HD 4747B (f) is done by comparing the goodness of fit:

$$\chi^2 = \sum_{i=1}^{n} \left(\frac{f_i - C_k F_{k,i}}{\sigma_i} \right)^2 \tag{1}$$
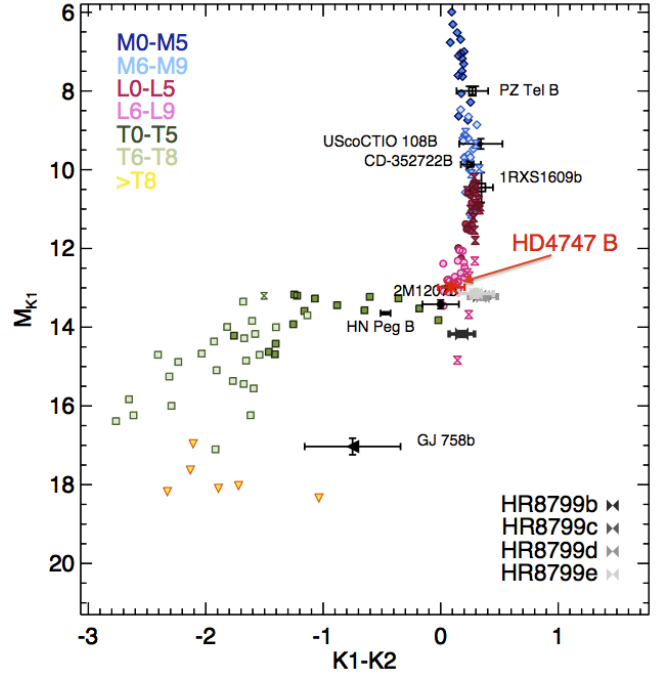
Fig. 9: Color-magnitude diagram of HD 4747B from the IRDIS K1 and K2 observations. Other known objects are shown for comparison.

where C_k is the flux scaling factor. Each standard spectrum was binned to the appropriate spectral resolution of the IFS measurements with a Gaussian convolution. We decided to use a FWHM of 1.5 times the separation between each wavelength in order to take into account the correlation between the IFS channels. The IRDIS fluxes were estimated by using the transmission curves of the K1 and K2 filters. The L' NIRC2 observation was not used as the spectra from this library stop in the K band. Fig. 10 shows the fitting results for the L8, L9 and T0 standards. The best fit corresponds to the L9 dwarf DENIS-P J0255-4700 (Burgasser et al. 2006) and matches the IFS and IRDIS data well. This is in good agreement with the color-magnitude diagram (Fig. 9). Crepp et al. (2016) derived also a late L type but a higher effective temperature of $T_{eff} = 1700 \pm 100$ K. This led them to a model dependent mass higher than in this study.
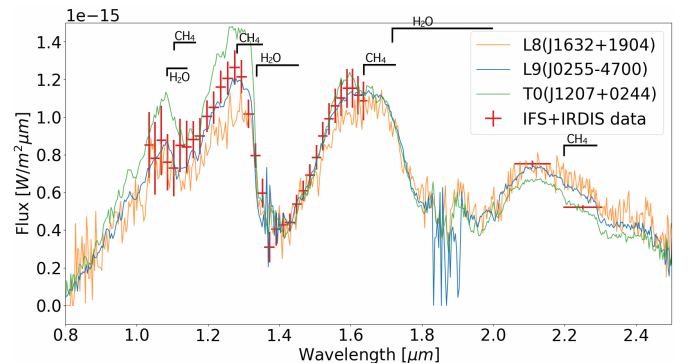

Fig. 10: Adjustments of standard known objects showing L8 (J16322911+1904407; Burgasser 2007a), L9 (J02550357-4700509; Burgasser et al. 2006) and T1 (J12074717+0244249; Looper et al. 2007). The best fit is done by the L9 object. The molecular absorption bands of CH_4 and H_2O are indicated.

6.3. Atmospheric forward modeling: Exo-REM

We characterized the observations with the forward model Exo-REM (Baudino et al. 2015, 2017) using grids of synthetic models generated with a T_{eff} between 400 and 1800 K (with a step of 50 K), a $\log(g[cgs])$ between 2.5 and 5.5 (with a step of 0.5), a diversity of clouds (without cloud, or with τ_{ref}=0.5 or 1, see in Baudino et al. 2015), a metallicity z = -0.2, 0, 0.5, 1.0 and taking account of the equilibrium chemistry or non-equilibrium chemistry (with a $k_{zz} = 10^8$ cm^{2}s^{-1}, see Baudino et al. (2017), for the non-equilibrium chemistry formalism). The parameters of the best model is summarized in Table 5 and the best fit spectra are shown Fig. B.3. The maximum mass at 1σ computed from the gravity and radius derived with Exo-REM is only 14.6 M_{Jup}, which is far below the dynamical mass measurement. The difference between the results with Exo-REM and the dynamical mass can be explained by the difficulty to generate the more extreme surface gravity with this model (built for giant planets, i.e. low gravity objects). HD 4747B is indeed the most massive brown dwarf studied with Exo-REM and is at the gravity limit available with this model.

Table 5: Results of the forward modeling Exo-REM at 5σ detection for HD 4747B

Parameter	Values
T_{eff} (K)	1300 ± 100
$\log(g)$ (dex)	4 ± 0.5
Cloud condition	cloudy
Chemistry	no conclusion
Radius (R_{Jup})	0.91 ± 0.16
Metallicity (solar)	0.63-1

6.4. Atmospheric retrieval modeling: HELIOS-R

For this analysis we used the atmospheric retrieval code HELIOS-R developed by Lavie et al. (2017). Atmospheric retrieval is a technique borrowed from the Earth remote sensing community. Some pieces of the atmospheric physical model are parametrised (i.e. Temperature-pressure profile, clouds etc.). It sacrifices self-consistency in order to speed up computational time, which in return allows for a more robust parameter space exploration and a better characterization of the uncertainties on the model parameters.

HELIOS-R allows for a direct comparison of different 1-dimensional emission forward model using the Nested Sampling algorithm (Skilling 2006). The model parameters and their priors are presented in Table 6. As in Lavie et al. (2017), we assume independent Gaussian errors so the likelihood takes the form of equation 2:

$$\mathcal{L}(D|M_i, \theta) = \prod_{k=1}^{N} \frac{1}{\sigma_k \sqrt{2\pi}} exp\left(-\frac{[D_{k,obs} - D_{k,model}]^2}{2\sigma_k^2}\right), \qquad (2)$$

where $D_{k,obs}$ is the k-th observational data point, $D_{k,model}(\theta)$ the model prediction for this data point given the parameters θ, σ_k the uncertainty of the k-th observational data point, and N the total number of data points. This approach does not account for covariances in the IFS data.

The models assume an Hydrogen/ Helium dominated atmosphere and include the four main absorbers in the infrared: carbon monoxide (CO), carbon dioxide (CO_2), water (H_2O) and methane (CH_4). Two sets of assumptions can be made regarding the atmosphere chemistry : equilibrium chemistry where the

two parameters are the carbon (f_c) and oxygen (f_o) abundances; and unconstrained chemistry where the parameters are the four molecules abundances assumed to be constant throughout the vertical 1D atmosphere. Clouds are modeled using a three parameter model, first introduced in Lee et al. (2013). See Lavie et al. (2017) in order to get more insight on HELIOS-R.

6.4.1. Companion mass, gravity and radius priors

As discussed in Lavie et al. (2017), retrieving the surface gravity and radius of directly imaged objects is challenging. With the current number of atmospheric data (spectrum and photometry) and their uncertainties, it is impossible with an atmospheric retrieval technique to constrain the surface gravity at the same level of precision as with the radial velocity data. In the case of HD 4747B, velocity data are available. This valuable information need to be taken into account in the atmospheric Bayesian analysis. We have updated HELIOS-R in order to take the companion mass as a parameter of the model. The mass, surface gravity and radius are linked by the following equation :

$$M_{comp} = g * R_{comp}^2 / G \qquad (3)$$

The companion mass constrained by the radial velocity can now be enforced in our prior in a straightforward manner. There is no direct measurement of the radius on this object as it does not transit. Consequently, our prior should reflect our current state of knowledge on the radius of brown dwarfs. The evolutionary track (e.g. Baraffe et al. 2003) gives a radius of 0.9 R_{Jup} for HD 4747B. However, there is not a unique mass-radius relationship for a given brown dwarf depending on what one assumes in the models (Burrows et al. 2011). Konopacky et al. (2010) showed as well that traditional evolutionary tracks are missing physics or chemistry. Observations of transiting brown dwarfs show that those objects have radii from ~0.8 to 1.2 R_{Jup}. We therefore set our prior as a Gaussian prior of R = 1.0 ± 0.1 R_{Jup}[7].

6.4.2. Results and discussion

The main output of the Nested Sampling algorithm is the Bayesian evidence, which allows the models comparison through the computation of the Bayes factor ($\mathcal{B}$). We considered four different models : equilibrium chemistry without cloud (EB) or with clouds (EC) and unconstrained chemistry without (UB) or with clouds (UC). For the models with unconstrained chemistry, we also considered all the different combinations of molecules in order to evaluate the significant of each molecules detection. Fig. 11 shows the Bayesian evidence for most of the models considered. Models with clouds are strongly preferred over the models without clouds, which indicates that this object is probably cloudy. The unconstrained chemistry model with clouds is the preferred model. The Bayes factor between this model (including all the molecules) and the models excluding some molecules indicate that CO_2 and CH_4 are only weakly detected ($\ln \mathcal{B} < 2.5$), while H_2O is strongly detected ($\ln \mathcal{B} > 5$). We have a low sensitivity to CO, since including it or not in the model does not change the constraints on the other parameters and does not improve the fit to the data. See also Trotta (2008) for a correspondence between the Bayes factor (B) and the significance in terms of the number of standard deviations. A

---

[7] This gaussian prior takes into account the 0.8 to 1.2 R_{Jup} distribution at 2σ.

Table 6: Parameters and Priors Used in the Retrieval analysis

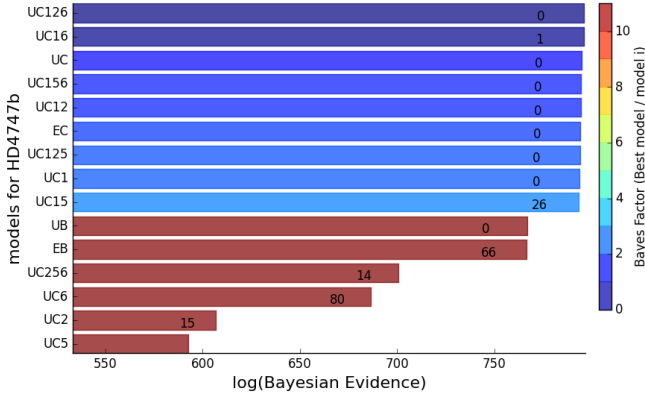| Parameter	Symbol	Prior Used	Value
Radius	R	Gaussian	$R_{comp} = 1.0 \pm 0.1$ R_{Jup}
Planet mass	M_{comp}	Gaussian	70.2 ± 1.6 M_{Jup}
Molecules abundances or elemental abundances	X_i, f_i	Log-uniform	10^{-15} to 10^{-1}
Longwave/infrared opacity (TP profile)	κ_0	Log-uniform	$\log \kappa_0 = 10^{-15}$ to 10 (mks)
Internal/interior temperature (TP profile)	T_{int}	Uniform	100 to 2300 K
Extinction coefficient	Q_0	Uniform	1 to 100
Cloud particles size	r_c	Log-uniform	10^{-7} to 10^{-3} m
Cloud particle abundance	f_{cloud}	Log-uniform	10^{-30} to 10^{-4}
Distance	d	Gaussian	19.25 ± 0.58 pc

Fig. 11: Bayes factors from a suite of models for HD 4747B. Four models were considered: equilibrium chemistry without cloud (EB) or with clouds (EC) and unconstrained chemistry without (UB) or with clouds (UC). The numbers associated with each model's name indicate the molecules included (1: H_2O, 2: CO_2, 5: CO and 6: CH_4); if there are no numbers then all four molecules are included. The Bayesian evidence clearly favors models with clouds and the most favored model is unconstrained chemistry including H_2O, CO_2 and CH_4. The number associated with each histogram is the logarithm of the Bayes factor between the model in question and its neighbor below. The color bar shows the logarithm of the Bayes factor between the model in question and the best model, which is the model placed at the top.

Table 7: Summary of Retrieved Results.

Property	Value
X_{H_2O}	$-3.57^{+0.07}_{-0.07}$
X_{CO_2}	$-6.13^{+1.92}_{-5.11}$
X_{CO}	$-9.65^{+3.28}_{-3.08}$
X_{CH_4}	$-4.62^{+0.25}_{-0.43}$
Q_0	$0.88^{+0.58}_{-0.50}$
r_c [m]	$-4.57^{+0.86}_{-0.73}$
X_c	$-21.00^{+1.32}_{-1.56}$
d [pc]	$19.56^{+0.35}_{-0.41}$
M_p [M_{Jup}]	$70.09^{+1.25}_{-1.21}$
R_p [R_{Jup}]	$0.85^{+0.03}_{-0.03}$
μ	$2.20^{+0.00}_{-0.00}$
C/O	$0.13^{+0.14}_{-0.08}$
C/H	$-4.72^{+0.47}_{-0.39}$
O/H	$-3.79^{+0.16}_{-0.08}$
$\log g$ [cgs]	$5.40^{+0.03}_{-0.03}$

Notes. We have listed the 1σ uncertainties, which were computed by locating the 15.87th and 84.13th percentile points on the horizontal axis. In the limit of a symmetric Gaussian function, these would yield to its fwhm. The mean molecular weight is given at 1 bar. Values are in $\log_{10}$ (except for C/O, d, M_p, R_p and μ) and dimensionless (except when units are shown).

summary of the retrieved parameters for the UC model (including all the molecules) is shown in Table 7, the best fit spectrum and temperature profile are shown in Fig. C.2 and the posterior distribution of each parameters are shown in Fig. C.3.

The dimensionless cloud parameter Q_0 serves as a proxy for the cloud composition. It is not possible to determine the composition as the posterior distribution is too broad and encompasses the refractory species composition (e.g., silicates - $Q_0 \sim 10$) and the volatile species composition (e.g., ammonia, methane, water - $Q_0 \sim 40$-80). However, the posterior distribution of the clouds particle size indicate that the cloud is composed of big particles, which will act as a constant absorbers as a function of the wavelength (Lavie et al. 2017).

The retrieved posterior distribution of the companion mass reflects our prior, which is normal as the radial velocity data (used to build our prior) provide a better constrain on this parameter than the spectrum. With the retrieved companion radius (0.85 R_{Jup}) and mass we are able to compute the surface grav-

ity of the companion using Eq. 3, which indicates a high gravity object ($\log g = 5.40$ cgs).

We have measured oxygen abundances by exploiting the O I triplet at 7771-7775 Angstroms, and applying 3D NLTE corrections by Amarsi et al. (2015), as done in D'Orazi et al. (2017). We have found a slight over-abundance being [O/Fe]=+0.16±0.08 dex. Considering our carbon abundance estimation given in Sect. 2, we obtained C/O=0.417. Using the retrieved molecular abundances, it is possible to derive the carbon to oxygen (C/O), the carbon to hydrogen (C/H) and the oxygen to hydrogen (O/H) ratios. The retrieved values are shown in Table 7. Fig. 12 shows a comparison of those values with the HR 8799 system from Lavie et al. (2017), where the data comes from Bonnefoy et al. (2016); Zurlo et al. (2016). Those values can be compared to the stellar abundance, which are $10^{-3.82}$ and $10^{-3.44}$ for carbon and oxygen respectively, derived from the results of Section 2.

The interest for C/O, C/H and O/H ratios lie in the implications for planet formation. Öberg et al. (2011) previously outlined a first order scenario based on the position of the different snow lines. The core accretion scenario is a multi-step process that will result in a broad-range elemental composition depend-
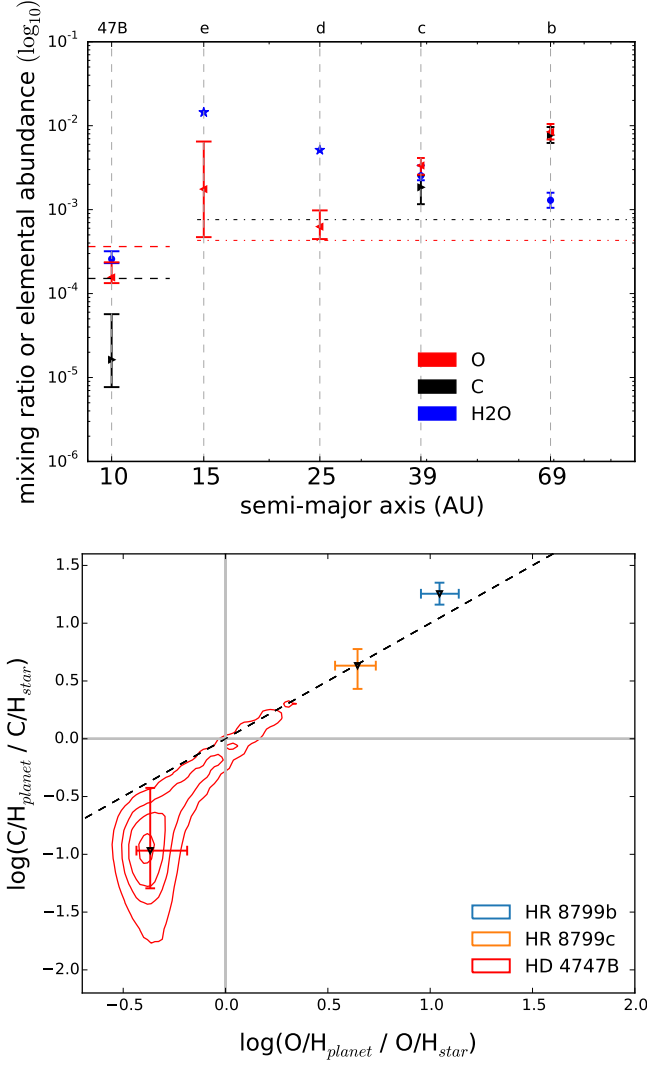
Fig. 12: Results from the atmospheric retrieval analysis. The top panel shows the retrieved water mixing ratios and elemental abundances of carbon and oxygen for HD 4747B as well as the four HR 8799 exoplanets as a function of the distance to the host star. For HR 8799d and e, we show the water abundance in chemical equilibrium at 1 bar (represented by the blue stars). The carbon abundance retrieved for these two planets is very small and is not shown on this figure, see Fig C.4. The carbon and oxygen abundances of the stars are shown with the dashed lines (HD 4747) and dashed dot lines (HR 8799). The bottom panel shows the companion elemental abundances normalized to its stellar values with the dashed black line denoting parity.

ing on the position of the object during those different steps. The HR 8799 planets are compatible with such a scenario. On the other hand a gravitational instability scenario is a quick one step process, which will form a companion with a similar composition to the host star formed from the same protoplanetary disk. Our retrieved values for HD 4747B are compatible within one sigma to the host star, which indicates that both scenarios are possible. However, the relative low mass of the star and the companion high mass indicate that a core accretion scenario would be difficult. It is therefore very likely that this system has formed like a binary system. More observations, especially spectroscopical one in the K-band to constrain the carbon abundance (Lavie

et al. 2017), are requested to confirm this scenario through the atmospheric retrieval analysis.

6.5. BT-Settl model comparison

To compare the Exo-REM forward modeling and HELIOS-R retrieval with evolutionary models, we used the BT-Settl atmospheric models (Allard et al. 2011), that are combined with the BHAC15 evolutionary tracks (Baraffe et al. 2015). This model is well suited to analyse objects that are at the L-T transition such as HD 4747B. We compared our extracted spectrum to model spectra with T_{eff} from 1200 K to 1700 K (with steps of 50 K), with a $\log(g)$ from 4.0 to 5.5 (steps of 0.5) and a metallicity of +0.5, 0.0 or -0.5. The four best fitting spectra (binned by a factor of 1000) are shown in Fig. 13. The results point towards a temperature $T_{\mathrm{eff}} = 1300 - 1400$ K, $\log(g) = 5.0 - 5.5$ and a metallicity between 0.0 and -0.5. The temperature agrees well with the result from the standard-objects fitting and Exo-REM forward modeling. The gravity is in good agreement with the HELIOS-R retrieval code. The metallicity is in good agreement with the metallicity of the host star ([Fe/H]= -0.23 ± 0.05, see Table 2), even if a thinner grid would be needed to constrain correctly this parameter.
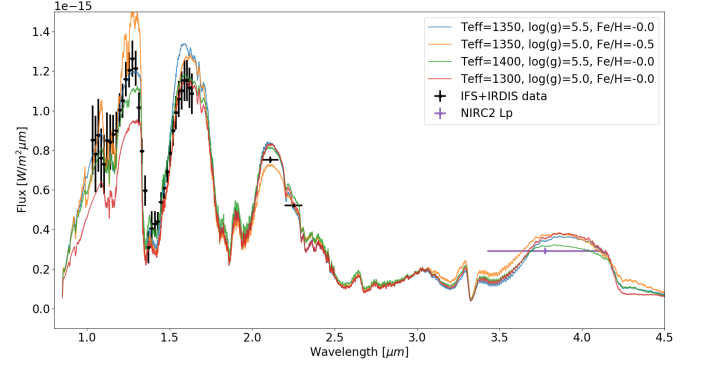
Fig. 13: Four best-fit spectra from the BT-Settl models (Allard et al. 2011) in order from the top (best) to the bottom (less good). The adjustment was done on a grid of T_{eff} from 1200 K to 1700 K, with a $\log(g)$ from 4.0 to 5.5 and a metallicity of +0.5, 0.0 or -0.5. The results are coherent with a $T_{\mathrm{eff}} = 1300 - 1400$ K, $\log(g) = 5 - 5.5$ and [Fe/H]= $0.0/ - 0.5$.
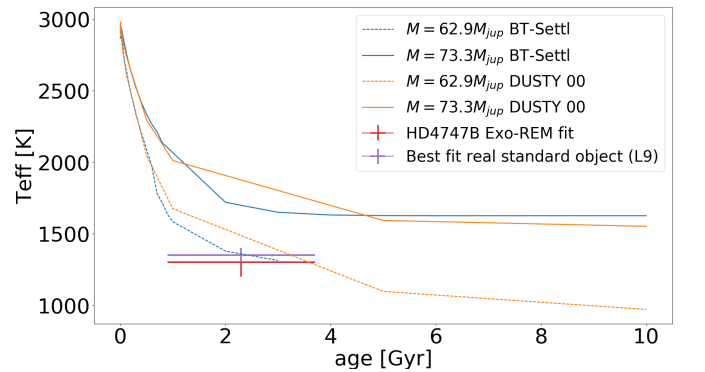

Fig. 14: Comparison between evolutionary models (BT-Settl Allard et al. 2011), real standard objects and the Exo-REM forward modeling. The predictions from the DUSTY model (Chabrier et al. 2000) are also shown. The evolutionary models seem to underestimate the cooling rate of the sub-stellar objects.

We observe that the peak at 1.2-1.3 μm is not well fitted by the BT-Settl models, despite the good match found when comparing with the spectra of standard objects. It could mean that the opacity at this wavelength is not perfectly computed in these models, or that the grid of spectra we used is not dense enough in metallicity as well as in log(g).

We can use our spectrum, the estimated age of the system and the model-independent dynamical mass measurement to compare with the predictions of evolutionary models. Using the measured effective temperature, which combines the information of the overall spectrum, the BHAC15 models (Baraffe et al. 2015) predict a mass around 65 $M_{\rm Jup}$ (Fig. 14). The BHAC15 evolutionary models tend apparently to overestimate the temperature for a given age and mass in this range of mass. In other words the object seems to cool faster than the models predict. However, the age uncertainty is quite high, and a more accurate value as well as thinner model grids at the H-burning limit would be needed to constrain correctly the models.

7. Conclusion

HD 4747B is a useful mass-age-metallicity benchmark object for comparison with brown dwarf atmospheric and evolutionary models. We used the SPHERE instrument to obtain high precision astrometric and spectroscopic measurements to refine its measured parameters and allow for a more thorough comparison with models.

The HD 4747AB system has been analyzed by combining radial velocity measurements and high contrast imaging. With a spectroscopic analysis we derive an effective temperature $T_{\rm eff} = 5400 \pm 60$ K, a log(g) = 4.60 ± 0.15 and a metallicity [Fe/H]= -0.23 ± 0.05 dex for the primary star. A primary mass of $M_{\rm star} = 0.856 \pm 0.014$ M$_\odot$ and an age of 2.3 ± 1.4 Gyr have been also derived. Combining the SPHERE data with new radial velocity measurements from the CORALIE spectrograph, and a detection in an archival NACO dataset with previously published epochs, we derived a dynamical mass of $m_{\rm B} = 70.2 \pm 1.6$ M$_{\rm Jup}$.

We adjusted the spectrum extracted from the SPHERE IFS and IRDIS data, with known standard objects and derived an L9 spectral type, which is in good agreement with our color-magnitude diagram derived from the IRDIS K1 and K2 filters and previous observations. A forward analysis was conducted by using Exo-REM and confirmed an effective temperature of $T_{\rm eff} = 1300 \pm 100$ K and a cloudy atmosphere. A radius $R = 0.91 \pm 0.16$ R$_{\rm Jup}$ has been derived, however the log(g) = 4 ± 0.5 found is not reproducing the dynamical mass derived in this study. HD 4747B is the most massive object analyzed with Exo-REM, and more work is needed to investigate why the gravity is apparently underestimated with this model.

A retrieval analysis allowed to derive the chemistry of the atmosphere, the Temperature-Pressure profile and the carbon and oxygen abundances (C/H=$-4.72^{+0.47}_{-0.39}$, O/H=$-3.79^{+0.16}_{-0.08}$). We compared these values to the HR 8799's planets and show that a formation scenario for HD 4747B by gravitational instability is compatible, which is favored as well by the mass ratio between the primary and its companion.

Finally a comparison with the BT-Settl evolutionary models was conducted. The effective temperature and log(g) derived are in good agreement with the spectral analysis in this paper. By comparing the age and the effective temperature, we obtain a model dependent mass estimation around 65 $M_{\rm Jup}$, which slightly differs to our dynamical one.

References

Allard, F., Homeier, D., & Freytag, B. 2011, in Astronomical Society of the Pacific Conference Series, Vol. 448, 16th Cambridge Workshop on Cool Stars, Stellar Systems, and the Sun, ed. C. Johns-Krull, M. K. Browning, & A. A. West, 91
Allard, F., Homeier, D., & Freytag, B. 2012, Philosophical Transactions of the Royal Society of London Series A, 370, 2765
Amarsi, A. M., Asplund, M., Collet, R., & Leenaarts, J. 2015, MNRAS, 454, L11
Anderson, D. R., Collier Cameron, A., Hellier, C., et al. 2011, ApJ, 726, L19
Baraffe, I., Chabrier, G., Barman, T. S., Allard, F., & Hauschildt, P. H. 2003, A&A, 402, 701
Baraffe, I., Homeier, D., Allard, F., & Chabrier, G. 2015, A&A, 577, A42
Baudino, J.-L., Bézard, B., Boccaletti, A., et al. 2015, A&A, 582, A83
Baudino, J.-L., Molliere, P., Venot, O., et al. 2017, Accepted by ApJ [arXiv:1710.08235]
Bayliss, D., Hojjatpanah, S., Santerne, A., et al. 2017, AJ, 153, 15
Bayo, A., Rodrigo, C., Barrado Y Navascués, D., et al. 2008, A&A, 492, 277
Bensby, T., Feltzing, S., & Oey, M. S. 2014, A&A, 562, A71
Beuzit, J.-L., Feldt, M., Dohlen, K., et al. 2008, in Proc. SPIE, Vol. 7014, Ground-based and Airborne Instrumentation for Astronomy II, 701418
Biller, B. A., Liu, M. C., Wahhaj, Z., et al. 2010, ApJ, 720, L82
Boccaletti, A., Riaud, P., Baudoz, P., et al. 2004, PASP, 116, 1061
Bonnefoy, M., Zurlo, A., Baudino, J. L., et al. 2016, A&A, 587, A58
Brewer, J. M., Fischer, D. A., Valenti, J. A., & Piskunov, N. 2016, ApJS, 225, 32
Burgasser, A. J. 2007a, ApJ, 659, 655
Burgasser, A. J. 2007b, ApJ, 658, 617
Burgasser, A. J. 2014, in Astronomical Society of India Conference Series, Vol. 11, Astronomical Society of India Conference Series
Burgasser, A. J., Aganze, C., Escala, I., et al. 2016, in American Astronomical Society Meeting Abstracts, Vol. 227, American Astronomical Society Meeting Abstracts, 434.08
Burgasser, A. J., Geballe, T. R., Leggett, S. K., Kirkpatrick, J. D., & Golimowski, D. A. 2006, ApJ, 637, 1067
Burningham, B., Cardoso, C. V., Smith, L., et al. 2013, MNRAS, 433, 457
Burrows, A., Heng, K., & Nampaisarn, T. 2011, The Astrophysical Journal, 736, 47
Burrows, A., Marley, M., Hubbard, W. B., et al. 1997, ApJ, 491, 856
Butler, R. P., Vogt, S. S., Laughlin, G., et al. 2017, AJ, 153, 208
Casagrande, L., Schönrich, R., Asplund, M., et al. 2011, A&A, 530, A138
Chabrier, G. & Baraffe, I. 2000, ARA&A, 38, 337

Chabrier, G., Baraffe, I., Allard, F., & Hauschildt, P. 2000, ApJ, 542, 464
Chauvin, G., Lagrange, A.-M., Bonavita, M., et al. 2010, A&A, 509, A52
Claudi, R. U., Turatto, M., Gratton, R. G., et al. 2008, in Proc. SPIE, Vol. 7014, Ground-based and Airborne Instrumentation for Astronomy II, 70143E
Crepp, J. R., Gonzales, E. J., Bechter, E. B., et al. 2016, ApJ, 831, 136
Crepp, J. R., Principe, D. A., Wolff, S., et al. 2018, ApJ, 853, 192
da Silva, L., Girardi, L., Pasquini, L., et al. 2006, A&A, 458, 609
Desidera, S., Covino, E., Messina, S., et al. 2015, A&A, 573, A126
Dohlen, K., Langlois, M., Saisse, M., et al. 2008, in Proc. SPIE, Vol. 7014, Ground-based and Airborne Instrumentation for Astronomy II, 70143L
D'Orazi, V., Biazzo, K., Desidera, S., et al. 2012, MNRAS, 423, 2789
D'Orazi, V., Desidera, S., Gratton, R. G., et al. 2017, A&A, 598, A19
Dupuy, T. J. & Liu, M. C. 2017, ApJS, 231, 15
Ehrenreich, D., Lagrange, A.-M., Montagnier, G., et al. 2010, A&A, 523, A73
Famaey, B., Jorissen, A., Luri, X., et al. 2005, A&A, 430, 165
Foreman-Mackey, D., Hogg, D. W., Lang, D., & Goodman, J. 2013, PASP, 125, 306
Fuhrmann, K., Chini, R., Kaderhandt, L., & Chen, Z. 2017, ApJ, 836, 139
Fusco, T., Sauvage, J.-F., Petit, C., et al. 2014, in Proc. SPIE, Vol. 9148, Adaptive Optics Systems IV, 91481U
Gaia Collaboration, Brown, A. G. A., Vallenari, A., et al. 2016, ArXiv e-prints [arXiv:1609.04172]
Galland, F., Lagrange, A.-M., Udry, S., et al. 2005, A&A, 443, 337
Gáspár, A., Rieke, G. H., & Balog, Z. 2013, ApJ, 768, 25
Goodman, J. & Weare, J. 2010, Communications in Applied Mathematics and Computational Science, Vol. 5, No. 1, p. 65-80, 2010, 5, 65
Grether, D. & Lineweaver, C. H. 2006, ApJ, 640, 1051
Hagelberg, J., Ségransan, D., Udry, S., & Wildi, F. 2016, MNRAS, 455, 2178
Halbwachs, J. L., Arenou, F., Mayor, M., Udry, S., & Queloz, D. 2000, A&A, 355, 581
Helling, C. & Casewell, S. 2014, A&A Rev., 22, 80
Katsova, M. M. & Livshits, M. A. 2011, Astronomy Reports, 55, 1123
Kaufer, A., Wolf, B., Andersen, J., & Pasquini, L. 1997, The Messenger, 89, 1
King, R. R., McCaughrean, M. J., Homeier, D., et al. 2010, A&A, 510, A99
Kirkpatrick, J. D. 2005, ARA&A, 43, 195
Konopacky, Q. M., Ghez, A. M., Barman, T. S., et al. 2010, The Astrophysical Journal, 711, 1087
Langlois, M., Vigan, A., Moutou, C., et al. 2013, in Proceedings of the Third AO4ELT Conference, ed. S. Esposito & L. Fini, 63
Lavie, B., Mendonça, J. M., Mordasini, C., et al. 2017, AJ, 154, 91
Lee, J.-M., Heng, K., & Irwin, P. G. J. 2013, ApJ, 778, 97
Line, M. R., Teske, J., Burningham, B., Fortney, J. J., & Marley, M. S. 2015, ApJ, 807, 183
Looper, D. L., Kirkpatrick, J. D., & Burgasser, A. J. 2007, AJ, 134, 1162
Maire, A.-L., Boccaletti, A., Rameau, J., et al. 2014, A&A, 566, A126
Maire, A.-L., Bonnefoy, M., Ginski, C., et al. 2016a, A&A, 587, A56
Maire, A.-L., Langlois, M., Dohlen, K., et al. 2016b, in Proc. SPIE, Vol. 9908, Ground-based and Airborne Instrumentation for Astronomy VI, 990834
Mamajek, E. E. & Hillenbrand, L. A. 2008, ApJ, 687, 1264
Marcy, G. W. & Butler, R. P. 2000, PASP, 112, 137
Marois, C., Correia, C., Véran, J.-P., & Currie, T. 2014, in IAU Symposium, Vol. 299, Exploring the Formation and Evolution of Planetary Systems, ed. M. Booth, B. C. Matthews, & J. R. Graham, 48–49
Mortier, A., Santos, N. C., Sousa, S., et al. 2013, A&A, 551, A112
Nakajima, T., Oppenheimer, B. R., Kulkarni, S. R., et al. 1995, Nature, 378, 463
Nidever, D. L., Marcy, G. W., Butler, R. P., Fischer, D. A., & Vogt, S. S. 2002, ApJS, 141, 503
Nordström, B., Mayor, M., Andersen, J., et al. 2004, A&A, 418, 989
Öberg, K. I., Murray-Clay, R., & Bergin, E. A. 2011, ApJ, 743, L16
Oppenheimer, B. R., Kulkarni, S. R., Matthews, K., & Nakajima, T. 1995, Science, 270, 1478
Pavlov, A., Möller-Nilsson, O., Feldt, M., et al. 2008, in Proc. SPIE, Vol. 7019, Advanced Software and Control for Astronomy II, 701939
Pinfield, D. J., Burningham, B., Lodieu, N., et al. 2012, MNRAS, 422, 1922
Queloz, D., Mayor, M., Naef, D., et al. 2000, in From Extrasolar Planets to Cosmology: The VLT Opening Symposium, ed. J. Bergeron & A. Renzini, 548
Rebolo, R., Zapatero Osorio, M. R., & Martín, E. L. 1995, Nature, 377, 129
Sahlmann, J., Lovis, C., Queloz, D., & Ségransan, D. 2011a, A&A, 528, L8
Sahlmann, J., Ségransan, D., Queloz, D., et al. 2011b, A&A, 525, A95
Santos, N. C., Israelian, G., Mayor, M., et al. 2005, A&A, 437, 1127
Siverd, R. J., Beatty, T. G., Pepper, J., et al. 2012, ApJ, 761, 123
Skilling, J. 2006, Bayesian Anal., 1, 833
Sokal, A. 1997, Monte Carlo Methods in Statistical Mechanics: Foundations and New Algorithms, ed. C. DeWitt-Morette, P. Cartier, & A. Folacci (Boston, MA: Springer US), 131–192
Thalmann, C., Carson, J., Janson, M., et al. 2009, ApJ, 707, L123
Trotta, R. 2008, Contemporary Physics, 49, 71
Troup, N. W., Nidever, D. L., De Lee, N., et al. 2016, AJ, 151, 85
Valenti, J. A. & Fischer, D. A. 2005, ApJS, 159, 141
van Leeuwen, F. 2007, A&A, 474, 653
Vigan, A., Bonnefoy, M., Ginski, C., et al. 2016, A&A, 587, A55
Vigan, A., Gry, C., Salter, G., et al. 2015, MNRAS, 454, 129
Vigan, A., Moutou, C., Langlois, M., et al. 2010, in Proc. SPIE, Vol. 7735, Ground-based and Airborne Instrumentation for Astronomy III, 77352X
Vogt, S. S., Allen, S. L., Bigelow, B. C., et al. 1994, in Proc. SPIE, Vol. 2198, Instrumentation in Astronomy VIII, ed. D. L. Crawford & E. R. Craine, 362
Wilson, P. A., Hébrard, G., Santos, N. C., et al. 2016, A&A, 588, A144
Zechmeister, M. & Kürster, M. 2009, A&A, 496, 577
Zurlo, A., Vigan, A., Galicher, R., et al. 2016, A&A, 587, A57

Appendix A: Archival NACO observation: χ^2 maps over double roll subtraction angles

As described in Sect. 4.3, we computed the χ^2 maps for each double roll subtraction angle from $5°$ to $25°$. Each map was computed from 20 to 55 pixel of separation (346"-953") and from $90°$ to $270°$, the rest of the image being excluded by the orbital information from the epochs from Crepp et al. (2016), our SPHERE observation and the radial velocities. In Fig. A.1 we show these maps and the median over the double roll subtraction angles (Fig. A.1f). The position of the companion is retrieved as the minimum χ^2 on each maps except for an angle of $20°$ where another minimum is detected. However a local minimum is clearly identified at the companion position. This comes from the fact that the larger the angle, the least signal is on the companion. Indeed by construction, a larger double roll subtraction angle means less images to add together and thus less signal for the detection.

Appendix B: MCMC orbital parameters

The MCMC simulation was performed by using *emcee* (Foreman-Mackey et al. 2013), a python stable implementation of the affine-invariant ensemble sampler for MCMC proposed by Goodman & Weare (2010). The data are modeled with a Keplerian and 4 RV offsets (one for HIRES, and 3 for the different versions of CORALIE: C98, C07, C14). The noise in the radial velocity data is modeled with a nuisance parameter for each instrument. The parallax and the mass of the primary star are also parameters of the MCMC. We ran the MCMC simulation with 39 walkers and 10^6 steps for each walker. We computed then the correlation time scale τ of each walker and got rid of the initialization bias by removing the first 20τ for each one of them (Sokal 1997). To build a statistical meaningful sample, we then sampled each walker by its coherence timescale.

At the end we have 358000 independent data points which means that we characterize the parameters at a $1/\sqrt{358000} = 0.17\%$ accuracy which corresponds to a 3σ confidence interval.

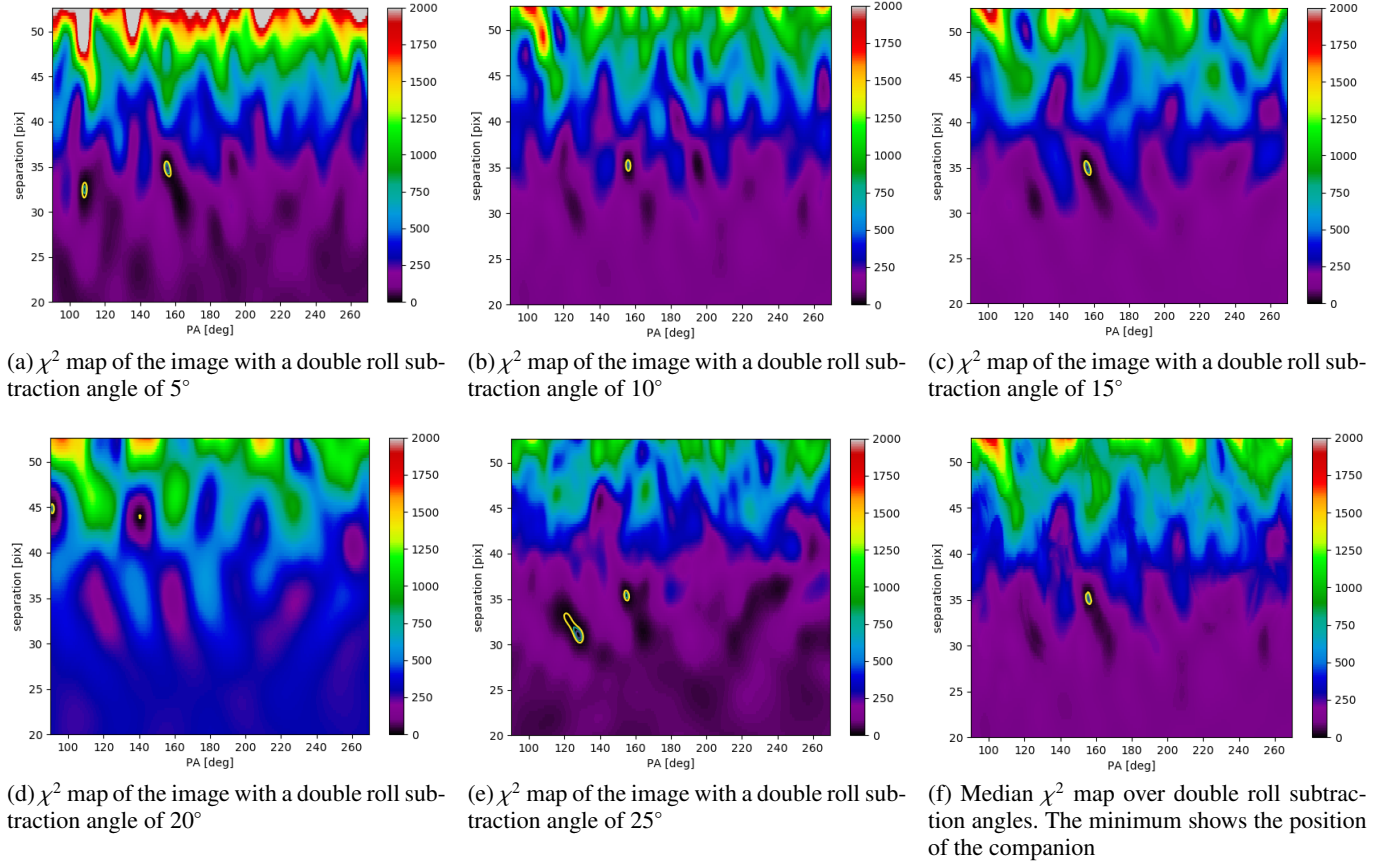## Appendix C: Retrieval additional results

(a) χ^2 map of the image with a double roll subtraction angle of 5°

(b) χ^2 map of the image with a double roll subtraction angle of 10°

(c) χ^2 map of the image with a double roll subtraction angle of 15°

(d) χ^2 map of the image with a double roll subtraction angle of 20°

(e) χ^2 map of the image with a double roll subtraction angle of 25°

(f) Median χ^2 map over double roll subtraction angles. The minimum shows the position of the companion

Fig. A.1: Archival NACO data reduction. χ^2 map of the image for each double roll subtraction angle. The maps shown have been computed for position angles between 90° and 270° and separation between 20 and 50 pixels as the companion is completely excluded in the rest of the image by the orbital analysis from the RV's, Keck and SPHERE observations.
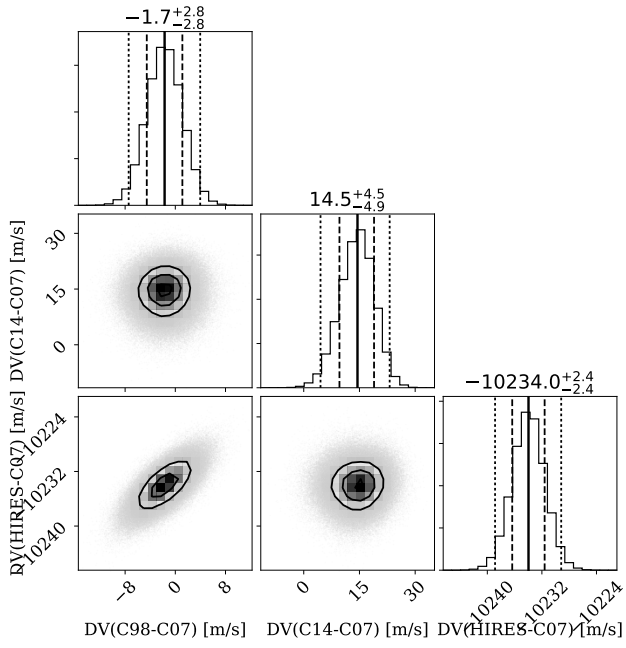
Fig. B.1: Marginalized 1-D and 2-D posterior distributions of the orbital global adjustment combining radial velocities and direct imaging data. Here are the offsets between the different radial velocity instruments. C98 stands for the first version of the CORALIE instrument, C07 for its first update in 2007 and C14 for the last one in 2014.
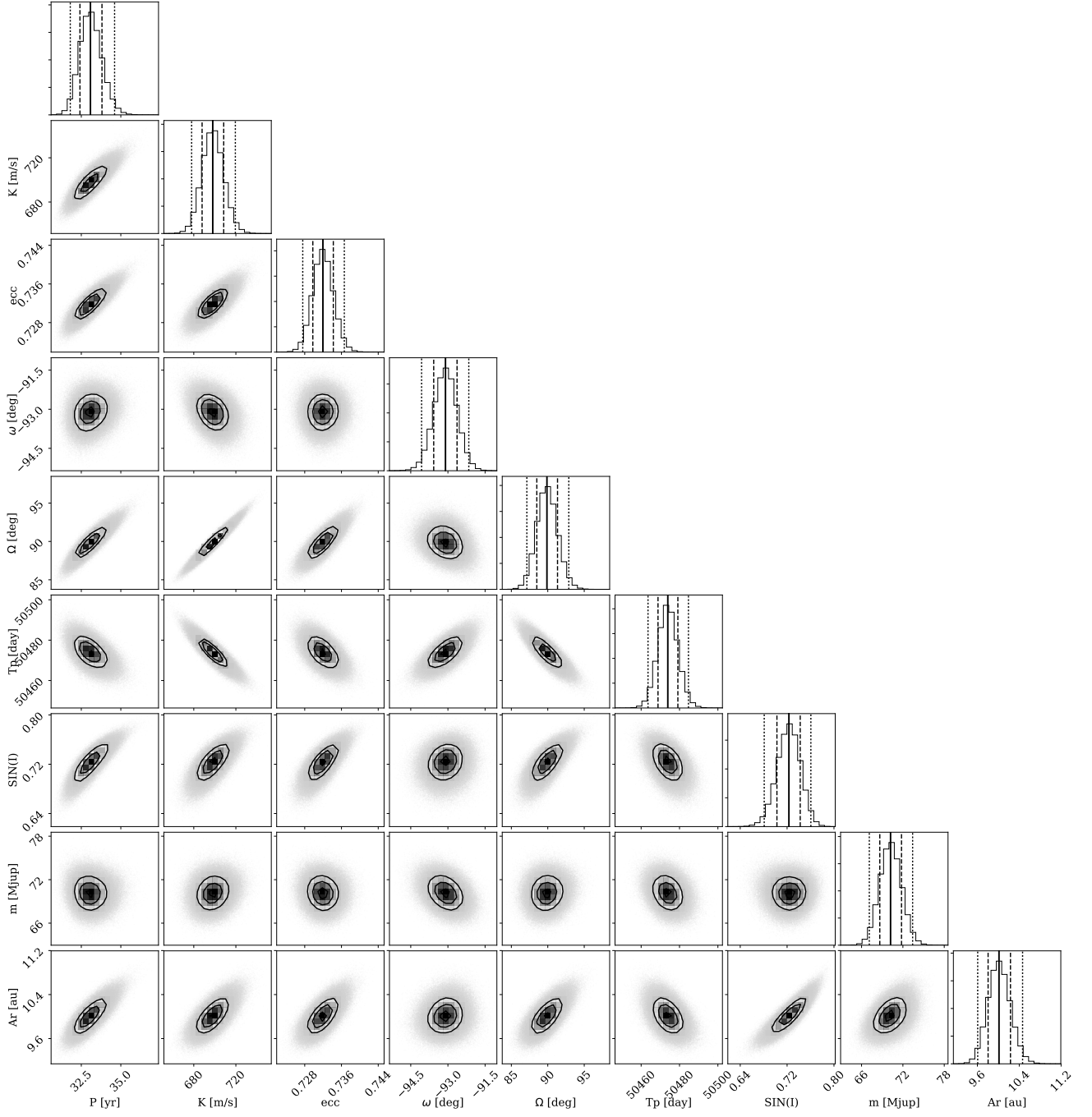
Fig. B.2: Marginalized 1-D and 2-D posterior distributions of the orbital global adjustment combining radial velocities and direct imaging data. The model parameters P, K, e, ω, Ω, T_p and sin(i) are shown as well as the derived quantities, the mass (m) and the orbital semi major axis (Ar).
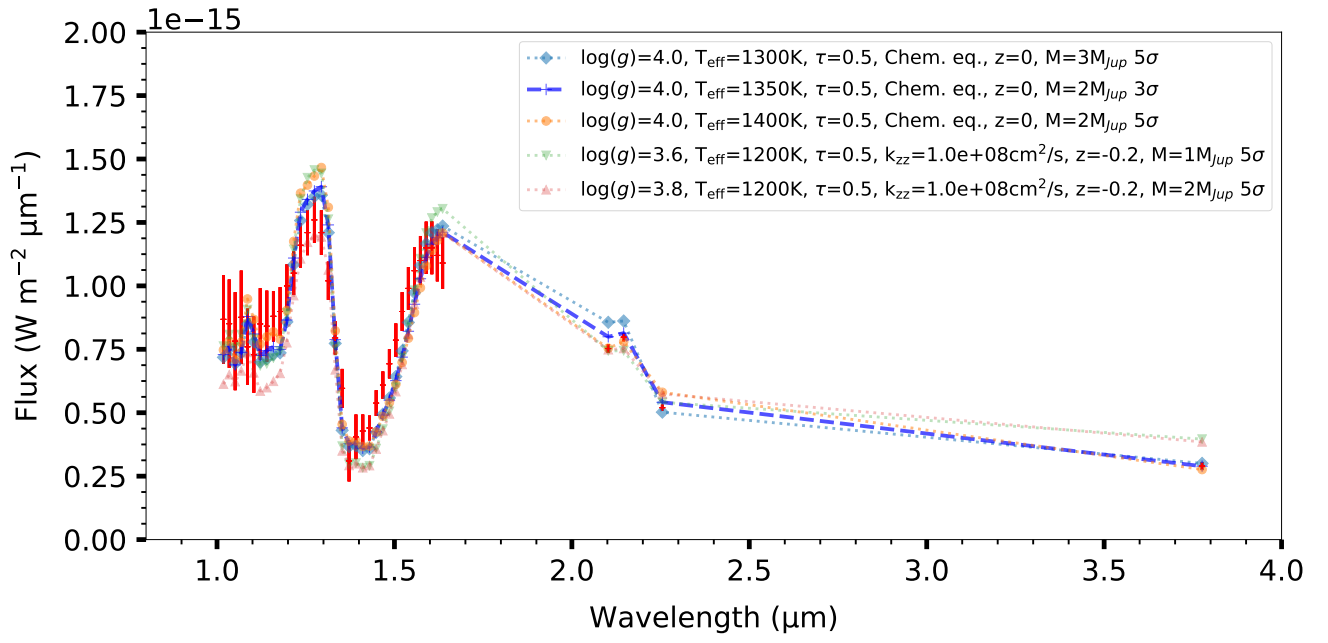
Fig. B.3: Exo-Rem best fit to spectrum. The data are represented in red and the best fit is in light blue dashed line
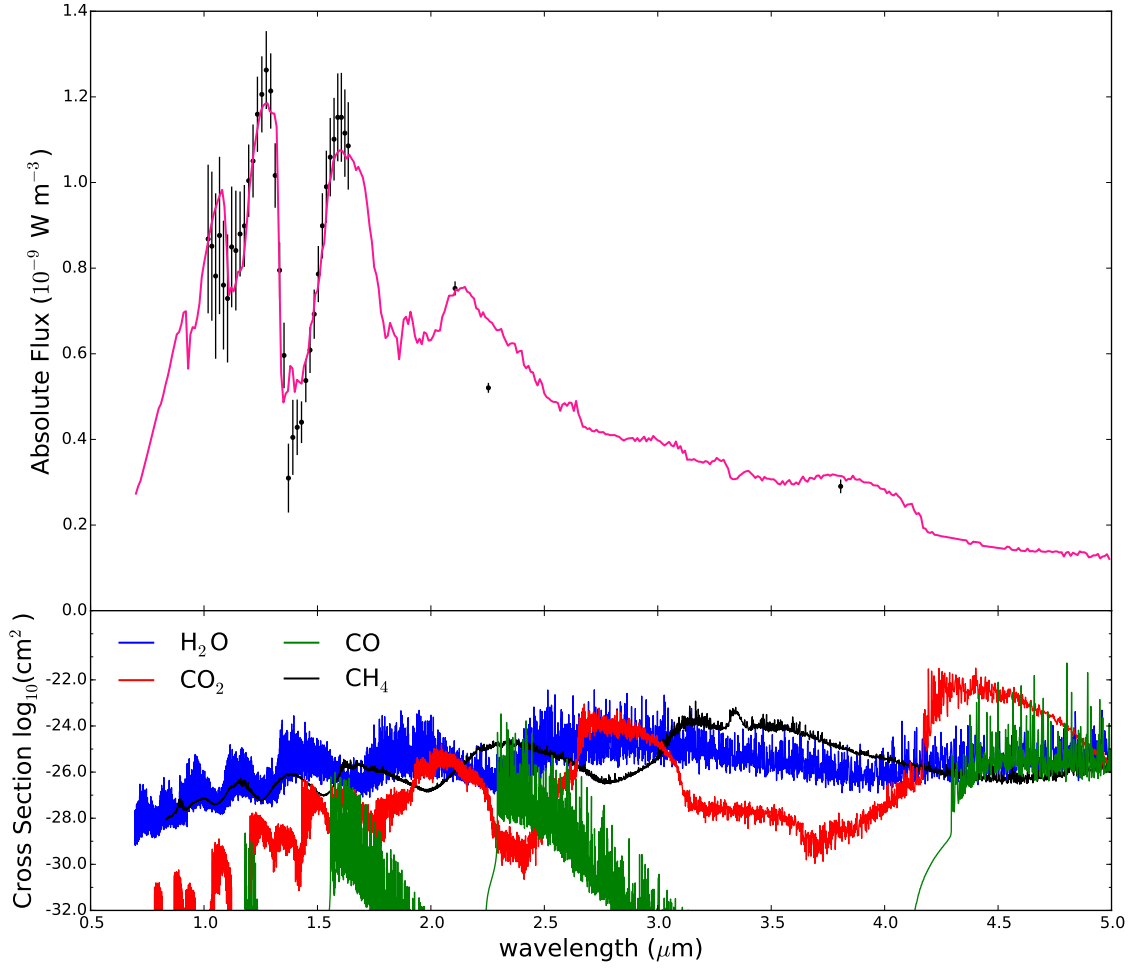
Fig. C.1: Best-fit spectra obtained with HELIOS-R (top panel) and cross-section of the four main absorbers (bottom panel) at a pressure of 0.1 bar and a temperature of 1900 K. Lack of observations in the K-band block the detection of CO (CO absorption band between 1.5 and 2 μm)
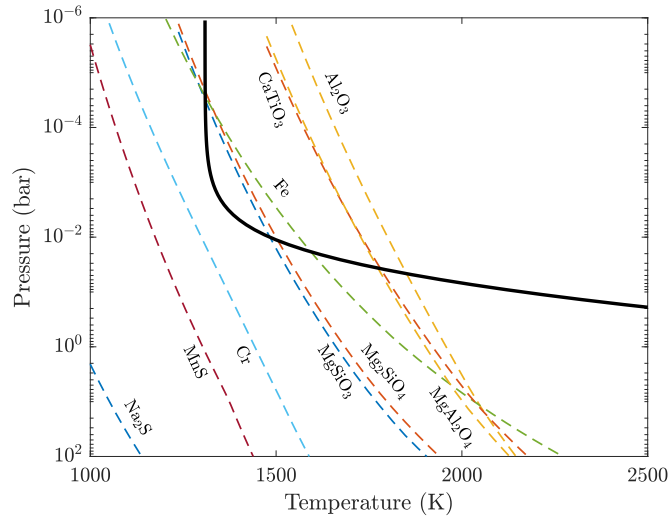
Fig. C.2: Temperature-pressure profiles for HD 4747B obtained with HELIOS-R. Dashed lines are condensation curves for some possible condensates (assuming solar composition)
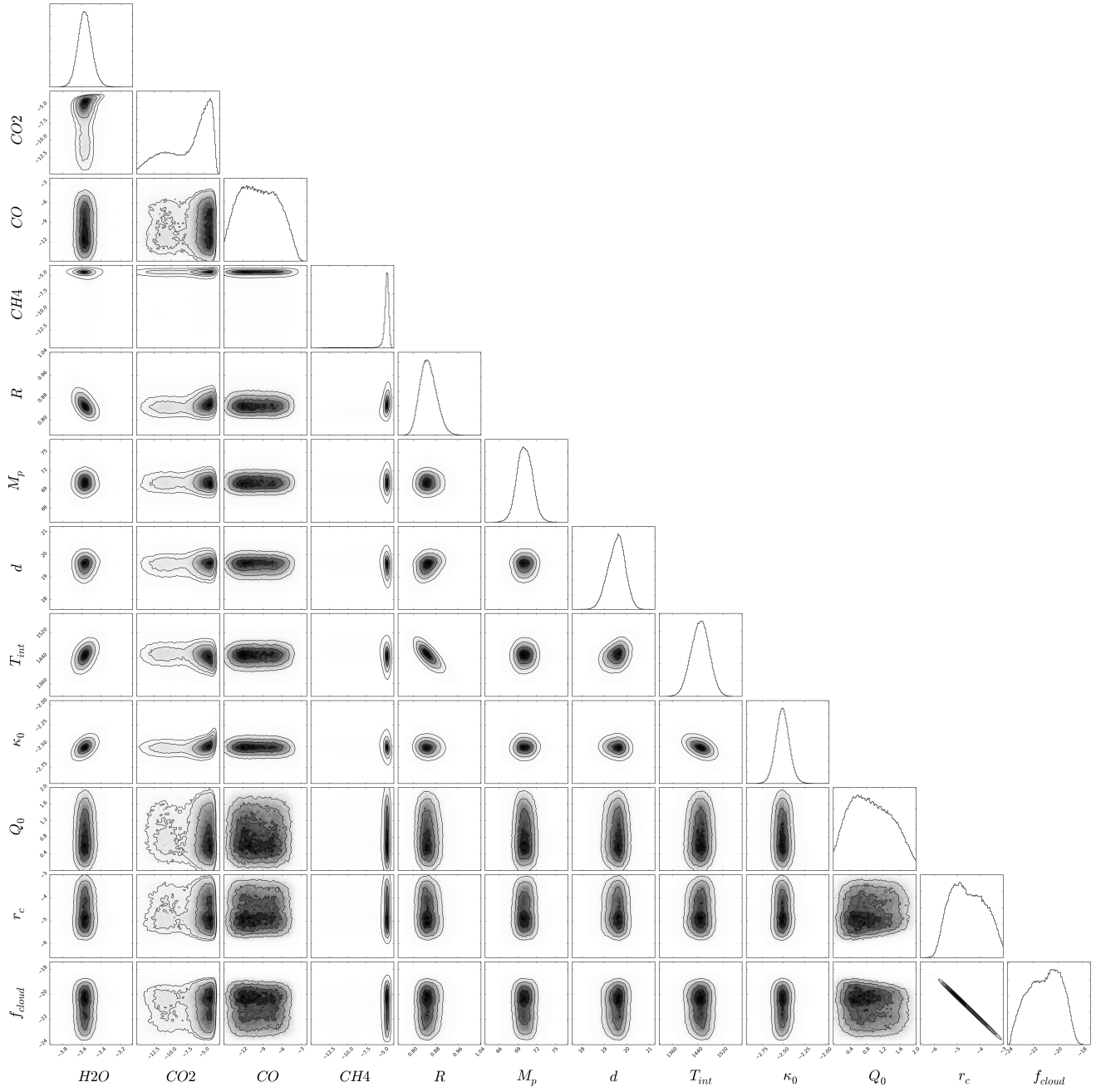
Fig. C.3: Results of the Retrieval. Montage of posterior distributions from the best model (Unconstrained chemistry with clouds) of HD 4747B
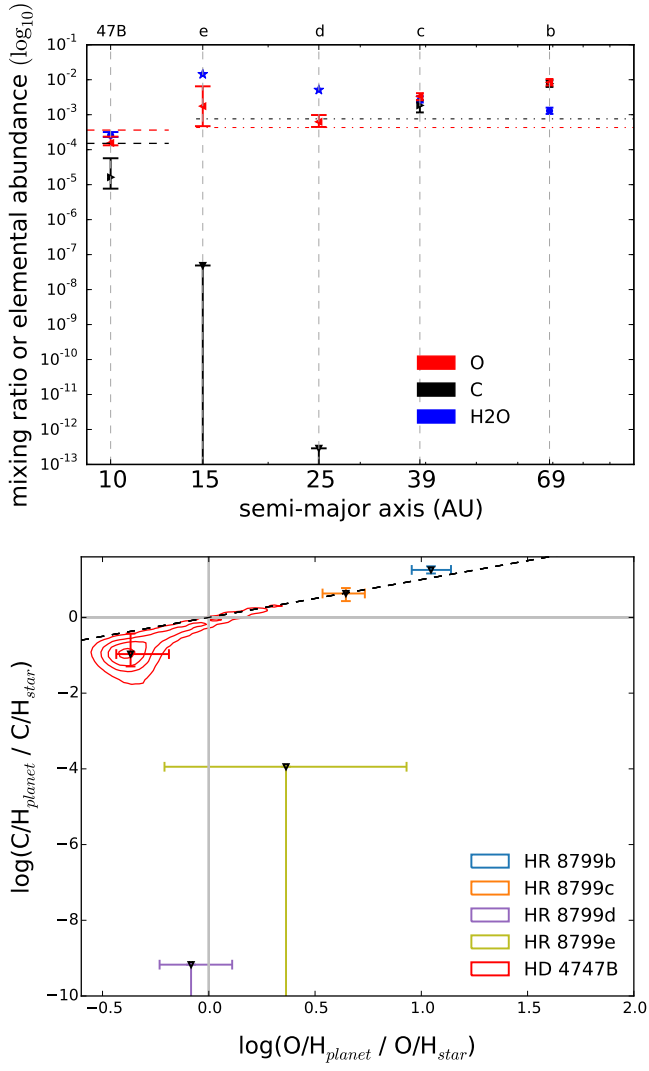
Fig. C.4: Summary of our main results. Same as Fig. 12 but with HR 8799e and HR 8799d. The top panel shows the retrieved water mixing ratios and elemental abundances of carbon and oxygen for HD 4747B as well as the four HR 8799 exoplanets as a function of the distance to the host star . For HR 8799d and e, we show the water abundance in chemical equilibrium at 1 bar (represented by the blue stars). The carbon and oxygen abundances of the stars are shown with the dashed lines (HD 4747) and dashed dot lines(HR 8799). The bottom panel shows the companion elemental abundances normalized to its stellar values with the dashed black line denoting parity.

Table 3.1:

model	Evidence	Temperature [K]	Radius [R_j]
Blackbody	93.4	2875±47	1.97±0.06
Blackbody + H_2O	93.5	2874± 45	1.97±0.06

3.4 Wasp-12b

3.4.1 Toy model

The retrieval code `HELIOS_R` has also been used to characterise the hot Jupiter Wasp-12b (Oreshenko et al. 2017). The data coverage is similar to the data coverage used in the "toy " inference problem in section 2.3 and includes WFC3 data from the Hubble Space Telescope (HST) and Spitzer data. For hot Jupiters the physical variable observed is the ratio of the stellar flux and the planet flux instead of the companion's flux in direct imaging. Adapting equation 2.9 with this fact, we obtain :

$$F_{\text{obs}} = \left(\frac{R_{comp}}{R_{star}}\right)^2 \frac{F_{\text{TOA}}}{F_{\text{star}}}, \qquad (3.1)$$

Instead of the distance we now have two new parameters, the radius of the host star and its flux, which is its temperature if one assumes a simple blackbody function for the stellar flux. For the properties of the star we set a gaussian prior of 6360± 140 K and 1.657±0.046 sun radius (Collins et al. 2017). The others prior are uniform between 500 and 3000 K for the planet temperature, 0.8 and 3 Jupiter radius for the planet radius and 10^{-15} to 10^{-1} for the water abundance proxy.

Results of the retrieval are presented in Table 3.1. The posterior distribution of the model with water is presented in Figure 3.6. The Bayes factor between the two models indicate that there is no detection of water. For both models the radius and the temperature are constrained within reasonable values. Wasp-12b is known to be one of the hottest planet with an equilibrium temperature of 2580K (Collins et al. 2017). The retrieved temperature is the effective temperature and is significantly higher than the equilibrium temperature. This indicate that there is some processes of energy retention at play in the atmosphere of the planet. The retrieved radius is compatible with the radius of 1.90 ± 0.06 retrieved by Collins et al. (2017).

3.4.2 Publication

It is clear from the above "toy" inference that the data coverage and the precision are not enough to constrained Wasp-12b atmospheric properties further. But many other studies have tried to extract more information from this planet with the same dataset (or its equivalent in transmission, where only the limbs of the planet are probed). We published a paper showing that
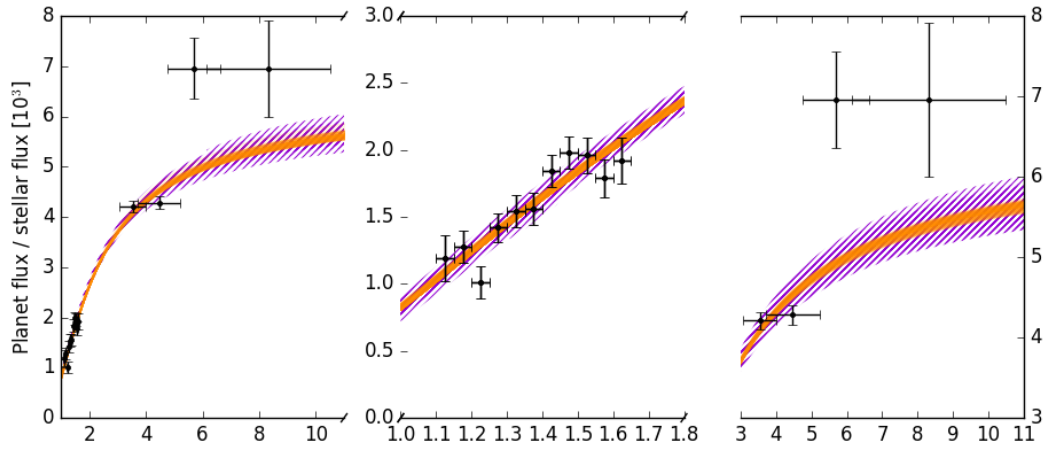
Figure 3.5:   WASP-12b data with 1000 models drawn from the retrieved posterior distribution for a single blackbody model (orange) and a model with water spectral features (violet).

retrieval analysis of the emission spectrum of Wasp-12b with WFC3 and Spitzer wavelength coverage is dominated by the priors distribution. The publication is presented below.
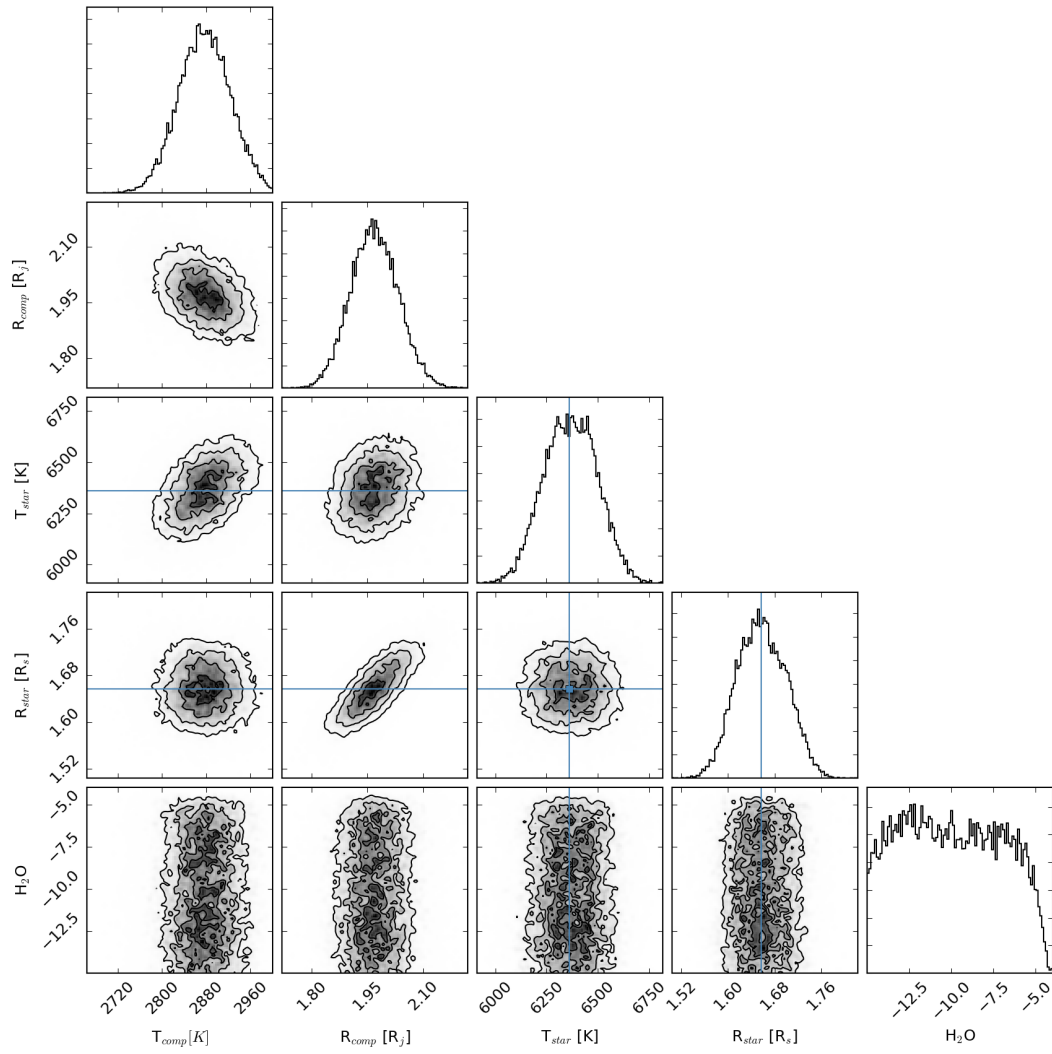
Figure 3.6: Posterior distribution of the toy model with water spectral features obtained with the retrieval on WASP-12 b dataset.

Retrieval Analysis of the Emission Spectrum of WASP-12b: Sensitivity of Outcomes to Prior Assumptions and Implications for Formation History

Maria Oreshenko[1], Baptiste Lavie[1,2] , Simon L. Grimm[1] , Shang-Min Tsai[1] , Matej Malik[1] , Brice-Olivier Demory[1] ,
Christoph Mordasini[1] , Yann Alibert[1] , Willy Benz[1], Sascha P. Quanz[3] , Roberto Trotta[4] , and Kevin Heng[1]
[1] University of Bern, Center for Space and Habitability, Gesellschaftsstrasse 6, CH-3012 Bern, Switzerland
maria.oreshenko@csh.unibe.ch, kevin.heng@csh.unibe.ch
[2] Observatoire de l'Université de Genève, 51 chemin des Mailettes, CH-1290 Sauverny, Switzerland
[3] ETH Zürich, Department of Physics, Wolfgang-Pauli-Strasse 27, CH-8093 Zürich, Switzerland
[4] Astrophysics Group, Imperial College London, Blackett Laboratory, Prince Consort Road, London SW7 2AZ, UK

Abstract

We analyze the emission spectrum of the hot Jupiter WASP-12b using our HELIOS-R retrieval code and HELIOS-K opacity calculator. When interpreting *Hubble* and *Spitzer* data, the retrieval outcomes are found to be prior-dominated. When the prior distributions of the molecular abundances are assumed to be log-uniform, the volume mixing ratio of HCN is found to be implausibly high. A VULCAN chemical kinetics model of WASP-12b suggests that chemical equilibrium is a reasonable assumption even when atmospheric mixing is implausibly rigorous. Guided by (exo)planet formation theory, we set Gaussian priors on the elemental abundances of carbon, oxygen, and nitrogen with the Gaussian peaks being centered on the measured C/H, O/H, and N/H values of the star. By enforcing chemical equilibrium, we find substellar O/H and stellar to slightly superstellar C/H for the dayside atmosphere of WASP-12b. The superstellar carbon-to-oxygen ratio is just above unity, regardless of whether clouds are included in the retrieval analysis, consistent with Madhusudhan et al. Furthermore, whether a temperature inversion exists in the atmosphere depends on one's assumption for the Gaussian width of the priors. Our retrieved posterior distributions are consistent with the formation of WASP-12b in a solar-composition protoplanetary disk, beyond the water iceline, via gravitational instability or pebble accretion (without core erosion) and migration inward to its present orbital location via a disk-free mechanism, and are inconsistent with both in situ formation and core accretion with disk migration, as predicted by Madhusudhan et al. We predict that the interpretation of *James Webb Space Telescope* WASP-12b data will not be prior-dominated.

Key words: planets and satellites: atmospheres

1. Introduction

WASP-12b is a well-studied hot Jupiter that has generated ample debate and controversy in the published literature. With an equilibrium temperature in excess of 2500 K (Hebb et al. 2009), it serves as a high-temperature laboratory for the study of atmospheric chemistry. We expect equilibrium chemistry to be a reasonable approximation, as the high temperatures should overwhelm disequilibrium due to atmospheric circulation or photochemistry. Figure 1 shows a chemical kinetics model of WASP-12b computed using our open-source VULCAN code (Tsai et al. 2017), which lends support to this expectation. Even with an eddy mixing coefficient of $K_{zz} \sim 10^{12}$ cm^2 s^{-1}, the model atmosphere is well-described by chemical equilibrium.[5] Later in the study, we will demonstrate that enforcing chemical equilibrium as a prior assumption circumvents the debate over whether the inferred molecular abundances in WASP-12b are physically and chemically plausible (Madhusudhan 2012; Stevenson et al. 2014; Heng & Lyons 2016).

An active topic of interest associated with WASP-12b is the inferred carbon-to-oxygen (C/O) ratio of its atmosphere, starting with the claim of Madhusudhan et al. (2011) and Madhusudhan (2012) that it equals or exceeds unity based on analyzing its emission spectrum. This inference on the C/O, if

true, would imply interesting constraints on the formation and/or evolutionary history of the exoplanet (Öberg et al. 2011; Ali-Dib et al. 2014; Madhusudhan et al. 2014; Mordasini et al. 2016; Öberg & Bergin 2016; Ali-Dib 2017; Brewer et al. 2017; Espinoza et al. 2017; Madhusudhan et al. 2017), as the C/O of its star has been measured to be 0.48 ± 0.08 (Teske et al. 2014). In fact, when compared to a sample of exoplanet-bearing stars, WASP-12 is unremarkably Sun-like (Teske et al. 2014; Brewer & Fischer 2016). Line et al. (2014) inferred C/O = 0.51 from their retrieval analysis, but their inferred volume mixing ratio for CO_2 was nearly 0.06, a factor of 26 higher than that for CO, which is chemically implausible unless the metallicity is several orders of magnitude above solar (Madhusudhan 2012; Heng & Lyons 2016). Stevenson et al. (2014) performed a uniform analysis of *Hubble* and *Spitzer* secondary-eclipse data, subjected them to a retrieval analysis and found a bimodal distribution for C/O. Oxygen-rich models were ruled out on the basis of chemical implausibility. By contrast, Kreidberg et al. (2015) ruled out a carbon-rich interpretation from analyzing the transmission spectrum of WASP-12b.

These properties of WASP-12b, and the attention it has garnered in the community, compel us to perform our own retrieval analysis of its emission spectrum, which probes the dayside of the exoplanet. Although no new data are being analyzed in the present study, we add value by offering an independent analysis using our own suite of tools (Fortney et al. 2016). Furthermore, we use updated and previously

---

[5] Using a sound speed of $c_s \sim 1$ km s^{-1} and a pressure scale height of $H \sim 100$ km yields $K_{zz} \sim c_s H \sim 10^{12}$ cm^2 s^{-1}. This may be considered an upper limit as vertical flow velocities are typically subsonic.
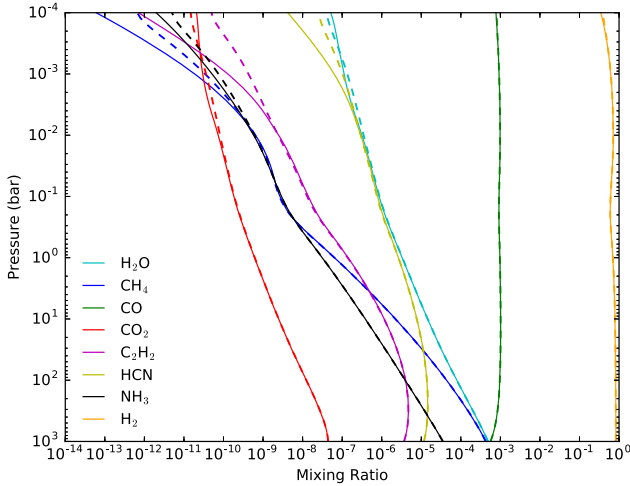
Figure 1. Chemical kinetics model of WASP-12b computed using the open-source VULCAN code (Tsai et al. 2017) and adopting the eddy mixing coefficient to be $K_{zz} = 10^{12}$ cm^2 s^{-1} (dashed curves). The solid curves are the molecular abundances in chemical equilibrium. Photochemistry has been omitted, as it is subdominant due to the high temperatures involved. Note that we do not use chemical-equilibrium boundary conditions at the bottom of the model atmosphere, but rather zero-flux boundary conditions. The temperature–pressure profile used is taken from the retrieval model with equilibrium chemistry and no clouds with prior assumptions on the elemental abundances set to twice the measurement errors ("EB, ×2"; see the text for details). The carbon-to-oxygen ratio is set to unity. Emission spectra typically probe ~0.01–1 bar, which implies that chemical equilibrium is a good assumption for the atmosphere of WASP-12b.

Figure 2. Examples of opacities computed using our HELIOS-K opacity calculator (Grimm & Heng 2015) for a temperature of 2500 K and a pressure of 1 bar. The ExoMol database is the source of our H_2O and CH_4 opacities. The CO and CO_2 opacities are from HITEMP, while the C_2H_2 and HCN opacities are from HITRAN.

unavailable and/or unused opacities for H_2O and CH_4. The high-temperature water line lists were published by Barber et al. (2006), while the high-temperature CH_4 line lists were published by Yurchenko et al. (2013) and Yurchenko & Tennyson (2014). For example, Line et al. (2014) did not include HCN opacities in their retrievals and used non-ExoMol CH_4 and H_2O opacities. The studies of Madhusudhan et al. (2011) and Madhusudhan (2012) also did not use the ExoMol CH_4 and H_2O opacities.

In the current study, our focus is on elucidating the dependence of the retrieval outcomes on the prior assumptions set on the metallicity or mixing ratios (relative molecular abundances by number). By "metallicity," we specifically mean the elemental abundances of carbon (C/H), oxygen (O/H), and nitrogen (N/H), since our six-molecule analysis only includes the major carbon-, oxygen-, and nitrogen-bearing species in their gaseous form. The assumptions made on the prior distributions of input parameters is an issue that has not been treated in detail in the literature. Log-uniform prior distributions are often assumed (sometimes without explicitly being stated), based on the misconception that they are the most plausible assumption—erroneously termed "uninformative priors" or "uninformed priors"—in the absence of further evidence (Trotta 2008). The key finding of our study is that conclusions, based on analyzing currently available data, drawn on C/O and chemistry are strongly tied to our prior assumptions, which are in turn informed by our ideas of physics and chemistry. Given assumptions on the priors, we then interpret the outcomes, using published studies of (exo)planet formation, by assuming that the retrieved elemental abundances are representative of the bulk composition of the exoplanet.
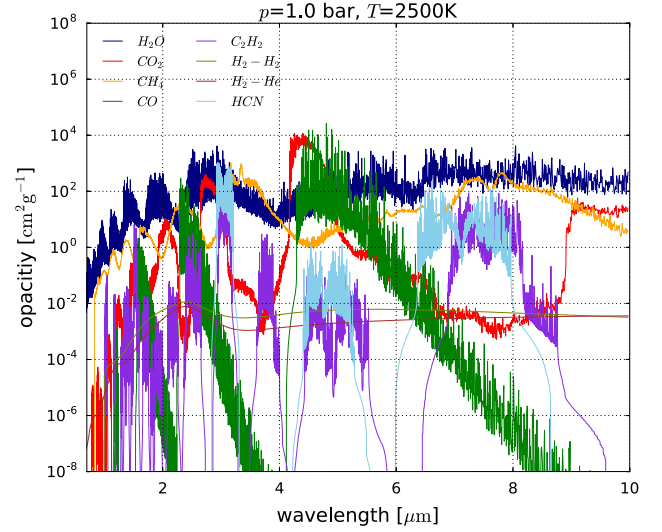
2. Methodology

Our nested-sampling retrieval code, HELIOS-R, and computational setup was previously described in Lavie et al. (2017). The stellar and exoplanetary parameters are taken from Hebb et al. (2009) and Chan et al. (2011). Our nested-sampling (Feroz et al. 2009) retrievals typically use 8 parallel runs of 4000 live points each. The model atmosphere is divided into 100 discrete layers. At every wavelength, the propagation of flux is performed using a direct, analytical solution of the radiative transfer equation in the limit of pure absorption (Heng et al. 2014). The opacities are computed using our customized, open-source opacity calculator, HELIOS-K (Grimm & Heng 2015), which takes the HITEMP (Rothman et al. 2010), HITRAN (Rothman et al. 1996, 2013), and ExoMol (Barber et al. 2006; Yurchenko et al. 2013; Yurchenko & Tennyson 2014) spectroscopic databases as inputs to compute the line shapes and strengths. We include the opacities of CO, CO_2, CH_4, C_2H_2, H_2O, and HCN, as well as collision-induced absorption associated with H_2–H_2 and H_2–He. Figure 2 shows examples of the opacities computed. We use the opacity sampling method with a spectral resolution of 1 cm^{-1}. Our line-wing cutoff is 100 cm^{-1} applied to all of the spectral lines. We use the analytical temperature–pressure profiles originally derived by Guillot (2010), and later generalized to include scattering by Heng et al. (2012) and Heng et al. (2014). These profiles enforce radiative equilibrium (local energy conservation) by construction, but are too isothermal at high altitudes due to the assumption that the Planck, absorption, and flux mean opacities are equal. By numerical experimentation (not shown), we find that the temperature–pressure profile in the limit of pure absorption suffices for our purposes, which is to describe the shape of the profile with as few parameters as possible: κ_{IR} (the mean infrared opacity associated with the temperature–pressure profile) and γ (the "greenhouse parameter," which is the ratio of the mean optical/visible to mean infrared opacities). There is no attempt to seek self-consistency between these parameters and the

wavelength-dependent opacities used.[6] Atmospheres without and with temperature inversions have $\gamma < 1$ and $\gamma > 1$, respectively.

For chemistry, we consider two types of models: unconstrained and equilibrium chemistry. The former is the typical approach, which assumes mixing ratios that are constant throughout the atmosphere and uses them as fitting parameters. In other words, no chemistry is actually being considered. The latter enforces chemical equilibrium via the analytical formulae of Heng & Tsai (2016), who validated these formulae against calculations of Gibbs free energy minimization and demonstrated that they are accurate at the ∼1% level or better. For chemical-equilibrium models, the fitting parameters are C/H, O/H, and N/H. The prior distribution of C/O is roughly uniform, unlike for unconstrained chemistry where it is double-peaked (Line et al. 2013). In chemical equilibrium, specifying the elemental abundances allows all of the molecular abundances to be computed, with no parametric freedom, given a temperature and pressure.

We are agnostic about the terms "cloud" and "haze" and use them interchangeably for this study.[7] We implement the simplified cloud model introduced by Lee et al. (2013) and used by Lavie et al. (2017), which describes a monodisperse population of spherical cloud particles with radii r_c, cloud volume mixing ratio f_{cloud} and a single composition (represented by the parameter Q_0). Refractory and volatile cloud species have $Q_0 \sim 1$ and ∼10, respectively. This cloud model accommodates both small and large particles, and correctly reproduces the limits of Rayleigh and gray scattering. It is based on the notion that curves of the extinction coefficient have a roughly universal shape (Pierrehumbert 2010).

3. Results

We begin by presenting a pair of retrieval models that make the common assumption of log-uniform priors (Figure 3). For the measured emission spectrum of WASP-12b, we use the published data of Stevenson et al. (2014) as stated in their Table 3. For the model with unconstrained chemistry, we set log-uniform priors on the six mixing ratios. For the model with equilibrium chemistry, we set log-uniform priors on the elemental abundances of carbon, oxygen, and nitrogen. As an improvement over the work of Stevenson et al. (2014), we include clouds in our analysis as part of the retrieval (i.e., the cloud parameters are not fixed to preset values). The other parameters also have log-uniform priors, except for Q_0, which has a (linearly) uniform prior.

In Figure 3, the first thing to notice is that the cloud parameters display degeneracies that match our physical intuition: the mixing ratios are degenerate with cloud composition, particle radius, and number density. In particular, it is possible to set bounds on the cloud particle radius, but the cloud composition is essentially—and unsurprisingly—unconstrained. When we include only CO, CO_2, CH_4, and H_2O in the retrieval, we reproduce the result of Line et al. (2014) and Stevenson et al. (2014) that unrealistically high abundances for CO_2 are obtained (not shown). (Heng & Lyons 2016 have previously elucidated this implausibility using validated analytical formulae.) Such high abundances of CO_2 drive the
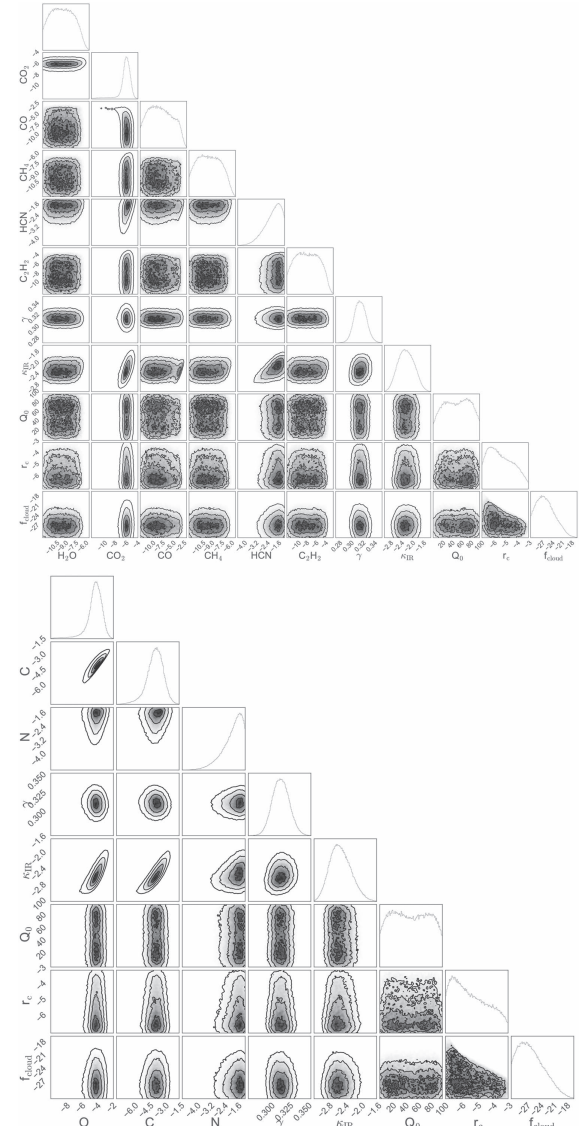

Figure 3. Posterior distributions of fitting parameters for cloudy retrieval models with unconstrained chemistry (top panel) and equilibrium chemistry (bottom panel) with log-uniform priors. κ_{IR} has physical units of $m^2\ kg^{-1}$, while r_c is given in m. The rest of the parameters are dimensionless.

retrieval predominantly toward a solution with C/O ≈ 0.5. Furthermore, the prior distribution of C/O is double-peaked at 0.5 and 1 (Line et al. 2013), which appears in the posterior distribution as well (Figure 4).

When C_2H_2 and HCN are included, we obtain the mixing ratio of HCN to be ∼10^{-2}–10^{-1} (top panel of Figure 3). This is chemically implausible, as suggested by the detailed chemical kinetics calculations of Moses et al. (2013), who estimated an upper limit to the mixing ratio of HCN of ∼10^{-3} for C/O < 2 and thrice the solar metallicity. When chemical equilibrium is enforced with log-uniform priors, we obtain N/H ∼ 10^{-2}–10^{-1} (bottom panel of Figure 3), which is similarly implausible. These anomalies arise because the opacity of HCN is driving the fit at the wavelengths of the *Spitzer* photometry (Stevenson et al. 2014; Figure 2). The lesson learned is that the "simplest" assumption made on the prior distributions of fitting parameters may not be the best one (Trotta 2008). Rather, we need to be guided by physics and chemistry.

---

[6] None of the practitioners of atmospheric retrieval are currently able to do this.
[7] These terms are either used to distinguish between size (Earth science convention) or formation origin (planetary science convention), and there is no consensus within the exoplanet community on their usage.
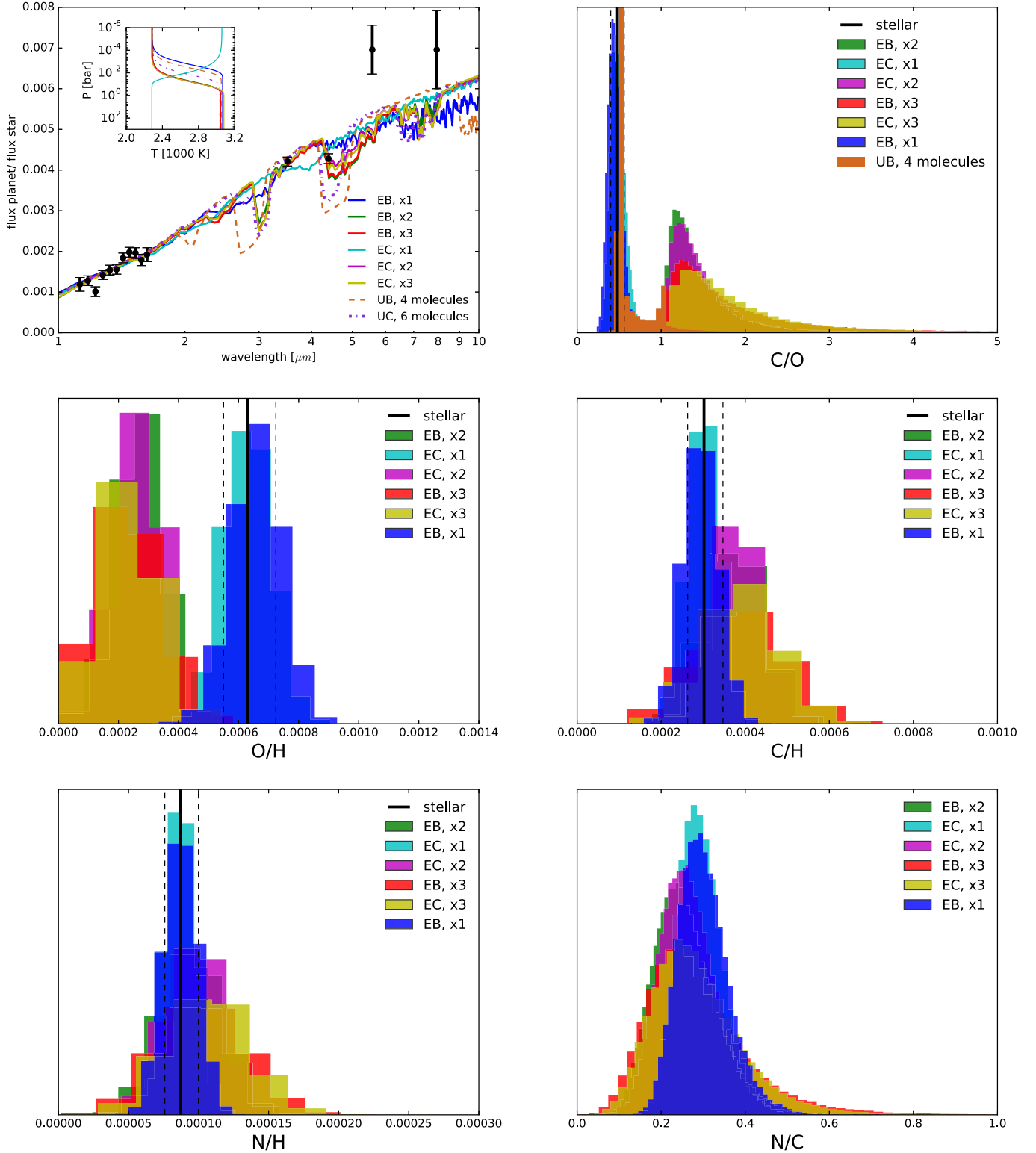
Figure 4. Best-fit spectra (top left panel) and the posterior distributions of C/O (top right panel), O/H (middle left panel), C/H (middle right panel), N/H (bottom left panel), and N/C (bottom right panel) for the six retrieval models with equilibrium chemistry. The cloudfree and cloudy models are labeled "EB" and "EC," respectively. The models labeled "×1," "×2," and "×3" adopt Gaussian widths on the prior distributions of the elemental abundances that are once, twice, and thrice the measurement errors of the stellar elemental abundances, respectively. The model labeled "UB, 4 molecules" assumes unconstrained chemistry and a cloudfree atmosphere with CO, CO_2, H_2O, and CH_4 only and is included as a reference to models previously published in the literature. The model labeled "UC, 6 molecules" assumes unconstrained chemistry and a cloudy atmosphere and is included for completeness as it gives an unrealistic/unphysical abundance for HCN. The marginal posterior distributions are all normalized to have unity area. Note that the C/O ≈ 0.5 peak for the "UB, 4 molecules" model extends beyond the plot and we have truncated it for clarity.

Motivated by the calculations in Figure 1, we enforce chemical equilibrium as a prior. Instead of log-uniform priors, we now set Gaussian priors on the elemental abundances, based on the measured[8] WASP-12 values by Teske et al. (2014): $C/H_\star = 3.02^{+0.45}_{-0.39} \times 10^{-4}$ and $O/H_\star = 6.31^{+0.93}_{-0.81} \times 10^{-4}$. Since Teske et al. (2014) did not report measured N/H values, we use $N/O_\odot = 0.138$ (Lodders 2003) to transform O/H into $N/H_\star = 8.71^{+1.28}_{-1.12} \times 10^{-5}$. We additionally compute models with Gaussian widths that are twice and thrice the measurement errors. The top panel of Figure 4 shows that the cloudfree model with $\times 1$ the measurement error as the Gaussian width produces a posterior distribution of C/O that is unsurprisingly peaked at the measured $C/O_\star = 0.48$ value of WASP-12. In other words, we simply reproduce the (tight) prior. Of greater interest are the posterior distributions when the widths of the Gaussian priors are doubled or tripled, which peak just above a C/O value of unity and trail off as it becomes 2–3. This outcome of a carbon-rich dayside atmosphere of WASP-12b is independent of whether clouds are included in the analysis, because the cloud layer is optically thin. The posterior distribution of O/H is substellar, while that of C/H is slightly superstellar but still consistent with being stellar. Our posterior distributions for C/H, O/H, and C/O are broadly consistent with those reported by Madhusudhan et al. (2011, 2014). We note that increasing the Gaussian widths of the priors to eight times the measurement errors does not alter our qualitative conclusions (not shown).

Another surprising outcome of this set of six retrievals is the shape of the temperature–pressure profile (bottom panel of Figure 4). While the best-fit spectra look similar among the six different cases, the temperature–pressure profile for the cloudy $\times 1$ model exhibits a temperature inversion that is entirely driven by the retrieval attempting to fit the four Spitzer photometric points. When the Gaussian width on the priors is doubled or tripled, the temperature inversion disappears. For illustration, the top panel of Figure 5 shows the posterior distributions for the cloudy case with $\times 2$ the measurement errors for the Gaussian width of the priors.

4. Discussion

4.1. Implications for Formation and Comparison to Previous Studies

Generally, it is challenging to make a hot Jupiter with substellar O/H (Brewer et al. 2017). Several studies have previously explored the link between the formation and migration history of hot Jupiters and their atmospheric chemistry. Madhusudhan et al. (2014) predicted that the formation of gas-giant exoplanets at large orbital distances via gravitational instability, from a solar-composition proto-planetary disk, and their subsequent migration inward via disk-free mechanisms produces hot Jupiters with stellar C/H, substellar O/H, and superstellar C/O. Our retrieval outcomes are consistent with this scenario. If the disk is instead constructed with molecular abundances based on observations of ice and gas in protoplanetary disks (Öberg et al. 2011), then it produces hot Jupiters with C/H and O/H that are both substellar. Core accretion with disk-free migration produces C/H and O/H that are either both substellar, both stellar, or both superstellar—neither of these scenarios are consistent with
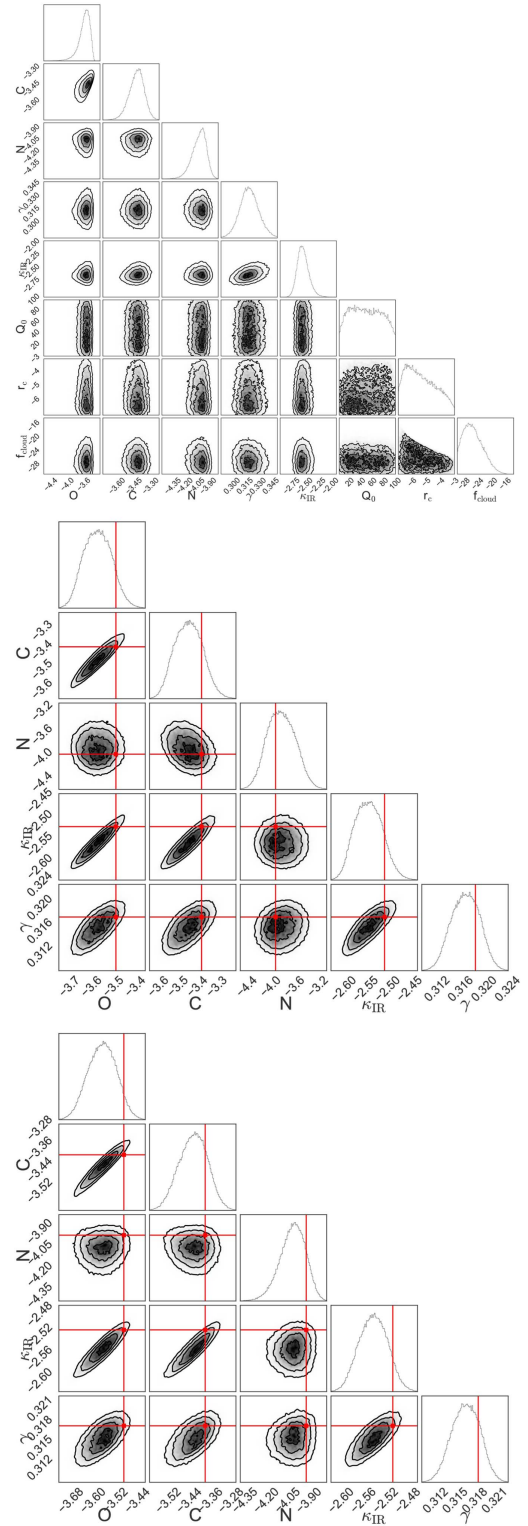

Figure 5. Posterior distributions of fitting parameters for the equilibrium-chemistry model. κ_{IR} has physical units of $m^2\ kg^{-1}$, while r_c is given in m. The rest of the parameters are dimensionless. Top panel: retrieval on WFC3 and *Spitzer* data with a Gaussian width on the prior distribution of the elemental abundances that is twice the measurement error of the stellar elemental abundances (i.e., the "EC, $\times 2$" model). Middle panel: retrieval on mock *JWST* data (see the text for more details) for EB, $\times 2$ cloudfree model. Bottom panel: cloudfree retrieval on mock *JWST* data with log-uniform priors. For the retrievals on mock data, the input values of parameters are given by the straight lines.

our retrieval outcomes. Core accretion with disk migration produces superstellar values for both C/H and O/H.

An active topic of debate concerns the role of pebbles in the protoplanetary disk (Ormel & Klahr 2010; Lambrechts & Johansen 2012). Pebbles are intermediate-sized solids with Stokes numbers on the order of unity, which are imperfectly coupled to the disk gas; their exact sizes are a function of the local conditions of the disk. The drift of pebbles across the CO_2, CO, and H_2O snowlines is capable of locally altering the values of C/H, O/H, and C/O in a disk (Öberg & Bergin 2016). The key difference between pebbles and regular planetesimals is that, to zeroth order, pebbles are purportedly able to accrete onto the core of the exoplanet directly without polluting the atmosphere, implying that the elemental abundances range from being substellar to stellar. In the scenario depicted by Madhusudhan et al. (2017), hot Jupiters accrete most of their gas within the H_2O snowline (Ali-Dib et al. 2014), which naturally yields a stellar C/H, substellar O/H, and superstellar $C/O \approx 0.7$–0.8. At face value, this is at odds with our finding that $C/O \approx 1$–2. Any erosion of the core tends to drive C/H and O/H to superstellar values and C/O to substellar values, further increasing the discrepancy between the theoretical prediction and our inferred posterior distributions. An alternative scenario is that WASP-12b formed at large orbital distances (as a cold Jupiter) via pebble accretion and migrated inward via a disk-free mechanism. In such a scenario, Madhusudhan et al. (2017) predict $O/H \approx 0.2$–0.5 $O/H_\star$, $C/H \approx 0.5$–0.9 $C/H_\star$, and $C/O \approx 1$. Our retrieved posterior distributions are consistent with such a scenario. Based on the inferred substellar O/H and superstellar C/O values, Brewer et al. (2017) claimed another hot Jupiter, HD 209458b, to also have undergone disk-free migration.

We note that WASP-12b is part of a triple-star system (Bechter et al. 2014) and has a measured spin–orbit alignment of 59^{+15}_{-20} degrees, which may be consistent with the disk-free migration scenario.

Our retrieved posterior distributions are inconsistent with the in situ formation of WASP-12b (Batygin et al. 2016; Boley et al. 2016), which Madhusudhan et al. (2017) predict to yield $O/H \approx 0.8$–1.5 $O/H_\star$, $C/H \approx C/H_\star$, and $C/O \approx 0.4$–0.7. Ali-Dib (2017) suggests that to produce $C/O \gtrsim 1$ via in situ formation requires that the parent star has $C/O \approx 0.8$.

Generally, our finding of substellar values for O/H provides counter-evidence against late-time planetesimal accretion or core erosion. Both processes would enrich the atmosphere of WASP-12b to beyond its stellar values. Furthermore, the posterior distribution of N/C, which is consistent with being solar (Lodders 2003), provides clues on the original site of formation in the outer protoplanetary disk (Öberg & Bergin 2016).

4.2. Are Retrievals of James Webb Space Telescope (JWST) Data in the Prior-dominated Regime?

Our findings beg the question: are retrievals of *JWST* spectra also in the prior-dominated regime? To address it specifically for WASP-12b, we produce mock spectra with a resolution of 100 over the wavelength range of 0.7–5 μm. We assume measurement uncertainties of 100 ppm. The middle and bottom panels of Figure 5 show the posterior distributions of parameters from retrievals assuming log-uniform and Gaussian priors, respectively. In both cases, the retrieved parameter

values are essentially the same and within $\sim$30% of the true (input) values, suggesting that the interpretation of *JWST* spectra will not be in the prior-dominated regime.

ORCID iDs

Baptiste Lavie ⓘ https://orcid.org/0000-0001-8884-9276
Simon L. Grimm ⓘ https://orcid.org/0000-0002-0632-4407
Shang-Min Tsai ⓘ https://orcid.org/0000-0002-8163-4608
Matej Malik ⓘ https://orcid.org/0000-0002-2110-6694
Brice-Olivier Demory ⓘ https://orcid.org/0000-0002-9355-5165
Christoph Mordasini ⓘ https://orcid.org/0000-0002-1013-2811
Yann Alibert ⓘ https://orcid.org/0000-0002-4644-8818
Sascha P. Quanz ⓘ https://orcid.org/0000-0003-3829-7412
Roberto Trotta ⓘ https://orcid.org/0000-0002-3415-0707
Kevin Heng ⓘ https://orcid.org/0000-0003-1907-5910

References

Ali-Dib, M. 2017, MNRAS, 467, 2845
Ali-Dib, M., Mousis, O., Petit, J.-M., & Lunine, J. I. 2014, ApJ, 785, 125
Barber, R. J., Tennyson, J., Harris, G. J., & Tolchenov, R. N. 2006, MNRAS, 368, 1087
Batygin, K., Bodenheimer, P. H., & Laughlin, G. P. 2016, ApJ, 829, 114
Bechter, E. B., Crepp, J. R., Ngo, H., et al. 2014, ApJ, 788, 2
Boley, A. C., Granados Contreras, A. P., & Gladman, B. 2016, ApJL, 817, L17
Brewer, J. M., & Fischer, D. A. 2016, ApJ, 831, 20
Brewer, J. M., Fischer, D. A., & Madhusudhan, N. 2017, AJ, 153, 83
Chan, T., Ingemyr, M., Winn, J. N., et al. 2011, AJ, 141, 179
Espinoza, N., Fortney, J. J., Miguel, Y., Thorngren, D., & Murray-Clay, R. 2017, ApJL, 838, L9
Feroz, F., Hobson, M. P., & Bridges, M. 2009, MNRAS, 398, 1601
Fortney, J. J., Robinson, T. D., Domagal-Goldman, S., et al. 2016, arXiv:1602.06305
Grimm, S. L., & Heng, K. 2015, ApJ, 808, 182
Guillot, T. 2010, A&A, 520, A27
Hebb, L., Collier-Cameron, A., Loeillet, B., et al. 2009, ApJ, 693, 1920
Heng, K., Hayek, W., Pont, F., & Sing, D. K. 2012, MNRAS, 420, 20
Heng, K., & Lyons, J. R. 2016, ApJ, 817, 149
Heng, K., Mendonça, J. M., & Lee, J.-M. 2014, ApJS, 215, 4
Heng, K., & Tsai, S.-M. 2016, ApJ, 829, 104
Kreidberg, L., Line, M. R., Bean, J. L., et al. 2015, ApJ, 814, 66
Lambrechts, M., & Johansen, A. 2012, A&A, 544, A32
Lavie, B., Mendonça, J. M., Mordasini, C., et al. 2017, AJ, 154, 91
Lee, J.-M., Heng, K., & Irwin, P. G. J. 2013, ApJ, 778, 97
Line, M. R., Knutson, H., Wolf, A. S., & Yung, Y. L. 2014, ApJ, 783, 70
Line, M. R., Wolf, A. S., Zhang, X., et al. 2013, ApJ, 775, 137
Lodders, K. 2003, ApJ, 591, 1220
Madhusudhan, N. 2012, ApJ, 758, 36
Madhusudhan, N., Amin, M. A., & Kennedy, G. M. 2014, ApJL, 794, L12
Madhusudhan, N., Betram, B., Johansen, A., & Eriksson, L. 2017, MNRAS, 469, 4102
Madhusudhan, N., Crouzet, N., McCullough, P. R., Deming, D., & Hedges, C. 2014, ApJL, 791, L9
Madhusudhan, N., Harrington, J., Stevenson, K. B., et al. 2011, Natur, 469, 64
Mordasini, C., van Boekel, R., Mollière, P., Henning, Th., & Benneke, B. 2016, ApJ, 832, 41
Moses, J. I., Madhusudhan, N., Visscher, C., & Freedman, R. S. 2013, ApJ, 763, 25
Öberg, K. I., & Bergin, E. A. 2016, ApJL, 831, L19
Öberg, K. I., Murray-Clay, R., & Bergin, E. A. 2011, ApJL, 743, L16
Ormel, C. W., & Klahr, H. H. 2010, A&A, 520, A43

Pierrehumbert, R. T. 2010, Principles of Planetary Climate (New York: Cambridge Univ. Press)

Rothman, L. S., Gordon, I. E., Babikov, Y., et al. 2013, JQSRT, 130, 4

Rothman, L. S., Gordon, I. E., Barber, R. J., et al. 2010, JQSRT, 111, 2139

Rothman, L. S., Rinsland, C. P., Goldman, A., et al. 1996, JQSRT, 60, 665

Stevenson, K. B., Bean, J. L., Madhusudhan, N., & Harrington, J. 2014, ApJ, 791, 36

Teske, J. K., Cunha, K., Smith, V. V., Schuler, S. C., & Griffith, C. A. 2014, ApJ, 788, 39

Trotta, R. 2008, ConPh, 49, 71

Tsai, S.-M., Lyons, J. R., Grosheintz, L., Rimmer, P. B., Kitzmann, D., & Heng, K. 2017, ApJS, 228, 20

Yurchenko, S. N., & Tennyson, J. 2014, MNRAS, 440, 1649

Yurchenko, S. N., Tennyson, J., Barber, R. J., & Thiel, W. 2013, JMoSp, 291, 69

3.5 Other papers

CrossMark

HELIOS: AN OPEN-SOURCE, GPU-ACCELERATED RADIATIVE TRANSFER CODE FOR SELF-CONSISTENT EXOPLANETARY ATMOSPHERES

MATEJ MALIK[1], LUC GROSHEINTZ[1], JOÃO M. MENDONÇA[1], SIMON L. GRIMM[1,2], BAPTISTE LAVIE[1],
DANIEL KITZMANN[1], SHANG-MIN TSAI[1], ADAM BURROWS[3], LAURA KREIDBERG[4,5], MEGAN BEDELL[4],
JACOB L. BEAN[4], KEVIN B. STEVENSON[4], AND KEVIN HENG[1]
[1] University of Bern, Center for Space and Habitability, Sidlerstrasse 5, CH-3012, Bern, Switzerland;
matej.malik@csh.unibe.ch, kevin.heng@csh.unibe.ch
[2] University of Zürich, Institute for Computational Science, Winterthurerstrasse 190, CH-8057 Zürich, Switzerland
[3] Department of Astrophysical Sciences, Princeton University Peyton Hall, Princeton, NJ 08544, USA
[4] Department of Astronomy and Astrophysics, University of Chicago, 5640 S. Ellis Avenue, Chicago, IL 60637, USA
[5] Harvard-Smithsonian Center for Astrophysics, 60 Garden Street, Cambridge, MA 02138, USA

ABSTRACT

We present the open-source radiative transfer code named HELIOS, which is constructed for studying exoplanetary atmospheres. In its initial version, the model atmospheres of HELIOS are one-dimensional and plane-parallel, and the equation of radiative transfer is solved in the two-stream approximation with nonisotropic scattering. A small set of the main infrared absorbers is employed, computed with the opacity calculator HELIOS−K and combined using a correlated-k approximation. The molecular abundances originate from validated analytical formulae for equilibrium chemistry. We compare HELIOS with the work of Miller-Ricci & Fortney using a model of GJ 1214b, and perform several tests, where we find: model atmospheres with single-temperature layers struggle to converge to radiative equilibrium; k-distribution tables constructed with $\gtrsim 0.01\,\mathrm{cm}^{-1}$ resolution in the opacity function ($\lesssim 10^3$ points per wavenumber bin) may result in errors $\gtrsim 1\%$–10% in the synthetic spectra; and a diffusivity factor of 2 approximates well the exact radiative transfer solution in the limit of pure absorption. We construct "null-hypothesis" models (chemical equilibrium, radiative equilibrium, and solar elemental abundances) for six hot Jupiters. We find that the dayside emission spectra of HD 189733b and WASP-43b are consistent with the null hypothesis, while the latter consistently underpredicts the observed fluxes of WASP-8b, WASP-12b, WASP-14b, and WASP-33b. We demonstrate that our results are somewhat insensitive to the choice of stellar models (blackbody, Kurucz, or PHOENIX) and metallicity, but are strongly affected by higher carbon-to-oxygen ratios. The code is publicly available as part of the Exoclimes Simulation Platform (exoclime.net).

Key words: methods: numerical – planets and satellites: atmospheres – radiative transfer

1. INTRODUCTION

The past few years have been marked by a slow, but steady, shift from the era of the detections of exoplanets to the new age of the characterization of their atmospheres. Exoplanets transiting in front of their host stars allow for atmospheric features to be imprinted onto the total system light (Seager & Sasselov 2000; Brown et al. 2001; Charbonneau et al. 2002). Secondary eclipses allow for photons from the exoplanetary atmosphere to be directly measured (Charbonneau et al. 2005; Deming et al. 2005). Extracting the spectroscopic signatures of these exoplanetary atmospheres is a challenging task, because they are typically many orders of magnitude fainter than the light from their host stars. Interpreting these signatures requires a profound understanding of radiative transfer and atmospheric chemistry, in order to infer the thermal structure and atomic/molecular abundances of the atmosphere from the data.

Hot Jupiters are particularly accessible to atmospheric characterization via transits and eclipses. They are hardly 1D objects, but a reasonable first approach is to study them using 1D, plane-parallel model atmospheres (Sudarsky et al. 2003; Barman et al. 2005; Fortney et al. 2005, 2006, 2008, 2010; Burrows et al. 2006, 2007, 2008), which may be used to mimic the dayside- or nightside-integrated emission. The simplest model one may construct of a dayside emission spectrum

(besides a Planck function) is a 1D model with an atmosphere in radiative and chemical equilibrium, if one neglects the effects of atmospheric dynamics and photochemistry. Despite these simplifications, there are several nontrivial demands associated with such a model: it should be able to consider a rich variety of chemistries, metallicities, irradiation fluxes from the star, and internal heat fluxes from the interior of the exoplanet. It should be able to take, as an input, arbitrary combinations of molecules and their opacities. The synthetic spectrum computed should be highly customizable, such that it may be readily compared to both photometric and spectroscopic data, often combined in a heterogeneous way across wavelength. To explore such a broad range of parameter space, the numerical implementation of a model (in short, the "code") needs to solve for radiative equilibrium very efficiently and also allow for numerical convergence to be checked in several different ways: number of model layers, spectral resolution of opacity function, number of wavelength bins used, etc. Such a code forms the basis of a flexible radiation package that one may couple to a chemical kinetics code or a 3D general circulation model. The challenges of constructing a 1D radiative–convective model are also discussed in the review article by Marley & Robinson (2015), where the "convective" part stands for the additional consideration of convective stability, which marks the next step in sophistication of an atmospheric model.

In-depth study of moderately young but extremely red, very dusty substellar companion HD 206893B[*]

P. Delorme[1],[**], T. Schmidt[2], M. Bonnefoy[1], S. Desidera[3], C. Ginski[4, 26], B. Charnay[2], C. Lazzoni[3], V. Christiaens[5, 23], S. Messina[6], V. D'Orazi[3], J. Milli[7], J. E. Schlieder[8, 9], R. Gratton[3], L. Rodet[1], A.-M. Lagrange[1], O. Absil[5],[***], A. Vigan[10], R. Galicher[2], J. Hagelberg[1], M. Bonavita[11], B. Lavie[22, 12], A. Zurlo[10, 13], J. Olofsson[8, 14], A. Boccaletti[2], F. Cantalloube[8], D. Mouillet[1], G. Chauvin[1], F.-J. Hambsch[15], M. Langlois[25, 10], S. Udry[22], T. Henning[8], J.-L. Beuzit[1], C. Mordasini[12], P. Lucas[16], F. Marocco[16], B. Biller[24], J. Carson[8, 17], A. Cheetham[22], E. Covino[18], V. De Caprio[18], A. Delboulbe[1], M. Feldt[8], J. Girard[7], N. Hubin[19], A.-L. Maire[8], A. Pavlov[8], C. Petit[20], D. Rouan[2], R. Roelfsema[21], and F. Wildi[22]

(Affiliations can be found after the references)

ABSTRACT

Context. The substellar companion HD 206893b has recently been discovered by direct imaging of its disc-bearing host star with the Spectro-Polarimetric High-contrast Exoplanet REsearch (SPHERE) instrument.

Aims. We investigate the atypical properties of the companion, which has the reddest near-infrared colours among all known substellar objects, either orbiting a star or isolated, and we provide a comprehensive characterisation of the host star-disc-companion system.

Methods. We conducted a follow-up of the companion with adaptive optics imaging and spectro-imaging with SPHERE, and a multi-instrument follow-up of its host star. We obtain a $R = 30$ spectrum from 0.95 to 1.64 μm of the companion and additional photometry at 2.11 and 2.25 μm. We carried out extensive atmosphere model fitting for the companions and the host star in order to derive their age, mass, and metallicity.

Results. We found no additional companion in the system in spite of exquisite observing conditions resulting in sensitivity to 6 M_{Jup} (2 M_{Jup}) at 0.5″ for an age of 300 Myr (50 Myr). We detect orbital motion over more than one year and characterise the possible Keplerian orbits. We constrain the age of the system to a minimum of 50 Myr and a maximum of 700 Myr, and determine that the host-star metallicity is nearly solar. The comparison of the companion spectrum and photometry to model atmospheres indicates that the companion is an extremely dusty late L dwarf, with an intermediate gravity (log $g \sim$ 4.5–5.0) which is compatible with the independent age estimate of the system.

Conclusions. Though our best fit corresponds to a brown dwarf of 15–30 M_{Jup} aged 100–300 Myr, our analysis is also compatible with a range of masses and ages going from a 50 Myr 12 M_{Jup} planetary-mass object to a 50 M_{Jup} Hyades-age brown dwarf. Even though this companion is extremely red, we note that it is more probable that it has an intermediate gravity rather than the very low gravity that is often associated with very red L dwarfs. We also find that the detected companion cannot shape the observed outer debris disc, hinting that one or several additional planetary mass objects in the system might be necessary to explain the position of the disc inner edge.

Key words. brown dwarfs – planets and satellites: atmospheres – techniques: high angular resolution – planet-disk interactions

1. Introduction

The discovery of young extrasolar giant planets found with high-contrast imaging techniques (Chauvin et al. 2004; Marois et al. 2008; Lagrange et al. 2010; Rameau et al. 2013; Delorme et al. 2013; Bailey et al. 2014; Macintosh et al. 2015; Gauza et al. 2015) offers the opportunity to directly probe the properties of their photosphere. The improved contrast and spectroscopic capabilities of the new generation of adaptive optics (AO) instruments such as Spectro-Polarimetric High-contrast Exoplanet REsearch (SPHERE; Beuzit et al. 2008) and GPI (Macintosh et al. 2012) have made it possible to study the molecular composition and physical processes taking place in

the atmospheres of extrasolar giant planets (Zurlo et al. 2016; Bonnefoy et al. 2016; Vigan et al. 2016; De Rosa et al. 2016; Chilcote et al. 2017).

These previous studies have shown that while young exoplanets have a spectral signature quite distinct from field brown dwarfs of equivalent effective temperature, they have many atmospheric properties in common with isolated brown dwarfs recently identified in young moving groups (Liu et al. 2013; Gagné et al. 2015a; Aller et al. 2016; Faherty et al. 2016). They notably share a very red spectral energy distribution (SED) in the near-infrared (NIR) that can be attributed to the presence of very thick dust clouds in their photosphere. This trend was qualitatively expected by atmosphere models because the lower surface gravity of these planetary mass objects inhibits dust settling and naturally increases the dust content within the photosphere. However, all atmosphere models fail to quantitatively match the very red NIR colours of young planetary mass objects via a self-consistent physical model, and have to resort to parametrising the sedimentation efficiency of the dust to match these observations, as done for instance in the *Dusty* models where there is no dust settling (Allard et al. 2001) or the parametrised cloud

The GJ 504 system revisited

Combining interferometric, radial velocity, and high contrast imaging data⋆

M. Bonnefoy[1], K. Perraut[1], A.-M. Lagrange[1], P. Delorme[1], A. Vigan[2], M. Line[3], L. Rodet[1], C. Ginski[4], D. Mourard[5], G.-D. Marleau[6], M. Samland[7], P. Tremblin[8], R. Ligi[9], F. Cantalloube[7], P. Mollière[4], B. Charnay[10], M. Kuzuhara[11, 12], M. Janson[13], C. Morley[14], D. Homeier[15], V. D'Orazi[16], H .Klahr[7], C. Mordasini[6], B. Lavie[17, 6], J.-L. Baudino[9, 18], H. Beust[1], S. Peretti[17], A. Musso Bartucci[7], D. Mesa[16, 19], B. Bézard[10], A. Boccaletti[10], R. Galicher[10], J. Hagelberg[17, 20], S. Desidera[16], B. Biller[7, 21], A.-L. Maire[7], F. Allard[15], S. Borgniet[10], J. Lannier[1], N. Meunier[1], M. Desort[1], E. Alecian[1], G. Chauvin[1, 22], M. Langlois[15], T. Henning[7], L. Mugnier[23], D. Mouillet[1], R. Gratton[16], T. Brandt[24], M. Mc Elwain[25], J.-L. Beuzit[1], M. Tamura[11, 12, 26], Y. Hori[11, 12], W. Brandner[7], E. Buenzli[7], A Cheetham[17], M. Cudel[1], M. Feldt[7], M. Kasper[1, 27], M. Keppler[7], T. Kopytova[1, 3], M. Meyer[28, 29], C. Perrot[10], D. Rouan[10], G Salter[2], T. Schmidt[10], E. Sissa[16], A. Zurlo[2, 30, 31], F. Wildi[17], P. Blanchard[2], V. De Caprio[16], A. Delboulbé[1], D. Maurel[1], T. Moulin[1], A. Pavlov[7], P. Rabou[1], J. Ramos[7], R. Roelfsema[32], G. Rousset[10], E. Stadler[1], F. Rigal[32], L. Weber[17]

(Affiliations can be found after the references)

ABSTRACT

Context. The G-type star GJ504A is known to host a 3 to 35 M$_{Jup}$ companion whose temperature, mass, and projected separation all contribute to making it a test case for planet formation theories and atmospheric models of giant planets and light brown dwarfs.

Aims. We aim at revisiting the system age, architecture, and companion physical and chemical properties using new complementary interferometric, radial-velocity, and high-contrast imaging data.

Methods. We used the CHARA interferometer to measure GJ504A's angular diameter and obtained an estimation of its radius in combination with the Hipparcos parallax. The radius was compared to evolutionary tracks to infer a new independent age range for the system. We collected dual imaging data with IRDIS on VLT/SPHERE to sample the NIR (1.02-2.25μm) spectral energy distribution (SED) of the companion. The SED was compared to five independent grids of atmospheric models (`petitCODE`, `Exo-REM`, `BT-SETTL`, Morley et al., and `ATMO`) to infer the atmospheric parameters of GJ 504b and evaluate model-to-model systematic errors. In addition, we used a specific model grid exploring the effect of different C/O ratios. Contrast limits from 2011 to 2017 were combined with radial velocity data of the host star through the `MESS2` tool to define upper limits on the mass of additional companions in the system from 0.01 to 100 au. We used an MCMC fitting tool to constrain the companion's orbital parameters based on the measured astrometry, and dedicated formation models to investigate its origin.

Results. We report a radius of 1.35 ± 0.04 R$_\odot$ for GJ504A. The radius yields isochronal ages of 21 ± 2 Myr or 4.0 ± 1.8 Gyr for the system and line-of-sight stellar rotation axis inclination of 162.4$^{+3.8}_{-4.3}$ degrees or 18.6$^{+4.3}_{-3.8}$ degrees. We re-detect the companion in the Y2, Y3, J3, H2, and K1 dual-band images. The complete 1-4 μm SED shape of GJ504b is best reproduced by T8-T9.5 objects with intermediate ages (≤ 1.5Gyr), and/or unusual dusty atmospheres and/or super-solar metallicities. All atmospheric models yield T$_{eff}$ = 550 ± 50K for GJ504b and point toward a low surface gravity (3.5-4.0 dex). The accuracy on the metallicity value is limited by model-to-model systematics; it is not degenerate with the C/O ratio. We derive log L/L$_\odot$ = −6.15 ± 0.15 dex for the companion from the empirical analysis and spectral synthesis. The luminosity and T$_{eff}$ yield masses of M = 1.3$^{+0.6}_{-0.3}$M$_{Jup}$ and M = 23$^{+10}_{-9}$M$_{Jup}$ for the young and old age ranges, respectively. The semi-major axis (sma) is above 27.8 au and the eccentricity is lower than 0.55. The posterior on GJ 504b's orbital inclination suggests a misalignment with the rotation axis of GJ 504A. We exclude additional objects (90% prob.) more massive than 2.5 and 30 M$_{Jup}$ with semi-major axes in the range 0.01-80 au for the young and old isochronal ages, respectively.

Conclusions. The mass and semi-major axis of GJ 504b are marginally compatible with a formation by disk-instability if the system is 4 Gyr old. The companion is in the envelope of the population of planets synthesized with our core-accretion model. Additional deep imaging and spectroscopic data with SPHERE and JWST should help to confirm the possible spin-orbit misalignment and refine the estimates on the companion temperature, luminosity, and atmospheric composition.

Key words. Techniques: high angular resolution, interferometric, radial velocities; Stars: fundamental parameters, planetary systems, brown dwarfs, individual: GJ 504; Planets and satellites: atmospheres, formation

1. Introduction

The most recent formation and dynamical evolution models of the solar system (e.g., Walsh et al. 2011; Raymond & Izidoro 2017) propose that the wide-orbit giant planets (Jupiter, Saturn) have largely influenced the composition and/or the architecture of the inner solar system. Those models are guided by the population of exoplanets established below ~8 au mainly

Imaging radial velocity planets with SPHERE

A. Zurlo,[1,2,3]★ D. Mesa,[4,5] S. Desidera,[5] S. Messina,[6] R. Gratton,[5] C. Moutou,[3]
J.-L. Beuzit,[7] B. Biller,[8] A. Boccaletti,[9] M. Bonavita,[8] M. Bonnefoy,[7] T. Bhowmik,[9]
W. Brandner,[10] E. Buenzli,[11] G. Chauvin,[7] M. Cudel,[9] V. D'Orazi,[5] M. Feldt,[10]
J. Hagelberg,[12] M. Janson,[10,13] A.-M. Lagrange,[7] M. Langlois,[3,14] J. Lannier,[7]
B. Lavie,[12] C. Lazzoni,[5] A.-L. Maire,[10] M. Meyer,[15] D. Mouillet,[7] S. Peretti,[12]
C. Perrot,[9] P. J. Potiron,[16] G. Salter,[3] T. Schmidt,[9] E. Sissa,[5] A. Vigan,[3] A. Delboulbé,[7]
C. Petit,[17] J. Ramos,[10] F. Rigal[18] and S. Rochat[7]

Affiliations are listed at the end of the paper

ABSTRACT

We present observations with the planet finder Spectro-Polarimetric High-contrast Exoplanet REsearch (SPHERE) of a selected sample of the most promising radial velocity (RV) companions for high-contrast imaging. Using a Monte Carlo simulation to explore all the possible inclinations of the orbit of wide RV companions, we identified the systems with companions that could potentially be detected with SPHERE. We found the most favourable RV systems to observe are: HD 142, GJ 676, HD 39091, HIP 70849, and HD 30177 and carried out observations of these systems during SPHERE Guaranteed Time Observing. To reduce the intensity of the starlight and reveal faint companions, we used principal component analysis algorithms alongside angular and spectral differential imaging. We injected synthetic planets with known flux to evaluate the self-subtraction caused by our data reduction and to determine the 5σ contrast in the J band versus separation for our reduced images. We estimated the upper limit on detectable companion mass around the selected stars from the contrast plot obtained from our data reduction. Although our observations enabled contrasts larger than 15 mag at a few tenths of arcsec from the host stars, we detected no planets. However, we were able to set upper mass limits around the stars using AMES-COND evolutionary models. We can exclude the presence of companions more massive than 25–28 $M_{\rm Jup}$ around these stars, confirming the substellar nature of these RV companions.

Key words: instrumentation: spectrographs – methods: data analysis – techniques: imaging spectroscopy – techniques: radial velocities – stars: individual: HD 142, HIP 70849, GJ 676A, HD 39091 – planetary systems.

1 INTRODUCTION

So far, 751 planets have been discovered with the radial velocity (RV) technique.[1] As stellar activity also produces RV variability and can mimic planet signals, these objects' hosts are old and non-active stars. This method can detect both close planets and massive long-period objects, but, due to the unknown inclination of the detected companions, only the minimum mass can be determined. The measured parameter is the mass of the companion multiplied by the sine of the inclination of its orbit, $M\sin i$. As the inclination is unknown from the RV measurements alone, the real mass of the object cannot be directly measured using this technique alone. Combining RV and high-contrast imaging measurements of the same companion allows us to constrain the companion orbit and thus measure its dynamical mass (see e.g. Boden, Torres & Latham 2006), providing a crucial benchmark for evolutionary models of substellar objects (e.g. Baraffe et al. 2015).

In the last years, a number of surveys have been conducted to image previously detected RV companion objects on wide orbits, for instance, direct imaging observations of targets with RV drifts from the High Accuracy Radial velocity Planet Searcher (HARPS) and CORALIE employing Very Large Telescope (VLT)/NACO (Hagel-

★ E-mail: alice.zurlo@mail.udp.cl
[1] www.exoplanet.eu

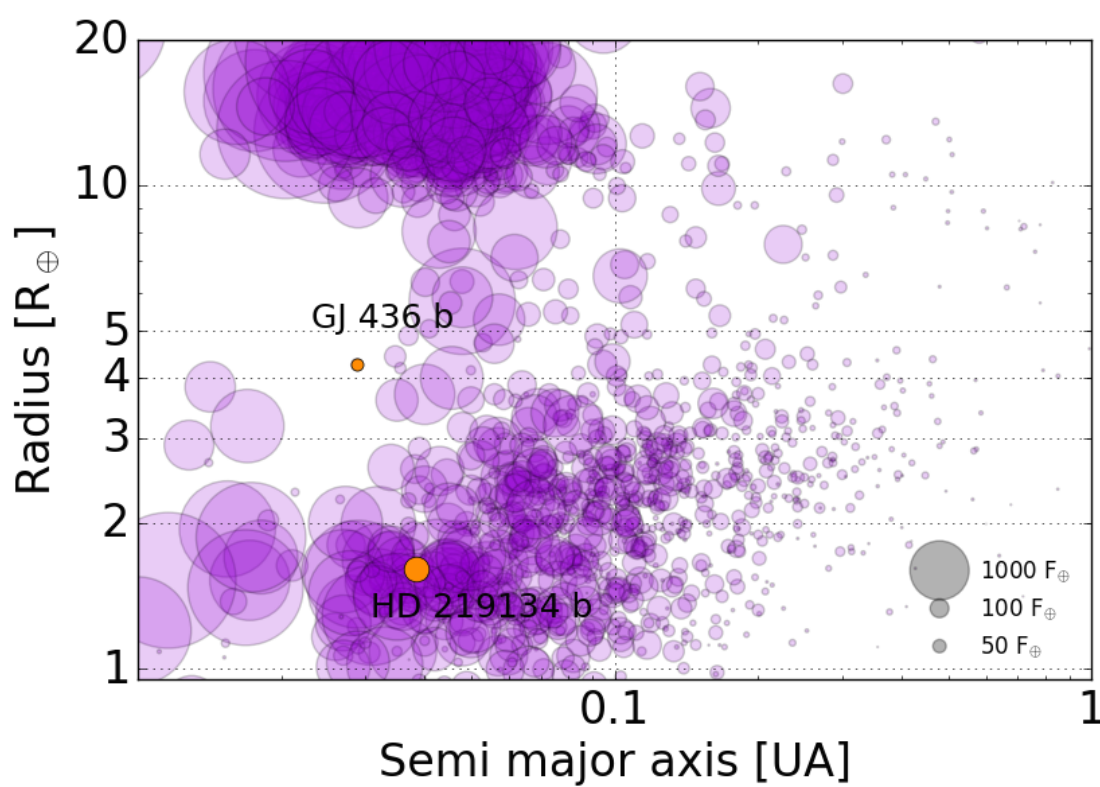# PROBING THE UPPER ATMOSPHERE - ATMOSPHERIC ESCAPE

With great power comes great responsibility
C'est toujours un succès

Uncle Ben

Misa brevis et spiritus maxima. Ça veut rien dire, mais je suis très en colère contre moi même.

Loth d'Orcanie

This chapter presents the analysis of observations in the far ultraviolet (FUV) of two stars, GJ 436 and HD 219134 during the transit of their inner most planets. The FUV is home to the Lyman-α (Lyα) line at 1 215.6702 Å of neutral hydrogen that have been used to bring out atmospheric escape of close-in planets (section 1.5). The warm Neptune GJ 436 b is already known to evaporate and is standing at the inner edge of the evaporation desert (Fig. 1.4). With a total of 27 orbits of the Hubble Space Telescope (*HST*), GJ 436 and its planet is the planetary system with the most complete set of observations in Lyα. Standing below the evaporation valley (Fig. 1.4), the super-Earth HD 219134 b belongs to the closest system known to have a close-in transiting super-Earth. Due to its proximity with Earth, HD 219134 b is the first planet to be observed in the FUV at high resolution with the Hubble Space Telescope (*HST*). Those properties make GJ 436 b and HD 219134 b unique planets to study atmospheric escape. Observations presented in this chapter are transmission spectrum. It is therefore the light of the star, eventually filtered by the upper atmosphere of the planet that is observed. The two three sections give some insights on the stellar atmosphere, *HST* and systematics correction needed when using this telescope. Those sections are common to the analysis of both planets, which are presented in the last sections of this chapter.

4.1 Stellar atmosphere

4.1.1 Formation of stellar spectral lines in the FUV

Stellar atmosphere can be divided into three part : the photosphere, the chromosphere and the corona. The photosphere is the sharp transition region where the gas suddenly becomes optically thin. It is the region where the continuum is emitted. The radiation is due to free-free processes in the hot gas and is well approximated by the blackbody model. The lower chromosphere lies above the photosphere and shows a smooth decrease in temperature until it reaches a minimum. Then the temperature starts to rise in the upper chromosphere until it reaches a transiting region where the temperature increases very rapidly to the corona region, which is a tenuous plasma at a very high temperature. As the lower part of the photospheric region radiates as a blackbody, absorption and emission lines are formed in the higher up layers depending on the temperature, see Fig. 2.8. Different elements can form in different part of the star atmosphere. In a more realistic stellar atmosphere model, a number of different layers can contribute to a spectral feature (Fig. 4.1).
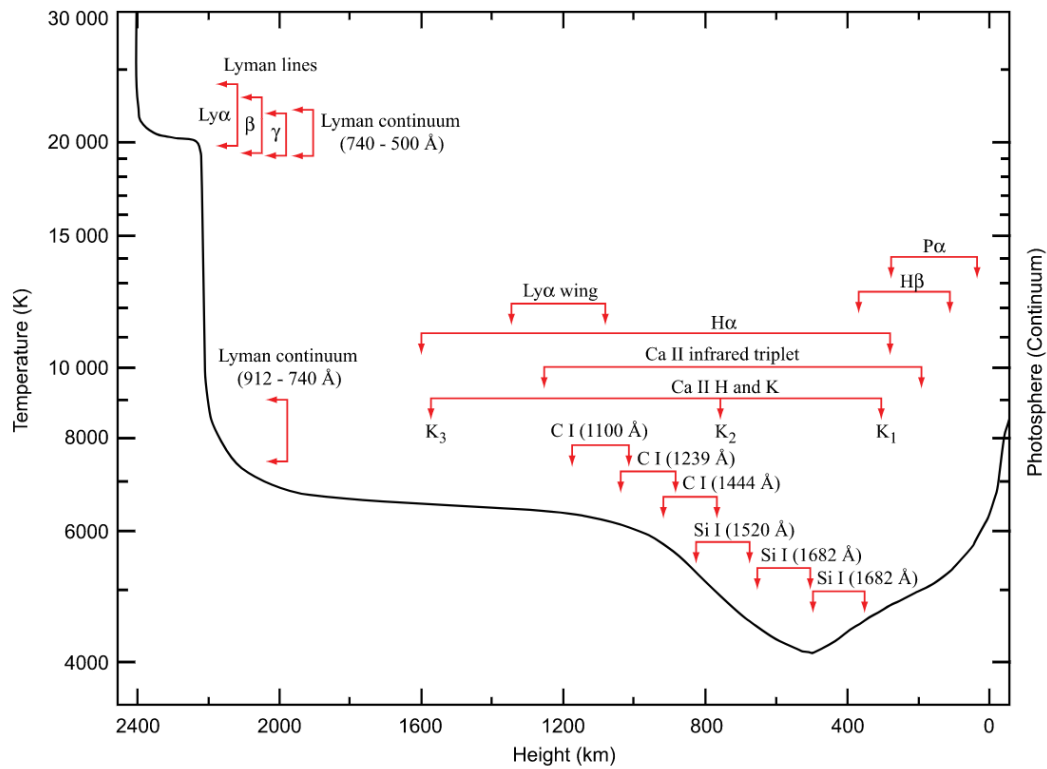
Figure 4.1: Formation layers of some chromospheric lines in the ultraviolet. Source: Gålfalk (2007)

The observed shape of a line is defined by a series of global and local physical mechanisms that occur in different layers of the stellar atmosphere (hence at a different temperature, pressure, velocity etc.) such as:

- The natural broadening comes from quantum mechanics and the Heisenberg's uncertainty principle.
- The thermal Doppler broadening comes from the different velocities of the gas particles that emit the radiation.
- The pressure broadening arise from the presence of nearby particles that affect the emission energy levels of atoms.
- The macroscopic movement of the star (for example the rotation) can induce a broadening effects due to the Doppler effect.

In the far ultraviolet part of the spectrum the blackbody continuum of G stars and later is very weak and emission lines dominate the spectrum.
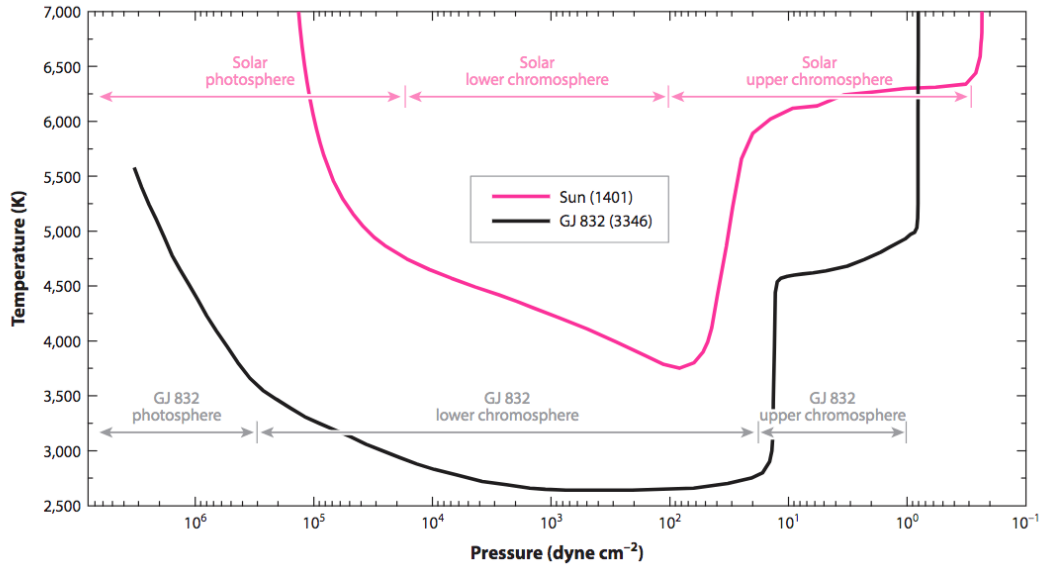
Figure 4.2: Comparison of the thermal structures from models of the Sun and the M dwarf GJ 832. Source: Fontenla et al. 2016; Linsky 2017

4.1.2   Emission lines in the FUV

The Lyman-α line

Hydrogen is the most abundant element in the Universe and since 1925 we know it is the main constituent of stars like our Sun (Payne 1925). The Lyman-α line (1 215.6702 Å) is the most intense spectral line of most abundant atom. It is therefore very important for astrophysics in general. The Lyman series are the transitions in the ultraviolet of the hydrogen atom when an electron goes from an energy level n $\geqslant$ 2 to the energy ground state level n = 1. The Lyman-α is the first line in this series and was discovered by Theodore Lyman (following Victor Schumann's - Schumann 1896) in its preliminary paper of 1904 (Lyman 1904a,b) and confirmed two years later (Lyman 1906). For an hydrogen atom to emit a Lyα photon it needs to have its electron in the 2p state. It can be made possible to excite the electron to a higher-level quantum state either by collisions with a free electron (part of its kinetic energy is transferred to the hydrogen atom) or by recombination (a free proton and a free electron recombined). Then a radiative cascade can occur giving rise to the emission of a Lyα photon Fig. 4.3 (Dijkstra 2017). In the FUV, the Lyα line dominates the spectrum by its intensity. For the coolest of stars - M-Dwarf, the blackbody continuum emission is shifted to the red and the Lyα line can represent more than 50% of the entire flux in the FUV (France et al. 2016). In some stars, the Lyα line presents a double peak (named self-reversal) due to the presence of hydrogen higher up (in regards to the emission layer) in the chromospheric region at a colder temperature (with a narrower width
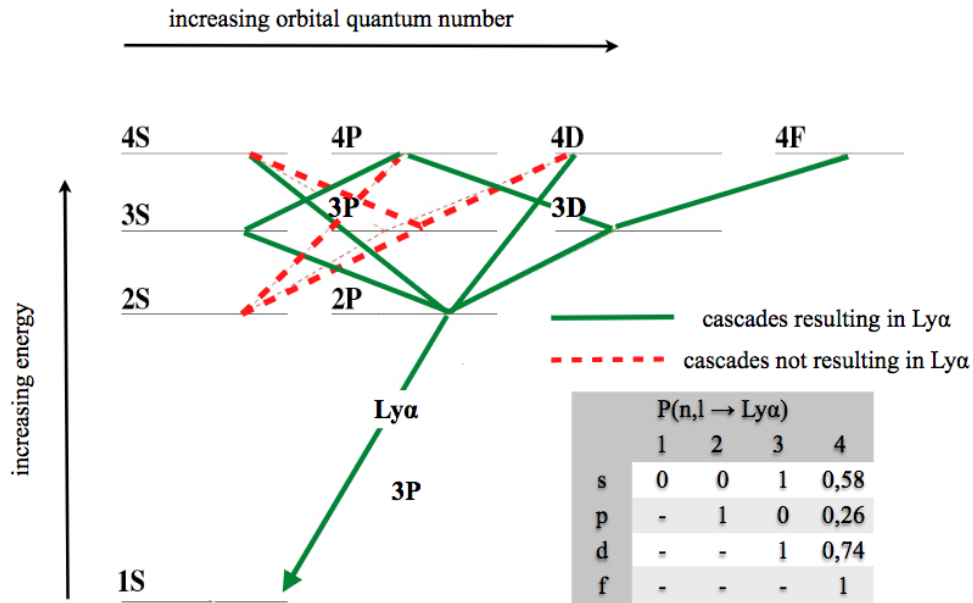
Figure 4.3: A schematic diagram of the energy levels of hydrogen atom. The energy of a quantum state increases from bottom to top. Each state is characterized by two quantum numbers n (principle quantum number) and l (orbital quantum number). Recombination can put atom in any state nl, which then undergoes a radiative cascade to the ground state (1S). Quantum selection rules dictate that the only permitted transitions have $\delta l = \pm 1$. These transitions are indicated in the Figure. Green lines [red dotted lines] show cascades that [do not] result in Lyα. The lower right panel shows that probability that a cascade from nl state results in Lyα. Source: Dijkstra 2014

profile) that will absorb the emission.

Other lines

The FUV spectrum of main sequence stars presents a numerous number of emission lines formed in the lower chromosphere (e.g. O I, C I, S I), in the upper chromosphere (C III,Mg II) or in the transition region (C IV,N V,O V,Si III), Linsky (2017). The stellar UV radiation is very important for the total energy budget and affects the photochemistry and composition of exoplanets' atmosphere, which impacts its evolution (see section 1.5). The upper part of a planet atmosphere is heated up by the UV and EUV radiations. Molecules in the upper atmosphere such as H_2O, CO_2 can be photodissociated by the high energy photons in the UV. (Kasting et al. 1985; Segura et al. 2005; Hu et al. 2012; Moses 2014; Parker Loyd et al. 2016). Finally, UV and EUV radiations play an important role in driving mass loss. A nearby example on the role of UV and EUV radiation on the evolution of a planetary atmosphere is Venus, which has lost most of its atmosphere and water (Kasting & Pollack 1983)

4.2   The Hubble Space Telescope

The Hubble space telescope (*HST*) was named after Edwin P. Hubble, an american astronomer who confirmed the expansion of the universe providing the foundation for the Big-Bang theory - credit for the Hubble's law and the expansion of the universe also go to G. Lemaître (Livio 2011), which was put to a vote at the previous IAU. The space telescope was launched in April 24, 1990. It is probably the most well known scientific instrument by the general public. HST made more than a million observations and has definitely helped the scientific community in addressing and answering numerous scientific challenges (Lallo 2012).

As the *HST* was launched before the first exoplanet was discovered, it has not been designed specifically for exoplanetary observations. Nevertheless, it has allowed our community to achieve important observations to constrain atmospheric properties of exoplanets (Deming & Seager 2017). In the scope of my thesis, the advantage of *HST* is its unique ability to do spectroscopic observations in the ultraviolet (UV) part of the spectrum. There are no other facilities at the moment with this capacity. New UV projects are being planned from large class telescope facilities like LUVOIR (France 2016; Bolcar et al. 2016) or smaller projects with 'cube' satellites like CUTE (Fleming et al. 2017), but *HST* will remain the only facility for further years before those projects become scientifically operationals.

The ultraviolet part of the spectrum is traditionally divided into three parts, the extreme ultra-violet (EUV) between 100 and 912 Å, the far-ultra-violet (FUV) between 912 and 1800 Å and the near-ultra-violet (NUV) between 1800 and 3200 Å. All the data used for my work in this chapter have been obtained with the Hubble space telescope in the FUV. I have used archive data already processed by other teams and new data obtained by the our research group, with Principal Investigator (PI) David Ehrenreich and myself.

4.3   UV Observations with STIS

4.3.1   The telescope breathing

Observations done with the Hubble space telescope are known to be impacted by a major instrumental systematic effect called the breathing effect of the telescope. It is a variation of the flux as a function of the orbital phase of the telescope. It is caused by temperature-dependent flexures in the telescope optical systems. These flexures result in a varying distance between the primary and secondary mirrors, leading to focus variations. When using a spectrograph slit, these variations could turn into slit losses, hence flux changes. In practice, a *HST* observation is divided into a certain number of orbits. On *HST* orbit (around Earth) lasts for approximately ninety-seven minutes. In this section, different approaches used to correct for systematics in
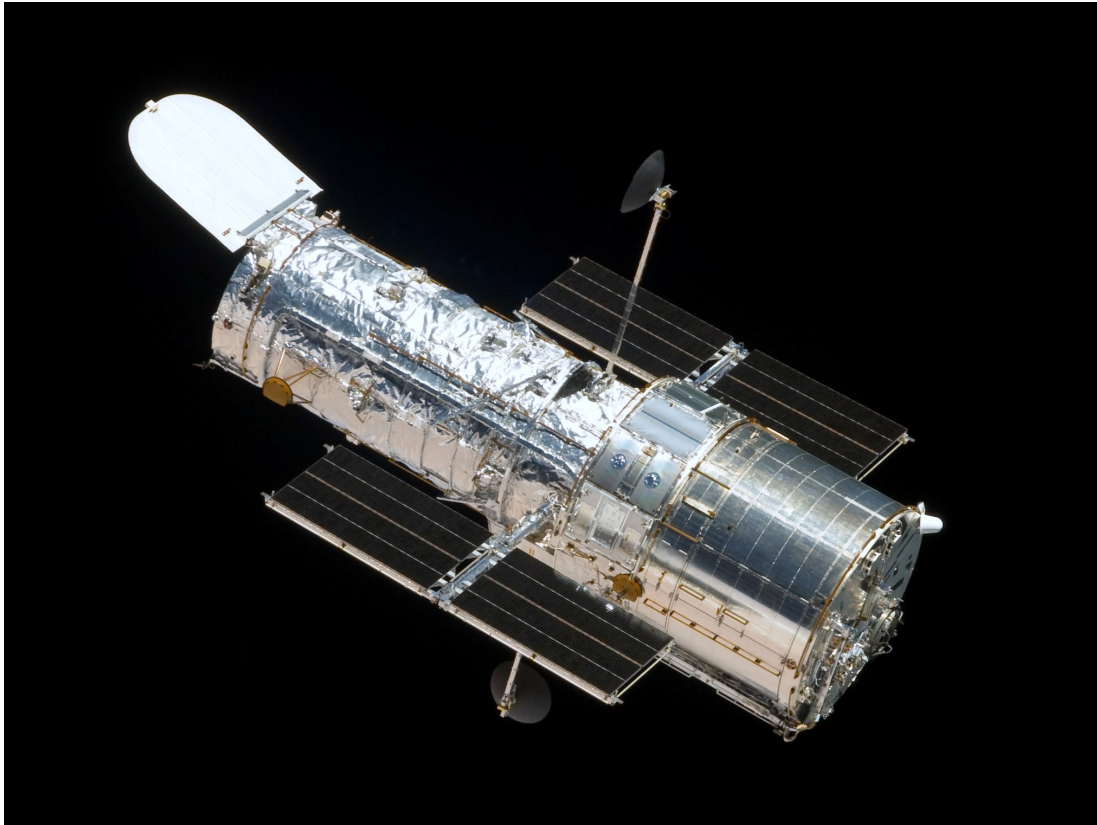
Figure 4.4: Photograph of HST taken on the fifth servicing mission to the observatory in 2009. Credits: NASA

the STIS observations are presented. Furthermore, stellar activity is observed for stars at all timescales, over a few minutes to decade-long cycles. The process of searching for planetary signatures is often done on a short timescale, during the transit of the planet, but also over different epochs of observations. Long-term cycle can be observed depending on the type and age of the star(Youngblood et al. 2016), but different observations epoch can be normalised in order to be compared. For example, GJ 436 appears very quiet in terms of flux variability. Our observations span over 6 years but the flux level in the Lyα line are very stable. A contrario, HD 219134 presents significant increase and decrease in the total Lyα line flux. The correction of the systematics is done by using some reference data, which are fluxes in time windows and spectral range not affected by the planetary signal that is studied. For observations in the Lyα line an extra complication arises because of the interstellar medium (ISM) and the geocoronal emission. The core of the line is absorbed by the hydrogen in the ISM and contaminated by the emission of hydrogen atoms surrounding Earth (geocoronal emission or also named airglow).

4.3.2 Parametric approach

This method uses a finite number of parameters to describe the systematics. All information about the data is captured in those parameters. The understanding of the model is straightforward as one have directly the parameters of the model in hand. However, any deviation of the data to this model will not be captured. Different parametric models have been used to correct HST/STIS breathing effect: a polynomial form (Bourrier & Lecavelier des Etangs 2013; Ehrenreich et al. 2012) and a Fourier series decomposition (Bourrier et al. 2017). Those two models are considered here. The stellar flux affected by systematics takes the following form :

$$F_{sys}(t) = F_{nom}(t) \times f_{breath}(\phi_{HST}(t)) \tag{4.1}$$

with $F_{nom}(t)$ the nominal stellar flux as a function of time t. We consider either a polynomial form $F_{nom}(t) = 1 + b_n t^n + b_{n-1} t^{n-1} + ... + b_1 \phi$ with b_* the coefficient of the polynomial and t the time or a free parameter for each HST orbit $F_{nom}(t) = F_{orb}$. The breathing model can take one of this form :

$$f_{breath}(\phi_{HST}) = 1 + \sum_{i=0}^{n} a_i \sin(2i\pi\phi) \tag{4.2}$$

or

$$f_{breath}(\phi_{HST}) = 1 + a_n \phi^n + a_{n-1} \phi^{n-1} + ... + a_1 \phi \tag{4.3}$$

a_* and t_{ref} (some reference time for the HST orbital phase) are the free parameters of the breathing model. The orbital phase is $\phi_{HST} = \phi = \frac{t - t_{ref}}{P_{HST}}$ with P_{HST} the orbital period of HST. For each form of the breathing model, we adjusted the reference data with equation 4.1, exploring the parameter space of the model $[F_{orb}/b_*, a_*/t_{ref}]$ with a minimisation algorithm (scipy.optimize). The degree n of the breathing model is chosen by comparing the Bayesian Information Criterion, $BIC = \chi^2 + n \times ln(N)$ where χ^2 is the deviance (here a chi-squared) to the data and N the number of data points. It avoids over-fitting the data by applying a malus to models with higher number of parameters.

4.3.3 Empirical approach

The empirical correction uses a reference observed flux to normalise the observations. This approach forces the integrated flux in the reference band to be exactly flat. However, it does not account for the white noise in the data, which results in a different dispersion in other bands than the one used for reference. More complex approaches to the normalization flux than a simple integral can be used, but they are beyond the scope of the present thesis (Deming et al. 2013; Wilkins et al. 2014; Berta et al. 2012; Ehrenreich et al. 2014).

4.3.4 Non-parametric approach: Gaussian processes

Non-parametric approaches differ from a parametric approach in that the shape of the function used to describe the systematics can be adjusted to capture any behaviour not encompassed by an analytical function. Gaussian processes (GPs) are one of these methods. GPs are widely use in machine learning and become more and more popular in the exoplanet community (see Williams 2006 for a global introduction and Gibson et al. 2012 for an application in the exoplanet field). Within a GP scheme, the joint probability distribution for the reference data is a multivariate gaussian distributed about a mean function, a flat line representing a stable flux in our case. Systematics and white noise are characterized by the covariance matrix which is defined by a covariance function (or kernel). In this analysis we adopt the squared exponential kernel in addition to a white kernel: $k(t, t') = \exp(\frac{-\|t'-t\|/^2}{2l^2}) + \delta_{tt'}\sigma^2$. The hyperparameter l of the squared exponential kernel defines a characteristic length-scale above what data points are not correlated. The white noise is incorporated through a variance term σ (an hyperparameter) with $\delta_{tt'}$ being the Kronecker function. The white noise should describe the pipeline error bars and the length-scale should be of the order of one HST visit duration. Having a shorter length-scale can allow us to reproduce shorter features providing a better correction of the systematics. However, it may lead to an over fitting. GP are implemented using the package George (Ambikasaran et al. 2014).

4.3.5 Comparison

The above methods are tested with the data obtained on the GJ 436 system, which are presented in section 4.4.2. The reference data is the integrated flux in the reference band $[-250, -150] \cup [+120, +250]$ km s^{-1}. Fig 4.5.1 shows the best fit obtained with each approach for each of the HST visits. The root-mean-square (rms) error is $0.24\,\mathrm{erg\,cm^{-2}\,s^{-1}}$ for both the Fourier decomposition and the polynomial, $0.15\,\mathrm{erg\,cm^{-2}\,s^{-1}}$ for the GP methods and $0\,\mathrm{erg\,cm^{-2}\,s^{-1}}$ (by construction) for the empirical method. The one standard deviation of the GP model contains the parametric models. Choosing one method over another does not affect our results on the evaporation of the planet. We note that the first visit (Visit 0) only has one orbit, which makes the correction of the breathing effect ambiguous, as its reproducibility between orbits of the same visit cannot be assessed. Therefore, we did not correct the fluxes from this visit. The correction of the systematics for HD 219134 observations were done with the GP method.
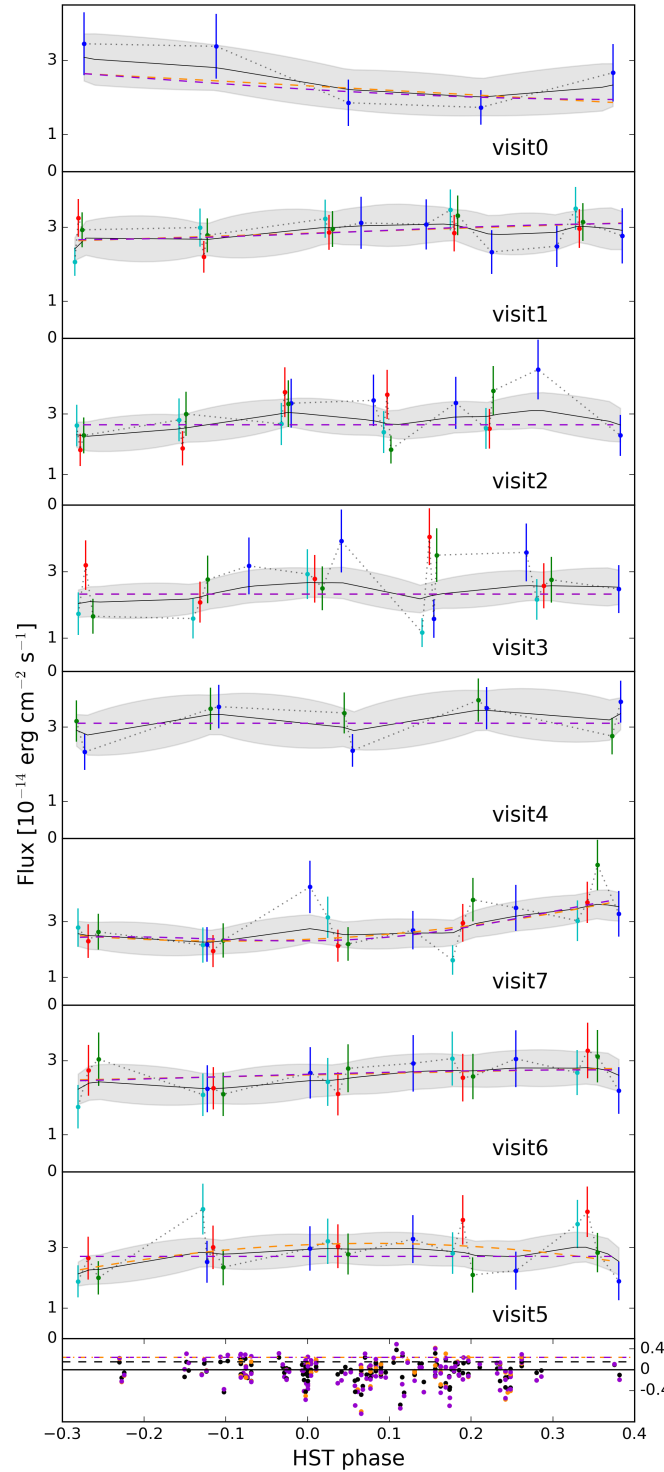
Figure 4.5: Comparison of the different methods we used to correct for systematics : empirical approach (grey), polynomial (orange), Fourier decomposition (violet) and GP (black). Points with error bars are the raw fluxes for the first (blue), the second (green), the third (red) and the fourth (cyan) HST orbits in each visit. Dashed lines show the best-fit in the parametric approach, dotted lines in the empirical approach. The black lines indicate the GP best-fits and the grey area their 1σ uncertainty. *Bottom panel*: Residuals for each approach (note that by definition residuals are null in the empirical approach). Horizontal dashed lines show the corresponding rms.
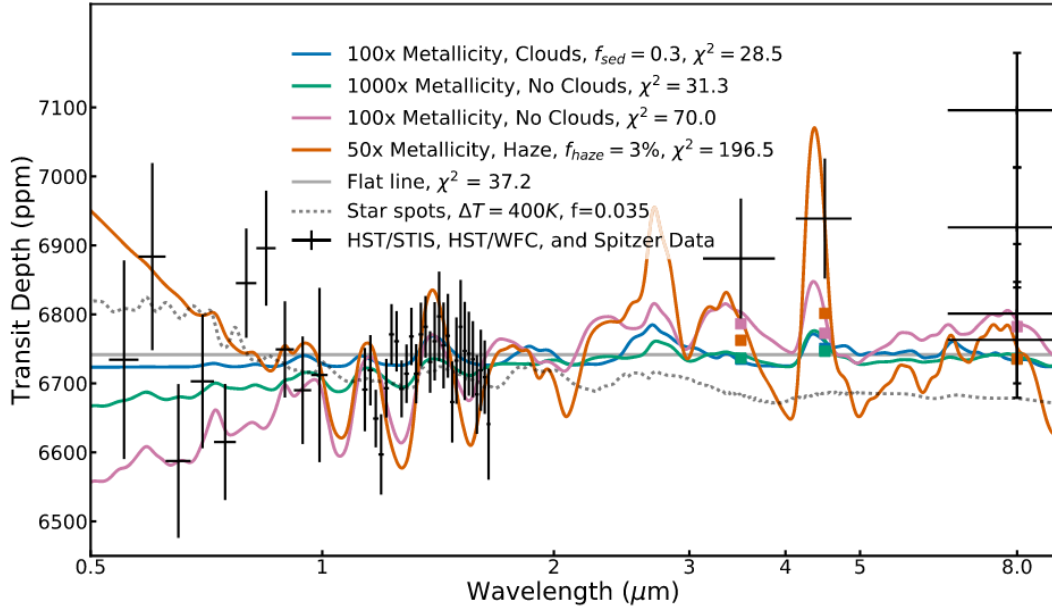
Figure 4.6: Combined optical-to-infrared transmission spectrum of GJ 436b. Each STIS data point (those shortward of 1 μm) is an average [of 108 different systematics models weighted by their evidence] (see section 3.3 of Lothringer et al. 2018). Data points from 1.2 to 1.7 μm are from HST/WFC3 (Knutson et al. 2014), and points at 3.6 μm and 4.5 μm are from Spitzer (Morello et al. 2015). The 8 μm Spitzer photometry points are from Knutson et al. (2011). This transmission spectrum reveals no identifiable features and is consistent with both high-metallicity scenarios and moderate-metallicity scenarios that include clouds. Source : Lothringer et al. (2018)

4.4 The warm-Neptune GJ 436 b

4.4.1 The figurehead for atmospheric escape

The warm Neptune GJ 436b was the first Neptune-mass exoplanet discovered in 2004 by velocimetry Butler et al. (2004); Maness et al. (2007). It was found to transit in front of its star by Gillon et al. (2007). It orbits a M2.5-dwarf star at a distance of 10.2 parsecs from Earth (Gaia Collaboration 2018). It is the only planet discovered around this star at the moment. It has an orbital period of 2.64 days (Cáceres et al. 2009; Maciejewski et al. 2018), a mass of 0.0673 $M_{\rm jup}$ and a radius of 0.37 $R_{\rm jup}$ (Turner et al. 2016; Trifonov et al. 2018). The planet has been observed from the optical to the infrared, Fig. 4.6, and does not present any significant spectral features. This has triggered a debate on the cause of this flatness, either a very high metallicity or the presence of clouds (Stevenson et al. 2010; Knutson et al. 2011; Lanotte et al. 2014; Morley et al. 2017; Lothringer et al. 2018). Using evolutionary models, Baraffe et al. (2005) suggested that GJ 436b may originate from more massive gas giants which have undergone significant atmospheric loss from evaporation.

The numerous observations performed with *HST* have make GJ 436 b the figurehead for

atmospheric escape. An initial observation of the Lyα line of the star allowed Ehrenreich et al. (2011) to predict the exospheric transit of the planet. Analysing follow-up observations Kulow et al. (2014) showed the existence of the exosphere by measuring a 8.8% absorptions in the Lyα line during its transit. A mistake in the ephemerides of the planet impeded those authors to truly unveil the gigantic exosphere of GJ 436 b. The apocalypse, in the greek sense of the word, happened with the observations and analysis of Ehrenreich et al. (2015), who showed that the exospheric transit absorbs as much as 56% of the transit. This massive absorption signature is with no comparison to any other transiting signal detected so far. State of the art modelling shows that its peculiar geometrical and dynamical structure arises from several mechanisms. The hydrogen exospheres of exoplanets around earlier-type stars (e.g. HD 209458) are swiftly blown away by a strong radiation pressure (300-500% of stellar gravity) and shortened by a high photo-ionization (Bourrier & Lecavelier des Etangs 2013). In contrast, the low UV radiation emitted by GJ 436 yields a low radiation pressure (70% of stellar gravity) and a low photoionization on escaping hydrogen atoms. Combined with a high planetary wind velocity (55 km/s), this allows the planetary outflow to diffuse within a large coma surrounding the planet, which further extends into a broad cometary tail (Bourrier et al. 2015). In addition, Bourrier et al. (2016b) showed that the M dwarf emits a low-velocity wind (85 km/s) that charge-exchanges with the planetary exosphere and abrades the dayside exosphere. These interactions further create a secondary tail of neutralized stellar wind protons, which move with the persistent dynamics of the stellar wind and therefore yield different Lyα absorption signatures over time than the primary tail.

Models including stellar wind interaction do a better job at fitting part of the data (June 2014 and December 2012 - see Table A.1 of Lavie et al. 2017b) but do not work as well as the radiation-pressure model for other part of the data (June 2013). These two models predict different cloud shapes, in particular in the tail signatures, which was not observe at the time. Moreover, the singular size of the cloud was not foreseen and it was not clear that the out-of-transit baseline has been properly determine. This has left us edgy. In that context, three more transits of GJ 436 b were obtained with *HST* for a total of 12 *HST* orbits (General Observer -GO- programme 14222; PI D. Ehrenreich) in order to address those unanswered questions.
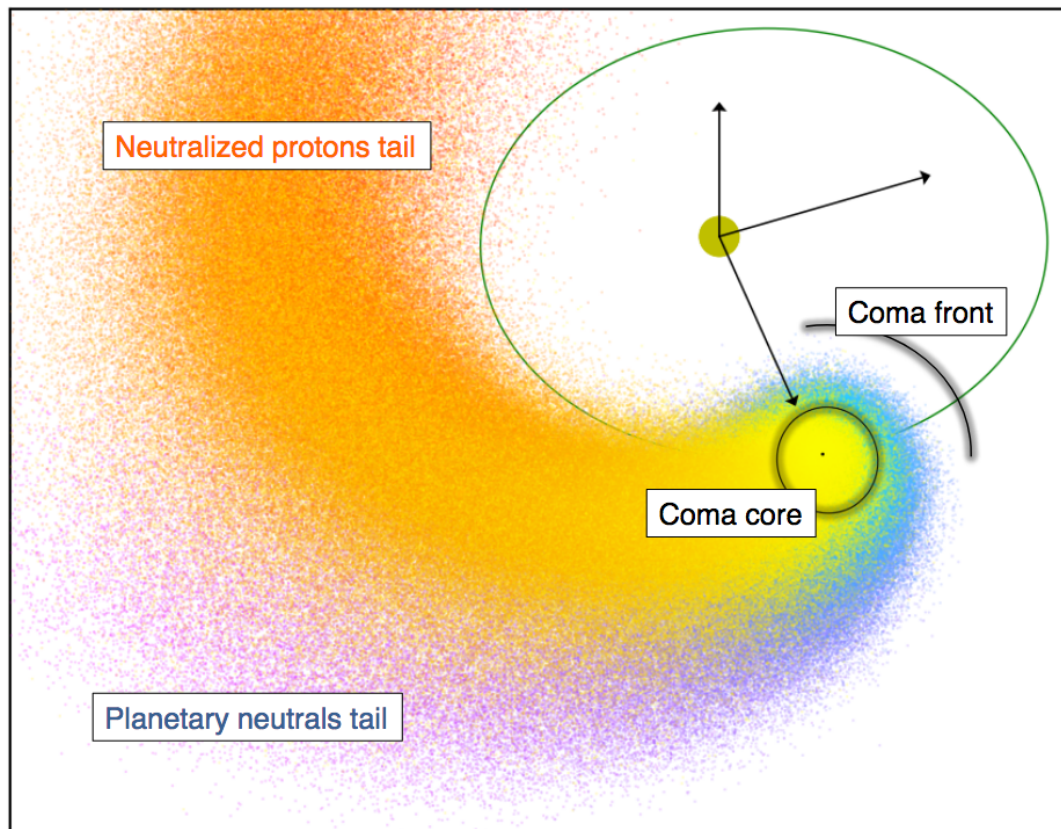
Figure 4.7: Schematic representation of the neutral hydrogen cloud surrounding GJ 436 b, displaying the different regions of the exosphere. Colors distinguish between the two populations of hydrogen atoms with different origins that compose the cloud. Source: Bourrier et al. 2016b

4.4.2   The long egress of GJ 436 b's giant exosphere

The new set of data acquired with *HST* are the starting point of my work on this object. Their analysis has strengthened our interpretation that the exosphere is shaped by both radiative braking and stellar wind interactions (Fig. 4.7). The exospheric cloud transit lasts for up to 25 hours and presence of silicon (Si III) in the out-flow is highly probable confirming the hydrodynamical state of the atmosphere. This new data set has also ungrounded new interrogations with the detection of a red-shifted absorptions correlated with the transit of the planet. This work has led to an article, Lavie et al. (2017b) reproduced below. This complete set of observations in the FUV also highlights the advantages of ultraviolet observations to probe upper atmospheres when no features are seen at longer wavelength from the lower atmosphere.

Astronomy & Astrophysics

LETTER TO THE EDITOR

The long egress of GJ 436b's giant exosphere

B. Lavie[1,2], D. Ehrenreich[1], V. Bourrier[1], A. Lecavelier des Etangs[3], A. Vidal-Madjar[3], X. Delfosse[5],
A. Gracia Berna[2], K. Heng[2], N. Thomas[2], S. Udry[1], and P. J. Wheatley[4]

[1] Observatoire de l'Université de Genève, 51 chemin des Maillettes, 1290 Sauverny, Switzerland
e-mail: baptiste.lavie@unige.ch
[2] University of Bern, Space Research and Planetary Sciences, Sidlerstrasse 5, 3012 Bern, Switzerland
[3] CNRS, Institut d'Astrophysique de Paris, UMR 7095, 98bis boulevard Arago, 75014 Paris, France
[4] Dept. of Physics, University of Warwick, Gibbet Hill Road, Coventry CV4 7AL, UK
[5] Univ. Grenoble Alpes, CNRS, IPAG, 38000 Grenoble, France

ABSTRACT

The M dwarf GJ 436 hosts a transiting warm Neptune known to experience atmospheric escape. Previous observations revealed the presence of a giant hydrogen exosphere transiting the star for more than 5 h, and absorbing up to 56% of the flux in the blue wing of the stellar Lyman-α line of neutral hydrogen (H I Lyα). The unexpected size of this comet-like exosphere prevented observing the full transit of its tail. In this Letter, we present new Lyα observations of GJ 436 obtained with the Space Telescope Imaging Spectrograph (STIS) instrument onboard the *Hubble* Space Telescope. The stability of the Lyα line over six years allowed us to combine these new observations with archival data sets, substantially expanding the coverage of the exospheric transit. Hydrogen atoms in the tail of the exospheric cloud keep occulting the star for 10–25 h after the transit of the planet, remarkably confirming a previous prediction based on 3D numerical simulations with the EVaporating Exoplanet code (EVE). This result strengthens the interpretation that the exosphere of GJ 436b is shaped by both radiative braking and charge exchanges with the stellar wind. We further report flux decreases of $15 \pm 2\%$ and $47 \pm 10\%$ in the red wing of the Lyα line and in the line of ionised silicon (Si III). Despite some temporal variability possibly linked with stellar activity, these two signals occur during the exospheric transit and could be of planetary origin. Follow-up observations will be required to assess the possibility that the redshifted Lyα and Si III absorption signatures arise from interactions between the exospheric flow and the magnetic field of the star.

Key words. planets and satellites: atmospheres – planets and satellites: gaseous planets – planets and satellites: individual: GJ 436

1. Introduction

Transit observations in the stellar Lyman-α line of neutral hydrogen (H I Lyα at 1215.67 Å) allowed the detection of atmospheric escape from the two hot Jupiters HD 209458b (Vidal-Madjar et al. 2003, 2004) and HD 189733b (Lecavelier des Etangs et al. 2010, 2012; Bourrier et al. 2013), the warm giant 55 Cnc b (Ehrenreich et al. 2012), and the warm Neptune GJ 436b (Kulow et al. 2014; Ehrenreich et al. 2015). The escaping hydrogen exospheres produce large Lyα absorption transit signatures ranging from $7.5 \pm 1.8\%$ for 55 Cnc b to $56.3 \pm 3.5\%$ for GJ 436b. Compared to close-in hot Jupiters, GJ 436b ($25.4 \pm 2.1\ M_\oplus$ and $4.10 \pm 0.16\ R_\oplus$, Butler et al. 2004; Gillon et al. 2007; Lanotte et al. 2014) is gently irradiated by its M2V host star (Ehrenreich et al. 2011), yet it spots an extended hydrogen envelope, first hinted at by Kulow et al. (2014) and fully revealed by Ehrenreich et al. (2015). These authors found that GJ 436b emits a comet-like cloud of H atoms, with a coma bigger than the star and a tail extending millions of kilometers (up to 40% of GJ 436b's orbit, 450 planetary radii), trailing the planet. Because of its unexpected, gigantic scale, past Lyα observations of GJ 436b's exosphere could only cover the transit of its coma and the onset of its comet-like tail. Bourrier et al. (2015, 2016b) have modelled the dynamics of GJ 436b exospheric cloud using the EVaporating Exoplanets code (EVE; Bourrier & Lecavelier des Etangs 2013). Adjusting Lyα spectra obtained between 2010 and 2014, they show that the geometry and dynamical structure of the exospheric cloud could be explained by radiative braking (i.e. the effect on exosphere

particles resulting from radiation pressure lower than stellar gravity; Bourrier et al. 2015) and stellar wind interaction (specifically, charge exchange; Bourrier et al. 2016b). The balance between both mechanisms, however, would shape the cloud tail, hence the egress of the UV transit, differently. Meanwhile, the full extent of the tail, provided by the egress duration, is unknown. Given the partial coverage (3–4h) of the egress, new data were needed to fully cover the UV transit egress and precisely determine the nature of the star-planet interaction sculpting the cloud.

In this Letter, we present new *Hubble* Space Telescope (HST) data obtained with the Space Telescope Imaging Spectrograph (STIS). The combined reduction and analysis of these data covering a much larger fraction of the planetary orbit, with all previously existing data, is presented in Sect. 3 and Appendix B. Our results (Sect. 4) confirm the blueshifted Lyα absorption signature of Ehrenreich et al. (2015) and strengthen the interpretation of Bourrier et al. (2015, 2016b). We also find new surprising absorption signatures in the red wing of the H I Lyα line and in the ionised silicon line (Si III) that could be of planetary or stellar origins.

2. Observations

In total, GJ 436b has been observed at eight epochs (hereafter Visits 0 to 7) with HST/STIS. All visits are listed in Table A.1. Visits 0 to 3 revealed the deep transit of GJ 436b's exosphere in the blue wing of the Lyα line (Ehrenreich et al. 2011, 2015; Kulow et al. 2014). Three new visits (Visits 5 to 7) were obtained

on 2016-Mar-30, 2016-Apr-06, and 2016-May-08 (General Observer (GO) programme 14222; PI: D. Ehrenreich) with the aim of completing the coverage of the exospheric transit, during the transit of the tail (∼+3,+20 h; Visit 6), before the transit of the coma (≲−3 h; Visit 7), and after the presumed end of the transit (≳+20 h; Visit 5). Times are calculated using the ephemeris from Lanotte et al. (2014). All observations were made with the Far Ultraviolet Multi-Anode Microchannel Array detector (FUV-MAMA) detector and the G140M grating with a central wavelength of 1222 Å. The eight visits represent 27 HST orbits. Each orbit-long[1] time-tag exposure has been divided into five sub-exposures (a reasonable balance between signal over noise ratio and time resolution) and processed through CALSTIS, the STIS pipeline, yielding a total of 135 spectra.

3. Analysis

3.1. Reference, unocculted Lyα flux

The new visits obtained before and after the exospheric transit allow us to reconstruct a reference spectrum seemingly unaffected by the exospheric absorption signature. We average the flux in the first HST orbits of Visits 0, 2, and 3 (as done by Ehrenreich et al. 2015) with the flux measured in all HST orbits obtained during Visits 4, 5, and 7. This average out-of-transit baseline spectrum appears stable in both the red wing of the Lyα line and the reference band ([−250, −120] ∪ [+120, +250] km s^{-1}), as can be seen in Fig. 1a,b. In the Lyα blue wing (Fig. 2), the flux of Visit 4 and the first exposure of Visit 5 are higher than in subsequent orbits used for the out-of-transit baseline. The origin of this wavelength-dependent rise is unclear, but in the following we chose to include them in the out-of-transit baseline flux. Excluding them will only decrease the out-of-transit baseline by less than 4%.

3.2. Correction of systematics

In addition to stellar variability, STIS G140M spectra are known to be impacted by an instrumental systematic effect caused by the telescope breathing. This effect is reported to be achromatic, thus to correct for it we need to locate a reference wavelength or velocity band in the Lyα emission feature devoid of astrophysical signal. The geocoronal emission line (airglow) contaminates the core of the observed stellar line, and varies in strength and position from one observation to another. This region is not adapted to our needs so we exclude it, setting conservative limits of [−40, +30] km s^{-1} (velocities are expressed with respect to the Lyα line centre in the stellar rest frame). Previous work reported absorption signatures in the Lyα blue wing ([−120, −40] km s^{-1}; Ehrenreich et al. 2015) and, tentatively, in the Lyα red wing ([+30, +120] km s^{-1}; Kulow et al. 2014). These two bands, over which we will search for exospheric signatures, cannot be used to monitor telescope breathing. A careful inspection of the Lyα spectra presented in Fig. 3 allowed us to find two bands seemingly free of astrophysical signal, over [−250, −120] and [+120, +250] km s^{-1}, which we call the reference band. The flux integrated over these two bands, which can be seen in Fig. A.1c, remains about stable within the uncertainties for all visits, spanning over six years of observations. We hypothesized that all variations in these reference bands could be attributed to instrumental effect. Different strategies have been developed to correct for telescope breathing (see e.g. Bourrier et al. 2017,
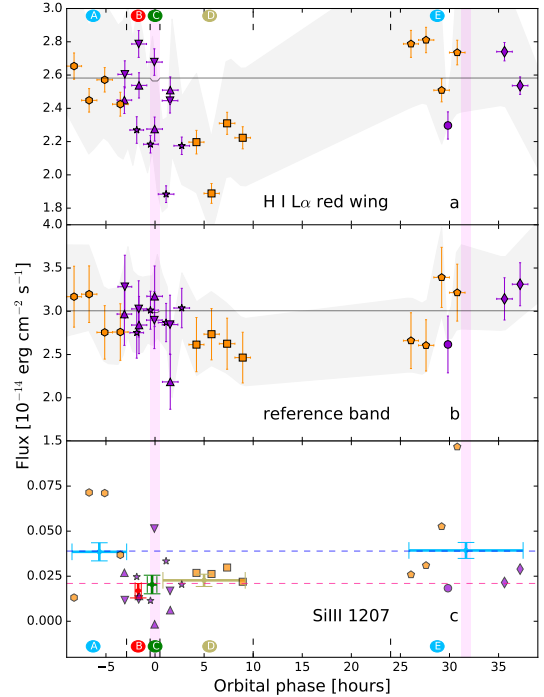
---

[1] The exposure time ranges from ∼1500 to 2900 s.

Fig. 1. Light curves of GJ 436 integrated Lyα red wing (*a*), Lyα reference band [−250, −120] ∪ [+120, +250] km s^{-1} (*b*) and Si III line (*c*). New visits described in this work are in orange while previous visits are plotted in violet. Symbols are in Table A.1. Different temporal regions are defined: (A) before transit, (B) ingress, (C) optical transit, (D) egress, and (E) after transit. The grey-filled region represents the 1σ confidence interval of the systematic correction method using the Gaussian processes (Appendix B). The vertical magenta zones show the optical primary and secondary transit. The optical transit light curve of GJ 436b is indicated with the black line. In *panel c*, fluxes are integrated for the different temporal region (see Fig. 2). Horizontal dashed lines indicate the out-of-transit flux (blue – regions A and E) and the in-transit flux (pink – regions B, C, and D).

and references therein). In this work, we compare three correction methods: parametric (Bourrier & Lecavelier des Etangs 2013; Ehrenreich et al. 2012; Bourrier et al. 2016a), empirical (Deming et al. 2013; Wilkins et al. 2014; Berta et al. 2012; Ehrenreich et al. 2014), and non-parametric using Gaussian processes (GP; Appendix B). All three methods yield similar results. In the following, we opt to rely on the GP-based approach.

3.3. Flux in other spectral lines

Besides the prominent Lyα line, we detect the following stellar emission features in the STIS/G140M range (1190–1250 Å): Si III at 1206.5 Å, N V doublet at 1238.8 and 1242.8 Å, and O V at 1218.3 Å (cf. Table C.1). The low signal-to-noise ratio in these lines prevented us from doing an orbit-to-orbit comparison and establishing the stability of the stellar baseline flux for those lines. We therefore averaged their spectra within the orbital phase regions labelled A to E in Fig. 2 (cf. Table A.2): (A) before the exospheric transit signature in the blue wing of Lyα, (B) during the exospheric transit ingress, (C) during the optical transit (i.e. the transit of the planetary disk alone), (D) during the exospheric transit egress, and (E) after the exospheric transit. Regions (B), (C), and (D) are considered "in transit"; regions (A) and (E) are "out of transit".

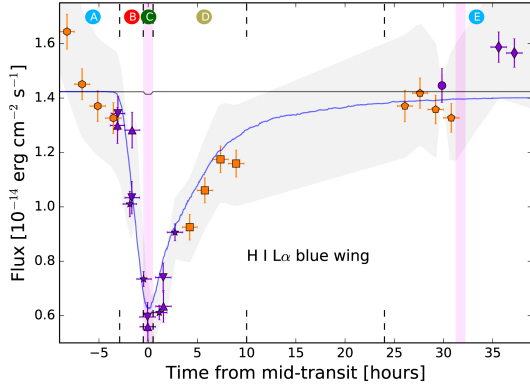**Fig. 2.** Light curves of GJ 436 integrated over the Lyα blue wing. Legend is the same as in Fig. 1. The blue curve is the model calculated with EVE that represents the best fit to previous data (Visit 0 to 3).

4. Results

4.1. Detection of the Lyα transit egress

The most significant absorption signal is detected in the Lyα blue wing between −120 and −40 km s^{-1} (Fig. 2), in agreement with Ehrenreich et al. (2015). Visit 6 (time from mid-transit $\tau = [+4.01, +9.18]$ h) prolongates and confirms the exospheric egress suggested by Visits 1, 2, and 3. The egress duration is now constrained to be longer than ∼10 h and shorter than ∼25 h. The Lyα flux measured during Visit 5 ($\tau = [+25.8, +31.0]$ h) is in good agreement with the Visit 0 measurement obtained ∼+30 h after the mid-transit time, close to superior conjunction. We stress that those compatible measurements were obtained more than six years apart, highlighting the temporal stability of GJ 436. Bourrier et al. (2015, 2016a) fitted the spectra obtained during Visits 0 to 3 (all violet curves in Fig. A.2) with EVE. Their best-fit theoretical spectra yield the light curve plotted in Fig. 2. The model is in remarkable agreement with the new data from Visits 6 and 7, strengthening the interpretation proposed in Bourrier et al. (2015, 2016a): the weak UV radiation emitted by GJ 436 yields a low radiation pressure (∼70% of stellar gravity) and a low photoionisation of escaping hydrogen atoms. This, combined with a high planetary wind velocity (∼55 km s^{-1}), allows the planetary outflow to diffuse within a large coma surrounding and comoving with the planet, which further extends into a broad cometary tail (Bourrier et al. 2015). In addition, escaping atoms interact with the slow stellar wind of the M dwarf (∼85 km s^{-1}) via charge exchanges abrading the day-side exosphere (Bourrier et al. 2016a). These interactions create a secondary tail of neutralised stellar wind protons[2], which move with the persistent dynamics of the stellar wind and therefore yield different Lyα absorption signatures over time than the primary tail. This model assumed that the out-of-transit baseline is provided by the flux measured during the "out-of-transit" region defined in the previous section. Visits 4 and 7 tentatively suggest (Fig. 2), however, that the unoccultedLyα line might be even brighter. This will have to be confirmed with additional measurements obtained between the superior conjunction and the first quadrature.

4.2. Detection of a redshifted Lyα absorption signature

Visits 1 and 6 show similar integrated fluxes in the Lyα red wing during and after the optical transit, with an average absorption
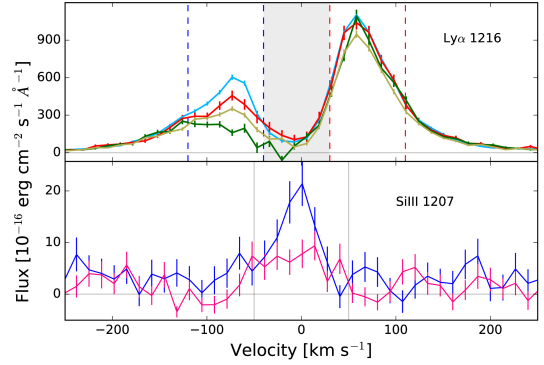
---

[2] These are stellar wind protons that gained an electron from the interaction with neutral hydrogen atoms in the exosphere.

Fig. 3. *Top panel*: averaged out-of-transit (blue), ingress (red), egress (khaki), and in-transit (green) spectra of the Lyα line at 1206.5 Å. The grey zone is the geocoronal emission (airglow) band. *Bottom panel*: averaged out-of-transit (blue) and in-transit (pink) spectra of the Si III at 1206.5 Å. Vertical grey line indicates the [−50, +50] km s^{-1} area.

depth of 15 ± 2% compared to the baseline level (Figs. 1a and 3). In both visits, the absorption signature is located within [+30, +110] km s^{-1} but at a different time from the mid-transit at +0.5 and +6.6 h, respectively. In comparison, the blueshifted absorption occurs around the mid-transit. This redshifted absorption is time variable. This was first noted by Kulow et al. (2014) from Visit 1 data; however, Ehrenreich et al. (2015) did not confirm it with same-phase data obtained during Visits 2 and 3. Visit 6 changes this picture and confirms the existence of a redshifted Lyα signature delayed in time with respect to the blueshifted signature. Interpretation of this redshifted Lyα signature is challenging: the EVE model that best fitted the blueshifted signature (Sect. 4.1) does predict the existence of H atoms moving towards the star, but redshifted by less than +50 km s^{-1} because this population is localised within the coma and could not create a signature in the tail (see Fig. 4 in Bourrier et al. 2016a). In the absence of radiation pressure or with a very strong self-shielding protecting the interior of the coma (which is not the case for GJ436b), Bourrier et al. (2015) showed that gravitational shear could lead to a stream of H atoms falling onto the star but ahead of the planet and thus yielding a redshifted signature before the optical transit (see their Fig. 2). Interestingly, tentative Lyα redshifted absorptions have been previously reported in HD 209458b and HD 189733b (Vidal-Madjar et al. 2003; Lecavelier des Etangs et al. 2012) but in phase with the respective blueshifted absorptions signature of those planets.

It is plausible that stellar variability (Tian et al. 2009; Llama & Shkolnik 2016; Vidal-Madjar 1975) is the origin of the variations, because they are located at the peak of the observed red wing, which traces higher altitudes in the chromosphere of the star which are more active than the lower chromosphere which is the source for the far wings of the Lyα line (e.g. Bourrier et al. 2017). However, the high stability of the stellar flux over six years of observations, the fact that the variations always correspond to a decrease of the flux with respect to the reference spectrum, and the fact that they appear to be phased during and after the planet transit, suggest another scenario.

Interaction of the exospheric flow with the star and planet magnetic fields could be one of the mechanisms that drives particles towards the star. A bow shock formed ahead of the planet by the interaction between the stellar wind and the planetary magnetosphere could only yield absorption before the planet transit (Alexander et al. 2016; Lai et al. 2010). Furthermore, Bourrier et al. (2016a) showed that the interactions between the

exosphere and the stellar wind required to explain the absorption in the Lyα blue wing imply that the planetary magnetosphere is embedded deep inside the coma. Strong magnetic connection could nonetheless link the embedded magnetosphere with the stellar magnetic field, forcing part of the planetary outflow to stream toward the star behind the planet (Strugarek 2016). One of the magnetised star-planet interactions proposed by Matsakos et al. (2015) (Type 4) bears some resemblance with our observations in the red wing, with planetary gas infalling nearly radially onto the star. The variability of the detected absorption could be explained by the continuous readjustment of the magnetic field topology as the planet orbits the star, with new magnetic accretion channels forming periodically. However, this scenario requires a high UV irradiation and a weak planetary outflow, which are not consistent with the mild irradiation from GJ 436 and the high velocities derived for the planetary outflow (Bourrier et al. 2016a). Furthermore, Matsakos et al. (2015) investigated the case of a hot Jupiter around a solar-type star, without accounting for radiation pressure despite its major role in shaping the exospheres of evaporating exoplanets. Gas in magnetised interaction regions is also expected to be strongly ionised, which would require either that massive amounts of neutral hydrogen infall toward the star or that shielding or recombination mechanisms allow for a significant portion of this gas to remain neutral.

4.3. Detection of an absorption signature from ionised silicon

The other stellar lines (Table C.1) are much fainter than Lyα, so we compared for each line the total fluxes averaged in transit (phase regions B, C and D) and out of transit (phase regions A and E). We report an absorption signal of $36 \pm 15\%$ in the O V line. The signal occurs during ingress and egress but not during the optical transit. Thus, it may not be of planetary origin. Loyd et al. (2017) observed GJ 436 with HST/Cosmic Origins Spectrograph (COS) from $[-4, +3]$ h around the optical transit. Within this time range, they reported no detection of N V or Si III absorption. This is in agreement with our analysis of the two N V lines. Meanwhile, we detect an absorption signal of $47 \pm 10\%$ in the Si III line within $[-50, +50]$ km s^{-1}, similar in intensity to the blueshifted Lyα absorption depth and occuring during the same phases as the exospheric transit. The flux is constant over the phase range covered by Loyd et al. (2017) (Fig. 1 c), suggesting that the stellar line was already absorbed during their observations, preventing them from detecting any variations. We note that our observations are compatible with their upper limit. We cannot exclude stellar variations in the Si III line (Loyd et al. 2017), which could be linked to the variation seen in the Lyα red wing (Sect. 4.2). A planetary origin for the Si III signal is tantalising, as it would demonstrate the hydrodynamic nature of GJ 436b atmospheric escape, constrain the star-planet magnetic interaction, and provide a possible tracer for the presence of enstatite clouds ($Mg_2Si_2O_6$), potentially responsible for the flat near-infrared transmission spectrum of the lower atmosphere (Knutson et al. 2014). This will require additional observations.

5. Conclusion

We report new HST/STIS UV observations of the exospheric cloud escaping from the warm Neptune GJ 436b. A combined analysis of all available UV data, making use of GP to correct for systematics, yields the following results:

1. We detect the UV transit egress and constrain its duration between 10 to 25 h. This corresponds to a size of the exospheric hydrogen tail between 5 and 12 millions km. This result confirms previous observations (Ehrenreich et al. 2015) and their interpretation (Bourrier et al. 2015, 2016a).

2. We detect an absorption signal in the red wing of the Lyα line, which is delayed in time compared to the blueshifted absorption. This signal could originate either from the planet or be due to stellar activity.

3. We detect an absorption signal in the Si III line, possibly linked with the Lyα redshifted signal (and stellar activity). More observations will be needed at other phases to discriminate the stellar activity scenario from a planetary origin.

4. We notice the remarkable stability of GJ 436's unocculted Lyα emission line over the six-year period (2010–2016) covered by the available observations.

References

Alexander, R. D., Wynn, G. A., Mohammed, H., Nichols, J. D., & Ercolano, B. 2016, MNRAS, 456, 2766
Ambikasaran, S., Foreman-Mackey, D., Greengard, L., Hogg, D. W., & O'Neil, M. 2014, ArXiv e-prints [arXiv:1403.6015]
Berta, Z. K., Charbonneau, D., Désert, J.-M., et al. 2012, ApJ, 747, 35
Bourrier, V., & Lecavelier des Etangs, A. 2013, A&A, 557, A124
Bourrier, V., Lecavelier des Etangs, A., Dupuy, H., et al. 2013, A&A, 551, A63
Bourrier, V., Ehrenreich, D., & Lecavelier des Etangs, A. 2015, A&A, 582, A65
Bourrier, V., Ehrenreich, D., King, G., et al. 2016a, A&A, 597, A26
Bourrier, V., Lecavelier des Etangs, A., Ehrenreich, D., Tanaka, Y. A., & Vidotto, A. A. 2016b, A&A, 591, A121
Bourrier, V., Ehrenreich, D., King, G., et al. 2017, A&A, 597, A26
Butler, R. P., Vogt, S. S., Marcy, G. W., et al. 2004, ApJ, 617, 580
Deming, D., Wilkins, A., McCullough, P., et al. 2013, ApJ, 774, 95
Ehrenreich, D., Lecavelier des Etangs, A., & Delfosse, X. 2011, A&A, 529, A80
Ehrenreich, D., Bourrier, V., Bonfils, X., et al. 2012, A&A, 547, A18
Ehrenreich, D., Bonfils, X., Lovis, C., et al. 2014, A&A, 570, A89
Ehrenreich, D., Bourrier, V., Wheatley, P. J., et al. 2015, Nature, 522, 459
Gibson, N. P., Aigrain, S., Roberts, S., et al. 2012, MNRAS, 419, 2683
Gillon, M., Pont, F., Demory, B.-O., et al. 2007, A&A, 472, L13
Knutson, H. A., Benneke, B., Deming, D., & Homeier, D. 2014, Nature, 505, 66
Kulow, J. R., France, K., Linsky, J., & Loyd, R. O. P. 2014, ApJ, 786, 132
Lai, D., Helling, C., & van den Heuvel, E. P. J. 2010, ApJ, 721, 923
Lanotte, A. A., Gillon, M., Demory, B.-O., et al. 2014, A&A, 572, A73
Lecavelier des Etangs, A., Ehrenreich, D., Vidal-Madjar, A., et al. 2010, A&A, 514, A72
Lecavelier des Etangs, A., Bourrier, V., Wheatley, P. J., et al. 2012, A&A, 543, L4
Llama, J., & Shkolnik, E. L. 2016, ApJ, 817, 81
Loyd, P. R. O., Koskinen, T. T., France, K., Schneider, C., & Redfield, S. 2017, ApJ, 834, L17
Matsakos, T., Uribe, A., & Königl, A. 2015, A&A, 578, A6
Strugarek, A. 2016, ApJ, 833, 140
Tian, H., Curdt, W., Marsch, E., & Schühle, U. 2009, A&A, 504, 239
Vidal-Madjar, A. 1975, Sol. Phys., 40, 69
Vidal-Madjar, A., Lecavelier des Etangs, A., Désert, J.-M., et al. 2003, Nature, 422, 143
Vidal-Madjar, A., Désert, J.-M., Lecavelier des Etangs, A., et al. 2004, ApJ, 604, L69
Wilkins, A. N., Deming, D., Madhusudhan, N., et al. 2014, ApJ, 783, 113
Williams, C. R. C. 2006, Gaussian Processes for Machine Learning (The MIT press)

Appendix A: Log of observations and raw light curves

All spectra were linearly interpolated on a common wavelength grid, chosen to be the grid of Visit 0 first sub-exposure.
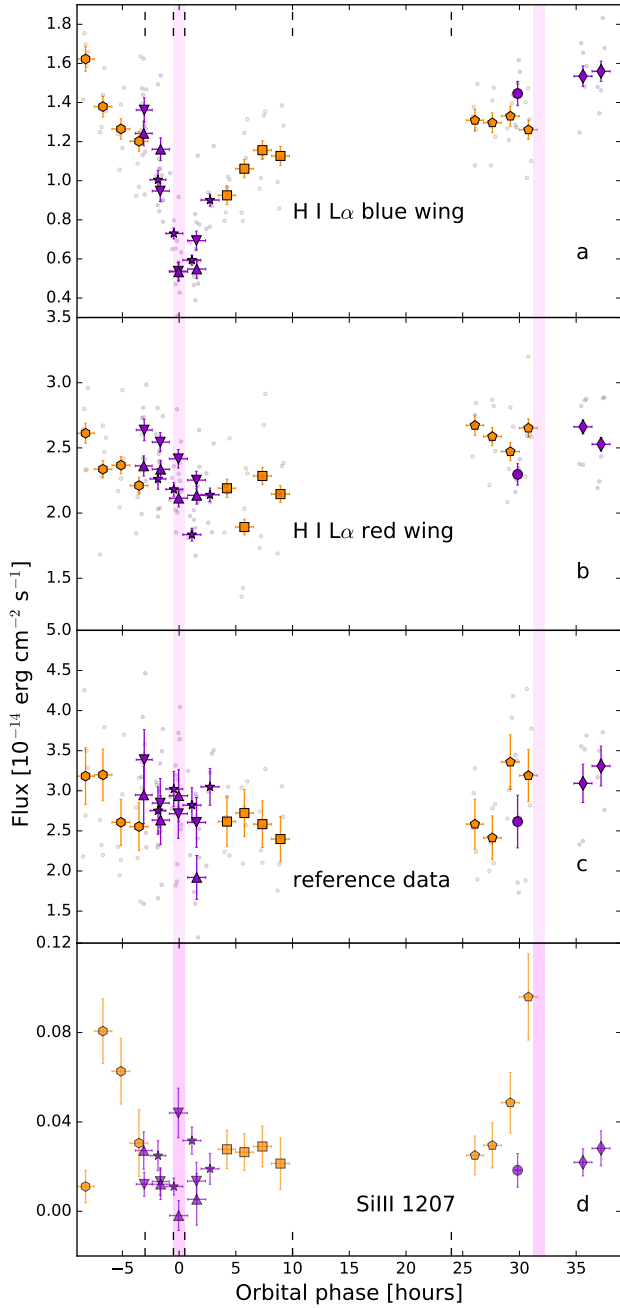

Fig. A.1. Lyα light curve of GJ 436 obtained from integrating the raw spectra uncorrected for systematics. The flux is integrated over the blue wing $[-120, -40]$ km s^{-1} (*a*), the red wing $[+30, +120]$ km s^{-1} (*b*), the reference band $[-250, -120] \cup [+120, +250]$ km s^{-1} (*c*), and the $[-50, 50]$ km s^{-1} band of the Si III line (*d*). The colour code is the same as in Fig. 1. Large coloured symbols with errors bars are the individual HST orbits (see Table A.1 for the visit symbols) while small grey circles are the time-tagged sub-exposures extracted from each HST orbit for *panel a, b*, and *c*.
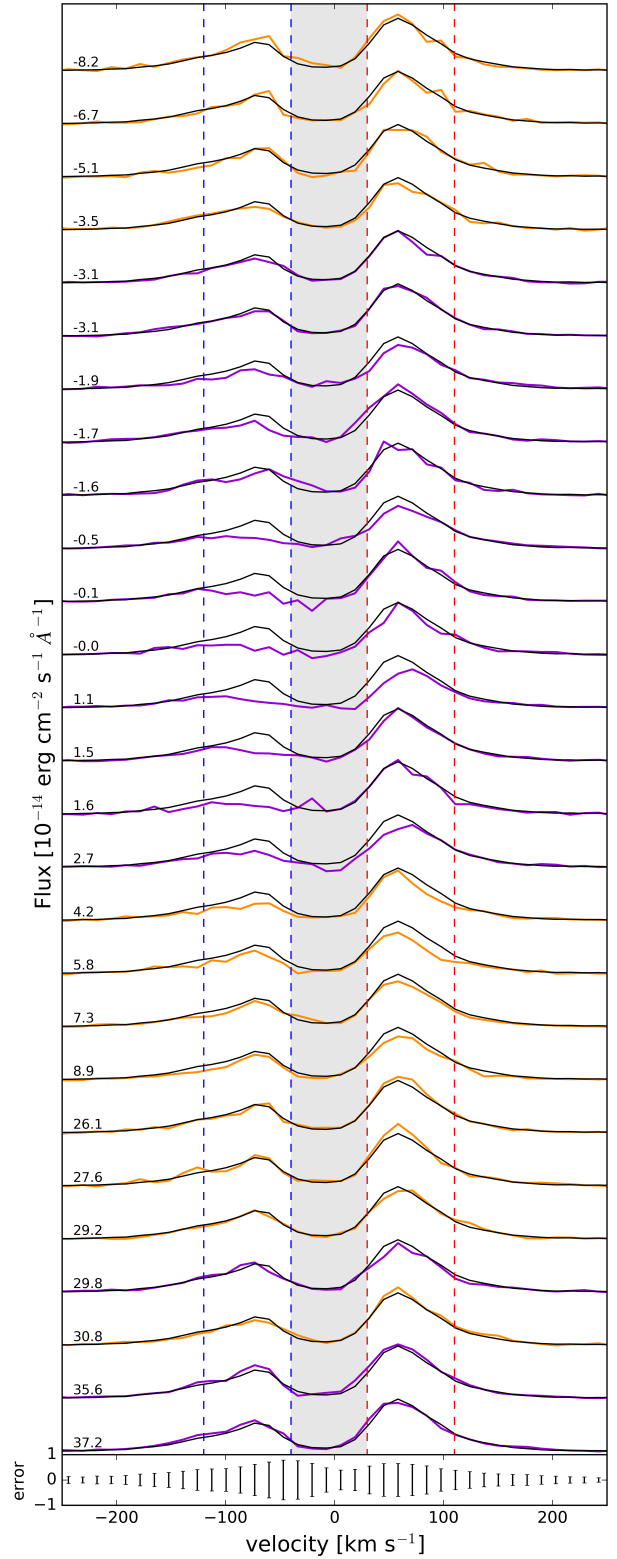

Fig. A.2. New visits described in this work are in orange while previous visits are plotted in violet. Lyα line spectra of GJ 436 of each HST orbit compared to the unocculted line (black curves) obtained by combining all spectra from the out-of-transit phases region (see Sect. 3.3). The number on top of each spectrum indicates the time in hours from the mid-transit time. Vertical dashed lines indicate the blue and the red bands showing absorption signatures. The grey zone is the geocoronal emission (airglow) band.

Table A.1. Observation log.

Visit	Date	Programme	PI	HST orbits	Time from mid-transit (h)	Phase range
0 (○)	01 May 2010	GO#11817	Ehrenreich	1	[29.64, 30.03]	[0.46, 0.47]
1 (★)	07 Dec. 2012	GTO#12034	Green	4	[−2.03, 3.04]	[−0.03, 0.05]
2 (△)	18 Jun. 2013	GO#12965	Ehrenreich	4	[−3.26, 1.75]	[−0.05, 0.03]
3 (▽)	23 Jun. 2014	GO#12965	Ehrenreich	4	[−3.30, 1.78]	[−0.05, 0.03]
4 (◇)	25 Jun. 2015	GO#13650	France	2	[35.29, 37.49]	[−0.44, −0.41]
5 (⬠)	30 Mar. 2016	GO#14222	Ehrenreich	4	[25.86, 31.04]	[0.40, 0.49]
6 (□)	06 Apr. 2016	GO#14222	Ehrenreich	4	[4.01, 9.18]	[0.06, 0.14]
7 (○)	08 May 2016	GO#14222	Ehrenreich	4	[−8.45, −3.28]	[−0.13, −0.05]

Notes. Symbols in the first column refer to plotting symbols in Fig. A.1.

Table A.2. Orbital phases range.

Phase range	HST orbits [visit #, (orbit #)]
Before transit	[2, (1)], [3, (1)], [7, (1, 2, 3, 4)]
Ingress	[1, (1)] , [2, (2)], [3, (2)]
Optical transit	[1, (2)] , [2, (3)], [3, (3)]
Egress	[1,(3, 4)] , [2, (4)], [3, (3)], [6,(1, 2, 3, 4)]
After transit	[0, (1)], [4,(1, 2)], [5, (1, 2, 3, 4)]

Appendix B: Correction of systematics: Gaussian processes

This method differs from the parametric approach in that the shape of the function used to describe the systematics can be adjusted to capture any behaviour not encompassed by an analytical function. Gaussian processes (GP) are one of these methods. GP are widely use in machine learning and are increasingly popular in the exoplanet community (see Williams 2006 for a global introduction and Gibson et al. 2012 for an application in the exoplanet field). Within a GP scheme, the joint probability distribution for the reference band is a multivariate gaussian distributed about a mean function, a flat line representing a stable flux in our case. Systematics and white noise are characterised by the covariance matrix, which is defined by a covariance function (or kernel). In this analysis we adopt the squared exponential kernel in addition to a white kernel: $k(t, t') = \exp(\frac{-\|t'-t\|^2}{2l^2}) + \delta_{tt'}\sigma^2$. The hyperparameter l of the squared exponential kernel defines a characteristic length scale above which data points are not correlated. The white noise is incorporated through a variance term σ (an hyperparameter) with $\delta_{tt'}$ being the Kronecker function. The white noise should describe the pipeline error bars and the length scale should be of the order of one HST visit duration. Having a shorter length scale can allow us to reproduce shorter features providing a better correction of the systematics. However, it may lead to an over fitting. GP are implemented using George (Ambikasaran et al. 2014).

We note that Visit 0 only has one orbit, which makes the correction of the breathing effect ambiguous as its reproducibility between orbits of the same visit cannot be assessed. Therefore, we did not correct the fluxes from this visit.

Appendix C: Other lines

Apart from the Lα line, we have identified several other lines: Si III at 1206.51 Å, N V at 1238.821, 1242.804 Å, and O V at 1218.344 Å. Those lines have a flux two magnitudes lower than
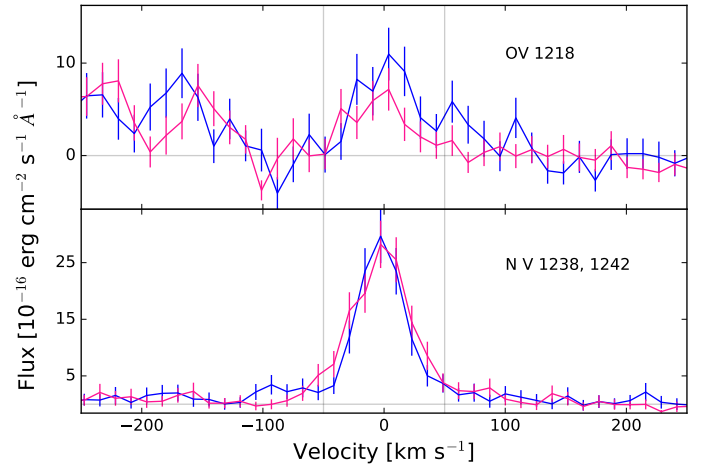

Fig. C.1. Averaged out-of-transit (blue) and in-transit (pink) spectra of the O V at 1218.344 Å (*top panel*) and the N V doublet at 1238.8 Å and 1242.8 Å (*bottom panel*) with both lines summed in velocity space. Vertical grey line indicates the [−50, +50] km s^{-1} area.

Table C.1. Identified stellar lines in STIS/G140M.

Species	Wavelength [Å]	Stellar flux (10^{-16} erg cm^{-2} s^{-1})	Absorption %
Si III	1206.510	3.8 ± 0.3	47 ± 10
O V	1218.344	2.2 ± 0.2	36 ± 15
N V	1238.8 1242.8	5.5 ± 0.3	−0.07 ± 12

the Lα line. The flux measured during one single orbit is in a photon-starved regime and can present strong variations of magnitude (even a negative flux) and shape from one orbit to another. We therefore averaged all the spectra within the orbital phase regions labelled A to E on Fig. 1 (cf. Table A.2): (A) before the exospheric transit signature in the blue wing of Lyα, (B) during the exospheric transit ingress, (C) during the optical transit, (D) during the exospheric transit egress, and (E) after the exospheric transit. Regions (B), (C), and (D) are considered "in-transit"; regions (A) and (E) are "out of transit". We consider the flux integrated in the velocity band [−50, 50] km s^{-1}. Let F_{in} and F_{out} be those fluxes during the transit and out of the transit respectively (dashed lines in Fig C.2). The absorption is defined as $1 − F_{in}/F_{out}$. Table C.1 shows results for each line. The N V lines are summed together in the velocity space. No absorption is observed for this specie. An absorption signal is measured in the O V line, but it may not be related to the planet as only the ingress
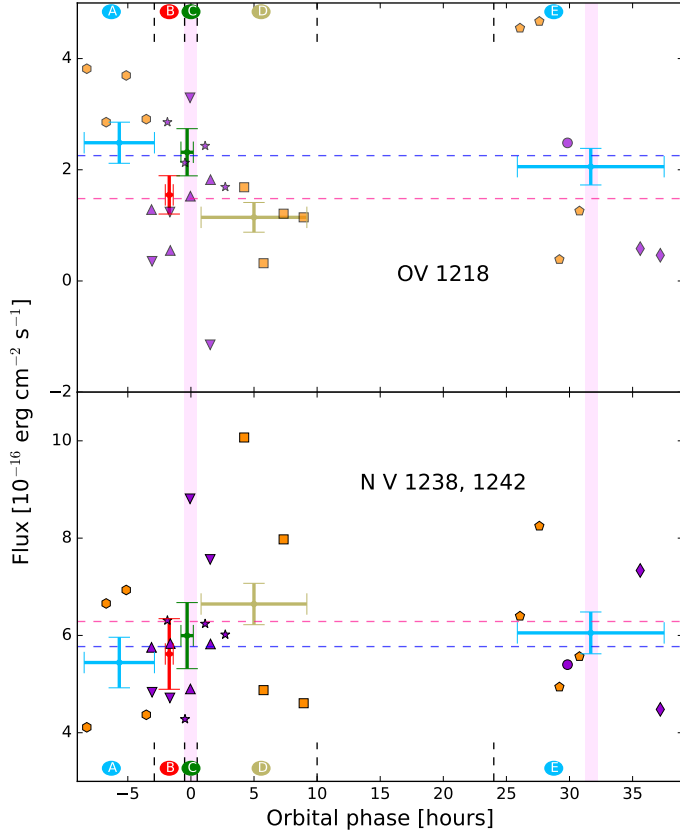
Fig. C.2. Light curves of GJ 436 O v line (*top panel*) and N v (*bottom panel*). Legend is the same as in Fig. 1. Fluxes are integrated for the different temporal regions (see Fig. 1). Horizontal dashed line indicates the out-of-transit flux (blue – regions A and E) and the in-transit flux (pink – regions B, C, and D). Symbols indicate the orbit fluxes (see Table A.1)

and egress fluxes are absorbed. Finally, an absorption signal in Si III line correlated with the planet transit is detected at almost five sigma (see Sect. 4.3).
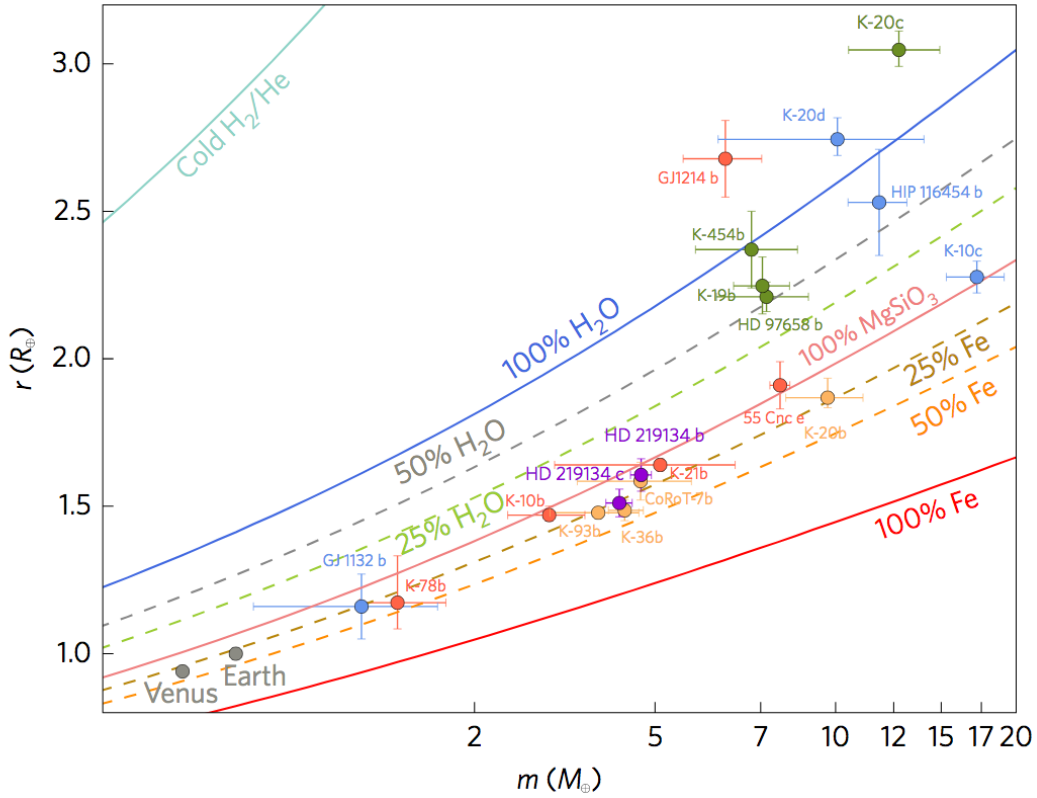
Figure 4.8: Mass-radius relationship for small planets with precisions on the masses better than 20%. The solid lines are theoretical mass-radius curves from Zeng & Sasselov 2013 Source: Gillon et al. 2017

4.5   The super-Earth HD 219134 b

This section describes the analysis of the first observation of HD 219134 in the ultraviolet (UV) obtained with the Hubble Space Telescope during the transit of the b planet. This work will be reported in a first-author article currently in preparation.

4.5.1   The closest system known to have a transiting super-Earth

The discovery of the closest system known to have a close-in transiting rocky planet HD 219134 b (Motalebi et al. 2015; Vogt et al. 2015; Gillon et al. 2017) has provided us with a unique opportunity to study atmospheric escape for super-Earth. HD 219134 is a K-dwarf star at a distance of 6.5 parsecs. The planet b is the innermost planet with an orbital period of 3.092926 ± 0.000010 days, a mass of 4.74 ± 0.19 Earth mass ($M_\oplus$), a radius of 1.602 ± 0.055 Earth radius ($R_\oplus$) and receives a bolometric flux 176.2 ± 5.5 times higher than the incident flux of the Earth ($S_\oplus$), Gillon et al. 2017.

Bayesian analysis based on the radius and mass of the planet and stellar abundances was

Table 4.1: Observation log

Visit (color)	Date	Programme	PI	*HST* orbits	Mode
1E (orange)	15 Oct 2016	GO#14461	Ehrenreich	1	E140H
1G (black)	15 Oct 2016	GO#14461	Ehrenreich	4	G140H
2 (pink)	16 Fev 2018	GO#15430	Lavie	4	E140H
3 (violet)	02 Jul 2018	GO#15430	Lavie	4	E140H

conducted by Dorn et al. (2017) to determine the composition of the bulk of HD 219134 b. They inferred that the planet may be composed of up to 20% of water. Another Bayesian inference based on the mass and radius of HD 219134 b (Dorn & Heng 2018) found that the planet probably holds an atmosphere of 0.18 radius. Those authors also found that HD 219134 b's possible atmosphere is unlikely to be hydrogen dominated and is enriched, thus possibly secondary. This is in accord with its XUV irradiation, its mass-radius relationship (Fig. 4.8) and its position below the evaporation valley.

An initial set of data was obtained in October 2016 (GO programme 14461; PI D. Ehrenreich) in order to assess a possible transit of its exosphere. The observations were divided in two different mode. The low resolution G140M, which is normally use for this type of observations, was used to evaluate the presence of an exosphere. One *HST* orbit was done with the high resolution mode E140H to gauge the feasibility of such observation. Because HD 219134 is very close to Earth, the observational test with the high resolution mode was conclusive. A signature in the red part of the Lyα line was observed in the low resolution data. Moreover, the high resolution observation displayed the presence of the sharp and well-defined carbon and oxygen lines in the stellar spectrum that can be use to probe those species in the planet's atmosphere. Based on those exciting results, I proposed and obtained new observations with the high resolution spectroscopic mode of *HST*. Two transits were obtained in 2018. It is the first time that the transit of a super-Earth is observed at high resolution in the FUV. The analysis of the three set of data is presented in section 4.5 and will be the subject of an article that is under preparation.

4.5.2 Observations

We observed three transits of HD 219134 b with *HST*/STIS, using the Far Ultraviolet Multi-Anode Microchannel Array detector (FUV-MAMA) and two different modes: the E140H gratings with a central wavelength of 1 271 Å (total range is 1 160 Å to 1 350 Å) and the G140M grating with a central wavelength of 1 222 Å (total range is 1 190 Å to 1 250 Å), same settings as the GJ 436 b observations.. The E140H and G140M gratings offer resolution of
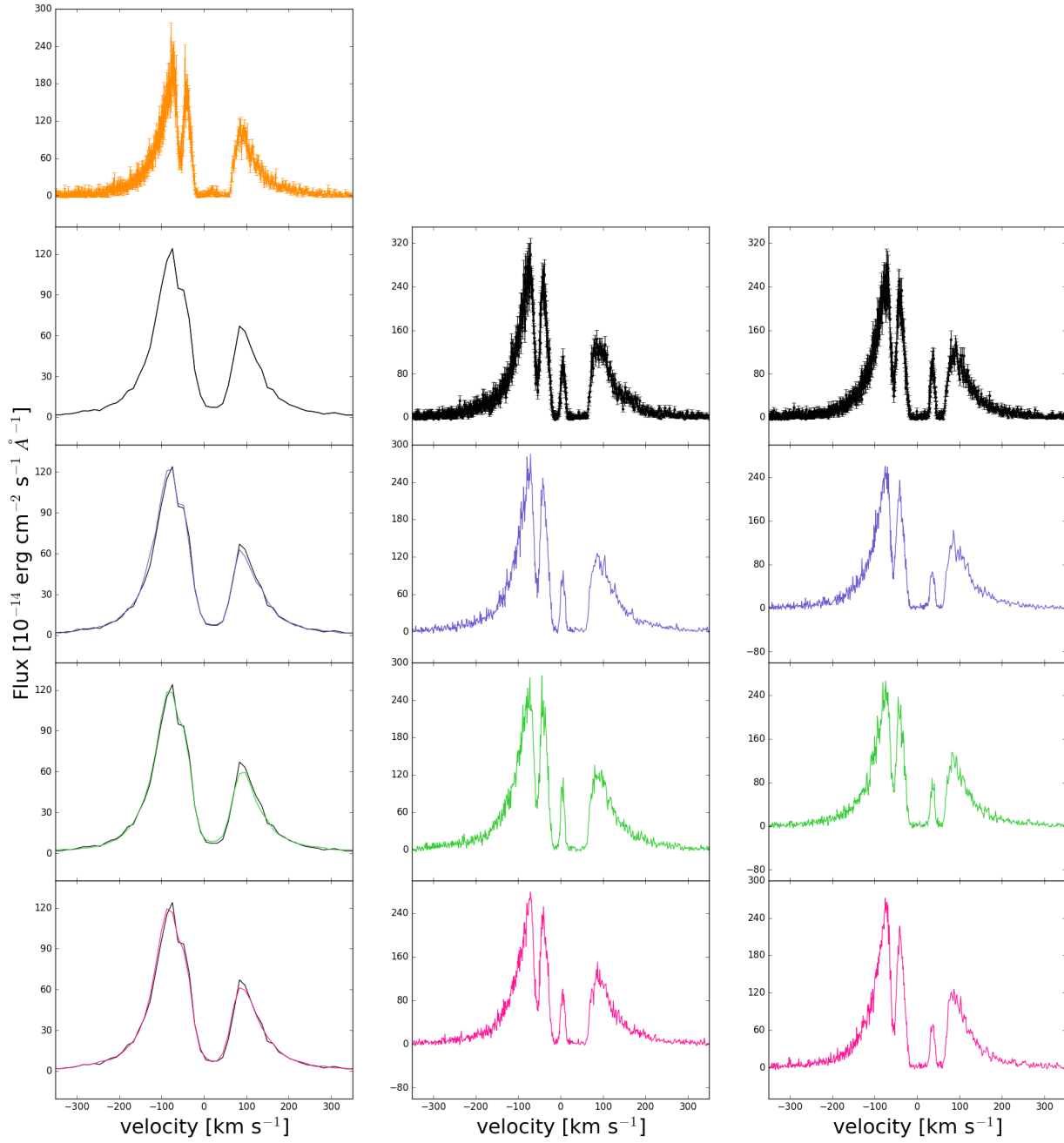
Figure 4.9: Lyα line obtained during each *HST* orbits of visit 1E,1G (first column), visit 2 (second column) and visit 3 (third column). The black spectrum is the reference spectrum for each visit. Contamination by the earth geo-corona (airglow) can be seen in the core of the line for visit 2 and visit 3.
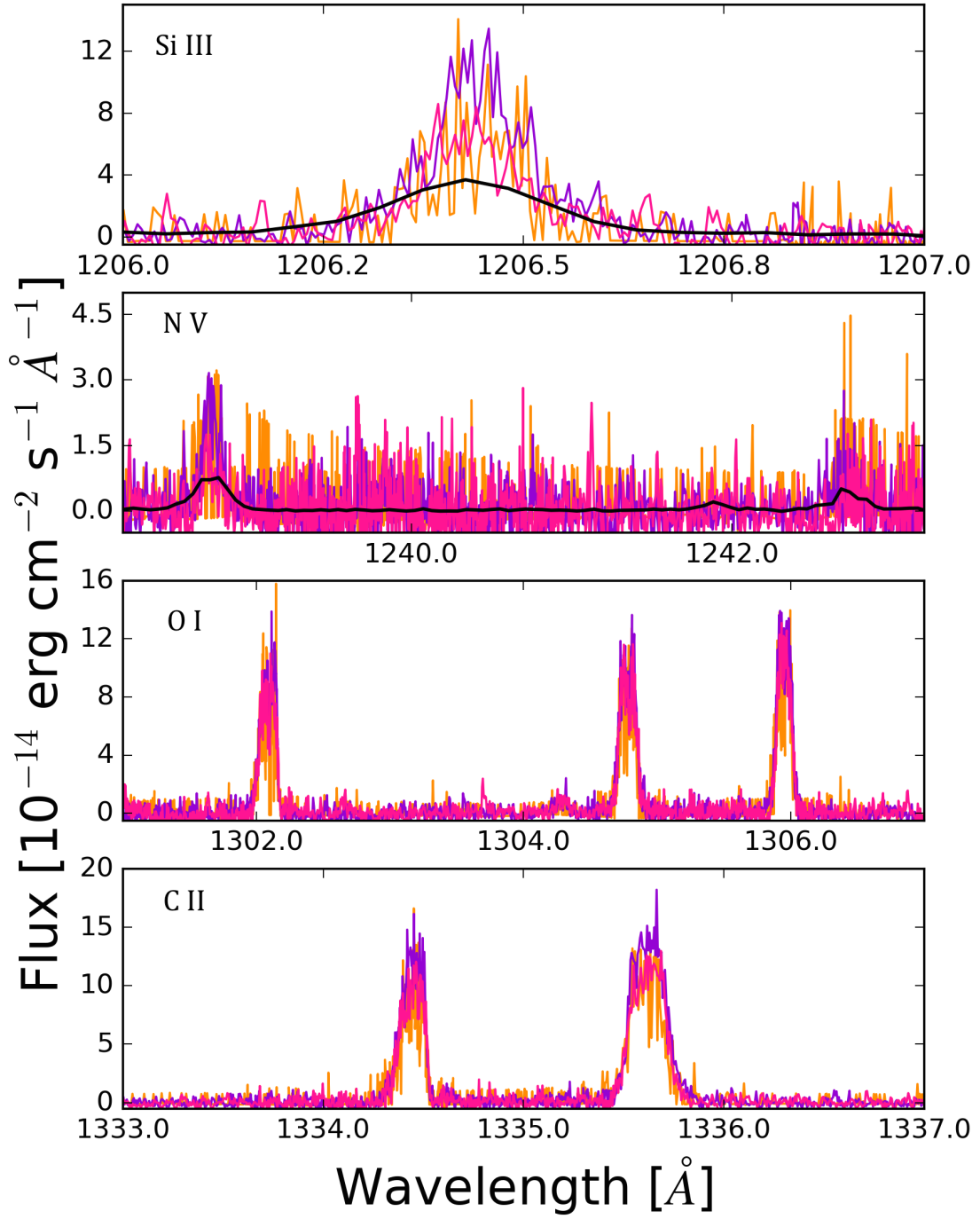
Figure 4.10: The main spectral lines available in the far ultraviolet observation of HD 219134 (excluding Lyα). The high resolution spectrum obtained with the E140H mode of *HST* are colour coded orange (Visit 1E), pink (Visit 2) and violet (Visit 3). The low resolution spectrum obtained with the G140M mode of *HST* is in black (Visit 1G). The silicon line at 1206.5 Å the oxygen triplet lines at 1302.17, 1304.86 and 1306.03 Å and the carbon doublet lines at 1334.53 and 1335.71 Å are clearly visible. The nitrogen doublet lines at 1238.8 and 1242.8 Å are barely visible.

Table 4.2: Spectral lines and observed stellar flux

Species	wavelengths [Å]	Stellar flux (1)	correlation with Lyα (2)
H I	1215.67	$107.10^{+14.05}_{-17.85}$	1
Si III	1206.50	$1.26^{+0.38}_{-0.19}$	0.75
N V	1 238.8	$0.26^{+0.10}_{-0.13}$	0.07
	1 242.8	$0.11^{+0.06}_{-0.08}$	0.05
O I	1302.17	$1.17^{+0.19}_{-0.15}$	0.93
	1304.86	$1.37^{+0.17}_{-0.21}$	1.0
	1306.03	$1.40^{+0.21}_{-0.12}$	0.80
C II	1334.53	$1.53^{+0.26}_{-0.22}$	0.94
	1335.71	$2.56^{+0.46}_{-0.31}$	0.87

(1): $[10^{-14} \text{ erg cm}^{-2} \text{ s}^{-1}]$
(2) : Pearson correlation coeficient

114'000 and 12'000 respectively. Compared to GJ 436, HD 219134 is bright because it is closer, which allowed the use of the high resolution mode. Observations log is provided in Table 4.1. The first visit is composed of one orbit using the E140H grating (Visit 1E) and 4 orbits using the G140M grating (Visit 1G). Ephemeris are taken from Gillon et al. (2017). Each orbit is divided into five sub-exposures chosen to maximise the temporal coverage while maintaining a good signal over noise ratio. The main feature visible in the spectrum is the Lyα line of neutral hydrogen at 1215.67 Å. Fig 4.9 shows this spectral line for each of the HST orbits observations. The core of the line is absorbed by the interstellar medium (ISM) and is contaminated by the airglow. Other spectral lines are visible in both modes and are presented in section 4.2.

4.5.3 Correction of the systematics

4.5.3.1 G140M vs E140H

A direct comparison of the spectra between the two instruments is not possible because the line spread function (LSF) of each mode is different. However, the integrated flux over the entire Lyα line must be conserved. Assuming no planetary absorptions between the Echelle spectrum visit 1E and the first orbit of visit 1G G140M observations, we compared the integrated Lyα line flux, which yields a 15% difference, Fig 4.11 panel a. This difference is likely instrumental: a variation in the focus, which might push some flux into the outer wings of the instrument point spread function (PSF), which is cut off by the narrow aperture used in the G140M observations(Youngblood et al. 2016; Parker Loyd et al. 2016)

4.5.3.2 Telescope Breathing

As we have seen in section 4.3, the correction is done by studying the variation of the flux in a reference wavelength or velocity band. This band is chosen in the Lyα emission line in order to maximise the flux but avoiding any astrophysical signatures. The geocoronal emission line (airglow), known to pollute the core of the Lyα line, is not visible in Visit 1G observations due to the brightness of HD 219134. This is due to the G140M mode, which has a LSF broad, flux from the stellar Lyα line wings is spreading to the core. For E140H observations, however, there is no flux in the core of the observed Lyα line because of the narrower LSF and contamination can be seen. Nevertheless, this contamination occurs in the core of the line that is already entirely absorb by the ISM. The velocity range between -20 to 60 km s^{-1} as respect to the Lyα wavelength can not be use. Observed flux in this region cannot be use in our analysis. A careful inspection of the Lyα spectra presented in Fig 4.9 combined with the signature searched procedure allow us to set the reference band for each visit. For Visit 1E we use the entire Lyα line $[-300, 300]$ km s^{-1}. To reproduce and correct the systematics the gaussian processes method described in section 4.3.4 is used. Figure 4.11 shows the integrated flux in the reference band in each subexposures as a function of the HST/orbital phase with the fitting of the GP.

4.5.4 Planetary signatures

The main spectral feature is the Lyα which dominates all the other spectral lines by at least a factor 10. However, others spectral lines in the spectrum can be resolved (Fig 4.10 and Table 4.2). Common to the G140M and E140H observations, four spectral lines have been identified : Si III at 1 206.5 Å, N v doublet at 1 238.8 and 1 242.8 Å, and O v at 1 218.3 Å. The N v doublet is very weak and hardly visible, and so is the O v line in the wing of the Lyα line. In
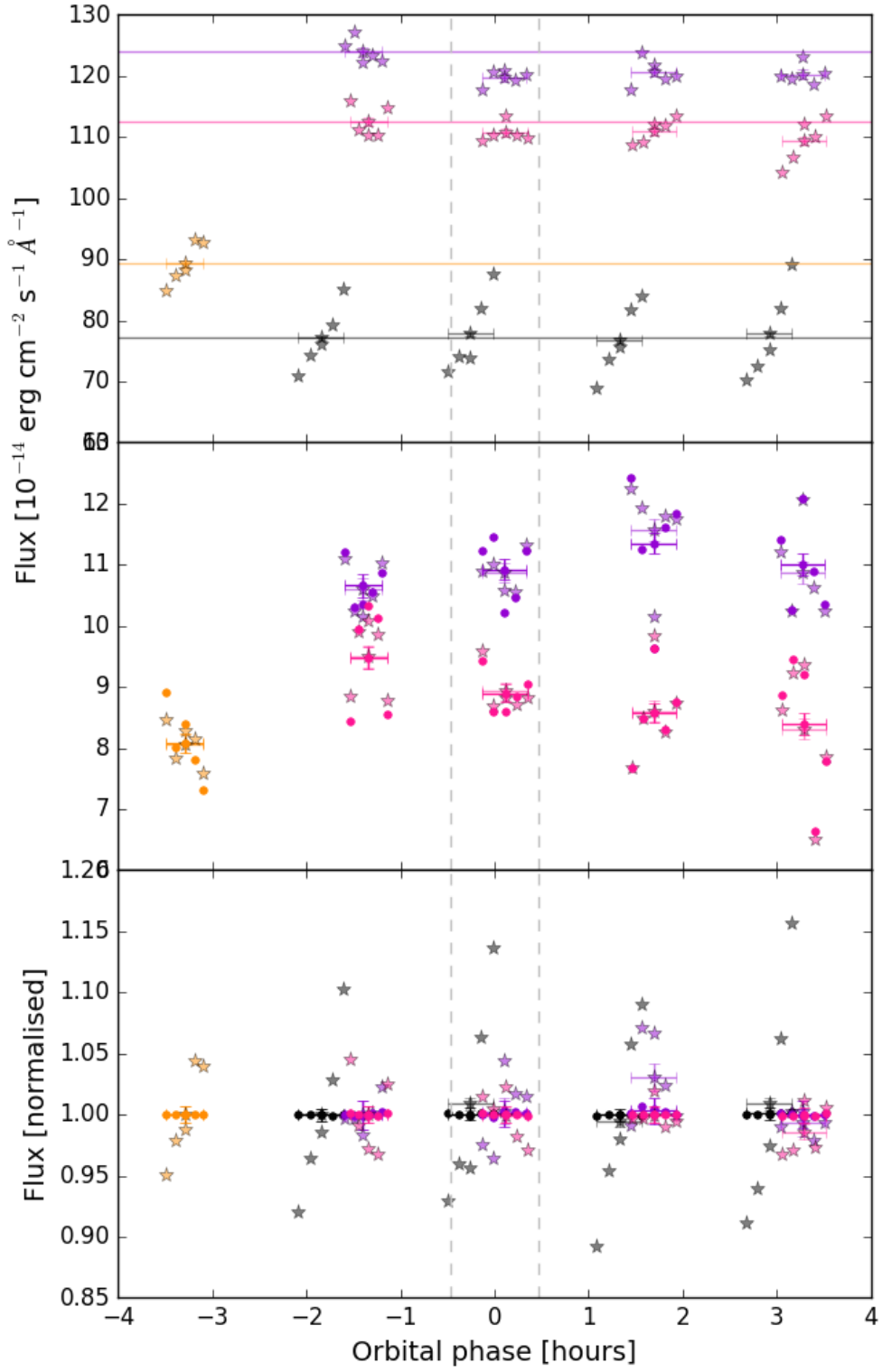
Figure 4.11: Lightcurves of HD 219134 b with flux integrated other the entire Lyα line (top - raw data), the spectral lines Si III,C II and O I (middle) and the reference band (bottom) for each visits 1E (orange), 1G (black), 2 (violet) and 3 (pink). Star points are raw data. Circles are detrended data.

addition to those lines, five spectral lines are clearly visible in the E140H observations at longer wavelength : O I triplet at 1 302.17, 1 304.86 and 1 306.03 Å; and the C II doublet at 1 334.53 and 1 335.71 Å.

The search for planetary signatures is done independently in each visit. The integrated flux in a given wavelength range of the first *HST* orbit of each visit is considered as the out of transit reference flux level. The consecutive *HST* orbit are then compared to this reference level. Observations after the optical transit are not used for the reference level because cometary tail shaped by the interaction of the escaping gas and the interplanetary medium (stellar wind, radiation pressure) have been observed for others targets. Increase or decrease of the flux can be observed. For all the spectral lines except Lyα the search is done by integrating the entire line between $[-50, 50]$ km s^{-1}. For the Lyα line, the flux is integrating for all combinations of pixels binning with a minimum width of 5 km s^{-1} between $[-300, 300]$ km s^{-1} for the E140H observations and with a minimum width of 10 km s^{-1} between $[-400, 400]$ km s^{-1} for G140M observations (due to the broader LSF of the instrument).

A threshold at three σ is set on all absorption and emission signatures when using the raw fluxes. No signatures is found for the metals lines and no emission signatures is found for all lines. In both wings of the Lyα line, different velocity ranges present significant absorption signals (see Fig. 4.12). The robustness of each signature is tested with (a) different telescope breathing correction (variations of the reference band) (b) reproducibility from one transit to another (c) eyes inspection in regards to the transit in the visible and the spectrum.

- Blue Wing

  Absorption signal in the blue wing of the Lyα line is only present in Visit 2 at high velocity $[-185, -170]$ and at smaller velocities $[-97, -21]$ km s^{-1}. A 2 σ absorption signal in Visit 1G at $[-300, -180]$ km s^{-1} is measured but excluded by our choice of threshold. The low velocity range $[-97, -21]$ km s^{-1} is very sensible to the telescope breathing correction and there is no similar signature in any of the others visits.

- Red Wing

  A broad signature is measured in the red wing of Visit 1G between $[70, 175]$ km s^{-1}. For the Echelle observations, two different type of signatures are measured at low velocity (Visit 2 : $[70, 120]$ km s^{-1}; Visit 3 : $[89, 95]$ km s^{-1}) and high velocity (Visit 2 : $[174, 186]$ km s^{-1}; Visit 3 : $[168, 177]$ km s^{-1}). The presence of two signatures at low and high velocities in Visit 1 is possible. If present similarly to Visit 2 and 3 those two velocity ranges would be broaden by the LSF of the instrument to eventually form one single signature.

It is not possible to compare directly the calibrated lightcurves because of the slightly different velocity ranges and the long term stellar variations. Therefore, each visit lightcurves

is normalised by the flux of the first *HST* orbit and similar signatures are compared (see Fig. 4.12). The absorption at low velocity in the red wing (LVR) of Lyα measured during visit 2 has the same relative amplitude variations as the broader absorption in the red wing measured during visit 1 G. The flux decreases by ∼ 7.6% during the visible transit and slightly increases after but without reaching its pre-transit value (absorption is still ∼ 4% 3 hours after the visible mid-transit time). The signal in the LVR during Visit 3 is deeper than in the other two transits with an absorption of ∼ 21.6% during the visible transit and does not reach as well its pre-transit level after. The absorption at high velocity in the red wing (HVR) of Lyα measured during Visit 2 and 3 are hardly compatible between each other and with the broad absorption in the red wing of Visit 1G. The flux decreases by nearly ∼ 36% during Visit 2 and 3 but at different orbital phases. The absorption is at its maximum during the visible transit for Visit 2 while this maximum absorption is only obtained at 3 hours after the visible mid-transit time for Visit 3.

Signatures in the red part of the Lyα line are tricky to explain as discussed in section 4.4.2. Magnetic interaction is often used as a possible explanation and indeed a weak magnetic field consistent with the very long rotation period of HD 219134 (Folsom et al. 2018). Further modelling and observations are needed to resolve this puzzling result. The absence of signature in the oxygen lines is in accordance with analysis of Vidotto et al. (2018). They used a theoretical 3D study to determine the transit depth in those lines and showed that present uncertainties in FUV observations do not allow the detection of oxygen in the exosphere of the planet. Folsom et al. (2018) observed the transit of HD 219134 b in the near-ultraviolet around the Mg ɪɪ h and k lines using the new cube satellite *AstroSat* (Singh et al. 2014) and did not detect any signatures. However, the telescope was still in its early science operations and problems occurred during their observations.

4.5.5   Reconstruction of the stellar Lyα line

A significant fraction of the flux radiated in the ultraviolet by the star is in the Lyα line. Estimation of the Lyα flux is therefore important to apprehend how much energy is delivered to the companion' upper atmosphere. When observations are available, most of the flux emitted by the star in the Lyα line is absorbed by the neutral hydrogen in the interstellar medium along the line of sight. It is thus necessary to reconstruct the stellar line without interstellar absorption. Linsky et al. (2013) identified five techniques to compute the intrinsic Lyα flux while Linsky (2014) regrouped them into four categories. Personally, I preferred to group those techniques into two associations: the ones using correlation between some stellar parameters and the integrated Lyα line flux and the ones using a retrieval technique to reconstruct the Lyα line. All techniques described in Linsky et al. (2013) can be classified in one of those two approaches.
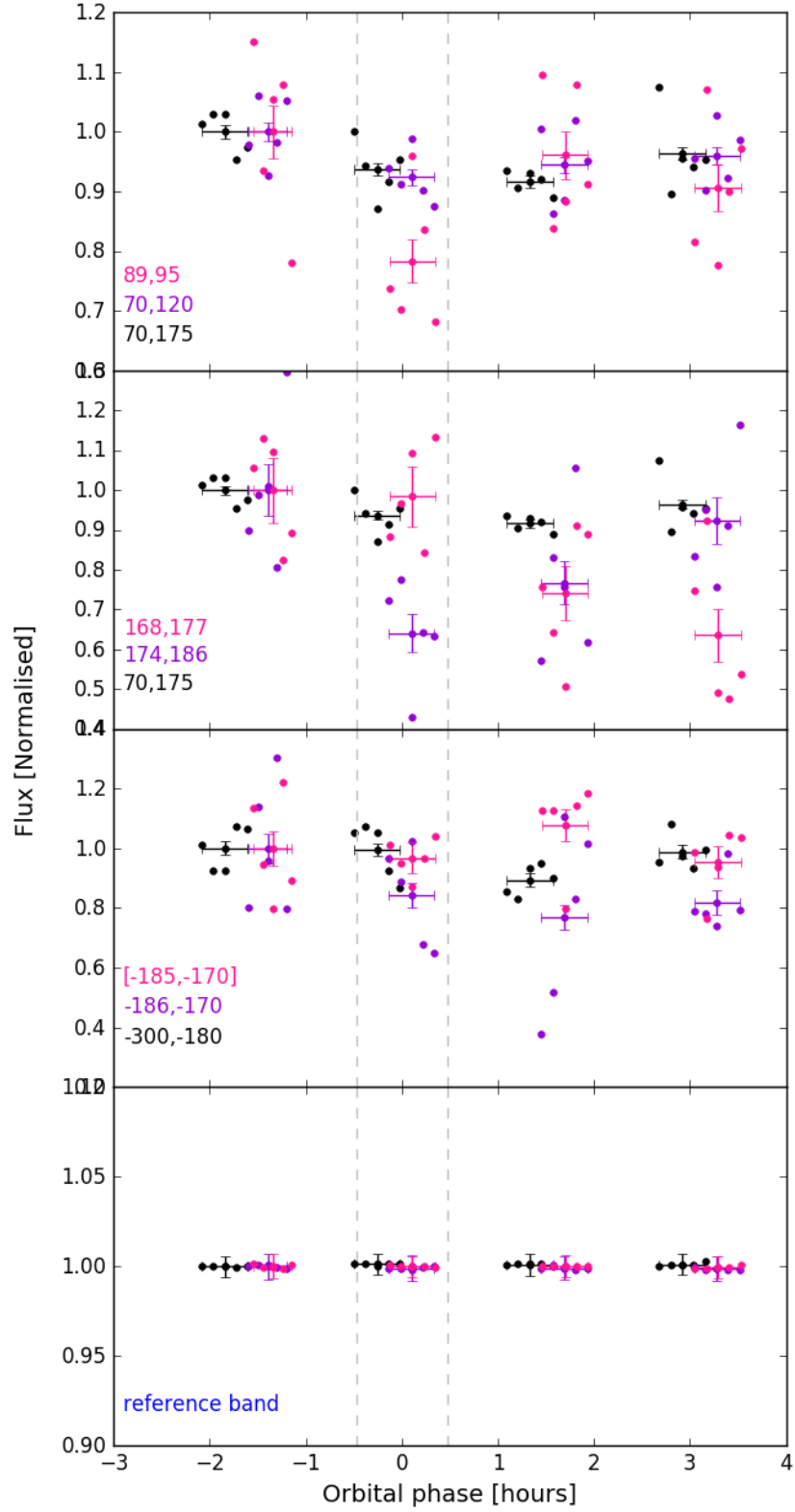
Figure 4.12: Normalised lightcurves for comparison of the planetary signatures between visits 1G (black), 2 (violet) and 3 (pink). First three panels show the lightcurve in the three different part defined in 4.5.4. The bottom panel shows the lightcurve when integrating in both wavelength ranges of the red wing. The colour coded numbers indicate the velocity range on which the light curve is computed. For the blue shifted signature (third panel), the light curve of Visit 3 is integrated on the velocity range of Visit 2 because no similar signature were found.

4.5.5.1   Spectral correlations

The idea of this approach is to use other stellar spectral lines as proxy to estimate the flux in the Lyα line. Linsky et al. (2013) used observations of 49 stars including the Sun to study correlations between the Lyα line and different part of the spectrum.

4.5.5.1.1   Correlation with spectral lines   The Lyα line is correlated with specific stellar lines that form at similar or different temperature range:

- Spectral lines that formed at slightly lower temperatures.
  The magnesium lines Mg II h and k at 2802.71 Å and 2795.53 Å but this require some sort of reconstruction of those lines as absorption by the interstellar medium is possible. The calcium lines Ca II H and K at 3933 Åand 3968 Å. The difficulty with those two ions is to distinguish the photospheric emission and the chromospheric emission that is of interest for the comparison to the Lyα line (Linsky et al. 1979; Pasquini et al. 1988; Robinson et al. 1990; Browning et al. 2010). The more active the star, the less important the photospheric emission is, as compared to the chromospheric emission.

- Spectral lines that formed in the same range of temperature than the Lyα line. The Lyα line is correlated with the last two lines of the neutral oxygen O I triplet at 1 304.86 and 1 306.03 Å, the last line of the ionised carbon C II doublet at 1 335.71 Å and the ionised carbon doublet C IV at 1 548.19 and 1550.77 Å (Fig 4.13).

  Estimation of the intrinsic Lyα flux using correlation with other spectral lines provides an uncertainty of 18 to 25 % for F5-K5 dwarfs stars (Linsky et al. 2013). The dispersion is higher for M dwarfs that are known to be more variable. This dispersion may be the consequence of variability as observations of the Lyα line were not done at the same time as the other spectral lines.

  4.5.5.1.2   X-Ray emission of the star   Using the correlation with X-ray emission of the star leads to a similar uncertainty on the estimate of the intrinsic Lyα line. For M dwarfs the correlation is weaker as X-ray time variability is higher than for others stars (Linsky et al. 2013).

4.5.5.2   Correlation with other stellar parameters

Linsky et al. (2013) also compared the correlation between the Lyα flux and the effective temperature of the star as well as its rotation period. As for the correlation with other spectral lines, this method leads to reasonable constrain for the hot stars but failed to estimate correctly the more active M dwarfs stars (Youngblood et al. 2016).
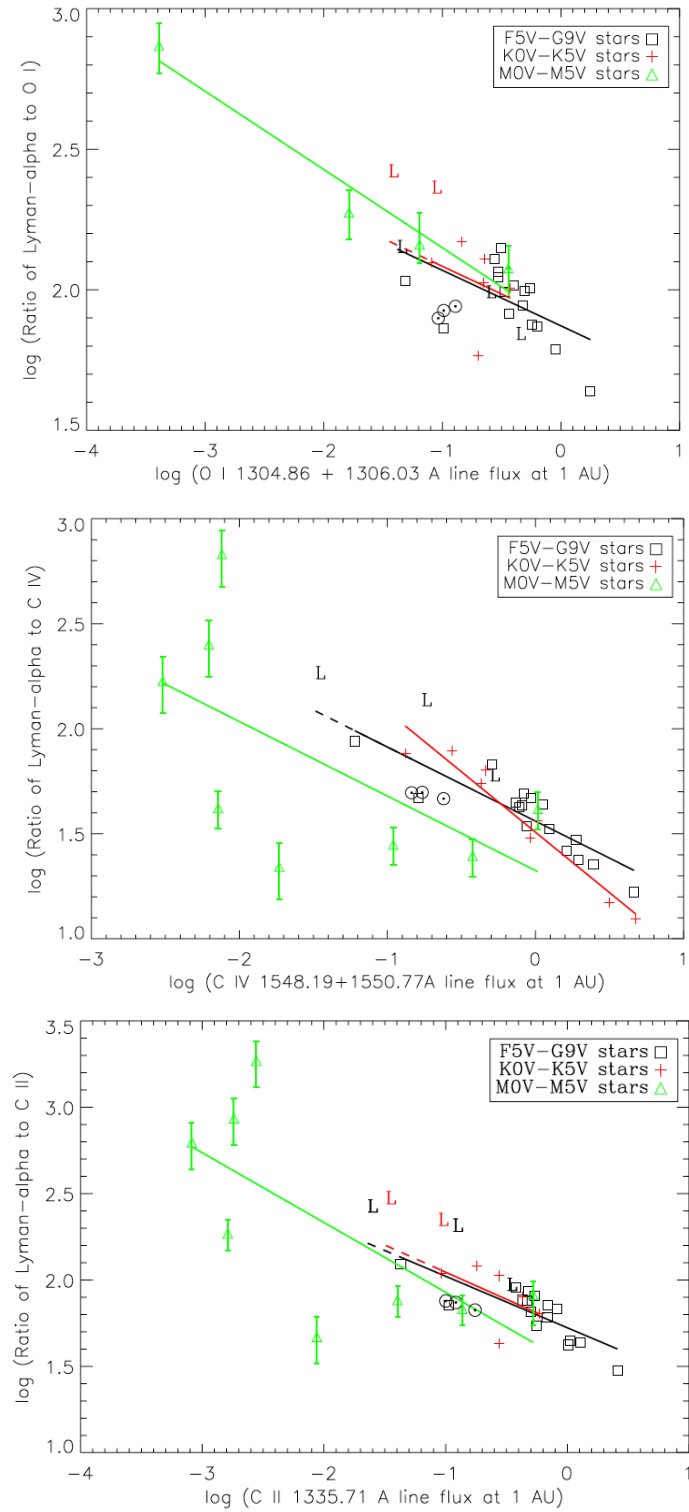
Figure 4.13: atio of the Lyα flux to the different spectral lines and for different type of stars. Source: Linsky et al. (2013)

4.5.5.3   Lyα spectral line retrieval

Reconstruction techniques of the Lyα line using a retrieval technique can be grouped into two different types:

- When information on the interstellar medium is retrieved with high-resolution spectra of the D I, Mg II and or Fe II lines. Wood et al. (2005) estimates that the reconstructed Lyα fluxes are accurate to $\pm15\%$. The retrieval is done in two steps. First, the interstellar medium properties are retrieved by combing analysis of the D I Lyα line with others ISM studies (Lallement & Bertin 1992; Lallement et al. 1995; Redfield & Linsky 2002). The absorption profile is then computed from those properties and the intrinsic Lyα line is estimated by reversing the absorption. There is no preconceived information set on the shape of the Lyα line profile.

- When information on the interstellar medium is retrieved only with the Lyα line and the D I Lyα. The retrieval is done in one step and a global model including the Lyα line shape and the ISM properties is used with some parameter space explorer (France et al. 2012, 2013; Youngblood et al. 2016; Bourrier et al. 2013; Bourrier et al. 2017a).

4.5.6   Characterisation of HD 219134

4.5.6.1   Long term stellar activity and spectral lines correlation

Comparing the integrated flux of all E140H first orbits yields significant differences from one visit to another, with variations up to 39% between the lowest integrated flux and the maximum. Youngblood et al. (2016) studied the Lyα line of 11 M and K dwarfs as part of the MUSCLES program (France et al. 2016) and found that variations of the stellar flux of the same order of what we observe for HD 219134 is usual for this type of stars. Johnson et al. (2016) observed HD 219134 with the 2.7 m Harlan J.Smith Telescope at the McDonald Observatory between 1988 and 2015. They detected a long-period activity cycle of 11.7 years measured in the Ca II S_{HK} index and a periodicity variation due to stellar rotation of 22.8 days. Our data span almost two years between October 2016 to July 2018 (Table 4.1) and are affected by flux variations.

In order to assess the correlation between the Lyα line and each spectral lines the Pearson correlation coefficient is computed and shown in Table 4.2 and can be seen in Fig. 4.14 . There is no correlation for the nitrogen lines N v but it may be the consequence of the weak observed flux in those lines, the noise dominates the signal. All other lines correlate positively with the Lyα line, i.e. if an increase in the Lyα flux is seen then an increase in the others spectral lines is seen as well. The carbon lines are well correlated with the Lyα line, which validate their use for the estimation of the intrinsic Lyα flux in the previous section. The oxygen line at
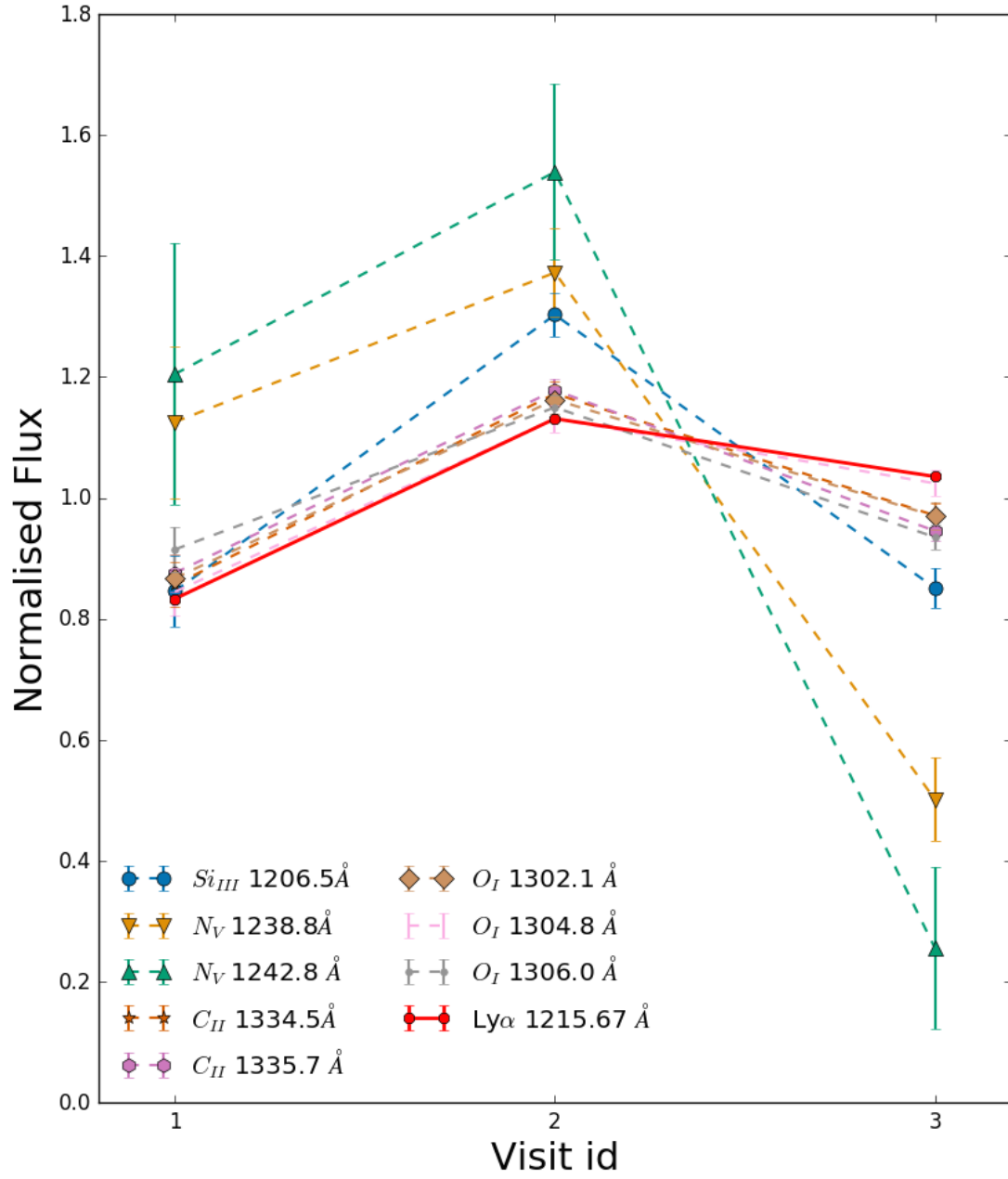
Figure 4.14: Stellar activity. Normalised flux as a function of the three visits observations of HD 219134 in the different spectral lines. The Lyα line is strongly correlated with the oxygen lines at 1 302.17 Å, 1 304.86 Åand carbon line at 1 334.53 Å.

1 306.03 Å show correlation with the Lyα line but to a lesser extent compared to the two other oxygen lines.

4.5.6.2   Reconstruction of the intrinsic Lyα line of HD 219134

4.5.6.2.1   Reconstruction model

In the absence of measurement of HD 219134 magnesium lines to estimate the ISM properties in this line of sight, the reconstruction is done using the retrieval technique with models including both the ISM properties and the intrinsic Lyα line. The nested sampling algorithm is used to explore the parameter space and select the best model. Each model is composed of three components : the intrinsic stellar line, the interstellar medium and the observing instrument. This latter component is the point spread function (PSF) of the instrument used for the observation and is obtained from the space telescope science institute[a] for both mode G140M and E140H. The PSF of the G140M is tabulated and a gaussian function for the E140H PSF is used, which parameters are muted (i.e. they are fixed to values determine with the information provided for this instrument).

- The intrinsic stellar line.

  Different assumptions can be made in order to reproduce the intrinsic stellar Lyα line : a single Gaussian or a Voigt profile. To mimic a self-reversal profile the intrinsic stellar line can be modelled by two Gaussians or two Voigt profiles separated by some wavelength shift. The stellar flux F_{star} is computed at the top of the stellar atmosphere, absorbed by the ISM and then propagated to the Earth distance using the radius of the star R_{star} and the distance d of the system, similar to equation 2.9. The star radius and the distance are fixed to 0.778 R_{Jup} and 6.55 parsecs, respectively.

- The Interstellar Medium (ISM).

  The ISM is composed of interstellar clouds (the parameter number of clouds : N_{clouds}). Between Earth and the target the light will pass different clouds with different properties. In practice, when using *HST*/STIS data the model selection favours models with only one cloud. The retrieved properties of this cloud can therefore be seen as an average of the different clouds that composed the real ISM. A cloud is defined by its temperature, its radial velocity relative to the Sun and the abundance of hydrogen and deuterium. The actual parameter is the ratio of hydrogen to deuterium as it has already been estimated to $1.5 \pm 0.5 \times 10^{-5}$ value from other studies can be directly enforced in our prior.

4.5.6.2.2   Retrieval on HD 219134

From one visit to another the observed Lyα line is showing significant variations. Therefore,

---

[a]http://www.stsci.edu/hst/stis/performance/spectral_resolution

each visit needs to have its unique intrinsic Lyα line. The interstellar medium is stable on the timescale of our observations, so the same ISM component is used for all visits. The flux variations seen between the G140M observations and the E140H in visit 1 is modelled by a single parameter that multiply the fluxes between the two modes. The model with one cloud and two Voigt profiles is always significantly preferred over the other models. The entire retrieval is done with a 20 parameters model : four parameters for the ISM cloud (temperature, velocity, hydrogen column density, deuterium to hydrogen ratio), five parameters per intrinsic line (line centres of both Voigt profile, amplitude, the full width at half maximum of the Gaussian and the Lorentzian) and the parameter for the G140M vs E140H flux variation in visit 1. The Voigt profile is computed using the real part of the Faddeeva function (Gautschi 1970; Poppe & Wijers 1990; Zaghloul & Ali 2011; Grimm & Heng 2015).

Results and Comparison with other study

Folsom et al. (2018) analysed the E140H visit 1E, which is publicly available on the archive. They followed the methodology of Wood et al. (2005), who used a retrieval in two steps by constraining the ISM properties with the deuterium absorption. Their initial model can not reproduce the blue part of the observed Lyα line. They interpreted this extra-absorption as a signature of astrospheric absorption. Astrosphere are analogous of the Sun heliosphere but for other stars. It is the region in space dominated by the star' influence. At the edge of this sphere the weak stellar winds collide with the ISM. Interactions by charge exchange processes create a population of hot hydrogen atoms that could produce a detectable absorption signature. For a given star observed from Earth, the astrosphere (of this star) is expected to create a blue shifted absorption and the heliosphere (of the Sun) a red shifted absorption Gayley et al. (1997); Izmodenov et al. (1998); Wood (2004). Using a two steps retrieval (also used by Folsom et al. 2018 for HD 219134), Wood et al. (2005) detected extra absorption than the ISM absorption for a couple of stars and explained it with heliospheric or astrospheric absorptions.

This technique does not assume any pre-conceived stellar line for the intrinsic Lyα line but sets a fixed deuterium to neutral hydrogen ratio for the ISM. The ISM hydrogen column density is computed using the deuterium absorption when available (i.e. with high resolution observations) and\or the observed Mg II h and k lines. The deuterium and neutral hydrogen line signature of the ISM are assumed to be Voigt profile. The main difference from this technique to the one used in my Ph.D work are that the intrinsic Lyα line is assumed to be a Voigt profile with the possibility of self-reversal absorption; and the deuterium to hydrogen ratio of the ISM is a free parameter with a Gaussian prior centred on the same value used by Wood et al. (2005) with the relevant uncertainty. Comparison of the best fit models to the same data set (i.e. visit 1E) is shown in Fig. 4.15. The red part of the Lyα line observed is well reproduced by our model and no astrospheric absorption is required. However, the blue part of the Lyα line is
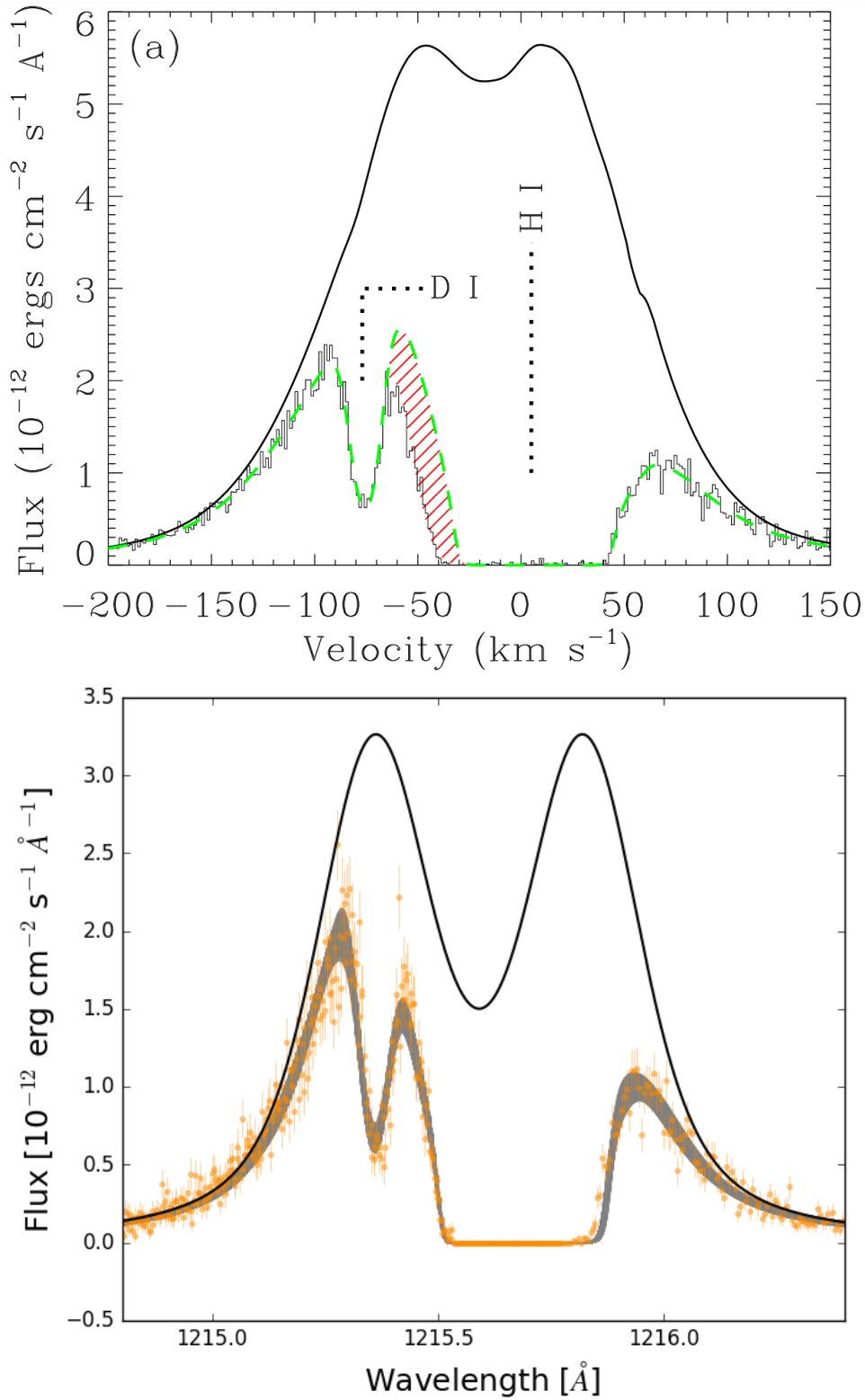
Figure 4.15: Comparison of Lyα reconstruction with the same data set. Top panel is from Folsom et al. 2018. Bottom panel is this work. The grey area is produced from 5000 draws from the posterior distribution. The black line is the intrinsic Lyα line as seen from Earth if there was no absorption from the ISM. The retrieved intrinsic line is different in both approach in terms of flux peak and self-reversal absorption depth. Folsom et al. 2018 includes astrospheric absorption, which is not included in our model.

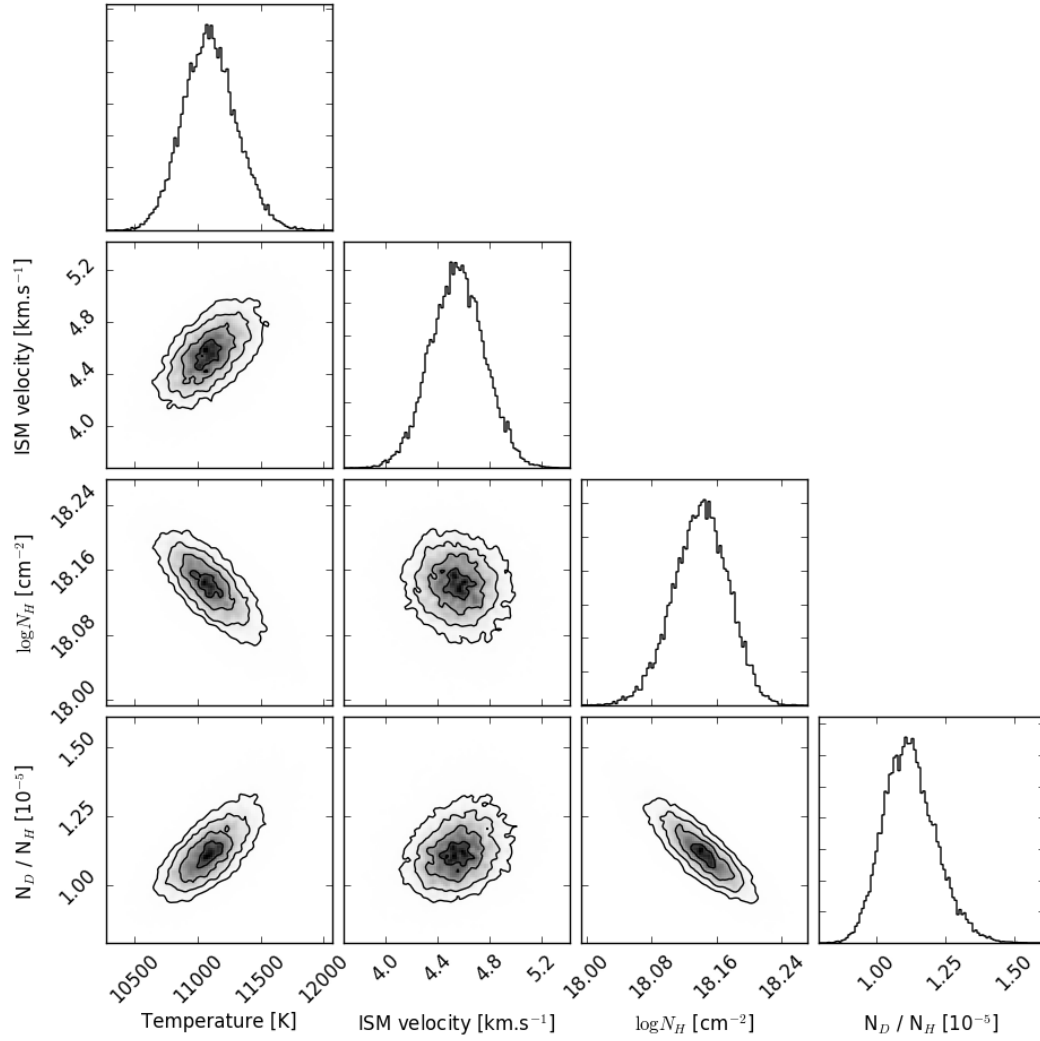**Figure 4.16:** Corner plot of the ISM parameters for the Lyα line reconstruction of visite 1E. In comparison, Folsom et al. (2018) obtain a temperature of $\sim$ 7500 K, a velocity of $\sim$ 7.3 km.s^{-1}, a column density of 18.03 cm^{-2}. Their deuterium to hydrogen ratio is fixed to 1.56.10^{-5}.

not well reproduced, which may indicate heliospheric absorption, which is not required in their analysis. In the absence of a common retrieval analysis it is difficult to compare both models and disentangle the 'correct' model. The retrieved column density of hydrogen are similar in both analysis to $\sim$ 18 cm^{-2}. The retrieved ISM velocities are relatively similar to $\sim$ 7. km.s^{-1} and 4.5 km.s^{-1}. Our retrieved value of $\sim$ 1.2e^{-5} for the hydrogen to deuterium ratio is smaller than their fixed value at $\sim$ 1.56e^{-5} . The shape of our intrinsic Lyα line is different than the one they published (Fig. 4.15) in terms of flux peak and self-reversal absorption depth. The higher depth of self-reversal absorption could explain why we better fit the blue wing of line and do

not need astrospheric absorptions. This need to be fully address for the publication. In any case, the presence or not of heliospheric or astrospheric absorptions does not perturb planetary signature because they are deemed to be stable on the timescale of the planetary transit.

4.6 Evolution of GJ 436 b and HD 219134 b by atmospheric escape

GJ 436 b may have formed as a more massive planet and atmospheric escape could have eroded its atmosphere up to its actual mass. On the other hand the planet may have formed as it is and erosion by atmospheric escape has been negligible. In both scenario, the atmosphere of the planet remains hydrogen-helium dominated. The source of the escaping hydrogen is therefore its primordial atmosphere and contribution of other sources of hydrogen such as photodissociation of water are slim. Hu et al. (2015) predicts that the planet may evaporate its hydrogen envelope and become helium dominated within 10 Gy. This depletion of hydrogen over a long period can have large effects on the composition of the planet and significantly affect the carbon to oxygen ratio by favouring CO as the main carrier of carbon rather than CH4, which can explain the observations in the near-infrared (Lanotte et al. 2014). However, this scenario seems to be ruled out by the age estimation, ~ 6Gy (Torres 2007; Bourrier et al. 2017b) of the system and the detection of the escaping hydrogen atoms. Also, the mass-loss rate estimated from the observation (Ehrenreich et al. 2015; Bourrier et al. 2016b) of hydrogen escape of the warm Neptune GJ 436 b is not enough to significantly affects the planet composition and the presence of hydrogen. With those consideration, the planet may have formed with its current composition. However, irradiation and mass-loss rate in the past may have been higher, which would impacted the planet evolution. Other facts also indicate that more complex assumptions are probably needed. First, the planet have a peculiar position at the edge of the evaporation desert, almost inside the desert. In the absence of other survivors in this area of the exoplanet population, one may ask how GJ 436 b survived if it has followed the main formation scheme. The warm Neptune GJ 3470 b stands not too far from GJ 436 b in the desert and also orbits a M dwarf. Atmospheric escape on this planet have been revealed recently with Lyα observations (private communication with Vincent Bourrier). This will provide more insight on the evolution of warm-Neptune enduring atmospheric escape around M-dwarfs. Secondly, GJ 436 b is misaligned and has a moderate eccentricity instead of being circularise as predicted by tidal interactions. This latter fact may be explained by the presence of a companion (Ribas et al. 2008; Maness et al. 2007; Bourrier et al. 2017b).

Observations of the transit of HD 219134 b in the FUV indicate the possibility that the planet endures some sort of atmospheric escape. Although more observations are needed as stellar activity cannot be ruled out. The origin of the escaping hydrogen atoms depends on the formation of the planet and its history. The planet either holds a primordial hydrogen-dominated atmosphere - not changed since its formation- or a secondary atmosphere as suggested by Dorn & Heng (2018). Using an evolutionary model and assuming different initial mass and radius

properties, Kubyshkina et al. (2018) computed that the planet losses its primordial atmosphere within a couple of million years. If the atmosphere is indeed secondary, then the planet is not hydrogen dominated and a probable source for the escaping hydrogen is the photo-dissociation of water. Formation in situ is unlikely as a planet too close to its host star is expected to be dry because there is no water available in that region of the disc and because of the low efficiency of water delivery from both comets (Levison 2000) and asteroids (Raymond et al. 2004). This delivery process may be more efficient for low-mass stars such as K-dwarfs like HD 219134 as the snowline is expected to be closer to the star. Nevertheless, HD 219134 b is the closest planet to the host star in the system and this hypothesis seems reasonable. The planet may have formed beyond its current position and have migrated to the position we observed it today. Raymond et al. (2008) showed that photo-evaporation of close-in gaseous planets within 0.05 AU can strip out most of the primordial atmosphere of not to massive giants. A planet of 25 $M_\oplus$ evaporated to its core in less than 25 Myr at 0.025 AU but required few Gyr at 0.05 AU.

Nevertheless, The presence of an atmospheric layer around the planet is yet to be answered. Therefore, any claims on its formation and evolution without further observations is premature.

4.7 Other papers

A NON-ISOTHERMAL THEORY FOR INTERPRETING SODIUM LINES IN TRANSMISSION SPECTRA OF EXOPLANETS

KEVIN HENG[1], AURÉLIEN WYTTENBACH[2], BAPTISTE LAVIE[1,2], DAVID K. SING[3], DAVID EHRENREICH[2], AND CHRISTOPHE LOVIS[2]
[1] University of Bern, Physics Institute, Center for Space and Habitability, Sidlerstrasse 5, CH-3012 Bern, Switzerland; kevin.heng@csh.unibe.ch
[2] Observatoire de l'Université de Genève, 51 chemin des Maillettes, CH-1290 Sauverny, Switzerland
[3] Astrophysics Group, School of Physics, University of Exeter, Stocker Road, Exeter EX4 4QL, UK

ABSTRACT

We present a theory for interpreting the sodium lines detected in transmission spectra of exoplanetary atmospheres. Previous analyses employed the isothermal approximation and dealt only with the transit radius. By recognizing the absorption depth and the transit radius as being independent observables, we develop a theory for jointly interpreting both quantities, which allows us to infer the temperatures and number densities associated with the sodium lines. We are able to treat a non-isothermal situation with a constant temperature gradient. Our novel diagnostics take the form of simple-to-use algebraic formulae and require measurements of the transit radii (and their corresponding absorption depths) at line center and in the line wing for both sodium lines. We apply our diagnostics to the HARPS data of HD 189733b, confirm the upper atmospheric heating reported by Huitson et al., derive a temperature gradient of $0.4376 \pm 0.0154 \, \mathrm{K \, km^{-1}}$, and find densities ~ 1–$10^4 \, \mathrm{cm^{-3}}$.

Key words: methods: analytical – planets and satellites: atmospheres – radiative transfer

1. INTRODUCTION

Due to its large cross section and favorable wavelength range, the sodium doublet lines have been a boon to astronomers seeking to characterize exoplanetary atmospheres (Seager & Sasselov 2000; Brown 2001). In fact, the first detection of an exoplanetary atmosphere (that of HD 209458b) was accomplished via measuring the sodium doublet (Charbonneau et al. 2002). Ever since that discovery, sodium has been detected in several hot Jupiters using both space- and ground-based transmission spectroscopy (Redfield et al. 2008; Sing et al. 2008a, 2008b, 2012; Snellen et al. 2008; Vidal-Madjar et al. 2011; Wood et al. 2011; Huitson et al. 2012; Zhou & Bayliss 2012; Pont et al. 2013; Nikolov et al. 2014; Burton et al. 2015; Wyttenbach et al. 2015).

As better instruments come online and our ability to resolve the sodium lines improves, it is worth revisiting and redeveloping a theory of how to interpret them. From a remote sensing perspective, a pair of fully resolved sodium lines can, in principle, map out the temperature–pressure profile of an atmosphere at high altitudes and yield the sodium abundance. A quantity used to interpret absorption lines is the equivalent width (Spitzer 1978; Draine 2011),

$$W = \int W_\lambda \, d\lambda,$$
$$W_\lambda = 1 - \exp(-\tau), \tag{1}$$

where τ is the optical depth of the intervening material and λ denotes the wavelength. The equivalent width is essentially the width of a box with the same depth as the trough of the absorption line, such that it encompasses the same area.

While it is not immediately obvious, W_λ and the transit radius (R) are actually independent observables. A simple thought experiment demonstrates this. Consider a fictitious star that emits achromatically. At the exact moment of transit, one may record an absorption spectrum of the exoplanetary atmosphere. If the wavelength coverage is sufficient, the

sodium doublet and the continuum and thus W_λ may be measured. To record the transit radius requires temporal information: the change in flux in and out of transit. In short, W_λ measures changes in absorption across wavelength, while R derives from the change in flux across time. Certainly, stars are not achromatic light sources and one needs to measure the stellar lines in and out of transit to properly subtract out their influence, but this is an observational, rather than a theoretical, obstacle.

Nevertheless, a theoretical challenge with interpreting W, for transmission spectra of exoplanets, is that the optical depth depends on the transit radius and the radius itself depends on wavelength (Figure 1). It is generally difficult to derive the functional form of $R(\lambda)$, but it is straightforward to measure it. Additionally, while W is associated with a fixed sightline in traditional studies of the interstellar medium, it is associated with a *set of sightlines* in transmission spectra, each corresponding to a different wavelength. Instead of a theory for W, we develop one for $W_\lambda(R)$. Observationally, it takes the form,

$$W_\lambda = \frac{F_c - F}{F_c}, \tag{2}$$

where F_c is the flux associated with the continuum and F is the flux at any point within the line. More specifically, both F_c and F are integrated over a (small) wavelength interval $\delta\lambda$ that is chosen based on practical constraints. We shall term F/F_c the *absorption depth* (and leave W_λ nameless).

2. THEORY

2.1. Order-of-magnitude Estimates

Since the line-center wavelength of both sodium lines is $\lambda_0 \approx 0.6 \, \mu\mathrm{m}$, the line-center frequency is $\nu_0 = c/$

LETTER

Orbital misalignment of the Neptune–mass exoplanet GJ 436b with the spin of its cool star

Vincent Bourrier[1], Christophe Lovis[1], Hervé Beust[2], David Ehrenreich[1], Gregory W. Henry[3], Nicola Astudillo-Defru[1], Romain Allart[1], Xavier Bonfils[2], Damien Ségransan[1], Xavier Delfosse[2], Heather M. Cegla[1], Aurélien Wyttenbach[1], Kevin Heng[4], Baptiste Lavie[1] & Francesco Pepe[1]

The angle between the spin of a star and the orbital planes of its planets traces the history of the planetary system. Exoplanets orbiting close to cool stars are expected to be on circular, aligned orbits because of strong tidal interactions with the stellar convective envelope[1]. Spin–orbit alignment can be measured when the planet transits its star, but such ground-based spectroscopic measurements are challenging for cool, slowly rotating stars[2]. Here we report the three-dimensional characterization of the trajectory of an exoplanet around an M dwarf star, derived by mapping the spectrum of the stellar photosphere along the chord transited by the planet[3]. We find that the eccentric orbit of the Neptune-mass exoplanet GJ 436b is nearly perpendicular to the stellar equator. Both eccentricity and misalignment, surprising around a cool star, can result from dynamical interactions (via Kozai migration[4]) with a yet-undetected outer companion. This inward migration of GJ 436b could have triggered the atmospheric escape that now sustains its giant exosphere[5].

Three transits of GJ 436b, which occur[2] every 2.64 days, were observed on 9 May 2007 (visit 1)[2], 18 March 2016 (visit 2) and 11 April 2016 (visit 3) with the HARPS (visit 1) and HARPS-N (visits 2 and 3) spectrographs[6,7]. All visits cover the full transit duration, with exposure times of 300–400 s, and provide baselines of 3–8 h before or after the transit. We corrected spectra for the variability in the distribution of their flux with wavelength caused by Earth's atmosphere (Methods) before using a binary mask to calculate cross-correlation functions (CCFs) that represent an average of the spectral lines from the M dwarf host GJ 436. We introduce a double-Gaussian model to accurately fit the distinctive CCF profiles of M dwarfs (Extended Data Figs 1 and 2) and to improve the stability and precision of their derived contrast, width and radial velocity. These properties show little dispersion around their average values in each visit and are stable between the HARPS-N visits, in agreement with the low activity[2,8] of GJ 436 (Extended Data Fig. 3).

The observed CCFs originate from starlight integrated over the disk of GJ 436 (CCF_{DI}). During the transit they are deprived of the light from the planet-occulted regions (CCF_{PO}), which we retrieve using the reloaded Rossiter–McLaughlin technique[3]. CCF_{DI} are shifted into the star's rest frame, then co-added and continuum-normalized outside the transit to build a master-out template CCF_{DI}^{OT} for each visit. In-transit CCF_{DI} are continuum-scaled according to the depth of the light curve derived from high-precision photometry[2], before subtracting them from the CCF_{DI}^{OT} to retrieve the CCF_{PO} (Methods). The local stellar line profile from the spatially resolved region of the photosphere occulted by GJ 436b along the transit chord is clearly detected in the CCF_{PO} (Fig. 1, Extended Data Fig. 4). We applied a double-Gaussian model to CCF_{PO} to derive their properties, linking the profiles of the Gaussian components in the same way as for the CCF_{DI} (Methods). We retained in our analysis all CCF_{PO} where the stellar line contrast is detected at more than 5σ. Excluded CCF_{PO}

(Extended Data Table 1) are faint, associated with darker regions of the stellar limb that are only partially occulted by GJ 436b. The radial velocity centroids of the CCF_{PO} directly trace the velocity field of the stellar photosphere (Extended Data Fig. 5). The three series of surface radial velocities are consistent over most of the transit (even though they were obtained with two instruments over a 9-year interval) and are predominantly positive (showing that GJ 436b occults redshifted regions of the stellar disk rotating away from us and excluding an aligned system). We simultaneously fitted the three radial velocity series with the reloaded Rossiter–McLaughlin model[3], using a Metropolis–Hasting Markov chain Monte Carlo algorithm[9] and assuming a solid-body rotation for the star (Methods). The model then depends on the sky-projected obliquity λ_b (the angle between the projected angular momentum vectors of the star and of the orbit of GJ 436b) and projected rotational velocity $V_{eq}\sin i_\star$ (where $i_\star$ is the inclination of the star spin axis relative to our line of sight). The best fit (Fig. 1, Extended Data Fig. 5) matches visits 1 and 2 well, and it yields a relatively large χ^2 of 42 for 19 degrees of freedom because three measurements in visit 3 deviate by 2.5σ–3σ. Excluding them yields the reduced chi-squared value $\chi^2_{red} = 1.1$ and does not change the derived properties beyond their 1σ uncertainties (Methods), so they were retained in the final fit. Posterior probability distributions of the Markov chain Monte Carlo parameters (Extended Data Fig. 6) are well defined and yield $V_{eq}\sin i_\star = 330^{+90}_{-70}$ m s^{-1} (>190 m s^{-1} with 99% confidence) and $\lambda_b = 72°^{+33°}_{-24°}$ ($>30°$ with 99% confidence). These properties do not change beyond their 1σ uncertainties when system parameters are varied within their error bars. The Bayesian information criterion for the best-fit solid-body model (48) is much lower than for a null velocity model (74) and an aligned model (88). The M dwarf GJ 436 is thus the coolest star across which the Rossiter–McLaughlin effect has been detected, with a highly misaligned orbit for its Neptune-mass companion (Fig. 2).

The slow rotation of GJ 436 is consistent with published upper limits[2,10]. It yields a small amplitude of 1.3 m s^{-1} for the classical radial velocity anomaly—much smaller than the stellar surface velocities measured with the reloaded Rossiter–McLaughlin technique—which could not be detected in earlier analyses[2] of visit 1. The widths of the CCF_{PO} show little dispersion around the width of the CCF_{DI}^{OT}, consistent with the non-detection of rotational broadening (Extended Data Fig. 5). The three visits show similar properties for the CCF_{PO} along the transit chord and for the CCF_{DI}^{OT}, consistent with the low activity[11,12] of GJ 436 and stable emission at ultraviolet[5], optical[8] and infrared[2,13] wavelengths. Nonetheless, small periodic variations in its visible flux[8] and the periodic modulation we measure in the HARPS[2] and Keck[14] chromospheric indices suggest the presence of active regions on the stellar surface.

This can be reconciled with the stability of GJ 436 emission if its spin axis is tilted[8] so that active regions could be frequently occulted by the planet while yielding a small rotational flux modulation. Using 14 years

[1]Observatoire de l'Université de Genève, 51 chemin des Maillettes, 1290 Versoix, Switzerland. [2]Université Grenoble Alpes, CNRS, IPAG, F-38000 Grenoble, France. [3]Center of Excellence in Information Systems, Tennessee State University, Nashville, Tennessee 37209, USA. [4]University of Bern, Center for Space and Habitability, Sidlerstrasse 5, CH-3012 Bern, Switzerland.

Astronomy
&
Astrophysics

Hot Exoplanet Atmospheres Resolved
with Transit Spectroscopy (HEARTS)

I. Detection of hot neutral sodium at high altitudes on WASP-49b[*]

A. Wyttenbach[1], C. Lovis[1], D. Ehrenreich[1], V. Bourrier[1], L. Pino[1,2], R. Allart[1], N. Astudillo-Defru[1], H. M. Cegla[1,3],
K. Heng[4], B. Lavie[1,4], C. Melo[5], F. Murgas[6,7], A. Santerne[8], D. Ségransan[1], S. Udry[1], and F. Pepe[1]

[1] Geneva Observatory, University of Geneva, ch. des Maillettes 51, 1290 Versoix, Switzerland
   e-mail: aurelien.wyttenbach@unige.ch
[2] Dipartimento di Fisica e Astronomia "Galileo Galilei", Università di Padova, Vicolo dell'Osservatorio 3, 35122 Padova, Italy
[3] Astrophysics Research Centre, School of Mathematics & Physics, Queen's University Belfast, University Road, Belfast BT7 1NN,
   UK
[4] University of Bern, Center for Space and Habitability, Sidlerstrasse 5, 3012 Bern, Switzerland
[5] European Southern Observatory, Alonso de Cordova 3107, Vitacura Casilla 19001, Santiago 19, Chile
[6] Univ. Grenoble Alpes, IPAG, 38000 Grenoble, France
[7] CNRS, IPAG, 38000 Grenoble, France
[8] Aix Marseille Univ, CNRS, LAM, Laboratoire d'Astrophysique de Marseille, 13388 Marseille, France

ABSTRACT

High-resolution optical spectroscopy during the transit of HD 189733b, a prototypical hot Jupiter, allowed the resolution of the Na I D sodium lines in the planet, giving access to the extreme conditions of the planet upper atmosphere. We have undertaken HEARTS, a spectroscopic survey of exoplanet upper atmospheres, to perform a comparative study of hot gas giants and determine how stellar irradiation affect them. Here, we report on the first HEARTS observations of the hot Saturn-mass planet WASP-49b. We observed the planet with the HARPS high-resolution spectrograph at ESO 3.6 m telescope. We collected 126 spectra of WASP-49, covering three transits of WASP-49b. We analyzed and modeled the planet transit spectrum, while paying particular attention to the treatment of potentially spurious signals of stellar origin. We spectrally resolve the Na I D lines in the planet atmosphere and show that these signatures are unlikely to arise from stellar contamination. The large contrasts of $2.0 \pm 0.5\%$ (D_2) and $1.8 \pm 0.7\%$ (D_1) require the presence of hot neutral sodium (2950^{+400}_{-500} K) at high altitudes ($\sim$1.5 planet radius or $\sim$45 000 km). From estimating the cloudiness index of WASP-49b, we determine its atmosphere to be cloud free at the altitudes probed by the sodium lines. WASP-49b is close to the border of the evaporation desert and exhibits an enhanced thermospheric signature with respect to a farther-away planet such as HD 189733b.

Key words. planets and satellites: atmospheres – planets and satellites: individual: WASP-49b – techniques: spectroscopic – instrumentation: spectrographs – methods: observational

1. Introduction

There has been enormous progress in the characterization of exoplanets and their atmospheres. The most amenable systems for atmospheric studies are the transiting systems. During the transit, a minute fraction of the starlight is filtered by the planet atmospheric limb. At wavelengths where atmospheric components absorb this light, the partial occultation of the star by the planet (or transit depth) appears larger than in white light. Observing a transit with a spectrograph yields the transmission spectrum of the planet atmosphere (Seager & Sasselov 2000; Brown 2001). From this, one can constrain the temperature profile, composition, winds, and diffusion processes (Rayleigh scattering, clouds) in the atmosphere (e.g., Madhusudhan et al. 2014).

The signature of the resonant neutral sodium doublet (Na I D) has proved to be a powerful probe of exoplanet atmospheres, especially with the medium-resolution ($\lambda/\Delta\lambda \sim 5500$) STIS spectrograph on board the *Hubble* Space

Telescope (Charbonneau et al. 2002; Sing et al. 2008a,b, 2016; Vidal-Madjar et al. 2011a,b; Huitson et al. 2012; Nikolov et al. 2014; Fischer et al. 2016). Owing to its high cross section, the resonant Na I doublet at 589 nm (Fraunhofer's D line) is extremely sensitive to small amounts of sodium, up to high altitudes in the planet atmosphere. The Na I line cores, in particular, can trace the temperature profile up to the planet thermosphere, which has been measured effectively with the HARPS spectrograph on HD 189733b (Wyttenbach et al. 2015; Heng et al. 2015). Sodium is arguably the easiest species to detect in a hot exoplanet atmosphere, and ground-based detections have been achieved for several gas giants (Redfield et al. 2008; Snellen et al. 2008; Wood et al. 2011; Jensen et al. 2011; Zhou & Bayliss 2012; Murgas et al. 2014; Burton et al. 2015; Khalafinejad et al. 2017; Nikolov et al. 2016).

Ground-based detections of atomic sodium in the atmospheres of HD 189733b (Redfield et al. 2008; Jensen et al. 2011) and HD 209458b (Snellen et al. 2008) were enabled by the use of high-resolution spectrographs ($\lambda/\Delta\lambda \sim 50\,000$). Using HARPS ($\lambda/\Delta\lambda = 115\,000$) at the ESO 3.6 m telescope in La Silla (Chile),

---

Astronomy & Astrophysics

High-energy environment of super-Earth 55 Cancri e

I. Far-UV chromospheric variability as a possible tracer of planet-induced coronal rain[⋆]

V. Bourrier[1], D. Ehrenreich[1], A. Lecavelier des Etangs[2], T. Louden[3],
P. J. Wheatley[3], A. Wyttenbach[1], A. Vidal-Madjar[2], B. Lavie[1], F. Pepe[1], and S. Udry[1]

[1] Observatoire de l'Université de Genève, 51 chemin des Maillettes, 1290 Sauverny, Switzerland
e-mail: vincent.bourrier@unige.ch
[2] Institut d'astrophysique de Paris, UMR7095 CNRS, Université Pierre & Marie Curie, 98bis boulevard Arago, 75014 Paris, France
[3] Department of Physics, University of Warwick, Coventry CV4 7AL, UK

ABSTRACT

The high-energy X-ray to ultraviolet (XUV) irradiation of close-in planets by their host star influences their evolution and might be responsible for the existence of a population of ultra-short period planets eroded to their bare core. In orbit around a bright, nearby G-type star, the super-Earth 55 Cnc e offers the possibility to address these issues through transit observations at UV wavelengths. We used the *Hubble* Space Telescope to observe the transit in the far-ultraviolet (FUV) over three epochs in April 2016, January 2017, and February 2017. Together, these observations cover nearly half of the orbital trajectory in between the two quadratures, and reveal significant short- and long-term variability in 55 Cnc chromospheric emission lines. In the last two epochs, we detected a larger flux in the C III, Si III, and Si IV lines after the planet passed the approaching quadrature, followed by a flux decrease in the Si IV doublet. In the second epoch these variations are contemporaneous with flux decreases in the Si II and C II doublets. All epochs show flux decreases in the N V doublet as well, albeit at different orbital phases. These flux decreases are consistent with absorption from optically thin clouds of gas, are mostly localized at low and redshifted radial velocities in the star rest frame, and occur preferentially before and during the planet transit. These three points make it unlikely that the variations are purely stellar in origin, yet we show that the occulting material is also unlikely to originate from the planet. We thus tentatively propose that the motion of 55 Cnc e at the fringes of the stellar corona leads to the formation of a cool coronal rain. The inhomogeneity and temporal evolution of the stellar corona would be responsible for the differences between the three visits. Additional variations are detected in the C II doublet in the first epoch and in the O I triplet in all epochs with a different behavior that points toward intrinsic stellar variability. Further observations at FUV wavelengths are required to disentangle definitively between star-planet interactions in the 55 Cnc system and the activity of the star.

Key words. methods: data analysis – techniques: spectroscopic – planets and satellites: individual: 55 Cnc e – stars: chromospheres – ultraviolet: stars

1. Introduction

The population of close-in planets is shaped by interactions with their host star. In particular, the deposition of stellar X-ray and extreme ultraviolet radiation (XUV) into an exoplanet upper atmosphere can lead to its hydrodynamic expansion and the escape of large amounts of gas from the gravitational well of the planet (e.g., Vidal-Madjar et al. 2003; Lecavelier des Etangs et al. 2004; Johnstone et al. 2015). This evaporation can sustain extended exospheres that have been detected around Jupiter-mass planets (Vidal-Madjar et al. 2003, 2004; Lecavelier des Etangs et al. 2010, 2012; Bourrier et al. 2013; Ehrenreich et al. 2012; Fossati et al. 2010; Haswell et al. 2012) and a Neptune- mass planet (Kulow et al. 2014; Ehrenreich et al. 2015; Lavie et al. 2017). While Jupiter-mass planets are too massive to be significantly affected by evaporation, losing a few percent of their mass over their lifetime (e.g., Lecavelier des Etangs 2007; Hubbard et al. 2007; Ehrenreich & Désert 2011), lower mass planets could be stripped of most of their atmosphere (e.g.,

Lecavelier des Etangs 2007; Owen & Jackson 2012) and evolve into chthonian planets (Lecavelier des Etangs et al. 2004). There is a desert in the population of close-in planets that was first identified as a lack of sub-Jupiter planets (e.g., Lecavelier des Etangs 2007; Davis & Wheatley 2009; Szabó & Kiss 2011; Beaugé & Nesvorný 2013) and later shown to extend to strongly irradiated super-Earths (Lundkvist et al. 2016). Theoretical studies show that this desert is explained well by planets with gaseous envelopes large enough to capture much of the stellar energy and evaporate, but too light to retain their escaping atmospheres (e.g., Lopez et al. 2012; Lopez & Fortney 2013; Owen & Wu 2013; Kurokawa & Nakamoto 2014; Jin et al. 2014). Recently, Fulton et al. (2017) have identified a deficit of small close-in planets with radii of about $1.7\,R_\oplus$ separating two peaks in the radius distribution at about 1.3 and $2.5\,R_\oplus$. There seems to be a dichotomy between large super-Earths massive enough to retain H/He envelopes with mass fractions of a few percent, and small rocky super-Earths with atmospheres that contribute negligibly to their size (Weiss & Marcy 2014; Rogers 2015). The absence of planets in between (the so-called evaporation valley) would arise because the planetary radius barely changes as the envelope mass decreases, resulting in more tenuous atmospheres

CONCLUSION AND PERSPECTIVES

"Moi-même, qui suis Limousin. [...] Nous avons
bien sûr notre humour limousin qui n'appartient
qu'à nous. [...] Il faut avoir souffert à Limoges pour
comprendre.

P.Desproges, 1979

We do not inherit the Earth from our ancestors; we
borrow it from our children.

Indian proverb

Atmospheric studies of exoplanets and brown-dwarfs is a very rich and growing field in
astrophysics. The field inherited massively from the extensive knowledge acquired by centuries
of research on the atmospheric studies of Earth and the other planets of the Solar System. It
has been both an advantage and a burden. An advantage because researchers in exoplanetology
did not have to reinvent the physic of atmosphere and because the very high quality of the Solar
System data allows strict checks on generic atmospheric models built for extra-solar objects.
A burden because the range of physical regimes encountered in exoplanet and brown-dwarf
atmospheres is much broader than the Solar System examples and preconceived assumptions
based on this knowledge bias the research on those objects. A specialisation process between
the two distinct communities of brown-dwarf and exoplanet but also within each of those
community is taking place. The impossibility to master every single aspect of the atmospheric

studies in terms of the diversity of objects and of observational techniques tends to create very specialised researchers. Mingling of specialists from diverse scientific horizons and cross-field researches trigger innovation and provide new ways of tackling problems. Thesis positions such as mine supervised by researchers with different profiles (a theoretician - Kevin Heng and an observer - David Ehrenreich) and their respective teams, different universities (Bern and Geneva), different objects (exoplanets and brown-dwarfs), different observational techniques (direct imaging and transit) and so on, are therefore important to form future researchers able to connect research studies from different sub-communities.

The main framework of my thesis is the link between the atmospheric properties of an exoplanet or a brown-dwarf, its formation mechanism and its evolution under atmospheric escape. This framework has been divided in this manuscript into two branches: the lower atmosphere observed in the infrared part of the spectrum and the upper atmosphere observed in the far ultraviolet.

The proxy variable used to link the formation mechanism and the lower atmospheric properties is the carbon to oxygen ratio of the companion compared to the one of its host star. The first order answer is derived by considering the gravitational instability scenario as a quick, one step process that forms objects with similar composition to the host star; and the core accretion scenario as a longer multi-steps process that forms objects with a broad range of possible composition. More complex solutions, like contamination by icy solids, can then be derived by considering the snow lines of the different carbon and oxygen bearers within the disk. I have developed a code named HELIOS_R that couples an atmospheric emission model with a nested sampling algorithm. This Bayesian tool focuses on the computation of the Bayesian evidence, which allows performing model selection. The posterior distribution of the models are given as a by-product of the algorithm, which allows the computation of the carbon and oxygen abundances once the best model has been selected. In the scope of my thesis, atmospheric retrieval of direct imaged companions have been performed. On one hand, the massive brown-dwarf HD 4747 B has a carbon to oxygen ratio compatible with its host star, which suggests formation by gravitational instability. On the other hand, the companions in the HR 8799 system present a broad range of carbon and oxygen ratios that suggest formation by core accretion. Retrieval techniques are data-driven tool. Retrieval analysis of the direct imaged companions GJ 504 b and HD 206893 b did not extract useful information because of the too sparse data or too high uncertainties.

Exoplanets and brown-dwarfs evolve during their lifetime and their atmospheric properties may change over time. Observing the atmospheric changes undergone by one specific companion during its evolution is not feasible, the typical lifetime of a brown-dwarf or a planet is too long. Nevertheless, the numerous objects discovered with the multiple observational tech-

niques provide snapshots of exoplanets and brown-dwarfs at different stages of their evolution. Deriving carbon to oxygen ratios for other populations of objects will help to understand the atmospheric changes undergo by a companion during its evolution. For example, close-in giant planets such as hot Jupiters are older than direct imaged planets and provide a snapshot of giant planets at another stage of their evolution. However, data available today are too sparse and the uncertainties on the carbon to oxygen ratios derived from them too high. A retrieval analysis of the hot Jupiter WASP 12 b with `HELIOS_R` highlighted that the retrieved results with typical data available today are driven by the choice of prior.

It is necessary, beyond retrieving carbon and oxygen ratios of companions at different stage of their evolution, to understand the mechanisms that influence changes in their atmosphere. Atmospheric escape is one of those mechanisms. It is thought to shape the so-called evaporation desert and valley. Dearth zones of objects between the hot Jupiter and the super-Earth populations and the sub-Neptune and the super-Earth populations. The upper layers of a close-in companion' atmosphere are exposed to the stellar XUV radiation that plays an important role in driving atmospheric escape. A handful of objects have now been observed to endure atmospheric escape. An important discovery of a planet enduring atmospheric escape is the warm Neptune GJ 436 b that lies in the inner edge of the evaporation desert and orbits a M-dwarf. It provides an example of a new regime of observation for atmospheric escape: close-in planets orbiting low-mass stars. The escaping gas is not swept away like for more massive stars resulting in the formation of extensive cloud surrounding the planet. The exospheric transit hides more than half of the star light at Lyman-α wavelengths. New data covering the transit of the tail and the out-of-transit baseline have been studied in this thesis. Hydrogen atoms in the tail of the exospheric cloud keep occulting the star up to 25 hours after the transit of the planet. Those new observations confirm that the exosphere of GJ 436 b is shaped by both radiative braking and charge exchanges with the stellar wind. The detection of the silicon ion Si III in the exosphere of the planet confirms the hydrodynamical escape of the planet atmosphere. The recent discovery of the exospheric cloud around GJ 3470 b that also orbits a M-dwarf and stands in the inner part of the evaporation desert, tends to confirm the importance of those kind of system to study atmospheric escape. Lying below the evaporation valley, the warm super-Earth HD 219134 b orbits a K-dwarf very close to us. It allowed, for the first time, observations with *HST* at high resolution of two transits of the planet in the FUV, which complete another transit at low resolution. Variations in the redshifted part of the Lyα line are seen in the three transits, which may indicate that some hydrogen atoms are escaping the planet. However, stellar activity can not be entirely ruled out and a better comprehension of the stellar environment is needed. Analysis of the stellar properties have been performed, which includes reconstruction of the intrinsic Lyα line and searching for correlations with the other spectral lines. The next step

regarding those data is to gather more insight on the stellar and ISM properties. Comparison with work performed by other teams on the same system indicate discrepancies with the results obtained in the scope of this thesis. Especially on the presence or not of heliospheric and astrospheric absorptions.

The night is still young. Possibilities on atmospheric studies of brown-dwarfs and exoplanets are expected to explode. The next generation of instruments such as JWST, LUVOIR or the ELT will provide better data. The next generation of computing facilities (CPU, GPU, biocomputers, quantum computer etc.) coupled with the rise of machine learning will provide new ways to extract information for those higher quality data. I provide below some general or specific suggestions of projects that I would love to explore myself or see explored by others in a near or far future.

- finalising the analysis of HD 219134 b and its host star. It seems unlikely that we obtain more time on *HST* and we will probably need to wait for the next generation of instrument to confirm the detection of hydrogen in its exosphere.
- Study the impact of the model resolution for atmospheric retrieval.
- Study the balance between wavelength coverage and data resolution to extract the properties of a companion's atmosphere in direct imaging.
- Study the difference when a retrieval is performed in transmission (probing the limb of the planet) and in emission (secondary eclipse).
- Obtaining better constraints on the mass of companions of direct imaged objects. We need additional observations (radial velocity, astrometry) to pinned down the uncertainties on the mass as evolutionary models are not sufficiently robust to be the only source of information.
- Investigate more deeply the star-planet interactions, especially magnetic interactions. Can it explain red-shifted signatures found for GJ 436 b and HD 219134 b.
- Observations of atmospheric escape with Helium. It will give us access to more objects because it is less impacted by the ISM absorption, which forbid observations of system that are to far.
- preparation for the next generation of instruments, especially METIS and HARMONI on the ELT.
- Evaluate the carbon to oxygen ratios for a large sample of bounded and in the field brown-dwarfs.
- Investigate astrospheric and heliospheric absorptions. From the work performed on HD 219134, it is not evident that such detections are possible.
- Observations of atmospheric escape of super-Earths in the desert. TESS will provide numerous target opportunities.

- Investigate if brown-dwarfs endure atmospheric escape. Close-in transiting brown-dwarfs are older and hence have a higher surface gravity. Nevertheless, it may be possible that the closer ones to their host star evaporate part of their atmosphere.
- Investigate new ways of exploring data such as AI algorithms.

The future seems bright. Although, I ask myself this question everyday: should all those beautiful minds in astrophysics be better use to find solutions for the climate change and its consequences for nature and wo-man-kind, my daughters? *Victoriae mundis et mundis lacrima. Bon, ça ne veut absolument rien dire, mais je trouve que c'est assez dans le ton pour finir ma thèse*[a].

---

[a]d'après une citation du roi Loth d'Orcanie

LIST OF FIGURES

BIBLIOGRAPHY

A. Lecavelier des Etangs, Vidal-Madjar, A., McConnell, J. C., & Hébrard, G. 2004, Astronomy & Astrophysics, 418, L1

Allison, R. & Dunkley, J. 2014, Monthly Notices of the Royal Astronomical Society, 437, 3918

Almasi, G. S. & Gottlieb, A. 1989, Highly parallel computing, The Benjamin/Cummings series in computer science and engineering (Redwood City, Calif: Benjamin/Cummings)

Ambikasaran, S., Foreman-Mackey, D., Greengard, L., Hogg, D. W., & O'Neil, M. 2014, arXiv:1403.6015 [astro-ph, stat], arXiv: 1403.6015

Asplund, M., Grevesse, N., Sauval, A. J., & Scott, P. 2009, Annual Review of Astronomy and Astrophysics, 47, 481

Baraffe, I., Chabrier, G., Barman, T. S., et al. 2005, Astronomy & Astrophysics, 436, L47

Barstow, J. K., Aigrain, S., Irwin, P. G. J., et al. 2013, Monthly Notices of the Royal Astronomical Society, 430, 1188

Batygin, K., Bodenheimer, P. H., & Laughlin, G. P. 2016, The Astrophysical Journal, 829, 114

Beaugé, C. & Nesvorný, D. 2013, The Astrophysical Journal, 763, 12

Ben-Jaffel, L. & Ballester, G. E. 2013, Astronomy & Astrophysics, 553, A52

Benneke, B. 2015, arXiv:1504.07655 [astro-ph], arXiv: 1504.07655

Benneke, B. & Seager, S. 2012, The Astrophysical Journal, 753, 100

Benneke, B. & Seager, S. 2013, The Astrophysical Journal, 778, 153

Berta, Z. K., Charbonneau, D., Désert, J.-M., et al. 2012, The Astrophysical Journal, 747, 35

Bolcar, M. R., Feinberg, L., France, K., et al. 2016, Edinburgh, United Kingdom, 99040J

Bonnefoy, M. & Chauvin, G. 2013, memsai, 84, 992

Bonnefoy, M., Perraut, K., & Lagrange, A. 2018, arXiv:1807.00657 [astro-ph, stat], arXiv: 1807.00657

Boss, A. P., Basri, G., Kumar, S. S., et al. 2003, in IAU Symposium, Vol. 211, Brown Dwarfs, ed. E. Martín, 529

Bourrier, V., Ehrenreich, D., Allart, R., et al. 2017, Astronomy & Astrophysics, 602, A106

Bourrier, V., Ehrenreich, D., King, G., et al. 2016a, Astronomy and Astrophysics, 597, A26

Bourrier, V., Ehrenreich, D., King, G., et al. 2017, , 597, A26

Bourrier, V., Ehrenreich, D., & Lecavelier des Etangs, A. 2015, Astronomy and Astrophysics, 582, A65

Bourrier, V., Ehrenreich, D., Wheatley, P. J., et al. 2017a, Astronomy & Astrophysics, 599, L3

Bourrier, V. & Lecavelier des Etangs, A. 2013, Astronomy and Astrophysics, 557, A124

Bourrier, V. & Lecavelier des Etangs, A. 2018, in Handbook of Exoplanets, ed. H. J. Deeg & J. A. Belmonte (Cham: Springer International Publishing), 1–18

Bourrier, V., Lecavelier des Etangs, A., Dupuy, H., et al. 2013, , 551, A63

Bourrier, V., Lecavelier des Etangs, A., Ehrenreich, D., Tanaka, Y. A., & Vidotto, A. A. 2016b, Astronomy and Astrophysics, 591, A121

Bourrier, V., Lovis, C., Beust, H., et al. 2017b, Nature, 553, 477

Bourrier, V., Wit, J. d., Bolmont, E., et al. 2017c, The Astronomical Journal, 154, 121

Brewer, J. M., Fischer, D. A., & Madhusudhan, N. 2017, The Astronomical Journal, 153, 83

Browning, M. K., Basri, G., Marcy, G. W., West, A. A., & Zhang, J. 2010, The Astronomical Journal, 139, 504

Buchner, J., Georgakakis, A., Nandra, K., et al. 2014, Astronomy & Astrophysics, 564, A125

Burrows, A. & Liebert, J. 1993, Reviews of Modern Physics, 65, 301

Butler, R. P., Vogt, S. S., Marcy, G. W., et al. 2004, The Astrophysical Journal, 617, 580

Cáceres, C., Ivanov, V. D., Minniti, D., et al. 2009, Astronomy & Astrophysics, 507, 481

Cassan, A., Kubas, D., Beaulieu, J.-P., et al. 2012, Nature, 481, 167

Chabrier, G. & Baraffe, I. 1997, aap, 327, 1039

Chabrier, G., Baraffe, I., Selsis, F., et al. 2007, Protostars and Planets V, 623

Chamberlain, J. W. 1963, Planetary and Space Science, 11, 901

Chamberlain, J. W. & Hunten, D. M. 1987, Theory of planetary atmospheres. An introduction to their physics andchemistry.

Charbonneau, D., Brown, T. M., Latham, D. W., & Mayor, M. 2000, The Astrophysical Journal, 529, L45

Chauvin, G., Lagrange, A.-M., Dumas, C., et al. 2004, Astronomy & Astrophysics, 425, L29

Chiappini, C., Romano, D., & Matteucci, F. 2003, mnras, 339, 63

Clegg, R. E. S., Tomkin, J., & Lambert, D. L. 1981, The Astrophysical Journal, 250, 262

Collier, M. R., Moore, T. E., Ogilvie, K. W., et al. 2001, Journal of Geophysical Research: Space Physics, 106, 24893

Collins, K. A., Kielkopf, J. F., & Stassun, K. G. 2017, The Astronomical Journal, 153, 78

DAngelo, G. & Lissauer, J. 2018, arXiv:1806.05649, arXiv: 1807.00657

Delorme, P., Schmidt, T., Bonnefoy, M., et al. 2017, Astronomy & Astrophysics, 608, A79

Deming, D., Wilkins, A., McCullough, P., et al. 2013, The Astrophysical Journal, 774, 95

Deming, L. D. & Seager, S. 2017, Journal of Geophysical Research: Planets, 122, 53

Dijkstra, M. 2014, Publications of the Astronomical Society of Australia, 31

Dijkstra, M. 2017, arXiv: 1704.03416, arXiv: 1704.03416

Dorn, C. & Heng, K. 2018, The Astrophysical Journal, 853, 64

Dorn, C., Hinkel, N. R., & Venturini, J. 2017, Astronomy & Astrophysics, 597, A38

Durisen, R. H. 2011, Disk Hydrodynamics, ed. P. J. V. Garcia, 149–236

Dyson, F. 2004, Nature, 427, 297

Ehrenreich, D., Bonfils, X., Lovis, C., et al. 2014, Astronomy and Astrophysics, 570, A89

Ehrenreich, D., Bourrier, V., Bonfils, X., et al. 2012, Astronomy and Astrophysics, 547, A18

Ehrenreich, D., Bourrier, V., Wheatley, P. J., et al. 2015, Nature, 522, 459

Ehrenreich, D. & Désert, J.-M. 2011, Astronomy and Astrophysics, 529, A136

Ehrenreich, D., Lecavelier des Etangs, A., & Delfosse, X. 2011, Astronomy and Astrophysics, 529, A80

Ehrenreich, D., Lecavelier des Etangs, A., Hébrard, G., et al. 2008, Astronomy & Astrophysics, 483, 933

Ehrenreich, D., Tinetti, G., Lecavelier des Etangs, A., Vidal-Madjar, A., & Selsis, F. 2006, Astronomy & Astrophysics, 448, 379

Esteban, C., García-Rojas, J., Peimbert, M., et al. 2005, The Astrophysical Journal, 618, L95

Esteban, C., Peimbert, M., García-Rojas, J., et al. 2004, Monthly Notices of the Royal Astronomical Society, 355, 229

Etangs, A. L. d., Vidal-Madjar, A., & Désert, J.-M. 2008, Nature, 456, E1

Feng, Y., Fortney, J. J., & Line, M. R. 2016, in AAS/Division for Planetary Sciences Meeting Abstracts, Vol. 48, AAS/Division for Planetary Sciences Meeting Abstracts #48, 212.03

Feroz, F. & Hobson, M. P. 2008, Monthly Notices of the Royal Astronomical Society, 384, 449

Feroz, F., Hobson, M. P., & Bridges, M. 2009, Monthly Notices of the Royal Astronomical Society, 398, 1601

Feroz, F., Hobson, M. P., Cameron, E., & Pettitt, A. N. 2013, arXiv:1306.2144 [astro-ph, physics:physics, stat], arXiv: 1306.2144

Fleming, B. T., France, K. C., Nell, N., et al. 2017, in UV, X-Ray, and Gamma-Ray Space Instrumentation for Astronomy XX, ed. O. H. Siegmund (San Diego, United States: SPIE), 46

Folsom, C. P., Fossati, L., Wood, B. E., et al. 2018, Monthly Notices of the Royal Astronomical Society

Fontenla, J. M., Linsky, J. L., Witbrod, J., et al. 2016, The Astrophysical Journal, 830, 154

France, K. 2016, Edinburgh, United Kingdom, 99040M

France, K., Froning, C. S., Linsky, J. L., et al. 2013, The Astrophysical Journal, 763, 149

France, K., Linsky, J. L., Tian, F., Froning, C. S., & Roberge, A. 2012, The Astrophysical

Journal, 750, L32

France, K., Loyd, R. O. P., Youngblood, A., et al. 2016, The Astrophysical Journal, 820, 89

Fulton, B. J. & Petigura, E. A. 2018, arXiv:1805.01453 [astro-ph], arXiv: 1805.01453

Fulton, B. J., Petigura, E. A., Howard, A. W., et al. 2017, The Astronomical Journal, 154, 109

Futaana, Y., Barabash, S., Grigoriev, A., et al. 2006, Icarus, 182, 413

Gaia Collaboration. 2018, VizieR Online Data Catalog, 1345

Gaia Collaboration, Brown, A. G. A., Vallenari, A., et al. 2016a, Astronomy & Astrophysics, 595, A2

Gaia Collaboration, Prusti, T., de Bruijne, J. H. J., et al. 2016b, Astronomy & Astrophysics, 595, A1

Gålfalk, M. 2007, Stellar and emission line spectra (Stockolm observatory)

Galli, A., Wurz, P., Bochsler, P., et al. 2008, Planetary and Space Science, 56, 807

Gandhi, S. & Madhusudhan, N. 2018, Monthly Notices of the Royal Astronomical Society, 474, 271

GarciaâRojas, J. & Esteban, C. 2007, The Astrophysical Journal, 670, 457

Gaudi, B. S. 2012, Annual Review of Astronomy and Astrophysics, 50, 411

Gaudi, B. S., Stassun, K. G., Collins, K. A., et al. 2017, Nature

Gautschi, W. 1970, SIAM Journal on Numerical Analysis, 7, 187

Gayley, K. G., Zank, G. P., Pauls, H. L., Frisch, P. C., & Welty, D. E. 1997, The Astrophysical Journal, 487, 259

Gibson, N. P., Aigrain, S., Roberts, S., et al. 2012, Monthly Notices of the Royal Astronomical Society, 419, 2683

Gillon, M., Demory, B.-O., Van Grootel, V., et al. 2017, Nature Astronomy, 1, 0056

Gillon, M., Pont, F., Demory, B.-O., et al. 2007, Astronomy and Astrophysics, 472, L13

Gilman, R. C. 1969, The Astrophysical Journal, 155, L185

Gregory, P. 2010, Bayesian Logical Data Analysis for the Physical Sciences

Grevesse, N. & Sauval, A. 1998, ssr, 85, 161

Grimm, S. L. & Heng, K. 2015, The Astrophysical Journal, 808, 182

Guillot, T. 2010, Astronomy and Astrophysics, 520, A27

Guillot, T., Gautier, D., & Hubbard, W. B. 1997, Icarus, 130, 534

Hansen, B. M. S. & Murray, N. 2012, The Astrophysical Journal, 751, 158

Hansen, C. J., Schwartz, J. C., & Cowan, N. B. 2014, Monthly Notices of the Royal Astronomical Society, 444, 3632

Hawking, S. 2004, The illustrated on the shoulders of giants: the great works of physics and astronomy (Philadelphia, Pa.; London: Running), oCLC: 973668259

Hébrard, G., Étangs, A. L. d., Vidal-Madjar, A., Désert, J.-M., & Ferlet, R. 2003, arXiv:astro-

ph/0312384, arXiv: astro-ph/0312384

Heng, K., Lyons, J. R., & Tsai, S.-M. 2016, The Astrophysical Journal, 816, 96

Heng, K., Mendonça, J. M., & Lee, J.-M. 2014, The Astrophysical Journal Supplement Series, 215, 4

Heng, K. & Tsai, S.-M. 2016, The Astrophysical Journal, 829, 104

Holmström, M., Ekenbäck, A., Selsis, F., et al. 2008, Nature, 451, 970

Hu, R., Seager, S., & Bains, W. 2012, The Astrophysical Journal, 761, 166

Hu, R., Seager, S., & Yung, Y. L. 2015, The Astrophysical Journal, 807, 8

Hubbard, W., Hattori, M., Burrows, A., Hubeny, I., & Sudarsky, D. 2007, Icarus, 187, 358

Hunten, D. M. 1973, Journal of the Atmospheric Sciences, 30, 1481

Hunten, D. M. & Donahue, T. M. 1976, Annual Review of Earth and Planetary Sciences, 4, 265

Hunten, D. M., Donahue, T. M., Walker, J. C. G., & Kasting, J. F. 1989, Escape of atmospheres and loss of water, ed. S. K. Atreya, J. B. Pollack, & M. S. Matthews, 386–422

Ida, S., Guillot, T., & Morbidelli, A. 2016, Astronomy & Astrophysics, 591, A72

Irwin, P., Teanby, N., de Kok, R., et al. 2008, Journal of Quantitative Spectroscopy and Radiative Transfer, 109, 1136

Izmodenov, V. V., Lallement, R., & Malama, Y. G. 1998, arXiv:astro-ph/9812372, arXiv: astro-ph/9812372

J.H., J. 1916, The dynamical Theory of Gases (Cambridge University Press)

Jin, S., Mordasini, C., Parmentier, V., et al. 2014, The Astrophysical Journal, 795, 65

Johnson, M. C., Endl, M., Cochran, W. D., et al. 2016, The Astrophysical Journal, 821, 74

Jura, M. 2004, The Astrophysical Journal, 605, L65

Kaltenegger, L. & Traub, W. A. 2009, The Astrophysical Journal, 698, 519

Kasting, J. F., Holland, H. D., & Pinto, J. P. 1985, Journal of Geophysical Research: Atmospheres, 90, 10497

Kasting, J. F. & Pollack, J. B. 1983, Icarus, 53, 479

Knutson, H. A., Benneke, B., Deming, D., & Homeier, D. 2014, Nature, 505, 66

Knutson, H. A., Charbonneau, D., Allen, L. E., Burrows, A., & Megeath, S. T. 2008, The Astrophysical Journal, 673, 526

Knutson, H. A., Madhusudhan, N., Cowan, N. B., et al. 2011, The Astrophysical Journal, 735, 27

Kreidberg, L. & Oklopčić, A. 2018, arXiv:1805.10671 [astro-ph], arXiv: 1805.10671

Kubyshkina, D., Fossati, L., Erkaev, N. V., et al. 2018, arXiv:1809.06645 [astro-ph], arXiv: 1809.06645

Kuiper, G. P. 1951, Proceedings of the National Academy of Sciences, 37, 1

Kulow, J. R., France, K., Linsky, J., & Loyd, R. O. P. 2014, The Astrophysical Journal, 786, 132

Kumar, S. S. 1963, The Astrophysical Journal, 137, 1126

Kumar, S. S. 1964, zap, 58, 248

Kurokawa, H. & Nakamoto, T. 2014, The Astrophysical Journal, 783, 54

Laird, J. B. 1985, The Astrophysical Journal, 289, 556

Lallement, R. & Bertin, P. 1992, , 266, 479

Lallement, R., Ferlet, R., Lagrange, A. M., Lemoine, M., & Vidal-Madjar, A. 1995, , 304, 461

Lallo, M. D. 2012, Optical Engineering, 51, 011011

Lambert, D. L. 1968, Monthly Notices of the Royal Astronomical Society, 138, 143

Lambrechts, M. & Johansen, A. 2012, Astronomy & Astrophysics, 544, A32

Lambrechts, M. & Johansen, A. 2014, Astronomy & Astrophysics, 572, A107

Lammer, H., Lichtenegger, H., Kolb, C., et al. 2003, Icarus, 165, 9

Lanotte, A. A., Gillon, M., Demory, B.-O., et al. 2014, Astronomy and Astrophysics, 572, A73

Lanz, T., Cunha, K., Holtzman, J., & Hubeny, I. 2008, The Astrophysical Journal, 678, 1342

Larimer, J. W. 1975, Geochimica et Cosmochimica Acta, 39, 389

Lavie, B., Ehrenreich, D., Bourrier, V., et al. 2017a, Astronomy & Astrophysics, 605, L7

Lavie, B., Mendonça, J. M., Mordasini, C., et al. 2017b, The Astronomical Journal, 154, 91

Lavie, Baptiste, e. a. 2018, The Astronomical Journal

Lavie, T., Fransisco, A., Fatu, A., & Villechaise, B. 2015, Tribology Transactions, 58, 490

Lecavelier des Etangs, A., Bourrier, V., Wheatley, P. J., et al. 2012, Astronomy and Astrophysics, 543, L4

Lecavelier Des Etangs, A., Deleuil, M., Vidal-Madjar, A., et al. 1994, in Circumstellar Dust Disks and Planet Formation, ed. R. Ferlet & A. Vidal-Madjar, 93

Lecavelier des Etangs, A., Ehrenreich, D., Vidal-Madjar, A., et al. 2010, Astronomy and Astrophysics, 514, A72

Lecavelier des Etangs, A. & Vidal-Madjar, A. 2009, Astronomy & Astrophysics, 497, 557

Lecavelier des Etangs, A., Vidal-Madjar, A., McConnell, J. C., & Hébrard, G. 2004, Astronomy and Astrophysics, 418, L1

Lee, J.-M., Heng, K., & Irwin, P. G. J. 2013, The Astrophysical Journal, 778, 97

Léger, A., Selsis, F., Sotin, C., et al. 2004, Icarus, 169, 499

Levison, H. 2000, Icarus, 143, 415

Levison, H. F., Kretke, K. A., & Duncan, M. J. 2015, Nature, 524, 322

Line, M. 2016, Testing Atmospheric Retrieval Modeling Assumptions for Transiting Planet Atmospheres: Preparatory science for the James Webb Space Telescope and beyond., NASA Proposal id.16-XPR16-5

Line, M. R., Knutson, H., Wolf, A. S., & Yung, Y. L. 2014, The Astrophysical Journal, 783, 70

Line, M. R., Stevenson, K. B., Bean, J., et al. 2016, The Astronomical Journal, 152, 203

Line, M. R., Zhang, X., Vasisht, G., et al. 2012, The Astrophysical Journal, 749, 93

Linsky, J. 2014, Challenges, 5, 351

Linsky, J. L. 2017, Annual Review of Astronomy and Astrophysics, 55, 159

Linsky, J. L., France, K., & Ayres, T. 2013, The Astrophysical Journal, 766, 69

Linsky, J. L., McClintock, W., Robertson, R. M., & Worden, S. P. 1979, The Astrophysical Journal Supplement Series, 41, 47

Linsky, J. L., Yang, H., France, K., et al. 2010, The Astrophysical Journal, 717, 1291

Lissauer, J. J., Hubickyj, O., D'Angelo, G., & Bodenheimer, P. 2009, Icarus, 199, 338

Livio, M. 2011, Nature, 479, 171

Liwshitz, M. 1967, Journal of Geophysical Research, 72, 285

Liwshitz, M. & Singer, S. 1966, Planetary and Space Science, 14, 541

Lopez, E. D. & Fortney, J. J. 2013, The Astrophysical Journal, 776, 2

Lopez, E. D., Fortney, J. J., & Miller, N. 2012, The Astrophysical Journal, 761, 59

Lothringer, J. D., Benneke, B., Crossfield, I. J. M., et al. 2018, The Astronomical Journal, 155, 66

Lovis, C. & Fischer, D. 2010, Radial Velocity Techniques for Exoplanets, ed. S. Seager, 27–53

Lucas, P. W. & Roche, P. F. 2000, Monthly Notices of the Royal Astronomical Society, 314, 858

Lundkvist, M. S., Kjeldsen, H., Albrecht, S., et al. 2016, Nature Communications, 7, 11201

Lyman, T. 1904a, The Astrophysical Journal, 19, 263

Lyman, T. 1904b, Nature, 69, 465

Lyman, T. 1906, The Astrophysical Journal, 23, 181

Maciejewski, G., Stangret, M., Ohlert, J., et al. 2018, Information Bulletin on Variable Stars

MacKay, D. J. C. 2003, Information theory, inference, and learning algorithms (Cambridge, UK ; New York: Cambridge University Press)

Mackay, D. J. C. 2003, Information Theory, Inference and Learning Algorithms (Cambridge University Press), 640

Madhusudhan, N. 2012, The Astrophysical Journal, 758, 36

Madhusudhan, N., Harrington, J., Stevenson, K. B., et al. 2011, Nature, 469, 64

Madhusudhan, N. & Seager, S. 2009, The Astrophysical Journal, 707, 24

Malik, M., Grosheintz, L., Mendonça, J. M., et al. 2017, The Astronomical Journal, 153, 56

Maness, H. L., Marcy, G. W., Ford, E. B., et al. 2007, Publications of the Astronomical Society of the Pacific, 119, 90

Manso Sainz, R. & González, M. J. M. 2012, The Astrophysical Journal, 760, 7

Marboeuf, U., Mousis, O., Ehrenreich, D., et al. 2008, The Astrophysical Journal, 681, 1624

Marois, C., Zuckerman, B., Konopacky, Q. M., Macintosh, B., & Barman, T. 2010, Nature, 468, 1080

Mayor, M., Marmier, M., Lovis, C., et al. 2011, ArXiv eprints [[arXiv]1109.2497]

Mayor, M. & Queloz, D. 1995, Nature, 378, 355

Mazeh, T., Naef, D., Torres, G., et al. 2000, The Astrophysical Journal, 532, L55

Mendonça, J. M., Grimm, S. L., Grosheintz, L., & Heng, K. 2016, The Astrophysical Journal, 829, 115

Mendonça, J. M., Tsai, S.-M., Matej, M., Grimm, S. L., & Heng, K. 2018, arXiv:1808.00501 [astro-ph], arXiv: 1808.00501

Mollière, P., Boekel, R. v., Dullemond, C., Henning, T., & Mordasini, C. 2015, The Astrophysical Journal, 813, 47

Morbidelli, A., Lambrechts, M., Jacobson, S., & Bitsch, B. 2015, Icarus, 258, 418

Morel, T., Butler, K., Aerts, C., Neiner, C., & Briquet, M. 2006, Astronomy & Astrophysics, 457, 651

Morello, G., Waldmann, I. P., Tinetti, G., et al. 2015, The Astrophysical Journal, 802, 117

Morley, C. V., Knutson, H., Line, M., et al. 2017, The Astronomical Journal, 153, 86

Moses, J. I. 2014, Philosophical Transactions of the Royal Society A: Mathematical, Physical and Engineering Sciences, 372, 20130073

Motalebi, F., Udry, S., Gillon, M., et al. 2015, Astronomy & Astrophysics, 584, A72

Nakajima, T., Oppenheimer, B. R., Kulkarni, S. R., et al. 1995, Nature, 378, 463

Newton, I. 1675, Isaac Newton letter to Robert Hooke, 1675, Letter

Öberg, K. I., Murray-Clay, R., & Bergin, E. A. 2011, The Astrophysical Journal, 743, L16

Oliphant, T. E. 2015, Guide to NumPy (Austin, Tex.: Continuum Press), oCLC: 982090469

Öpik, E. J. & Singer, S. F. 1961, Physics of Fluids, 4, 221

Oreshenko, M., Lavie, B., Grimm, S. L., et al. 2017, The Astrophysical Journal, 847, L3

Ormel, C. W. & Klahr, H. H. 2010, Astronomy and Astrophysics, 520, A43

Ormel, C. W. & Kobayashi, H. 2012, The Astrophysical Journal, 747, 115

Parker Loyd, R. O., France, K., Youngblood, A., et al. 2016, The Astrophysical Journal, 824, 102

Pasquini, L., Pallavicini, R., & Pakull, M. 1988, , 191, 253

Payne, C. H. 1925, PhD thesis, RADCLIFFE COLLEGE.

Perets, H. B. & Murray-Clay, R. A. 2011, The Astrophysical Journal, 733, 56

Peretti, S., Ségransan, D., Lavie, B., et al. 2018, arXiv: 1805.05645, arXiv: 1805.05645

Pinfield, D. J., Beaulieu, J.-P., Burgasser, A. J., et al. 2013, , 84, 1154

Piso, A.-M. A., Youdin, A. N., & Murray-Clay, R. A. 2015, The Astrophysical Journal, 800, 82

Pollack, J. B., Hubickyj, O., Bodenheimer, P., et al. 1996, Icarus, 124, 62

Poppe, G. P. M. & Wijers, C. M. J. 1990, ACM Transactions on Mathematical Software, 16, 38

Press, W. H. 2007, Numerical recipes: the art of scientific computing (Cambridge, UK; New York: Cambridge University Press), oCLC: 212427139

Przybilla, N., Nieva, M.-F., & Butler, K. 2008, The Astrophysical Journal, 688, L103

Rafikov, R. R. 2005, The Astrophysical Journal, 621, L69

Rafikov, R. R. 2006, The Astrophysical Journal, 648, 666

Raymond, S. N., Barnes, R., & Mandell, A. M. 2008, Monthly Notices of the Royal Astronomical Society, 384, 663

Raymond, S. N., Quinn, T., & Lunine, J. I. 2004, Icarus, 168, 1

Rebolo, R., Osorio, M. R. Z., & Martín, E. L. 1995, Nature, 377, 129

Redfield, S. & Linsky, J. L. 2002, The Astrophysical Journal Supplement Series, 139, 439

Ribas, I., Font-Ribera, A., & Beaulieu, J.-P. 2008, The Astrophysical Journal, 677, L59

Robinson, R. D., Cram, L. E., & Giampapa, M. S. 1990, The Astrophysical Journal Supplement Series, 74, 891

Rogers, P. D. & Wadsley, J. 2011, Monthly Notices of the Royal Astronomical Society, 414, 913

Rosenthal, M. M., Murray-Clay, R. A., Perets, H. B., & Wolansky, N. 2018, The Astrophysical Journal, 861, 74

Sanchis-Ojeda, R., Rappaport, S., Winn, J. N., et al. 2014, The Astrophysical Journal, 787, 47

Sanders, J. & Kandrot, E. 2011, CUDA by example: an introduction to general-purpose GPU programming (Upper Saddle River, NJ: Addison-Wesley)

Santerne, A., Fressin, F., Díaz, R. F., et al. 2013, Astronomy & Astrophysics, 557, A139

Schuler, S. C., Flateau, D., Cunha, K., et al. 2011, The Astrophysical Journal, 732, 55

Schumann, V. 1896, The Astrophysical Journal, 4, 144

Segura, A., Kasting, J. F., Meadows, V., et al. 2005, Astrobiology, 5, 706

Shu, F. H., Adams, F. C., & Lizano, S. 1987, Annual Review of Astronomy and Astrophysics, 25, 23

Singh, K. P., Tandon, S. N., Agrawal, P. C., et al. 2014, Montréal, Quebec, Canada, 91441S

Smith, B. A. & Terrile, R. J. 1984, Science, 226, 1421

Spake, J. J., Sing, D. K., Evans, T. M., et al. 2018, Nature, 557, 68

Stevenson, K. B., Harrington, J., Nymeyer, S., et al. 2010, Nature, 464, 1161

Suess, H. E. 1962, Journal of Geophysical Research, 67, 2029

Takeda, Y. & Honda, S. 2005, Publications of the Astronomical Society of Japan, 57, 65

Teske, J. K., Cunha, K., Smith, V. V., Schuler, S. C., & Griffith, C. A. 2014, The Astrophysical Journal, 788, 39

Teske, J. K., Schuler, S. C., Cunha, K., Smith, V. V., & Griffith, C. A. 2013, The Astrophysical Journal, 768, L12

The Microlensing Observations in Astrophysics (MOA) Collaboration & The Optical Gravitational Lensing Experiment (OGLE) Collaboration. 2011, Nature, 473, 349

Tian, F. 2015, Annual Review of Earth and Planetary Sciences, 43, 459

Tomkin, J., Lemke, M., Lambert, D. L., & Sneden, C. 1992, The Astronomical Journal, 104, 1568

Toomre, A. 1964, The Astrophysical Journal, 139, 1217

Torres, G. 2007, The Astrophysical Journal, 671, L65

Trifonov, T., Kürster, M., Zechmeister, M., et al. 2018, Astronomy & Astrophysics, 609, A117, arXiv: 1710.01595

Trotta, R. 2008, Contemporary Physics, 49, 71

Turner, J. D., Pearson, K. A., Biddle, L. I., et al. 2016, Monthly Notices of the Royal Astronomical Society, 459, 789

Van Eylen, V., Agentoft, C., Lundkvist, M. S., et al. 2018, Monthly Notices of the Royal Astronomical Society, 479, 4786

Vidal-Madjar, A., Blamont, J. E., & Phissamay, B. 1973, Journal of Geophysical Research, 78, 1115

Vidal-Madjar, A., Désert, J.-M., Lecavelier des Etangs, A., et al. 2004, , 604, L69

Vidal-Madjar, A., Huitson, C. M., Bourrier, V., et al. 2013, Astronomy & Astrophysics, 560, A54

Vidal-Madjar, A., Lecavelier des Etangs, A., Désert, J.-M., et al. 2003, Nature, 422, 143

Vidal-Madjar, A. & Thomas, G. 1978, Planetary and Space Science, 26, 863

Vidotto, A. A., Lichtenegger, H., Fossati, L., et al. 2018, arXiv:1808.00404 [astro-ph], arXiv: 1808.00404

Visser, R. G. & Ormel, C. W. 2016, Astronomy & Astrophysics, 586, A66

Vogt, S. S., Burt, J., Meschiari, S., et al. 2015, The Astrophysical Journal, 814, 12

Volkov, A. N., Johnson, R. E., Tucker, O. J., & Erwin, J. T. 2011, The Astrophysical Journal, 729, L24

Waldmann, I. P., Rocchetto, M., Tinetti, G., et al. 2015a, The Astrophysical Journal, 813, 13

Waldmann, I. P., Tinetti, G., Rocchetto, M., et al. 2015b, The Astrophysical Journal, 802, 107

Watson, A. J., Donahue, T. M., & Walker, J. C. 1981, Icarus, 48, 150

Wheeler, J. C. & Sneden, C. 1989, Annual Review of Astronomy and Astrophysics, 27, 279

Wilkins, A. N., Deming, D., Madhusudhan, N., et al. 2014, The Astrophysical Journal, 783, 113

Williams, C. R. . C. 2006, Gaussian Processes for Machine Learning (The MIT press)

Winn, J. N. 2010, Exoplanet Transits and Occultations, ed. S. Seager (University of Arizona Press), 55–77

Wolszczan, A. & Frail, D. A. 1992, Nature, 355, 145

Wood, B. E. 2004, Living Reviews in Solar Physics, 1

Wood, B. E., Redfield, S., Linsky, J. L., Muller, H., & Zank, G. P. 2005, The Astrophysical Journal Supplement Series, 159, 118

Wu, C. Y. R. & Chen, F. Z. 1993, Journal of Geophysical Research: Planets, 98, 7415

Xu, Z., Bai, X.-N., & Murray-Clay, R. A. 2017, The Astrophysical Journal, 847, 52

Yelle, R. V. 2004, Icarus, 170, 167

Youngblood, A., France, K., Loyd, R. O. P., et al. 2016, The Astrophysical Journal, 824, 101

Zaghloul, M. R. & Ali, A. N. 2011, ArXiv e-prints [[arXiv]1106.0151]

Zeng, L. & Sasselov, D. 2013, Publications of the Astronomical Society of the Pacific, 125, 227